

Institute of Physics
Faculty of Materials Engineering and Technical Physics
Poznań University of Technology

DISSERTATION

Influence of structure and composition on
properties of Fe-based magnetic
materials — a DFT study

Wojciech Marcin Marciniak

Supervisor: dr hab. inż Mirośław Werwiński, prof. IFM PAN



Poznań 2024

An expert is a person who has found out by his own painful experience all the mistakes that one can make in a very narrow field.

—Niels Bohr^a—

I thank all the people whose influence ultimately, despite all the hardships, led to the creation of this work: family, friends, and teachers — at all stages of education. I am grateful to all collaborators and fellow researchers, whose insights and constructive critique led to the improvements of articles constituting this thesis. I appreciate the support — of my friends, supervisors throughout my academic career, and, last but foremost, my wonderful wife — in this long yet valuable voyage.

This work has been conducted as part of my employment in the Sonata Bis grant awarded to Dr. Mirosław Werwiński under the decision DEC-2018/30/E/ST3/00267. The work on the conformation-picking scheme development has been financed by the Polish Ministry of Science and Higher Education under the grant DI2017/007947. Calculations were performed in the Poznan Supercomputing and Networking Center (PSNC/PCSS) on software compiled with the substantial involvement of Daniel Depcik and Paweł Leśniak. I am grateful for over a year spent in the Materials Theory Division at the Physics and Astronomy Department of Uppsala University in Uppsala, Sweden, partly thanks to the Sonata Bis project and mainly thanks to the financial support of the Polish National Agency for Academic Exchange under the decision BPN/BEK/2022/1/00179/DEC/1 in the Bekker NAWA program. Discussions with the open and welcoming MT community influenced many articles that are part of this thesis.

Tack så mycket!

^aAttributed to Niels Bohr by Edward Teller; the Author of this thesis is currently more inclined toward the notion that the principles of mathematical induction apply here — there is always room for the $(n + 1)^{\text{th}}$ mistake.

Abstract

Magnetic materials lay the foundations for a significant part of modern technology. From efficient bulk permanent magnets containing rare earth elements such as $\text{Nd}_2\text{Fe}_{14}\text{B}$, through rare earth-free thin films based on L1_0 phases, hexaferrites, to magnetically soft ferrite phases. The chemical element that connects the above-mentioned materials is iron. These materials can be found in the ton-weighting cores of electric transformers and the stators and rotors of electric generators present in wind turbines and hydroelectric power plants. Smaller electric motors are prevalent all around us. A single, non-electrical car can have dozens of them. Magnetic materials are also indispensable in acoustics, being part of microphones and speakers. Magnetic micro- and nanostructures are the basis of hard disk drives and some types of transistors.

Magnetic materials studied in this thesis include both ferromagnetic [$\text{Fe}_{1-x}\text{Co}_x$, Fe-Co-C, L1_0 FePt, $(\text{Fe}_{1-x}\text{Co}_x)_2\text{B}$] and antiferromagnetic [YbFe_4Al_8] systems. The influence of structural parameters on the magnetic properties, i.e., magnetocrystalline anisotropy energy, spin and orbital magnetic moments, and magnetic phase transition temperatures, is investigated here using quantum mechanical methods with particular emphasis on density functional theory. Electronic structure analysis in the YbFe_4Al_8 antiferromagnet, based mainly on the electronic density of states, focuses on elucidating the effects of computational treatment on the proper ytterbium valence reproduction. The magnetism of YbFe_4Al_8 , determined by the iron sublattice, is also resolved based on the energetic preference of one of the multiple possible antiferromagnetic orderings. The influence of structural deformations and short- and long-range ordering on magnetic properties are investigated in the $\text{Fe}_{1-x}\text{Co}_x$ and carbon-doped $\text{Fe}_{1-x}\text{Co}_x$ systems. Following the lead of the influence of heavier dopants on the electronic structure of iron and consequently on its magnetic properties, the influence of $5d$ atoms is studied in the $(\text{Fe}_{1-x}\text{Co}_x)_2\text{B}$ matrix. The same aspect was investigated in combination with the structural order in the L1_0 FePt phase. Methods for producing structures with potentially favorable magnetic properties are proposed based on parameters such as the enthalpy of formation/mixing or phase-transition energy profiles.

The articles constituting this dissertation contribute to the understanding of the influence of the structure and chemical composition on the magnetic properties of iron alloys. This work presents the effect of the chemical neighborhood of iron atoms on the electronic structure of the material and, consequently, their magnetic properties. Part of the study concerns ordered structures, such as L1_0 FePt, with a magnetocrystalline anisotropy value of up to extremely high 20 MJ m^{-3} . The range of iron and cobalt concentrations in $\text{Fe}_{1-x}\text{Co}_x$, for which it is possible to obtain favorable magnetocrystalline anisotropy energy with values of the order of $1\text{--}3 \text{ MJ m}^{-3}$ (satisfactory for most applications), is extended to alloys containing between 25% and 100% cobalt.

Streszczenie

Materiały magnetyczne stanowią podwaliny znacznej części nowoczesnej technologii. Od wydajnych magnesów trwałych zawierających pierwiastki ziem rzadkich, takich jak $\text{Nd}_2\text{Fe}_{14}\text{B}$, poprzez cienkie warstwy bez pierwiastków ziem rzadkich oparte na fazach $L1_0$, heksaferryty, po magnetycznie miękkie fazy ferrytowe. Pierwiastkiem chemicznym łączącym wyżej wymienione materiały jest żelazo. Materiały te można znaleźć w ważących wiele ton stojanach i wirnikach generatorów elektrycznych, które znajdują się w turbinach wiatrowych i elektrowniach wodnych, a także w rdzeniach transformatorów elektrycznych. Mniejsze silniki elektryczne są wszechobecne. Pojedynczy, nieelektryczny samochód może mieć ich dziesiątki. Materiały magnetyczne są również niezbędne w akustyce, będąc częścią mikrofonów i głośników. Mikro- i nanostruktury magnetyczne są podstawą działania dysków twardych i niektórych typów tranzystorów, a więc tanich i sprawdzonych rozwiązań w elektronice.

Materiały magnetyczne badane w niniejszej rozprawie obejmują zarówno układy ferromagnetyczne [$\text{Fe}_{1-x}\text{Co}_x$, Fe-Co-C , $L1_0$ FePt , $(\text{Fe}_{1-x}\text{Co}_x)_2\text{B}$], jak i antyferromagnetyczne [YbFe_4Al_8]. Wpływ parametrów strukturalnych na właściwości magnetyczne, tj. energię anizotropii magnetokrystalicznej, wartości spinowych i orbitalnych momentów magnetycznych oraz temperatury przejścia fazowego, jest badany przy użyciu metod mechaniki kwantowej, ze szczególnym naciskiem na teorię funkcjonału gęstości. Analiza struktury elektronowej w antyferromagnetyku YbFe_4Al_8 , oparta głównie na gęstości stanów elektronowych, koncentruje się na wyjaśnieniu wpływu parametrów obliczeń na właściwą reprodukcję walencyjności iterbu. Prezentowana jest także struktura magnetyczna YbFe_4Al_8 , wynikająca z konfiguracji podsięci atomów żelaza, która została wyznaczona na podstawie preferencji energetycznej jednego z wielu możliwych uporządkowań antyferromagnetycznych. Wpływ odkształceń strukturalnych oraz uporządkowania krótko- i dalekosiężnego na właściwości magnetyczne jest badany w układach czystego i domieszkowanego węglem stopu $\text{Fe}_{1-x}\text{Co}_x$. Podążając za tropem wpływu cięższych domieszek na strukturę elektronową żelaza, a w konsekwencji na jego właściwości magnetyczne, badany jest wpływ domieszek atomów 5d w matrycy $(\text{Fe}_{1-x}\text{Co}_x)_2\text{B}$. Ten sam efekt w połączeniu z uporządkowaniem strukturalnym w fazie $L1_0$ FePt . Na podstawie parametrów, takich jak entalpia tworzenia/mieszania lub profile energii przejścia fazowego, proponowane są metody wytwarzania struktur o potencjalnie korzystnych parametrach magnetycznych.

Artykuły wchodzące w skład niniejszej rozprawy przyczyniają się do zrozumienia wpływu struktury i składu chemicznego na właściwości magnetyczne stopów żelaza. W pracy przedstawiono wpływ sąsiedztwa chemicznego atomów żelaza na strukturę elektronową materiału, a w konsekwencji na jego właściwości magnetyczne. Część badań dotyczy struktur ekstremalnie uporządkowanych, takich jak $L1_0$ FePt , o wartości anizotropii magnetokrystalicznej sięgającej 20 MJ m^{-3} . Zakres stężeń żelaza i kobaltu w $\text{Fe}_{1-x}\text{Co}_x$, dla których możliwe jest uzyskanie korzystnych parametrów magnetycznych o wartościach rzędu $1-3 \text{ MJ m}^{-3}$ (zadowalających dla większości zastosowań), rozszerzono na stopy zawierające od 25% do 100% kobaltu.

Contents

1	Guide	7
1.1	Motivation, aim, context	7
1.2	Introduction to the theory	8
1.3	Methods implementation	12
1.4	Considered materials	15
1.5	Articles description	16
2	Copies of the articles	19
2.1	Electronic structure of YbFe_4Al_8 antiferromagnet: A combined X-ray photoelectron spectroscopy and first-principles study	19
2.2	Giant magnetocrystalline anisotropy energy in Fe–Co alloy under uniaxial compression: first-principles prediction	30
2.3	Structural and magnetic properties of Fe–Co–C alloys with tetragonal deformation: A first-principles study	37
2.4	Structural transformation and magnetic properties of $(\text{Fe}_{0.7}\text{Co}_{0.3})_2\text{B}$ alloys doped with $5d$ elements: A combined first-principles and experimental study	55
2.5	DFT calculation of intrinsic properties of magnetically hard phase L1_0 FePt	68
3	Summary and Conclusions	74
	Appendices	87
A	Co-authors contribution statements	87

The following PhD thesis is based on five scientific articles (four published and one manuscript available online and submitted for publication). The manuscripts are accompanied by a short Guide, which is intended to be a concise yet complete reference that gives a proper context for analyzing the articles constituting the thesis. The goal of this accompanying material is not to provide any solid theoretical background by itself, though it summarizes the main literature about the subject. The formulas presented there serve the purpose of showing the practical side of performed calculations. The articles constituting the dissertation are listed below. Then, the detailed contents of the Guide, which is the first part of the thesis, are presented. The core of this work consists of copies of the above-mentioned articles. The manuscripts are being republished according to the respective publishers' guidelines for inclusion in a proper thesis. The dissertation is concluded with a brief summary of the key results presented in the articles, followed by a popular science version of this summary, delivered in Polish and English. Other works of the Author, which offer the broader context of the conducted research, are summarized in a separate bibliography list at the end of the thesis. The five articles constituting the thesis are referenced henceforth by Roman numerals [I–V].

Scientific Articles Constituting the Dissertation

- ^IW. Marciniak, G. Chełkowska, A. Bajorek, A. Kowalczyk, A. Szajek, and M. Werwiński, “Electronic structure of YbFe_4Al_8 antiferromagnet: A combined X-ray photoelectron spectroscopy and first-principles study”, [Journal of Alloys and Compounds](#) **910**, 164478 (2022).
- ^{II}W. Marciniak, J. Marciniak, J. Á. Castellanos-Reyes, and M. Werwiński, “Giant magnetocrystalline anisotropy energy in Fe–Co alloy under uniaxial compression: first-principles prediction”, [arXiv preprint](#), [10.48550/arXiv.2409.11388](#) (2024).
- ^{III}W. Marciniak and M. Werwiński, “Structural and magnetic properties of Fe-Co-C alloys with tetragonal deformation: A first-principles study”, [Physical Review B](#) **108**, 214433 (2023).
- ^{IV}A. Musiał, W. Marciniak, Z. Śniadecki, M. Werwiński, P. Kuświk, B. Idzikowski, M. Kołodziej, A. Grabias, M. Kopcewicz, J. Marcin, and J. Kováč, “Structural transformation and magnetic properties of $(\text{Fe}_{0.7}\text{Co}_{0.3})_2\text{B}$ alloys doped with $5d$ elements: A combined first-principles and experimental study”, [Journal of Alloys and Compounds](#) **921**, 166047 (2022).
- ^VJ. Marciniak, W. Marciniak, and M. Werwiński, “DFT calculation of intrinsic properties of magnetically hard phase L1_0 FePt”, [Journal of Magnetism and Magnetic Materials](#) **556**, 169347 (2022).

As stated in the beginning, the Guide aims to provide context for non-trivial elements of the discussion delivered in the articles. It begins with a short introduction to the work's aim and motivation, followed by the necessary theoretical background on magnetism, a description of the considered materials, and an overview of methods providing context for understanding the choices made throughout the research process. The extent of details

provided in the Guide is aimed at being sufficient to explain the selection of computational codes and methods used throughout the work. As such, it is a short yet handy supplement to the articles that do not go into much detail about the computational background.

The introductory part, which discusses the motivation, aim, and context of the work, focuses on the repercussions of the geopolitical situation on the fragile market of elements crucial for the development of modern technology. It shows how iron is still a vital matrix for various materials engineering methods in the context of this development. The theoretical introduction provides a basic understanding of the inclusion of magnetism within the density functional theory (DFT) framework.

The methods' description begins with a presentation of the topics regarding computational solutions of equations, which are given in the theoretical introduction. It concerns basis selection, methods for building potential, and integration/differentiation schemes. Then, the two methods of relativity treatment are described. The topics regarding the scalability of the calculations come after, such as the atomic ordering treatment and mapping the system's configurational space. A brief summary of chemical disorder treatment methods follows—the virtual crystal approximation (VCA), the coherent potential approximation (CPA), and special quasirandom structures (SQS)—compared to a full configurational space mapping. The Methods section concludes with a brief description of the codes used throughout the work.

Iron is presented as an excellent ingredient in the fabrication of magnetic materials, which is well-known yet still surprising. Then, various methods of structural changes for the enhancement of the magnetic properties of a material are listed. Those include inducing energetically non-optimal states, utilizing topological states, or various degrees of atomic ordering. The methods of manufacturing such materials from the experimental point of view are then briefly summarized. Subsequently, the focus is changed to the internal structure of the materials, starting from presenting relevant types of magnetism and contributions from the electronic structure. The materials description part concludes with a discussion of the orbital hybridization effects on the magnetic properties and introducing higher-dimensionality of orbitals by $3d$, $4d$, and $5d$ doping, as well as the influence of rare-earth elements. The Guide ends with a description of articles presented in this broader context. A more general link between the papers is delivered as the conclusion of the subsection.

The key part of the thesis consists of five article manuscripts, reprinted here. They are preceded by a short description of the Author's contribution to each paper. The contribution statements of the co-authors are compiled separately into the Appendix A and included after the Thesis. The articles are presented as published in the final author form. Four of the works have been published in prestigious international journals: the Journal of Magnetism and Magnetic Materials, the Journal of Alloys and Compounds, and Physical Review B. The fifth manuscript is—as of the submission of this thesis—unpublished yet and available online as an open preprint on the arXiv platform.

The achievements resulting from the research presented in the thesis are then summarized and delivered along with the main conclusions from the articles. The thesis constituents conclude with a popular science summary for a broader audience.

1 Guide

1.1 Motivation, aim, context

With magnetic devices shrinking in size and improving in efficiency, as in the case of magnetic recording media, there is a growing effort to improve both the effectiveness and precise customization of the materials themselves [1]. Several promising candidates have emerged for specific applications. In particular, in renewable energy applications, rare-earth-based permanent magnets, such as Nd–Fe–B, Sm–Co, and Sm–Fe–N, are attracting attention [2, 3]. Ordered high-symmetry layered structures like $L1_0$ FePt and $L1_0$ CoPt are being investigated for their suitability as magnetic thin films [4, 5]. There is also a wide range of medium-range solutions, spanning applications between small and large scales. These include magnets for cost-effective lower-end recording media and other traditional applications, like voice transmission. Traditional options such as alnico and hexaferrites dominate this range with emerging manganese-based compounds, postulated recently as an optimal new research direction [6, 7].

Rare-earth (RE) elements are undoubtedly prominent in the mentioned materials, mainly due to their large spin-orbit coupling (SOC). However, the so-called *rare earth crisis* of 2011 raised concerns about the fragility of the rare-earth-elements market and started a widespread discussion on their application in the most efficient permanent magnets [2]. This crisis, which resulted in a several-fold increase in the prices of REs, was caused by a combination of factors. First, the majority of RE purification has been performed in a narrow set of countries, mainly in China, due to less strict policies regarding labor costs, work conditions, and air pollution. Secondly, during the last twenty years, we have seen a tremendous growth of new high-tech solutions—mainly for digital data processing and renewable energy—that resulted in a vastly growing demand for efficient magnetic materials (a field dominated by REs). Such a significant increase in demand, combined with political tensions between the USA and China, resulted in the RE prices being used as leverage, resulting in the RE market instability [8].

Even though the situation stabilized in subsequent years, concerns remain. This has been especially true in recent years, following the semiconductor crisis of 2018 and the COVID-19 pandemic of 2019–2021, when the REs market instability simultaneously hit again (though with less impact than the semiconductor shortage itself). The situation regarding new technologies’ strong dependency on rare-earth elements in the context of the pandemic and the recent war in Ukraine has been summarized in a recent econometrical work by Yang *et al.* [9]. Although the authors there do not provide exact prescriptions besides a vague statement about the still observed strong correlation between the high-tech industry (and renewable energy market) and REs, the solutions have been proposed since before the rare-earth crisis. One such option was to revisit the ideas proposed in the late 20th century. A notable example of this approach was the investigation of the $\text{Fe}_{1-x}\text{Co}_x$ disordered alloy for x of about 0.6 and the ratio of lattice parameters of about 1.22—indicating strong tetragonal deformation. This structure attracted particular interest due to the predicted high magnetocrystalline anisotropy energy (MAE) of $\sim 800 \mu\text{eV atom}^{-1}$ and average magnetic moment of approximately $2.5 \mu_{\text{B}} \text{ atom}^{-1}$. The new alloy joined ordered high-symmetry layered structures (like FePt, FeNi, and CoPt $L1_0$ phases), alnico, and hexaferrites in the expanding family of rare-earth-free hard magnetic materials. Also, rare-earth-based permanent magnets, like Nd–Fe–B alloys, have

been optimized for lowering the RE content while retaining satisfactory magnetic properties [3]. Many of those materials share a common component—iron. This relatively cheap and long-known 3d material, from which (lat. *ferrum*) the ferromagnetic behavior has taken its name, still provides an excellent object of study, unveiling new intricacies of the behavior at the quantum level.

The articles constituting the thesis aim to improve the understanding of the influence of chemical composition and crystal structure on intrinsic magnetic properties of iron-based magnetic alloys, mainly through density functional theory (DFT) calculations. The study’s goal is to search for new magnetic materials to support technological advances and elucidate processes governing the structural contribution to the alloy’s magnetic properties at the atomic scale. Various magnetic, structural, and magneto-structural phases are studied. The calculations’ outcomes are compared to experimental results present in the literature and, wherever possible, directly supplemented by experimental results obtained by groups with which the Author has collaborated.

Together, the works [I–V] provide a considerable overview of the iron magnetism in iron-based alloys and compounds, concluding in several promising candidates for magnetic material applications. The works are at the center of current efforts in the research group and already gained attention in the magnetic materials community.

1.2 Introduction to the theory

At the core of computational quantum physics lies the determination of the energetic structure of the examined system. In the simplest approximation it starts with solving the Shrödinger equation—eigenvalue equation of the quantum system:

$$\hat{\mathcal{H}}|\Psi\rangle = E|\Psi\rangle, \quad (1.1)$$

where the system’s physics is encoded in the Hamiltonian $\hat{\mathcal{H}}$, which for the classic solution of interacting set of particles should consider nucleus–nucleus, nucleus–electron, and electron–electron interactions, as well as the interaction with any external field. Several widely used approximations simplify the problem. The atomic nuclei can be considered fixed in place at the timescales of the electron motion. They are also considerably heavier. As such, the coordinates of electrons and nuclei can be decoupled in the so-called Born-Oppenheimer approximation. The electron–electron interaction remains the analytically unsolvable many-body problem. Hence, another widely used approximation is the linear combination of atomic orbitals (LCAO), where the electron–electron part is expressed in terms of non-interacting single-electron basis functions.

In the solution to this equation, as proposed in the Hartree-Fock theory, each energy eigenfunction is assumed to be definable in terms of a single antisymmetrized product of those basis functions, called a Slater determinant. This whole recipe was provided almost 100 years ago by Hartree [10] and shortly after reformalized simultaneously yet separately by Fock and Slater [11, 12]. However, in real systems, the exact wave function cannot be fully described by a single Slater determinant. This leads to omitting part of the electron correlation stemming from the Coulomb interaction, as pointed out in the 1950s by Löwdin [13]. However, this approach to the solution is mathematically exact regarding the included terms.

Leaving Hartree, Fock, and Slater alone and proceeding further over 30 years, another approach to the same problem has been undertaken by Hohenberg and Kohn [14], and shortly after Kohn and Sham [15], resulting in the Kohn-Sham density functional theory (DFT). In this approach, the electron-density-dependent energy functional is solved in place of the wavefunction-dependent energy, as the electron density ρ shown in Ref. [14] to carry the same information. This functional can be expressed as^a:

$$E[\rho] = T_S[\rho] + E_H[\rho] + \int v_{\text{ext}}(\vec{r})\rho(\vec{r})d\vec{r} + E_{\text{XC}}[\rho], \quad (1.2)$$

where $T_S[\rho]$ is the Kohn-Sham kinetic energy summed over Kohn-Sham orbitals φ_i :

$$T_S[\rho] = \sum_{i=1}^N \int \varphi_i^*(\vec{r}) \left(-\frac{\hbar^2}{2m} \nabla^2 \right) \varphi_i(\vec{r}) d\vec{r}, \quad (1.3)$$

E_H is the Hartree — or Coulomb — energy:

$$E_H[\rho] = \frac{e^2}{2} \iint \frac{\rho(\vec{r})\rho(\vec{r}')}{|\vec{r} - \vec{r}'|} d\vec{r}' d\vec{r}, \quad (1.4)$$

and v_{ext} is the external potential acting on the system — minimally the electron–nuclei interaction. $E_{\text{XC}}[\rho]$ is the electron exchange–correlation energy. It is the only unknown in which dependency on ρ can only be approximately derived.

The exact, non-approximated solution to the eigenstate problem of the quantum system is traditionally called an *ab initio* or first-principles approach. Hence, the bare Hartree-Fock method is *ab initio*. The situation is more complicated in both the Kohn-Sham DFT and a hybrid Hartree-Fock approach. The only part of Eq. 1.2, which is not guaranteed to be derived from first-principles, is the exchange–correlation potential $V_{\text{XC}}[\rho]$. This thesis focuses on *ab initio* solutions to problems, which is a major factor in the exchange–correlation potential choice. The functional parametrization proposed by Perdew, Burke, and Ernzerhof [16] — extensively used in this work — is *ab initio*, similar to its later modification PBE0 [17]. It is important to note, however, that there exist multiple exchange–correlation potentials in the PBE family, which are not *ab initio*, like PBEsol [18].

Solving Eq. 1.1 or Eq. 1.2 yields information about the energy eigenstates in relation to the wavevector in reciprocal space, called the energy band plot $n(E, \vec{k})$, where the states n are represented in the basic approach by δ -like function. Adding spin polarization to the equation, as most modern implementations do, allows the system’s magnetism to be captured at several different theory levels. Obtaining the spin magnetic moment (the total difference in occupation of two spin channels) is trivial and usually does not require user input in most DFT codes.

The majority of the interesting, magnetism-related phenomena and properties appear only in the relativistic regime. Here, due to, at minimum, the atom’s internal mag-

^aThroughout the work, standard physical properties and constant denotations are used — i.e., m for mass, q for electric charge, p for momentum, c for the speed of light, e for the elementary charge, k_B for the Boltzmann constant, and \hbar for the reduced Planck constant. \uparrow denotes the majority and \downarrow the minority spin channel. Mathematical notions are as verbose as possible, i.e., \vec{x} denotes vector x , \hat{y} denotes operator y . Real-space positions are denoted by \vec{r} , and the reciprocal space of the wave vector is described by \vec{k} . Convention for the imaginary unit is i .

netic field, the system's eigenstates undergo splitting, revealing a so-called fine structure. From this splitting originates the second property of interest—the magnetocrystalline anisotropy energy (MAE). A material possesses MAE if its internal energy depends on the spontaneous magnetization direction with respect to the main crystallographic axes. A phenomenological formula:

$$\text{MAE}(\theta, \phi) = K_1 \sin^2 \theta + K_2 \sin^4 \theta + K_3 \sin^4 \theta \cos 4\phi \quad (1.5)$$

describes MAE dependency on polar angles (θ, ϕ) in the tetragonal crystal symmetry [19].

Assuming K_3 is relatively small compared to K_1 and K_2 , the $\text{MAE}(\theta, \phi)$ amplitude, henceforth simplified to MAE, is the difference of the energy of the system in two magnetization directions:

$$\text{MAE} = E(\theta = 90^\circ) - E(\theta = 0^\circ) = E_{100} - E_{001}. \quad (1.6)$$

Simultaneously, treating the system's energy as an integral over the electronic states density n —or a sum over all energy eigenvalues ϵ_i —MAE can also be decomposed, according to mean field theory, in the following way [20]:

$$\text{MAE} = \int_V \int_0^{E_F} E [n(E, \vec{r})_{100} - n(E, \vec{r})_{001}] dE d\vec{r} \stackrel{\text{Ref. [21]}}{=} \sum_{occ} \epsilon_{i_{100}} - \sum_{occ'} \epsilon_{i_{001}} + O(\delta\rho^n), \quad (1.7)$$

where $O(\delta\rho^n)$ is the correction term. Estimating MAE from Equations 1.5 and 1.6 is code-independent. Applicability of Eq. 1.7 depends on the code implementation, but this approach is the most flexible as the sums can be wave-vector-, real-space-, or orbital-resolved, depending on the basis. Similarly to the spin magnetic moment, the orbital magnetic moment usually does not require any interaction from the user side, provided the proper relativistic treatment of the system.

The last essential part of understanding the context of this thesis is critical temperature estimation. Equation 1.1 solves the stationary, ground state of a system. Time-dependent DFT (TD-DFT) allows for consideration of non-equilibrium spectroscopic properties, and dynamic mean-field theorem (DMFT) allows for temperature calculation. Full thermal properties incorporation requires a proper statistical ensemble construction, which can also be provided via molecular dynamics methods. There, the calculations can be performed not only by explicitly including quantum mechanics but also by DFT-derived machine-learning interatomic potentials. Such calculations are still immensely costly.

However, some of the system's thermal properties can be deduced from its ground state, given a few basic principles. Such reasoning has been applied, e.g., in work [V]. Averaging according to thermal statistical distributions can also be a surprisingly accurate approximation [III]. Atom movement (molecular dynamics) can also be decoupled from magnetic moments movement (spin dynamics), which can then be treated in the Landau-Lifshitz-Gilbert formalism [22]. Temperature-dependent properties like critical temperatures—Curie temperature (T_C) or Néel temperature (T_N) can also be stochastically sampled according to the Metropolis (quantum) Monte Carlo algorithm [23]. For the system energy evaluation in the case of the Monte Carlo simulations, usually, the Heisenberg Hamiltonian is applied:

$$\hat{\mathcal{H}}_{\text{Heisenberg}} = \sum_i \sum_j J_{ij} \vec{e}_i \cdot \vec{e}_j, \quad (1.8)$$

written in the basis $\vec{e}_i = \frac{\vec{m}_i}{m_i}$ (notation of Liechtenstein *et al.* [20]). This Hamiltonian can be extended in terms of Dzyaloshinskii–Moriya interaction \vec{D}_{ij} , magnetic anisotropy constant K , external magnetic field \vec{B}_{ext} , etc. [24]:

$$\begin{aligned} \hat{\mathcal{H}}_{\text{Extended}} = & \sum_i \sum_j J_{ij} \vec{e}_i \cdot \vec{e}_j + \sum_i \sum_j \vec{D}_{ij} \cdot (\vec{e}_i \times \vec{e}_j) + \\ & + \sum_i K_i \left(\hat{e}_i \cdot \vec{e}_i^K \right) + \sum_i \vec{B}_{\text{ext}} \cdot \vec{e}_i + (\dots). \end{aligned} \quad (1.9)$$

In this work, in the case where the Monte Carlo method has been used [II], there is no external magnetic field, and the influence of magnetic anisotropy and Dzyaloshinskii–Moriya interaction has proven to be negligible.

The critical temperature can also be estimated from zero-kelvin ground-state calculations. This approach, which is called disorder local moments and originates in mean field theory (DLM-MFT), approximates the temperature needed for the magnetic phase transition as the temperature at which the classical movement of magnetic moments in the system overcomes the energy preferability of the magnetically ordered system [25, 26]:

$$T_{\text{critical}}^{\text{DLM}} = \frac{2}{3} \frac{E_{\text{DLM}} - E_{\text{ordered}}}{k_{\text{B}} \cdot c}, \quad (1.10)$$

if the ferromagnetic state is energetically favorable, and:

$$T_{\text{critical}}^{\text{DLM}} = 0 \quad (1.11)$$

otherwise. Here, c stands for magnetic atoms content. Such an approach is doomed to bear significant quantitative error, yet it has proven to be accurate enough for qualitative analysis. Obtaining a proper DLM disordered state is a challenge that will be addressed further in the Guide.

Another approach can be chosen to study the influence of temperature on the system. Proper equations can be solved with constraints on chosen degrees of freedom in the system. Such an approach devised by Moruzzi *et al.* is called the fixed spin moment (FSM) method, described in Ref. [27] and references therein. It can provide for extrapolating even as complicated values as MAE for finite-temperature conditions by fixing magnetic moments at realistic, non-zero T values — as applied in works [IV, V].

In the end, the outlined background shows the basic derivation principles of magnetocrystalline anisotropy energy and the critical temperature. Determining spin and orbital magnetic moments is fully implemented in the utilized codes. These properties are key aspects studied in works [I–V]. Article-specific parameters are introduced in *Calculation Details* or *Results* sections of respective manuscripts — like the ordering parameters in work [III].

1.3 Methods implementation

Equations provided in Sec. 1.2 can be solved in DFT using different basis wavefunction sets, mathematical formalisms, relativity treatments, exchange-correlation potentials, and various methods of chemical disorder treatment. Those choices lead to differences in the efficiency and accuracy of the performed calculations. One has to judge the desired level of this trade-off for each case separately. Despite being rough and quantitatively incorrect, some approximations can also be particularly useful in describing specific system properties.

The exact nature of the exchange-correlation potential is unknown. Initial approximations related to the free electron gas model were based on the potential being dependent on a charge (or spin) density at a given point. This assumption is called local (spin) density approximation [L(S)DA] and led to the development of numerous exchange-correlation potentials. Exchange-correlation contribution to the system's energy in L(S)DA picture, as summarized by Gunnarsson and Lundqvist, and references therein [28] can hence be generally expressed as:

$$E_{\text{XC}}^{\text{LSDA}} = \int \rho_0(\vec{r}) \epsilon_{\text{XC}}[\rho_{\uparrow}(\vec{r}), \rho_{\downarrow}(\vec{r})] d\vec{r}. \quad (1.12)$$

Such an approximation has proven insufficient, leading to the sprouting of potentials dependent on local charge density and its gradient. These exchange-correlation potentials, stemming from so-called generalized gradient approximation (GGA) [29], can be described as summarized by Perdew *et al.* [16]:

$$E_{\text{XC}}^{\text{GGA}} = \int \rho_0(\vec{r}) \epsilon_{\text{XC}}[\rho_{\uparrow}(\vec{r}), \rho_{\downarrow}(\vec{r}), \vec{\nabla} \rho_{\uparrow}(\vec{r}), \vec{\nabla} \rho_{\downarrow}(\vec{r})] d\vec{r}. \quad (1.13)$$

One of the most widely used GGA potentials is the one in the parametrization of Perdew, Burke, and Ernzerhof, known as PBE or—in older works—PBE96 [16]. It is possible to include higher order ρ dependencies, resulting in meta-GGA potentials. These are commonly used for the description of molecules in quantum chemistry and defects in solid-state physics. Hence, they are also a well-known tool in materials science. Such approaches are, however, beyond the scope of this work.

A few points are here to be made regarding the magnetism treatment, considering the bare Schrödinger equation is undoubtedly ruled out, as it does not care about the particle spin, and electrons are $\frac{1}{2}$ -spin particles. It was Pauli in 1927, who included spin into the equation, though still in the non-relativistic limit, where for the $\frac{1}{2}$ -spin particles in the external field \vec{A} and the electric scalar potential ϕ , the Hamiltonian resolves to [30]:

$$\hat{\mathcal{H}} = \left[\frac{1}{2m} (\vec{\sigma} \cdot (\hat{\vec{p}} - 1\vec{A}))^2 + q\phi \right]. \quad (1.14)$$

The spontaneous emergence of spin is only observed in the relativistic treatment of the system. Such an approach was devised by Dirac in 1928 [31]. In the most general form, including effective field \vec{B}_{eff} and potential \vec{V}_{eff} , which incorporate external effects and effects stemming from the exchange-correlation potential as implemented in code by Ebert *et al.* [32], this Hamiltonian takes the form:

$$\hat{\mathcal{H}}_{\text{Dirac,SPR-KKR}} = \frac{\hbar}{i} c \hat{\alpha} \cdot \vec{\nabla} + \hat{\beta} m c^2 + V_{\text{eff}}(\vec{r}) + \hat{\beta} \vec{\sigma} \cdot \vec{B}_{\text{eff}}(\vec{r}), \quad (1.15)$$

where anti-commutative operators $\hat{\alpha}$ and $\hat{\beta}$ are:

$$\hat{\alpha}_i = \begin{pmatrix} 0 & \sigma_i \\ \sigma_i & 0 \end{pmatrix}, \hat{\beta} = \begin{pmatrix} \mathbb{1} & 0 \\ 0 & -\mathbb{1} \end{pmatrix}, \quad (1.16)$$

and 0 are 2×2 empty matrices, $\mathbb{1}$ are 2×2 unitary matrices, and σ_i are the 2×2 Pauli matrices:

$$\sigma_x = \begin{pmatrix} 0 & 1 \\ 1 & 0 \end{pmatrix}, \sigma_y = \begin{pmatrix} 0 & -i \\ i & 0 \end{pmatrix}, \sigma_z = \begin{pmatrix} 1 & 0 \\ 0 & -1 \end{pmatrix}. \quad (1.17)$$

Simultaneously, in the first-order perturbation, in the angular form, Dirac equation can take the form:

$$\hat{\mathcal{H}}_{\text{rel}} = \hat{\mathcal{H}}_0 - \frac{\hat{p}^4}{8m^3c^2} - \frac{\hbar^2}{4m^2c^2} \frac{dV}{dr} \frac{\partial}{\partial r} + \frac{dV}{dr} \vec{S} \cdot \vec{L}, \quad (1.18)$$

where spin angular momentum vector components $S_i = \hbar/2 \cdot \sigma_i$, and \vec{L} is the orbital angular momentum. In short:

$$\hat{\mathcal{H}}_{\text{rel}} = \hat{\mathcal{H}}_{\text{Schrödinger}} + \hat{\mathcal{H}}_{\text{mass-velocity}} + \hat{\mathcal{H}}_{\text{Darwin}} + \hat{\mathcal{H}}_{\text{SOC}}, \quad (1.19)$$

where the computationally-demanding spin-orbit coupling term $\hat{\mathcal{H}}_{\text{SOC}}$ can be cut and substituted by simplified alternatives. Such approximation is called the scalar-relativistic approximation, as the three vector components can be easily decoupled.

Calculating the effective potential is a costly operation. Hence, various methods have been developed to simplify the shape and radial distribution of the interatomic potentials, including muffin-tin orbitals (MTO) approximation originating from works of Korringa [33], and Kohn and Rostoker [34], and linearized version of such approach — LMTO [35, 36].

An approximate solution to the computational cost problem may also be relatively simply solved by fitting the potential to specific properties-conserving functions. The all-electron interatomic potential varies significantly in the closest vicinity of the atomic core. In this regime, it is also relatively weakly affected by electron–electron interactions. Hence, the notion of *pseudopotential* has been introduced in an attempt to replace the complicated effects of the core (non-valence) electrons of an atom with the nucleus with an effective potential. This change is then incorporated into the Coulombic (or Hartree) potential term in Eq. 1.2 [37]. Unfortunately, this approach does not describe well strongly-correlated systems. Additionally, such an extreme approximation of the potential shape can considerably affect the accuracy of the MAE estimation. On the other hand, the proper implementation allows for $\mathcal{O}(n)$ complexity order of calculations [38, 39].

An intermediate solution is to approximate the potential shape while not restricting it to a particular solution. Atomic sphere approximation (ASA), where the basis functions are set to be contained and screened within a homogeneous sphere of the volume equal to

this of the Wigner-Seitz cell, was soon applied to the LMTO method [40]. Not long after, a similar solution was applied to Green's function-based Korringa-Kohn-Rostoker (KKR) method [41, 42]. This method has been shown to work well for the electronic structure of transition metals [43]. Yet, for higher dimensionality of the required atomic basis, the discrepancies between ASA and full-potential calculations increase dramatically [44]. Hence, the intricate properties of systems going beyond tight-binding models are best treated in the full-potential approach without shape approximations.

More considerable savings can be made with the incorporation of chemical disorder treatment. Investigating random alloy properties and ordering dependencies typically requires sampling a considerable portion of the alloy's configurational space. As work [III] shows, it is—in principle—possible. Such a method of investigation is immensely costly at calculations walltime usage, which can easily exceed one million core-hours^b. This toll is especially significant if the research goal is not a broad-range study of the system but rather the derivation of a single desired property of the system. In this case, one can apply approximation by introducing an effective medium or a sort of averaged atom at the atomic place that is about to be subject to a random population.

The most basic yet surprisingly qualitatively accurate method is the virtual crystal approximation (VCA) [45]:

$$Z_{A_xB_{1-x}}^{\text{VCA}} = xZ_A + (1-x)Z_B, \quad (1.20)$$

which assumes replacement of the disordered system A_xB_{1-x} with an effective atom of the atomic number Z being an arithmetic average of those of elements A and B. This approximation, however, is limited only to alloys of elements neighboring in the periodic table and can yield vast quantitative errors.

More complicated coherent potential approximation (CPA) [46, 47] is based on spectral response of the effective system, measured by scattering operator τ^{nn} being an average of the responses of the two sublattices $\tau^{nn,A}$ and $\tau^{nn,B}$:

$$\tau^{nn,\text{CPA}} = x_A\tau^{nn,A} + x_B\tau^{nn,B}, \quad (1.21)$$

which is converged self-consistently. This approach has one massive advantage over others. It makes it possible to realize the DLM approach to critical temperature calculation in practice by creating a pseudo-CPA state of disordered A_xB_{1-x} system as $A_{\uparrow\frac{x}{2}}B_{\uparrow\frac{1-x}{2}}B_{\downarrow\frac{1-x}{2}}A_{\downarrow\frac{x}{2}}$ on top of the standard CPA chemical disorder treatment.^c

Despite both VCA and CPA allowing for some research on ordering dependencies in a system, the most accurate solution is still as complete as possible explicit configurational space mapping. The sampling can be optimized by employing neighbor radial distribution analysis, e.g., special quasirandom structures (SQS) [48]. This method relies on finding the most random neighbor patterns by identifying the most disordered structures with respect to all radial correlation functions, similar to the α parameter described in work [III].

Based on the above theory summary, the codes utilized across the works in this thesis can be introduced with a brief reasoning of why they were employed.

^bTypical measure of computing power usage, equivalent to using one CPU core for one hour, sometimes restricted also by RAM/core. Note that, due to multithreading, a typical research project can utilize tens or even hundreds of years worth of core-hours in a single calendar year.

^cThe seemingly weird order of spin and chemical content contributions here are strict and related to specific computational procedures.

The spin-polarized relativistic Korringa-Kohn-Rostoker method, as implemented in the SPR-KKR package (ver. 7.6.0 and 7.7.1) [32], was used primarily due to its fully relativistic CPA treatment of systems. ASA calculations were performed limitedly, especially for preliminary calculations in works [II, V]. The code is well parallelized, including an embarrassingly parallel solution for energy path integration, reasonable for up to 32 CPU cores in the case of the presented calculations. However, the non-localized, system geometry-dependent basis was a non-optimal solution, rendering initial geometry optimization doubtful.

The most utilized code across all of the articles included in this work [I–V], as well as in a few other works by the Author [A, B], is the full-potential local-orbital (FPLO) code, mainly in version 18.00 [49, 50]. It was primarily due to being full-potential—which is critical for MAE calculations—with the highly localized basis, combined with an excellent single-thread optimization at the expense of the lack of multithreading. The flaw of being single-threaded was negligible in the applications in this work as, in many solutions, big-scale calculations were performed, which relied on the embarrassingly parallel solution of multiple simultaneous program instance invocations, reaching up to several thousand on a 30-thousand-core cluster at the Poznan Supercomputing and Networking Center. In a few instances [II, V], the older, 5.00 version of the code was used due to its inclusion of CPA. The CPA calculation mode, though, incorporates neither fully relativistic nor GGA treatment of the system, and hence, it has been used only for basic calculations like the unit cell volume optimization in work [II].

Uppsala atomistic spin dynamics (UppASD) [22] is an implementation of atomistic spin dynamics and Monte Carlo simulations utilized in work [II].

Other popular DFT codes exist, including VASP, SIESTA, ONETEP, or Gaussian. However, they were not used because they were either pseudopotential (inaccurate), plane-wave basis (costly for future layered systems calculations), or a combination of both.

1.4 Considered materials

Magnetic materials are indispensable components of modern technology. Soft magnetic materials with low MAE are key elements in all solutions where efficient trapping of the electromagnetic field is needed, from transformer cores to low-frequency alternating current ferrite filters, such as those found on data cords like USB cables. High MAE (hard) magnets are used in tonnes in electric generators and motors, which are at the core of renewable energy solutions. Hard magnetic materials in the form of magnetic recording media are also the basis of data manipulation and storage. This recording method is the most widely used today and will probably remain an undisputed leader of mass data storage with the advent of new technologies, such as heat-assisted magnetic recording (HAMR) [51].

In 2004, Burkert *et al.* published an article in Physical Review Letters in which they announced the results of a study predicting the existence of the region of giant magnetocrystalline anisotropy energy in uniaxially strained Fe–Co random alloy. They proposed this structure belonging to the Bain path [52], with x equal to about 0.6 and c/a lattice parameters ratio close to 1.22, to be achievable by epitaxial growth [53]. Strained Fe–Co was fabricated in following years as an epitaxial thin layer on Pd(001) [54–56], Ir(001) [55, 56], and Rh(001) substrates [55–57]. Bulk Fe–Co with Pt interlayers has been

also obtained [58–60]. In either case, the measured magnetic properties—energy product and coercive field indicated a much lower MAE value than predicted by Burkert *et al.*

This discrepancy was addressed by several groups using more sophisticated chemical disorder treatment methods such as SQS in the work by Neise *et al.* [61], CPA in the article by Turek *et al.* [62], and random mapping of the configurational space in $2 \times 2 \times 2$ supercells performed by Steiner *et al.* [63]. A promising result has been shown by Turek *et al.*, indicating that although these chemical disorder treatment methods reveal four-fold lower MAE values that are also closer to experimental values, the MAE can be significantly increased in ordered FeCo B2 structure. However, Fe–Co films were soon after shown to relax rapidly towards the bcc structure with a negligible MAE above a critical thickness of about 2 nm (15 atomic monolayers) [64]. As a method of stabilizing the system, interstitial doping with small atoms was proposed [65], akin to the strain-inducing N-doping of α'' -Fe in Fe_{16}N_2 [66, 67]. Systems stabilized by boron [68] and carbon [64, 69–71] were soon created experimentally, but these realizations did not reach the strain predicted by calculations regarding the (B, C, N)-doped systems [65, 66, 72–76].

Another method of increasing magnetocrystalline anisotropy energy and magnetic moments in the system is doping the system with heavier atoms, which exhibit higher SOC [77]. Such additions were studied, e.g., as an interlayer in pure bcc Fe [78], in Fe_5PB_2 system [79], and in $(\text{Fe}_{1-x}\text{Co}_x)_2\text{B}$ [80]. Speaking about spin-orbit coupling, the undisputed leaders in this topic are 4f rare-earth additives. Rare-earth-based permanent magnets did not fall out of the scope. The topic of looking for better RE-based magnets has been discussed by Coey [3] (and in many other works by Skomski and Coey). Much effort is also being put into developing efficient recycling methods [81–83].

Turek *et al.* showed that atomic ordering towards the B2 structure in the FeCo stoichiometric alloy greatly enhances MAE [62]. B2 structure is a layered bcc AB system in which atomic planes of atom types A and B are alternately layered. The fcc equivalent of this structure is the L1_0 phase, shown to possess exceptional magnetic hardness in FePt, FeNi, or CoPt phases [84–88]. FeNi—*tetrataenite*—discovered as a constituent of meteorites is, however, extremely difficult to obtain [A]. FePt and CoPt are, on the other hand, proposed for HAMR applications—a new technology yet currently being introduced in data storage by Seagate in their *Mosaic 3+* platform, announced to allow for exceeding 30 TB per disk limit soon and 50 TB in near future [89]. This company has successfully followed the roadmap announcing planned HAMR commercialization in recent years.

1.5 Articles description

Electronic structure of YbFe_4Al_8 antiferromagnet: A combined X-ray photoelectron spectroscopy and first-principles study

The first work [I] is the only one regarding iron in magnetic ordering other than ferromagnetic, and the study’s subject is the only studied RE-containing (specifically, ytterbium-containing) alloy. In particular, this work concerns antiferromagnetic 1–4–8 alloy YbFe_4Al_8 , in which the magnetism is governed by the iron sublattices. It was carried out in collaboration with experimentalists, and the key findings concern the revision of computational methods’ influence on reproducing the correct valence of the dopant atom. Three antiferromagnetic arrangements were investigated, and the influence of the intra-

atomic exchange correction term U on electronic state occupancy was studied. Calculations were mainly performed using the FPLO code within the fully relativistic treatment of the system. As described in the work, such an approach is particularly important for a system containing $4f$ electrons. The extent of this work is limited compared to further articles presented in this dissertation due to the size of the required unit cell. Results suggest that the system prefers AFM-C (antiparallel columns) antiferromagnetic configuration. Given the GGA treatment, no $+U$ amendment is needed for the best results. Overall, the topic is niche, and the work, though comprehensive, has received limited attention so far. Nevertheless, this article resulted from fruitful collaboration with the experimental group and laid the foundations for future works.

Giant magnetocrystalline anisotropy energy in Fe–Co alloy under uniaxial compression: first-principles prediction

Work [II] enters the scope of high throughput calculations in a relevant and lively topic. It focuses on revisiting the tetragonal distortion in the Fe–Co system with state-of-the-art computational methods and presenting the painted picture in a broader scope. The initial idea originated during the realization of the Master’s thesis from the co-author’s experience at the Materials Theory Division of Uppsala University, Sweden [65], where the first discovery of the giant magnetocrystalline anisotropy in distorted Fe–Co alloy have been reported in 2004 [53]. An earlier article regarding the disordered Fe–Co alloy has already been published in the group, including a contribution from the Author [C]. Ever since the work has evolved into its current form and now considers fundamental magnetic properties of the Fe–Co alloy along one of the proposed pathways of the full face-centered cubic (fcc) \leftrightarrow body-centered cubic (bcc) \leftrightarrow hexagonal close-packed (hcp) \leftrightarrow fcc structure transition. Also, the different magnetic states of iron are considered, including the fcc high-spin phase. Cobalt adds another layer to the material’s intricate electron structure by introducing the interplay between iron and cobalt’s ferromagnetism types. Most of the calculations are performed in full-potential SPR-KKR scheme with PBE exchange-correlation potential. Curie temperature for $\text{Fe}_{0.3}\text{Co}_{0.7}$ was calculated utilizing the Monte Carlo module in UppASD, using an immense exchange integral cutoff radius. Performing such calculations for the whole T_C map was deemed inadequate in computational time cost compared to the scientific value of such results. Quantitative results for the single scan were enough to judge the usability of the newly proposed high-MAE structure. Hence, for a qualitative investigation of T_C change across differing cobalt concentrations in the system, DLM approximation has been employed. For the structural stability evaluation and assessing the influence of geometry optimization on the MAE results, the calculations were started in FPLO5, with LDA potential, and using the scalar-relativistic approach. It is worth noting that particular structure deformations can be achieved via lattice vibrations and play a crucial role, e.g., in the currently studied topic of ultrafast de- and remagnetization processes. This topic is beyond the scope of this work—it has been, however, considered by the Author for other system [D]. Ultimately, this work reports an entirely new Fe–Co structure with high Co content, which possesses excellent magnetic properties—very high MAE coupled with high average magnetic moment per atom and outstanding Curie temperature.

Structural and magnetic properties of Fe–Co–C alloys with tetragonal deformation: A first-principles study

As discussed in Sec. 1.4, stabilizing the Fe–Co structure is challenging. Work [III] discusses the energetic considerations of interstitially-doped Fe–Co alloys. It describes the relation between atomic structure and magnetic properties in the material by studying a vast portion of the configurational space of $(\text{Fe–Co})_{16}\text{C}$ alloy, which has a composition close to many experimental realizations. This article focuses on the heightened MAE region in the already-known regime of uniaxial strain in the system. Calculations began with initial cell volume and atomic position optimization in VCA, with the fully relativistic system treatment in FPLO code. The work focuses on chemically ordered structures and the influence of chemical ordering on the magnetic properties of the Fe–Co system. Using the full-potential FPLO approach, with PBE exchange-correlation potential, all inequivalent atomic arrangements possible in the stoichiometric $(\text{Fe,Co})_{16}\text{C}$ are studied. It is shown that some ordered structures exhibit exceptionally good magnetic properties for atomic content as high as 75% of iron. The structure has already been the base for further thin film studies of particular structures of this system [90].

Structural transformation and magnetic properties of $(\text{Fe}_{0.7}\text{Co}_{0.3})_2\text{B}$ alloys doped with $5d$ elements: A combined first-principles and experimental study

Next, another modification to the Fe–Co-based alloy is studied. In work [IV], high throughput calculations give way to a thorough, systematic search. Article presents influence of different $3d$, $4d$ and $5d$ impurities on magnetic properties of the $(\text{Fe}_{0.7}\text{Co}_{0.3})_2\text{B}$ system. FPLO code with PBE exchange-correlation potential and the fully relativistic approach is used. Chemical disorder between iron and cobalt is treated in the VCA, and the dopant is modeled as a single iron/cobalt atom substitution in a supercell containing four formula units. Two systems, $(\text{Fe}_{0.675}\text{Co}_{0.275}\text{Re}_{0.05})_2\text{B}$, and $(\text{Fe}_{0.675}\text{Co}_{0.275}\text{W}_{0.05})_2\text{B}$, are investigated more thoroughly, with the Re-doped system treated in the FSM approach. The results are compared to an earlier work conducted in ASA and experimental results delivered by coworkers. DFT calculations are complemented with experimental measurements performed by a collaborating group.

DFT calculation of intrinsic properties of magnetically hard phase L1_0 FePt

In the end, with work [V], the scope of the calculations narrows to a single system belonging to the L1_0 phase family — yet the computational analysis is comprehensive and incorporates various approaches in two computational codes. It regards L1_0 FePt phase, which is analogous to L1_0 FeNi studied by the Author previously [A]. Earlier approaches to this candidate for HAMR applications are revisited. Anisotropy constants K_1 and K_2 are calculated alongside the Curie temperature and the magnetostriction coefficient. MAE and magnetic moment values obtained using various exchange-correlation potentials and approaches in two codes (SPR-KKR and FPLO) are compared. The FSM method is used in the argument about realistic-temperature MAE values. This work has already found its continuation as a thin-film study performed in the group by J. Marciniak and M. Werwiński [91], and continued further for similar other systems [B].

2 Copies of the articles

This section is the core of the thesis. It contains the Author's contribution statements, followed by copies of the manuscripts [I–V] in the order presented in Sec 1.1.

Electronic structure of YbFe_4Al_8 antiferromagnet: A combined X-ray photoelectron spectroscopy and first-principles study

I am the first and corresponding author of work [I]. I contributed to all stages of the research, starting from conceptualization through calculations, results analysis, and visualization of part of the calculations. I also wrote part of the section regarding calculations and reviewed and edited the whole manuscript. I coordinated the work on this manuscript and have been the contact person during the submission process.

Giant magnetocrystalline anisotropy energy in Fe–Co alloy under uniaxial compression: first-principles prediction

I am the first and one of the corresponding authors of work [II]. I ran all of the calculations included in the manuscript and most of the preliminary calculations which laid the foundations for this work. I analyzed the data and prepared aggregated csv data files containing the results. I also prepared all the figures and wrote the initial version of the manuscript, subsequently incorporating the co-authors' suggestions. I was responsible for coordinating the collaboration of this article and submitting it to a scientific journal.

Structural and magnetic properties of Fe–Co–C alloys with tetragonal deformation: A first-principles study

In work [III], I have been the first and corresponding author. I ran all the calculations, analyzed data, prepared all figures, and wrote the whole article. Subsequently, I implemented the co-author's suggestions and amendments to data visualization and text. I have also been the contact person during the submission process. Due to the massively parallel nature of the calculations, I also prepared aggregated csv data files containing the results.

Structural transformation and magnetic properties of $(\text{Fe}_{0.7}\text{Co}_{0.3})_2\text{B}$ alloys doped with 5d elements: A combined first-principles and experimental study

I have been the second author of work [IV] and the first author doing calculations. My main contribution concerns the analysis of the calculation results, with minor assistance in results validation, writing, reviewing, and editing proper sections of this article.

DFT calculation of intrinsic properties of magnetically hard phase L1_0 FePt

I am the second author of work [V]. I participated in preparing the overall concept, conducted SPR-KKR calculations, and validated the FPLO results. Subsequently, I significantly altered the manuscript, followed by other minor review and editing-related tasks. I also contributed to revising the referees' comments.



Contents lists available at ScienceDirect

Journal of Alloys and Compounds

journal homepage: www.elsevier.com/locate/jalcom

Electronic structure of YbFe₄Al₈ antiferromagnet: A combined X-ray photoelectron spectroscopy and first-principles study



Wojciech Marciniak^{a,b,*}, Grażyna Chełkowska^c, Anna Bajorek^c, Andrzej Kowalczyk^a,
Andrzej Szajek^a, Mirosław Werwiński^a

^a Institute of Molecular Physics, Polish Academy of Sciences, M. Smoluchowskiego 17, 60-179 Poznań, Poland

^b Institute of Physics, Faculty of Materials Engineering and Technical Physics, Poznań University of Technology, Piotrowo 3, 61-138 Poznań, Poland

^c Institute of Physics, University of Silesia in Katowice, 75 Pułku Piechoty 1A, 41-500 Chorzów, Poland

ARTICLE INFO

Article history:

Received 23 September 2021

Accepted 6 March 2022

Available online 29 March 2022

Keywords:

Density functional theory

X-ray photoelectron spectroscopy

YbFe₄Al₈

Transition metal rare-earth alloys

Antiferromagnetism

ABSTRACT

Depending on their chemical composition, Yb compounds often exhibit different valence states. Here we investigate the valence state of YbFe₄Al₈ using X-ray photoelectron spectroscopy (XPS) and first-principles calculations. The XPS valence band of YbFe₄Al₈ consists of two contributions coming from divalent (Yb²⁺) and trivalent (Yb³⁺) configurations. The determined value of the valence at room temperature is 2.81. Divalent and trivalent contributions are also observed for core-level Yb 4d XPS spectra. We study several collinear antiferromagnetic models of YbFe₄Al₈ from the first-principles and for comparison we also consider LuFe₄Al₈ with a fully filled 4f shell. We predict that only Fe sublattices of YbFe₄Al₈ carry significant magnetic moments and that the most stable magnetic configuration is AFM-C with antiparallel columns of magnetic moments. We also present a Mulliken electronic population analysis describing charge transfer both within and between atoms. In addition, we also study the effect of intra-atomic Coulomb U repulsion term applied for 4f orbitals on Yb valence and Fe magnetic moments.

© 2022 Published by Elsevier B.V.

1. Introduction

Yb-based compounds exhibit a number of interesting properties that include mixed-valence, heavy fermion behavior, Kondo effect, magnetic ordering, and superconductivity [1]. The compound considered in this work, YbFe₄Al₈, belongs to the ThMn₁₂ family of intermetallic compounds with the general formula XT₄Al₈, where X is the rare-earth or actinide element and T is the transition-metal element [2–4]. Other examples of Yb-based compounds in the XT₄Al₈ family are YbCr₄Al₈, YbMn₄Al₈, and YbCu₄Al₈ [2], while the isostructural configuration with Co has not been confirmed. In this section, we will introduce the subject of the valency of YbFe₄Al₈ in comparison with other Yb compounds. We will also discuss the issues related to the complex magnetic configuration of YbFe₄Al₈ and present a model of the crystallographic structure of the considered compound.

1.1. Valence of Yb-based compounds

One motivation for studying YbFe₄Al₈ is to determine its valence. Most lanthanides in the metallic state are trivalent, except for Eu and Yb, which are divalent [5,6]. Since Yb has sixteen electrons outside the core, a 4f orbital filled with fourteen electrons is usually stable, and two electrons can participate in the bond. And indeed, a divalent state is observed for metallic Yb [7]. However, the small energy difference observed between the divalent and trivalent states means that Yb in compounds often occurs in the trivalent state or states with valence between two and three.

The set of valence values estimated from measurements for a series of Yb compounds takes on a wide range from two to three [8]. Examples of valence estimates made from measurements are 2.38 for YbFe₂Al₁₀ [9], 2.68 for Yb₂Si₂Al [10], and 2.93 for YbRh₂Si₂ [11]. Yb compounds with mean valence are usually classified as fluctuating (mixed) or intermediate valence compounds. While fluctuating valence suggests dynamic transition processes between two valence states, intermediate valence implies the simultaneous presence of two valence states with specific ratios. It is not uncommon to put the same material into both categories based on similar experimental results, where a well-known example is YbAl₃ [12–14]. A valence band, similar to the one observed for YbFe₄Al₈ [15], consisting of

* Corresponding author at: Institute of Molecular Physics, Polish Academy of Sciences, M. Smoluchowskiego 17, 60-179 Poznań, Poland.

E-mail address: wojciech.robe.marciniak@doctorate.put.poznan.pl (W. Marciniak).

contributions from Yb²⁺ and Yb³⁺ has been previously observed for both materials classified as valence fluctuating, such as YbCu₂Si₂ [16], YbAl₂ [17,18], YbB₁₂ [19], Yb₂Pt₆Ga₁₅ and Yb₂Pt₆Al₁₅ [20], as well as for materials of intermediate valence, such as YbFe₄Sb₁₂ [21], YbInCu₄ [22], YbNi_{0.8}Al_{4.2} [23], YbRh₂Si₂ [11], Yb₄Ga₂₄Pt₉ [24], and Yb₂Si₂Al [10]. Since our experimental analysis is based solely on XPS measurements, we cannot unambiguously resolve the membership of the compound under consideration, YbFe₄Al₈, in the class of fluctuating or intermediate valence materials. However, previous studies remain consistent that the valence of the considered compound is close to three [2,4,15]. Suski cites hard-to-find results of Shcherba *et al.* indicating for YbFe₄Al₈ a valence of 3.00(5) [4], which is consistent with the observed slight positive volume deviation of YbFe₄Al₈ from the trend for a series of mostly trivalent RFe₄Al₈ compounds. As noted by Kummer *et al.* [25], compounds in which the deviation from trivalency is small are among the most interesting since, in this regime, there is a transition from a magnetically ordered ground state to a paramagnetic one.

1.2. Magnetic properties of YbFe₄Al₈

Although the YbFe₄Al₈ compound has been known since at least 1976 [2], it attracted the most interest in the first decade of the 21st century [26–29,30,15,31]. This was probably due to its misassignment [26,32] to the group of RFe₄Al₈ superconducting compounds, like, for example, ScFe₄Al₈ ($T_c = 6$ K), YFe₄Al₈ ($T_c = 6$ K), and YCr₄Al₈ ($T_c = 4.5$ K) [32,33]. However, a later study denied YbFe₄Al₈ membership in the superconducting group [29,30]. A critical analysis of the presence of a superconductive phase in YbFe₄Al₈ has led to an explanation of the phenomenon of thermally driven magnetization reversal, sometimes also called negative magnetization [29,30]. The Néel point of the Fe antiferromagnetic sublattice of YbFe₄Al₈ is about 140 K [34]. As the temperature decreases, a decrease in magnetization in the external field is observed, and a change in the sign of magnetization occurs when the compensation temperature exceeds 34 K [29,30]. Andrzejewski *et al.* concluded that the negative magnetization comes from antiferromagnetic interactions between the magnetic moments on Yb and the canted effective magnetic moments on Fe. The above results for YbFe₄Al₈ are compared by Andrzejewski *et al.* with the results for isostructural LuFe₄Al₈, for which the magnetization observed as a function of temperature is always positive, which the authors relate to the absence of magnetic moments on the Lu sublattice [30]. However, the above explanation of the negative magnetization in YbFe₄Al₈ is somewhat controversial due to the assumption of the presence of a magnetic moment on Yb atoms, which has not yet been explicitly confirmed, while Suski *et al.* indicated the absence of a magnetic moment on Yb in the considered compound [27]. Although the magnetic ordering for the Yb sublattice below 8 K was detected with the ¹⁷⁰Yb Mössbauer effect [27,35] and the effective magnetic moment on Yb ion equal to 4.1 μ_B was indirectly deduced from the magnetic susceptibility measurements [34], Suski *et al.* have shown that at temperatures above 200 K the Yb_{1-x}Sc_xFe₄Al₈ alloys follow the Curie-Weiss law with effective magnetic moments of about 7–8 μ_B /f.u. which do not depend on the composition, indicating that all magnetism in this compound is determined by the Fe sublattice [27]. In a subsequent paper, Suski showed that the magnetic susceptibility of YbFe₄Al₈ is strongly field-dependent, even at temperatures clearly above the antiferromagnetic phase transition, suggesting the existence of a ferromagnetic correlation of unknown origin [36]. Suski, therefore, suggests that ferromagnetic clusters of Fe impurities are responsible for the appearance of negative magnetization in YbFe₄Al₈, which may mimic the presence of a second magnetic sublattice [36]. This seems likely, given that about 5% of the Fe atoms in the YbFe₄Al₈ sample may be located at 8i or 8j sites, as shown by Mössbauer effect measurements [31]. Gaczyński *et al.* suggest that partial disorder

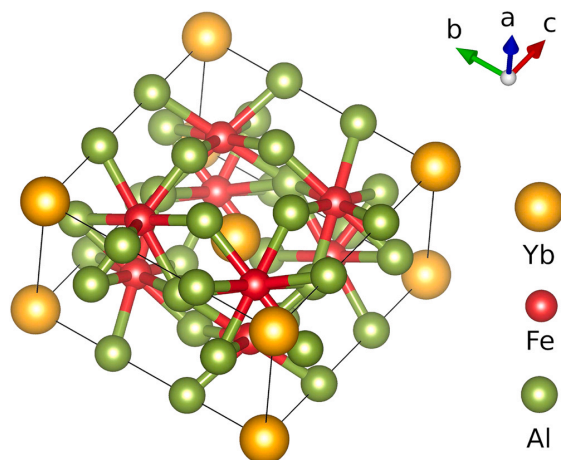


Fig. 1. A model of the crystal structure of the YbFe₄Al₈ compound that crystallizes in a tetragonal structure of the CeMn₄Al₈ type (space group *I4/mmm*, lattice parameters $a = 8.712$ and $c = 5.044$ Å) and is a superstructure of the ThMn₁₂ type.

leads to interacting antiferromagnetic and spin-fluctuating subsystems [28].

The thermally driven reversal magnetization observed in YbFe₄Al₈ is also related to the phenomenon of negative magnetoresistivity detected at low magnetic fields in RM₄Al₈ compounds (including YbFe₄Al₈) [37]. A proposed explanation for this phenomenon is a combination of the Kondo effect with a spin-glass state resulting from crystallographic disturbance [37]. The occurrence of a similar effect, which was the inverse magnetocaloric effect observed in Y_{1-x}Gd_xCo₂ alloys, has been associated with antiferromagnetic or cluster glass behavior [38].

1.3. Crystal structure of YbFe₄Al₈

YbFe₄Al₈ crystallizes in a tetragonal structure of CeMn₄Al₈ type (*I4/mmm* space group, lattice parameters $a = 8.712$ and $c = 5.044$ Å [15]) that is a superstructure of ThMn₁₂ type, see Fig. 1. Lanthanide contraction is the reason that the unit cell volume of YbFe₄Al₈ is one of the smallest among the RFe₄Al₈ compounds [2]. YbFe₄Al₈ unit cell consists of 26 atoms (two formula units) [39,40]. Yb and Fe atoms occupy the 2a and 8f sites, respectively, while Al atoms occupy the 8i and 8j positions. As shown in the example of YbCu₄Ga₈, it is also possible to create more complex superstructures in 1–4–8 systems, which require eight non-equivalent atomic positions for a complete description [1].

2. Methods

2.1. Experimental details

A polycrystalline YbFe₄Al₈ sample was obtained by induction melting of stoichiometric amounts of elements in an argon atmosphere. Details of the preparation are given in earlier work [15,29,30]. X-ray photoelectron spectra were obtained with an Al-K_α source at room temperature using a PHI 5700/660 Physical Electronics Spectrometer. The electron energy spectra were analyzed using a hemispherical mirror analyzer with an energy resolution of approximately 0.3 eV. The Fermi level $E_F = 0$ was related to the binding energy of Au 4f at 84 eV. All emission spectra were measured immediately after breaking up the sample in a vacuum of 10⁻⁹ Torr. High vacuum breaking produced clean surfaces free of oxygen and carbon contamination.

2.2. Computational details

The second part of this paper will present the results of computations performed under density functional theory (DFT). The YbFe₄Al₈ model was investigated using the full-potential local-orbital scheme (FPLO version 18.00–52) [41,42]. The use of the full potential approach is particularly important for 4*f*-electron compounds, for which the results are strongly dependent on the quality of the potential [41]. The second important element of our method is the treatment of relativistic effects in the full 4-component formalism. The use of a fully relativistic method (accounting for spin-orbit coupling) significantly improves the description of 4*f* electrons characterized by a large spin-orbit coupling. For the exchange-correlation potential, we chose the generalized gradient approximation (GGA) with the Perdew–Burke–Ernzerhof (PBE) parametrization [43]. For elements containing 4*f* electrons, it is worth investigating how the results might be affected by the inclusion of an additional Coulomb *U* term of intra-atomic repulsion to the energy functional, described by the GGA+*U* method [44]. In the present work, we used the fully-localized limit of the LSDA+*U* (GGA+*U*) proposed by Czyżyk and Sawatzky [45], which is also known as the atomic limit. The effect of the value of the parameter *U* on the obtained results in the range from 0 to 10 eV has been investigated. Previously, a similar LDA+*U*(4*f*) approach was adopted for YbFe₄Sb₁₂ [46,47]. Furthermore, our previous experience with modeling alloys containing 3*d* elements shows that including the LDA+*U* correction for 3*d* atoms has very little effect on the position of the 3*d* band [48,49], so to simplify the model, we have not included this correction. The calculations were performed on a 20 × 20 × 20 k-mesh with a density accuracy of 10⁻⁶. The site geometry optimization was performed with a force accuracy of 10⁻³ eV Å⁻¹. Details of the geometry optimization will be presented in the next section. Drawings of the crystalline and antiferromagnetic structures were made using the VESTA code [50].

3. Results and discussion

The properties of YbFe₄Al₈, such as the thermally driven magnetization reversal, magnetism of Yb ions, non-trivial valence and antiferromagnetic configuration motivated us to perform studies that we hope will resolve some of the ambiguities. In our previous work on YbFe₄Al₈, we investigated its magnetic and transport properties [15,29,30]. Here we will extend the analysis of X-ray photoelectron spectra presented before [15]. The analysis of the valence band will be followed by the interpretation of selected core-level spectra. In the second part of the work, we will present the results of first-principles calculations focusing on the structural and magnetic properties of the system.

3.1. X-ray photoelectron spectroscopy

3.1.1. Valence band spectrum

While for divalent metallic Yb we observe a rather simple valence band with a 2*F* spin-orbit doublet [7], Yb compounds with a mean valence between two and three reveal a valence band composed of two parts associated with different states before photoemission [52]. Such binary valence band spectra have been observed before for YbFe₄Sb₁₂ [21] and YbInCu₄ [22], for example. As we see in Fig. 2, the valence band of YbFe₄Al₈ also consists of two contributions, from divalent (Yb²⁺) and trivalent (Yb³⁺) configurations. The divalent part (Yb²⁺) is characterized by a doublet derived from the final state 4*f*¹³, while the trivalent part (Yb³⁺) is characterized by a multiplet derived from the final state 4*f*¹². The distance separating the two parts, which in this case is just under 6 eV, is interpreted as the intra-atomic correlation energy [52].

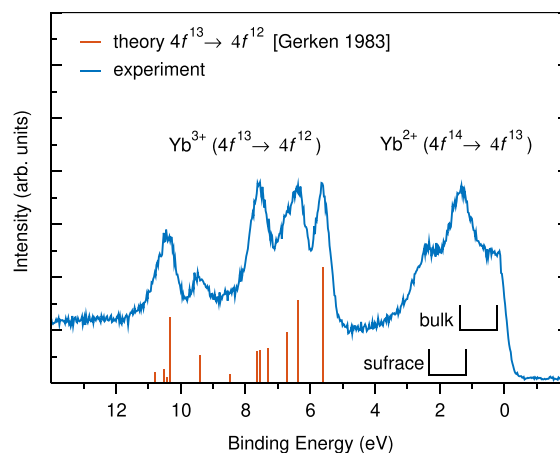


Fig. 2. Valence band of YbFe₄Al₈ measured by X-ray photoelectron spectroscopy at room temperature using Al K_α source with photon energy 1486.6 eV. The experimental result is compared with the multiplet structure of the 4*f*¹³ → 4*f*¹² transition calculated by Gerken [51].

However, we see that the divalent part does not resemble a doublet. This is because XPS measurements using a source with an energy of about 1.5 keV are sensitive to surface effects, resulting in the appearance of a second doublet shifted by about 1 eV toward higher binding energies [11]. Depending on the mutual shift of the doublets, a structure of four or three peaks may appear. A structure similar to the triple one seen in Fig. 2 has been observed, for example, for Yb₂Pt₆Al₁₅ [20]. One way to discard the signal from the surface would be to use hard X-rays with photon energy on the order of a few keVs [20]. Alternatively, also reducing the energy of the source allows to determine the impact of the surface [11]. Since, at a binding energy of about 1 eV, there is a maximum in the signal coming from the Fe 3*d* states, it can be suspected that they may significantly affect the valence band in the vicinity of the Fermi level [15]. Nevertheless, a comparison of photoionization cross-sections for Yb 4*f* (0.0820) and Fe 3*d* (0.0022) orbitals contradicts these speculations [53]. The almost forty-fold difference in favor of Yb 4*f* states, combined with their much larger localization, leads to the conclusion that the contribution from Fe is not significant in the considered range of a few eV from the Fermi level. Similarly, also the contributions from Yb 5*d* 6*s* and Al 3*s* 3*p* states can be neglected [52]. Empirical confirmation of the above predictions is provided by comparing the XPS valence bands of YbFe₄Sb₁₂ and LaFe₄Sb₁₂, showing an absolutely dominant contribution from the Yb 4*f* states [54].

Now we turn to the trivalent multiplet. In Fig. 2, we compared the experimental result with the multiplet structure of the 4*f*¹³ → 4*f*¹² transition calculated by Gerken [51]. However, we shifted the transition diagram by 5.6 eV towards higher binding energies. We determined the value of the 4*f* level shift relative to the Fermi level from the energy difference of the trivalent and tetravalent metallic Yb calculated by Johansson [6]. The observed surface contribution in the divalent part of the valence band provokes the question of an analogous contribution in the trivalent part. Although our result obtained for a photon energy of 1486.6 eV is not conclusive on this question, a series of measurements made for YbRh₂Si₂ at beam energies of 600, 350, and 115 eV revealed that also the multiplet of trivalent Yb consists of contributions from the bulk and surface [11]. However, the small difference in their mutual position (on the order of 0.2 eV) does not allow us to distinguish them as easily as in the case of the divalent part of the valence band. In addition to the beam energy, the observed valence band spectrum is also affected by the

W. Marciniak, G. Chetkowska, A. Bajorek et al.

Journal of Alloys and Compounds 910 (2022) 164478

temperature. For example, XPS valence bands measured for YbInCu₄ at temperatures of 10 and 150 K showed that at a lower temperature, the trivalent contribution decreases and the divalent contribution increases, which is naturally due to the decrease in mean valence (of about 0.1 in this case) [22].

The measured valence band spectra can be used to determine valence. For this purpose, the relative intensity η is determined from the formula:

$$\eta = \frac{I^{(2+)}}{I^{(2+)} + I^{(3+)}} \quad (1)$$

where $I^{(2+)}$ and $I^{(3+)}$ are the integral intensities [11]. The determined value of η is affected by choice of background correction [22] and the difficulty in separating the surface and volume contributions. Assuming that surface and the volume components of the divalent contribution are equal, we obtain η equal to 0.315. Although the relationship $\nu = 3 - \eta$ is usually used to determine the valence (ν) from the relative intensities in Yb compounds, Kummer *et al.* have shown that a more accurate result can be obtained using the cubic function

$$\nu(\eta) = 3 - 0.55\eta - 0.01\eta^2 - 0.44\eta^3. \quad (2)$$

Thus, for YbFe₄Al₈ at room temperature, the determined valence value is 2.81. The effect of surface contributions on the result can be minimized in the future by performing the hard X-ray photoemission spectroscopy (HAXPES) measurements [20]. Using the example of YbFe₄Sb₁₂, Okane *et al.* have shown that low-temperature soft-X-ray synchrotron radiation photoemission spectroscopy (SRPES) can also be very helpful in the valence band analysis of Yb compounds [54].

3.1.2. Core level spectra Yb 4d, Fe 2p, and Al 2p

The mean valence of YbFe₄Al₈ also affects its core-level states. As can be seen in Fig. 3, the core-level spectrum of the Yb 4d orbital is relatively complex and consists of parts derived from the Yb³⁺ and Yb²⁺ configurations. The Yb 4d spectrum can be interpreted based on theoretically predicted multiplets calculated for Yb³⁺ and Yb²⁺ by Ogasawara *et al.* [55]. The divalent doublet consists of spin-orbit split levels, while the trivalent multiplet arises from more complex 4d-4f Coulomb-exchange interactions resulting from incomplete 4f shell occupancy. The measured spectrum reveals that the contributions from the divalent doublet are rather small, confirming that the valence of the compound is closer to three. This also agrees with the

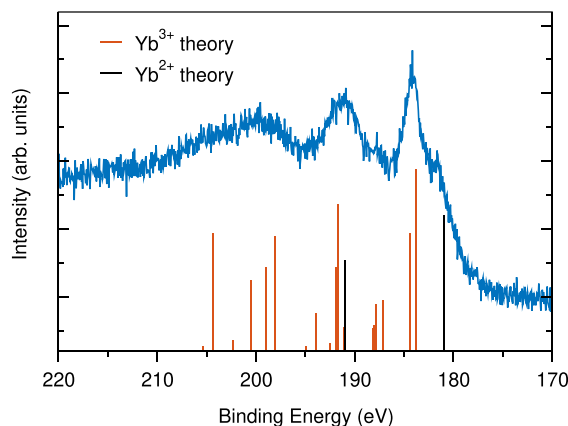


Fig. 3. X-ray photoelectron spectrum of Yb 4d for YbFe₄Al₈ measured at room temperature using Al K_α source with photon energy 1486.6 eV. The experimental result is compared with the multiplet structures of Yb²⁺ and Yb³⁺ computed by Ogasawara *et al.* [55].

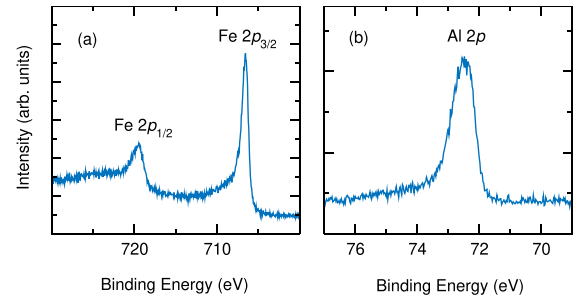


Fig. 4. The XPS spectra of Fe 2p (a) and Al 2p (b) states for YbFe₄Al₈ measured at room temperature using Al K_α source with photon energy 1486.6 eV.

result deduced for the valence band. The presented Yb 4d spectrum can also be compared with the results for Yb metal [56] and other Yb compounds [22,57,58]. This comparison confirms the nature of the spectrum similar to the trivalent state of Yb with a smaller divalent contribution. For mixed-valence compound YbInCu₄ [22], it has been observed that the intensity of the 4d_{5/2} divalent peak around 182 eV strongly decreases with decreasing temperature, which was associated with an increase in valence. Whereas for the mixed-valence alloy (Lu_{1-x}Yb_x)₃Rh₄Ge₁₃ [58] it has been shown that the peak associated with the Yb³⁺ state located around 185 eV increases significantly with increasing Yb concentration.

The spin-orbit split doublet of asymmetric Fe 2p lines having a Doniach-Sunjić shape resembles the corresponding result for pure iron [59] and also shows none of the chemical shifts and charge-transfer satellites characteristic of iron oxides [60], see Fig. 4(a). The determined spin-orbit coupling of Fe 2p doublet (about 13 eV) is similar to the value observed in pure Fe. The position of the Al 2p peak (72.6 eV) observed in Fig. 4(b) is similar to that of pure metal Al (72.7 eV). The observed spectral line broadening we ascribe to spin-orbit splitting and differences in level positions for the two non-equivalent Al positions present in the compound. Relativistic atomic calculations, to be presented later, show that the spin-orbit splitting between the Al 2p_{1/2} and Al 2p_{3/2} states is equal to 0.44 eV.

3.2. First-principles calculations

3.2.1. Theoretical models for Yb and DFT results for XFe₄Al₈ compounds

Although DFT-based models perform quite well in predicting a range of properties of many rare-earth compounds [61], the single-electron nature of local density approximation (LDA), which does not adequately take correlation into account severely limits the quality of results obtained for mixed-valence Yb-based compounds [62]. As a result, the LDA (LDA+U) framework yields a single divalent-type Yb 4f valence band [63,64], instead of a complex two-part divalent/trivalent band as observed from spectroscopy. The successful step toward overcoming this barrier was made in a paper analyzing the effect of pressure on Yb properties, which used LDA-based Quantum Monte Carlo (QMC) methods to determine the valence and to model the valence band of Yb [62]. An alternative approach to modeling the valence band of Yb compounds is the single-impurity Anderson model (SIAM) [11]. This method, although it leads to a two-part 2+/3+ valence band, is based on the approximation of Yb as an impurity, so it is also not applicable to modeling Yb compounds from first-principles.

Earlier DFT results for YbFe₄Al₈ were presented in 2019 by Wang *et al.* in a review paper on RFe₄Al₈ compounds [65], in which, among other things, the authors calculate lattice parameters of YbFe₄Al₈ (8.703 and 5.049 Å), spin magnetic moment on Fe (1.559 μ_B), elastic constants, phonon spectra, bulk, shear, and Young's modulus. Their calculations are based on the full potential (FP) projector augmented

wave (PAW) approach with Perdew-Burke-Ernzerhof (PBE) approximation. In this work, we will improve their model by using a fully relativistic approach and considering an antiferromagnetic configuration. Previously, the antiferromagnetic configuration of Fe sublattices was also addressed in the works of Grechnev *et al.* on RFe₄Al₈ superconductors (R = Sc, Y, Lu) [66–68].

3.2.2. Antiferromagnetic configurations, geometry optimization, and site preferences

Although it is confirmed that there are two magnetic Fe sublattices in the YbFe₄Al₈, the exact type of antiferromagnetic configuration is not known. The powder neutron diffraction at 4 K for the isostructural compound CaFe₄Al₈ has shown that the magnetic moments on the Fe atoms form antiparallel chains oriented along the *c*-direction and slightly canted from the axis [69], which can be described as a canted AFM-C configuration. Since the FPLO code only allows the calculation of collinear magnetic configurations, we consider for the YbFe₄Al₈ a simplified collinear AFM-C model. As the initial lattice parameters, we take the values 8.714 and 5.026 Å measured for YbFe₄Al₈ [2]. Since the literature does not provide atomic positions for the studied compound, we take initial positions from the isostructural CaFe₄Al₈ (neutron powder data, *T* = 4 K) [69]. As a result of optimizing the lattice parameters and atomic positions, we obtain the AFM-C structure presented in Table 1. AFM-C structure can be further reduced to a form with only one Fe sublattice, which results we also present in Table 1. We see that the optimized lattice parameters (8.702 and 5.019 Å) are in very good agreement with the experimental results (8.714 and 5.026 Å) [2].

In addition, we have prepared two more models of antiferromagnetic configurations, AFM-A and AFM-G, and compared them in terms of the total energy in order to identify the most favorable and hence the most stable structure at the lowest temperature, see Fig. 5. The AFM-A configuration has proven to be unstable, difficult to converge, and its total energy was considerably higher than for the other two. In contrast, the AFM-C configuration is 0.7 eV f.u.⁻¹ more stable than AFM-G, so results presented from now on will be based on the AFM-C configuration unless otherwise noted.

On the sidelines of the work to prepare structural models, we decided to answer the question of the preference of Fe atoms to occupy particular sites in the crystal structure. For this purpose, we prepared three YbFe₄Al₈ structures in which Fe atoms occupied the 8*f*, 8*i*, or 8*j* sites. In agreement with the experiment [39,40], our calculations show that Fe atoms prefer to occupy the 8*f* sites and that the structures with Fe occupying the 8*j* and 8*i* sites are higher in energy by 0.58 and 0.97 eV/Fe atom, respectively. The calculated values are relatively high [70], indicating a rather strong preference for Fe to occupy sites 8*f*.

3.2.3. Effect of on-site Coulomb repulsion *U* on Yb 4*f* orbital

LDA+*U* calculations for YbFe₄Sb₁₂ showed that the on-site Coulomb repulsion *U* significantly affects the position of the Yb 4*f* states in the valence band [46,47]. In the following, we would like to determine whether the effect that the correction induces is beneficial against the previously presented valence band measurements.

Table 1

Crystallographic data for YbFe₄Al₈ as optimized with the FPLO code. The lattice parameters for antiferromagnetic configuration AFM-C are *a* = 12.306 Å and *c* = 5.019 Å, see Fig. 5(b), whereas for basic non-magnetic configuration (NM) lattice parameters are *a* = 8.702 Å and *c* = 5.019 Å.

AFM-C s.g. <i>Fm</i> <i>mmm</i> (69)			NM s.g. <i>I4</i> / <i>mmm</i> (139)			
Yb	0	0	Yb 2 <i>a</i>	0	0	0
Fe _{up}	-1/4	0	Fe 8 <i>f</i>	1/4	1/4	1/4
Fe _{dn}	0	-1/4	Al 8 <i>i</i>	0.3307	0	0
Al ₁	0.1693	0.1693	Al 8 <i>j</i>	0.2784	1/2	0
Al ₂	0.3896	-0.1104				

For this purpose, we examine how the properties of YbFe₄Al₈ change as *U* applied to 4*f* orbitals increases from 0 to 10 eV. In Fig. 6, we see that the valence band region of the densities of states (DOS) is dominated by two spin-orbit split peaks of Yb 4*f* states. As a result of the aforementioned limitations of the GGA/GGA+*U* method, we observe only a single 4*f* doublet rather than a complex 2+/3+ binary spectrum as in the XPS measurement presented earlier. We observe that as *U* increases, the Yb 4*f* states shift toward lower energies. Also, as *U* increases, the occupancy of orbital Yb 4*f* increases, while the occupancy of orbital Yb 5*d* decreases, see Fig. 7, which shows the close relationship between these two orbitals. The occupancy of the 4*f* orbital for bare GGA is equal to 13.53, which is closest to the experimental value equal to about 13.2 at 300 K. Given the above, we conclude that the most appropriate approximation for the description of YbFe₄Al₈ is the GGA model without the on-site Coulomb repulsion *U*. Therefore, the detailed results presented below will be based specifically on GGA (PBE).

3.2.4. Relativistic atomic energies

Fig. 8 shows the calculated relativistic atomic energies, which represent the broadest picture of the electronic structure covering all energy levels of YbFe₄Al₈. Since these are obtained before the self-consistent cycle, they may change after the calculations converge. The results are presented in three consecutive ranges, and where readability is maintained, energy levels are assigned to individual orbitals. The levels shown in the top graph do not appear in the results of XPS measurement using a standard X-ray source such as Al-K_α with a photon energy of 1486.6 eV. The lowest level at -61 keV belongs to the most strongly bound electron Yb 1*s*. The middle panel shows the binding energy range typical of an Al-K_α source, such as the one used in the experimental part of this work, while the bottom panel covers the energy range from -120 eV to the Fermi level. The calculated levels for Yb 4*d* (-183.1 and -173.9 eV), Fe 2*p* (-706.5 and -694.0 eV), and Al 2*p* (-69.9 and -69.5 eV) are in good agreement with the measured XPS spectra showed before. The differences are due to Coulomb exchange interactions with the valence band levels, the effect of spin polarization, and in the case of Al nonequivalent atomic positions in the unit cell. Finally, the part of the XPS spectrum, which covers the area of a few eV around the Fermi level, can be interpreted more accurately on the self-consistently calculated valence band structure. For all-electron methods, like FPLO, accurate positions of the core-electrons energy levels in the range up to about 200 eV of binding energy can also be obtained from self-consistent calculations.

3.2.5. Densities of states

We will start the valence band analysis by presenting the density of states in the range of a few eV around the Fermi level, see Fig. 9. In this region, the most important contributions come from the Yb 4*f* and Fe 3*d* orbitals. 13.53 4*f* electrons, as determined by Mulliken electron population analysis, uniformly fill the two spin channels. However, as a result of spin-orbit splitting, the 4*f* states split into two narrow bands with energies of about -0.2 and -1.6 eV. The observed spin-orbit doublet resembles the divalent part of the XPS spectrum, compare Fig. 2. However, in the PBE picture, we do not observe the second trivalent Yb 4*f* component present in the XPS spectrum below -5 eV.

Since we are considering a model with the antiferromagnetic ordering of moments on Fe atoms, red and blue colors are used to draw 3*d* contributions from Fe sublattices with opposite spin polarization. As can be seen in Fig. 9, the DOSs of the two Fe sublattices are polarized in opposite directions, and their resulting spin magnetic moment is fully compensated. In the occupied region, the characteristic maxima of the Fe 3*d* orbitals are located at about -0.8 eV, just between the split Yb 4*f* bands. For clarity, the figure does not show contributions from the less occupied valence orbitals,

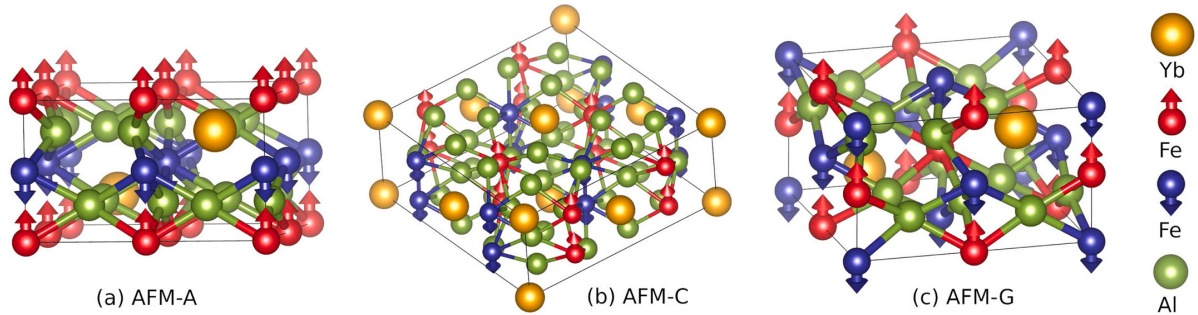


Fig. 5. Considered antiferromagnetic configurations of spin magnetic moments on Fe sites for YbFe₄Al₈: AFM-A (a), AFM-C (b), and AFM-G (c).

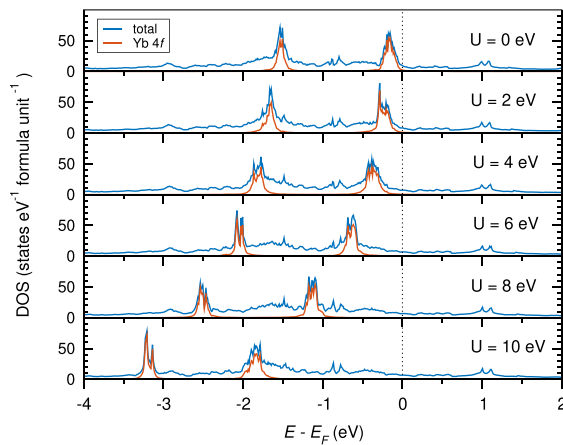


Fig. 6. The densities of states of Yb 4f orbitals as a function of on-site repulsion U_{4f} calculated for YbFe₄Al₈ with an antiparallel configuration of magnetic moments on Fe sites (AFM-C). Calculations are performed with FPLO18 in a fully relativistic approach, using PBE+U, and for the [001] quantization axis.

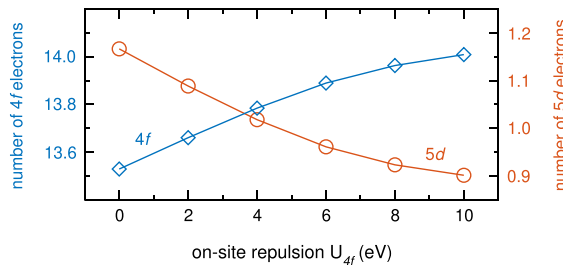


Fig. 7. Occupancy of Yb 4f and 5d orbitals as a function of on-site repulsion U_{4f} calculated for YbFe₄Al₈ with an antiparallel configuration of magnetic moments on Fe sites (AFM-C). Calculations were performed with the FPLO18 in a fully relativistic approach, using PBE+U, and for the [001] quantization axis.

e.g., Yb 5d or Al 3s and 3p, a more complete list of which can be found in the next section of this paper on Mulliken analysis.

3.2.6. Density of states at the Fermi level and electronic specific heat coefficient γ

The density of states at the Fermi level [$DOS(E_F)$] is 9.4 states eV^{-1} f.u.⁻¹ and consists mainly of contributions from Yb 4f (2.5 states eV^{-1} f.u.⁻¹) and Fe 3d (3.0 states eV^{-1} f.u.⁻¹). The $DOS(E_F)$ calculated here is relatively close to the values calculated earlier for the antiferromagnetic phases ScFe₄Al₈, LuFe₄Al₈, and YFe₄Al₈, equal to about

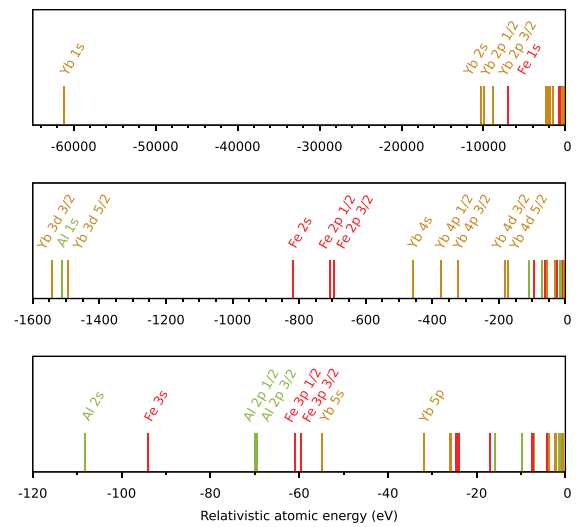


Fig. 8. The relativistic atomic energies for YbFe₄Al₈ as calculated using FPLO18 in a fully relativistic approach.

14.5 states eV^{-1} cell⁻¹ [66] and to a calculated $DOS(E_F)$ value for YbFe₄Sb₁₂ equal to 31 states eV^{-1} f.u.⁻¹ [46].

In the Sommerfeld model, the electronic specific heat coefficient γ is determined from $DOS(E_F)$ according to the equation $\gamma = \frac{1}{3}\pi^2 k_B^2 DOS(E_F)$ [71], where k_B is Boltzmann constant. For YbFe₄Al₈ this leads to γ equal to 22.2 $mJ mol^{-1} K^{-2}$, which is much lower than experimental γ values for isostructural compounds YFe₄Al₈ (60 $mJ mol^{-1} K^{-2}$) and LuFe₄Al₈ (75 $mJ mol^{-1} K^{-2}$) [32,72]. However, the underestimation of γ is a recognized weakness of the DFT method, resulting from the neglect of spin fluctuations and many-body effects in low-energy excitations [73]. Moreover, the γ value of 22.2 $mJ mol^{-1} K^{-2}$ calculated for YbFe₄Al₈ is more than twice the value of 9.1 $mJ mol^{-1} K^{-2}$ that we obtained for another compound containing lanthanides and 3d-metal (Y_{0.9}Ti_{0.1}Co₂) [74]. The difference is due to the absence of the 4f contribution in the latter case and the slightly higher filling of the 3d shell in Co than in Fe.

3.2.7. Mulliken electronic population analysis

In YbX₄Al₈ compounds, the valence of Yb ions is strongly dependent on the transition metal. For example, the Yb ion is divalent in YbMn₄Al₈ and possibly in a mixed state in YbCr₄Al₈ and YbCu₄Al₈ [35]. The previous results suggest that Yb ion in YbFe₄Al₈ is close to trivalent [35,75]. However, the valence determined in this work for YbFe₄Al₈ from the relative intensity of divalent and trivalent peaks in

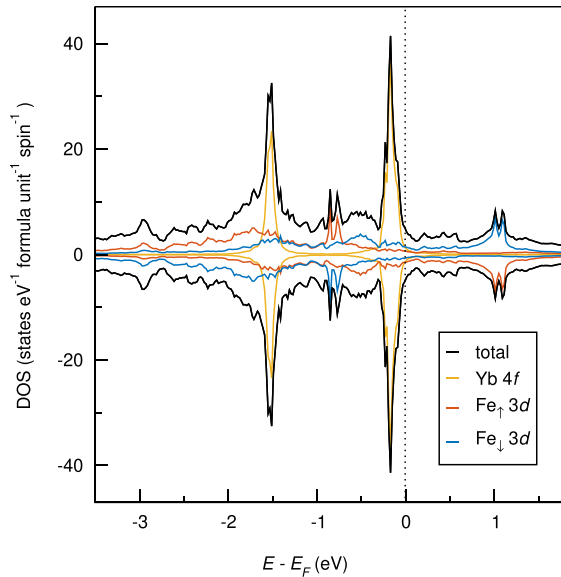


Fig. 9. The densities of states (DOS) of YbFe₄Al₈. The model is based on the AFM-C configuration of magnetic moments on Fe sublattices (Fe_γ and Fe_δ). The total DOS is shown with contributions from selected orbitals (Yb 4f and Fe 3d). Calculations were performed with FPLO18 in a fully-relativistic approach and using PBE functional.

the XPS valence band is 2.81 at room temperature, implying occupancy of Yb 4f orbitals close to 13.2. As shown by the measurements [22], the mean valence of the Yb compound may decrease with temperature, suggesting that the Yb 4f occupancy in YbFe₄Al₈ may be above 13.2, close to 0 K.

Table 2 and Table 3 show the results of the Mulliken electronic population analysis [76]. The application of Mulliken's approach is possible because the linear combination of atomic orbitals method is the basis of the FPLO code. For YbFe₄Al₈, we observe that the charge taken from the Yb and Fe sites (-0.65 and -0.10) is transferred to the Al sites (+0.12 and +0.14). The excess electron number for Yb (-0.65) is very different from -2 or -3, values one would expect for a divalent or trivalent configuration. This is due, among other things, to the fact that first-principles calculations involve a much larger basis than assumed by the conventional valence model (e.g. polarization orbitals Yb 6s and 6p) and also allow fractional occupancy of individual orbitals. Similarly large differences between nominal valence and the calculated occupancy are typically observed in DFT calculations. For Yb in YbFe₄Al₈ we observe fractional occupation of orbital 4f (13.53) and low occupations of orbitals 5d (1.17) and polarization orbitals 6s and 6p (0.36 and 0.32). For Fe sites, with regard to the ground state electronic configuration of a neutral Fe atom (3d⁶ 4s²), we observe an increase in the occupation of the 3d orbital while depopulating the 4s orbital.

For comparative analysis, we chose LuFe₄Al₈, a compound containing a filled 4f shell with a much more stable and simpler to predict electronic structure. The calculated occupancy of the 4f orbital for LuFe₄Al₈ is 13.96, which is almost the maximum. For LuFe₄Al₈, we observe a similar picture of charge transfer as for

Table 2

Excess electron number for YbFe₄Al₈ and LuFe₄Al₈ compounds calculated using FPLO18 in a fully-relativistic approach.

formula\ site	Yb/Lu	Fe	Al ₁	Al ₂
YbFe ₄ Al ₈	-0.65	-0.10	0.12	0.14
LuFe ₄ Al ₈	-0.88	-0.08	0.14	0.17

Table 3

The Mulliken electronic population analysis for YbFe₄Al₈ and LuFe₄Al₈ compounds calculated using FPLO18 in a fully-relativistic approach. Notation of lattice sites of AFM-C structure according to Table 1.

	site	6s	5d	6p	4f
YbFe ₄ Al ₈	Yb	0.36	1.17	0.32	13.53
LuFe ₄ Al ₈	Lu	0.43	1.33	0.39	13.96
	site	4s	3d	4d	4p
YbFe ₄ Al ₈	Fe	0.65	6.73	0.11	0.42
LuFe ₄ Al ₈	Fe	0.64	6.74	0.11	0.42
	site	3s	3p	3d	
YbFe ₄ Al ₈	Al ₁	1.16	1.73	0.28	
LuFe ₄ Al ₈	Al ₁	1.15	1.75	0.28	
	site	3s	3p	3d	
YbFe ₄ Al ₈	Al ₂	1.12	1.75	0.30	
LuFe ₄ Al ₈	Al ₂	1.12	1.77	0.31	

YbFe₄Al₈, but with a significant difference at the position of the 4f element (charge transfer -0.88 for Lu versus -0.65 for Yb). Comparing in more detail the occupation of Yb and Lu, we see that at the cost of over-occupation of Yb 4f orbital (above 13.0), the other three Yb orbitals under consideration (5d, 6s, and 6p) are depopulated compared to LuFe₄Al₈. Of particular importance is the under-occupation of the Yb 5d orbital, which leads to a positive deviation of volume from the trend observed for trivalent RFe₄Al₈ compounds. While experiments have shown that the type of transition metal affects the valence of Yb in YbM₄Al₈ compounds [35], the change of the 4f element between YbFe₄Al₈ and LuFe₄Al₈ compounds shows no significant effect on the occupancy of Fe and Al orbitals. However, the greatest changes in electron structure occur on the 4f elements themselves, see Table 3.

3.2.8. Spin and orbital magnetic moments

In the last section, we will focus on the detailed analysis of magnetic moments. For YbFe₄Al₈, the calculated spin magnetic moments on antiferromagnetically oriented Fe sublattices are equal to 1.523 μ_B and compensate each other. The additional orbital contributions occurring on the Fe atoms are 0.037 μ_B/Fe atom. Since no magnetic moments have been measured for YbFe₄Al₈ so far, our result can at best be compared with moments experimentally obtained for LuFe₄Al₈. Neutron diffraction studies at 1.5 K have shown that for LuFe₄Al₈, the magnetic moments on the Fe atoms are 1.8(2) μ_B [40]. We can see that the value of the total magnetic moment (spin plus orbital) on the Fe atom for YbFe₄Al₈ equal to about 1.6 μ_B is within the range of accuracy of the measurement for LuFe₄Al₈ [40]. The calculated spin magnetic moments on Fe in YbFe₄Al₈ (1.523 μ_B) are significantly lower than the corresponding values for bcc Fe (2.16 μ_B) calculated under the same theoretical model, as well as compared to the experimental value for bcc Fe (1.98 μ_B [77]). The calculated orbital magnetic moments on Fe in YbFe₄Al₈ (0.037 μ_B/Fe atom) and in bcc Fe (0.045 μ_B/Fe atom) are comparable. However, both of these values are reduced from the experimental value for bcc Fe (0.086 μ_B) [77]. Underestimation of the orbital magnetic moment for transition metals is considered one of the weaknesses of GGA and LDA. For YbFe₄Al₈ we do not observe any magnetic moments on the Yb and Al sites. Since the calculations based on the AFM-C model with a single Yb position cannot account for a possible antiferromagnetic ordering on Yb atoms, we prepared an alternative structural model with two non-equivalent Yb positions in addition to two non-equivalent Fe positions. The calculations for this model, however, led to identical results as presented for a simpler model with a single Yb position, showing no magnetic moments on the Yb atoms. It is worth noting the limitations of our DFT model, which lead to a description of the Yb 4f valence states that is inconsistent

with the results observed in XPS and thus can affect the obtained magnetic state of Yb ions. In conclusion, although the results of our calculations indicate the absence of a magnetic moment on Yb ions, calculations within a more advanced theoretical model than the one used in this work are needed to unambiguously resolve the question of the magnetic state of Yb ions in YbFe₄Al₈.

4. Summary and conclusions

We have investigated the valence state of YbFe₄Al₈ using X-ray photoelectron spectroscopy and first-principles calculations. We interpreted XPS measurements of the valence band and selected core-levels based on previously predicted theoretical energy level multiplets. We have identified that the XPS valence band of YbFe₄Al₈ consists of two contributions coming from divalent (Yb²⁺) and trivalent (Yb³⁺) configurations. The YbFe₄Al₈ valence is determined from the relative intensity of divalent and trivalent peaks and is equal to 2.81 at room temperature.

The second part of the paper consisted of first-principles calculations performed using a full-potential local-orbital scheme (FPLO). Since atomic positions of YbFe₄Al₈ are not available in the literature, we performed full structure optimization and presented the resultant complete structural model. Due to the antiferromagnetic arrangement of magnetic moments revealed in the YbFe₄Al₈ compound, we considered several collinear antiferromagnetic configurations (AFM-A, AFM-C, and AFM-G), of which AFM-C was found to be the most stable. The AFM-C configuration is characterized by the arrangement of magnetic moments on Fe in the form of antiparallel chains. The calculations predicted no magnetic moments at the Yb and Al sites and showed that the antiparallel moments at the Fe chains completely compensate. Mulliken analysis showed that the charge taken from the Yb and Fe sites is transferred to Al and that the fractional occupation of the 4f orbital is about 13.5 (at 0 K), although the valence deduced from the XPS spectra suggests an occupation closer to 13.2 (at 300 K). The calculated valence band densities of states presenting a spin-orbit split Yb 4f doublet stand in opposition to the complex XPS spectrum consisting of a divalent doublet and a trivalent multiplet of Yb 4f states. In order to more accurately describe the valence band and resolve the magnetism of Yb ions, calculations beyond the GGA must be performed.

Data availability

The processed data required to reproduce these findings are shown in the text.

Declaration of Competing Interest

The authors declare that they have no known competing financial interests or personal relationships that could have appeared to influence the work reported in this paper.

Acknowledgments

We acknowledge the financial support of the National Science Center Poland under the decision DEC-2018/30/E/ST3/00267. Part of the computations was performed on the resources provided by the Poznań Supercomputing and Networking Center (PSNC). We thank Paweł Leśniak and Daniel Depcik for compiling the scientific software and administration of the computing cluster at the Institute of Molecular Physics, Polish Academy of Sciences. We thank Justyna Rychły and Justyn Snarski-Adamski for reading the manuscript and useful comments.

References

- [1] U. Subbarao, M.J. Gutmann, S.C. Peter, New structure type in the mixed-valent compound YbCu₄Ga₈, *Inorg. Chem.* 52 (4) (2013) 2219–2227, <https://doi.org/10.1021/ic302688n>
- [2] K.H.J. Buschow, J.H.N. Van Vucht, W.W. Van Den Hoogenhof, Note on the crystal structure of the ternary rare earth-3d transition metal compounds of the type RT₄Al₈, *J. Common Met.* 50 (1) (1976) 145–150, [https://doi.org/10.1016/0022-5088\(76\)90261-7](https://doi.org/10.1016/0022-5088(76)90261-7)
- [3] A.M. van der Kraan, K.H.J. Buschow, Magnetic properties of rare earth compounds of the type RFe₄Al₈, *Phys. B+C* 86–88 (1977) 93–94, [https://doi.org/10.1016/0378-4363\(77\)90241-8](https://doi.org/10.1016/0378-4363(77)90241-8)
- [4] W. Suski, The ThMn₁₂-Type compounds of rare earths and actinides: structure, magnetic and related properties, *Handb. Phys. Chem. Rare Earths* 22 (1996) 143–294, [https://doi.org/10.1016/S0168-1273\(96\)22006-9](https://doi.org/10.1016/S0168-1273(96)22006-9)
- [5] P. Strange, A. Svane, W.M. Temmerman, Z. Szotek, H. Winter, Understanding the valency of rare earths from first-principles theory, *Nature* 399 (6738) (1999) 756–758, <https://doi.org/10.1038/21595>
- [6] J. Johansson, Energy position of 4f levels in rare-earth metals, *Phys. Rev. B* 20 (4) (1979) 1315–1327, <https://doi.org/10.1103/PhysRevB.20.1315>
- [7] J.K. Lang, Y. Baer, P.A. Cox, Study of the 4f and valence band density of states in rare-earth metals. II. Experiment and results, *J. Phys. F. Met. Phys.* 11 (1) (1981) 121, <https://doi.org/10.1088/0305-4608/11/1/015>
- [8] J. Klaasse, F. de Boer, P. de Châtel, Systematics in intermetallic compounds containing intermediate-valent ytterbium, *Phys. B+C* 106 (2) (1981) 178–194, [https://doi.org/10.1016/0378-4363\(81\)90078-4](https://doi.org/10.1016/0378-4363(81)90078-4)
- [9] P. Khuntia, P. Peratheepan, A.M. Strydom, Y. Utsumi, K.-T. Ko, K.-D. Tsuei, L.H. Tjeng, F. Steglich, M. Baenitz, Contiguous 3d and 4f magnetism: strongly correlated 3d electrons in YbFe₂Al₁₀, *Phys. Rev. Lett.* 113 (21) (2014) 216403, <https://doi.org/10.1103/PhysRevLett.113.216403>
- [10] W.J. Gannon, K. Chen, M. Sundermann, F. Strigari, Y. Utsumi, K.-D. Tsuei, J.-P. Rueff, P. Bencok, A. Tanaka, A. Severing, M.C. Aronson, Intermediate valence in single crystalline Yb₃Si₂Al, *Phys. Rev. B* 98 (7) (2018) 075101, <https://doi.org/10.1103/PhysRevB.98.075101>
- [11] K. Kummer, Y. Kucherenko, S. Danzenbächer, C. Krellner, C. Geibel, M.G. Holder, L.V. Bekenov, T. Muro, Y. Kato, T. Kinoshita, S. Huotari, L. Simonelli, S.L. Molodtsov, C. Laubschat, D.V. Vyalykh, Intermediate valence in Yb compounds probed by 4f photoemission and resonant inelastic x-ray scattering, *Phys. Rev. B* 84 (24) (2011) 245114, <https://doi.org/10.1103/PhysRevB.84.245114>
- [12] K.H.J. Buschow, M. Campagna, G.K. Wertheim, Intermediate valence in YbAl₃ and EuCu₂Si₂ by X-ray photoemission (XPS), *Solid State Commun.* 24 (3) (1977) 253–256, [https://doi.org/10.1016/0038-1098\(77\)91208-X](https://doi.org/10.1016/0038-1098(77)91208-X)
- [13] R.S. Kumar, A. Svane, G. Vaitheeswaran, V. Kanchana, E.D. Bauer, M. Hu, M.F. Nicol, A.L. Cornelius, Pressure-induced valence change in YbAl₃: a combined high-pressure inelastic x-ray scattering and theoretical investigation, *Phys. Rev. B* 78 (7) (2008) 075117, <https://doi.org/10.1103/PhysRevB.78.075117>
- [14] S. Chatterjee, J.P. Ruf, H.I. Wei, K.D. Finkelstein, D.G. Schlom, K.M. Shen, Lifshitz transition from valence fluctuations in YbAl₃, *Nat. Commun.* 8 (1) (2017) 852, <https://doi.org/10.1038/s41467-017-00946-1>
- [15] T. Toliński, B. Andrzejewski, A. Kowalczyk, G. Chetkowska, A. Szałaferek, J. Frąckowiak, Magnetic and electronic properties of the antiferromagnetic YbFe₄Al₈ compound, *J. Phys. Chem. Solids* 67 (4) (2006) 751–755, <https://doi.org/10.1016/j.jpcs.2005.11.007>
- [16] M. Matsunami, A. Chainani, M. Taguchi, R. Eguchi, Y. Ishida, Y. Takata, H. Okamura, T. Nanba, M. Yabashi, K. Tamasaku, Y. Nishino, T. Ishikawa, Y. Senba, H. Ohashi, N. Tsujii, A. Ochiai, S. Shin, Combining photoemission and optical spectroscopies for reliable valence determination in YbS and Yb metal, *Phys. Rev. B* 78 (19) (2008) 195118, <https://doi.org/10.1103/PhysRevB.78.195118>
- [17] M. Matsunami, A. Chainani, M. Taguchi, R. Eguchi, Y. Takata, M. Oura, M. Yabashi, K. Tamasaku, Y. Nishino, T. Ishikawa, M. Kosaka, S. Shin, Photoemission evidence for valence fluctuations and Kondo resonance in YbAl₂, *J. Phys. Soc. Jpn.* 81 (7) (2012) 073702, <https://doi.org/10.1143/JPSJ.81.073702>
- [18] M. Matsunami, T. Hajiri, H. Miyazaki, M. Kosaka, S. Kimura, Strongly hybridized electronic structure of YbAl₂: an angle-resolved photoemission study, *Phys. Rev. B* 87 (16) (2013) 165141, <https://doi.org/10.1103/PhysRevB.87.165141>
- [19] A. Rousuli, H. Sato, F. Iga, K. Hayashi, K. Ishii, T. Wada, T. Nagasaki, K. Mimura, H. Anzai, K. Ichiki, S. Ueda, A. Kondo, K. Kindo, T. Takabatake, K. Shimada, H. Namatame, M. Taniguchi, Hard x-ray photoemission study of Yb_{1-x}Zr_xB₁₂: the effects of electron doping on the Kondo insulator YbB₁₂, *J. Phys. Condens. Matter* 29 (26) (2017) 265601, <https://doi.org/10.1088/1361-648X/aa6f70>
- [20] A. Rousuli, S. Nakamura, H. Sato, T. Ueda, Y. Matsumoto, S. Ohara, E.F. Schwier, T. Nagasaki, K. Mimura, H. Anzai, K. Ichiki, S. Ueda, K. Shimada, H. Namatame, M. Taniguchi, Photoemission study of the electronic structure of the Kondo lattices Yb₂Pt₆X₁₅ (X = Al, Ga), *Phys. Rev. B* 96 (4) (2017) 045117, <https://doi.org/10.1103/PhysRevB.96.045117>
- [21] H. Anno, J. Nagao, K. Matsubara, Electronic and thermoelectric properties of Yb_{1-x}Fe_xNi_{1-x}Sb₁₂ filled skutterudites, In: *Proceedings of the 21st International Conference on Thermoelectrics*, 2002, pp. 56–59, <https://doi.org/10.1109/ICT.2002.1190264>
- [22] S. Schmidt, S. Hüfner, F. Reinert, W. Assmus, X-ray photoemission of YbInCu₄, *Phys. Rev. B* 71 (19) (2005) 195110, <https://doi.org/10.1103/PhysRevB.71.195110>
- [23] V.H. Tran, W. Müller, A. Kowalczyk, T. Toliński, G. Chetkowska, Intermediate valence behaviour of Yb in a new intermetallic compound YbNi_{0.8}Al_{4.2}, *J. Phys. Condens. Matter* 18 (46) (2006) 10353–10363, <https://doi.org/10.1088/0953-8984/18/46/004>

- [24] O. Sichevych, Y. Prots, Y. Utsumi, L. Akselrud, M. Schmidt, U. Burkhardt, M. Coduri, W. Schnelle, M. Bobnar, Y.-T. Wang, Y.-H. Wu, K.-D. Tsuei, L.H. Tjeng, Y. Grin, Intermediate-valence ytterbium compound Yb₄Ga₂₄Pt₉: synthesis, crystal structure, and physical properties, *Inorg. Chem.* 56 (15) (2017) 9343–9352, <https://doi.org/10.1021/acs.inorgchem.7b01530>
- [25] K. Kummer, C. Geibel, C. Krellner, G. Zwirknagl, C. Laubschat, N.B. Brookes, D.V. Vyalikh, Similar temperature scale for valence changes in Kondo lattices with different Kondo temperatures, *Nat. Commun.* 9 (1) (2018) 2011, <https://doi.org/10.1038/s41467-018-04438-8>
- [26] H. Drulis, P. Gaczyński, W. Iwasieczko, W. Suski, B.Y. Kotur, Magnetic properties of YbFe₄Al₈ intermetallic compound. New antiferromagnetic superconductor, *Solid State Commun.* 123 (9) (2002) 391–394, [https://doi.org/10.1016/S0038-1098\(02\)00372-1](https://doi.org/10.1016/S0038-1098(02)00372-1)
- [27] W. Suski, K. Wochowski, B.Y. Kotur, Magnetic and electrical properties of Yb_{1-x}Sc_xFe₄Al₈ alloys, *Czechoslov. J. Phys.* 52 (2002) A189–A192, <https://doi.org/10.1007/s10582-002-0045-9>
- [28] P. Gaczyński, H. Drulis, Magnetic and hyperfine interaction in YbFe₄Al₈ compound, *Nukleonika* 49 (Suppl. 3) (2004) 33–36.
- [29] B. Andrzejewski, A. Kowalczyk, J.E. Fraćkowiak, T. Toliński, A. Szaferek, S. Pal, C. Simon, Unusual negative magnetisation effect in antiferromagnetic YbFe₄Al₈ compound, *Phys. Status Solidi B* 243 (1) (2006) 295–298, <https://doi.org/10.1002/psbb.200562452>
- [30] B. Andrzejewski, A. Kowalczyk, T. Toliński, Negative magnetisation and absence of superconductivity in RFe₄Al₈ (R=Lu, Yb) compounds, *Acta Phys. Pol. A* 109 (4–5) (2006) 561–564, <https://doi.org/10.12693/APhysPolA.109.561>
- [31] K. Szymański, D. Satała, B. Kalska, W. Olszewski, L. Dobrzyński, H. Drulis, P. Gaczyński, W. Iwasieczko, L. Bottyan, Advantages of Mössbauer polarimetric methods in material studies, *Hyperfine Interactions* 182 (1) (2008) 125–136, <https://doi.org/10.1007/s10751-008-9717-6>
- [32] A.M. Gurevich, V.M. Dmitriev, V.N. Eropkin, B.Y. Kotur, N.N. Prentslau, V. Suski, A.V. Terekhov, L.V. Shlyk, Impedance and specific heat of RM₄Al₈ and RAgIn₆ compounds, *Low. Temp. Phys.* 27 (11) (2001) 967–973, <https://doi.org/10.1063/1.1421464>
- [33] V.M. Dmitriev, N.N. Prentslau, I.V. Zolochovskii, L.A. Ishchenko, A.V. Terekhov, B.Y. Kotur, W. Suski, E. Talik, Superconductivity, negative magnetoresistance, and anisotropy of the conductivity of YFe₄Al₈ and ScFe₄Al₈ single crystals in the frequency range 0–10⁸ Hz, *Low. Temp. Phys.* 29 (11) (2003) 901–909, <https://doi.org/10.1063/1.1614234>
- [34] I.D. Shcherba, M.D. Koterlyn, A.P. Kushnir, R.R. Kutjanskij, V.G. Synjushko, Y.D. Tsybukh, B.M. Yatsyk, I.I. Margolych, Peculiarities of the valence state of Ce and Yb in RM₄Al₈ (R = rare earth; M = Cr, Mn, Fe, Cu), *J. Magn. Magn. Mater.* 157–158 (1996) 688–689, [https://doi.org/10.1016/0304-8853\(95\)00988-4](https://doi.org/10.1016/0304-8853(95)00988-4)
- [35] I. Felner, I. Nowik, Magnetism and hyperfine interactions of ⁵⁷Fe, ¹⁵¹Eu, ¹⁵⁵Gd, ¹⁶¹Dy, ¹⁶⁶Er and ¹⁷⁰Yb in RM₄Al₈ compounds (R = rare earth or Y, M = Cr, Mn, Fe, Cu), *J. Phys. Chem. Solids* 40 (12) (1979) 1035–1044, [https://doi.org/10.1016/0022-3697\(79\)90135-5](https://doi.org/10.1016/0022-3697(79)90135-5)
- [36] W. Suski, About negative magnetization in non-superconducting intermetallics, *Mater. Sci. Pol.* 25 (2007) 333–341.
- [37] V. Dmitriev, A. Terekhov, W. Suski, L. Ishchenko, J. Čwik, T. Palewski, B. Kotur, E. Talik, Negative magnetoresistivity of the RM₄Al₈ (R=Sc, Y, Ce, Yb, Lu; M=Cr, Mn, Fe) ternaries with the ThMn₁₂-type crystal structure, *J. Alloy. Compd.* 452 (2) (2008) 217–224, <https://doi.org/10.1016/j.jallcom.2006.11.015>
- [38] N. Pierunek, Z. Śniadecki, M. Werwiński, B. Wasilewski, V. Franco, B. Idzikowski, Normal and inverse magnetocaloric effects in structurally disordered Laves phase Y_{1-x}Gd_xCo₂ (0 < x < 1) compounds, *J. Alloy. Compd.* 702 (2017) 258–265, <https://doi.org/10.1016/j.jallcom.2017.01.181>
- [39] O. Moze, R.M. Ibberson, K.H.J. Buschow, On the preferential site occupation of Fe in RFe₄Al₈ and related compounds, *J. Phys. Condens. Matter* 2 (7) (1990) 1677–1681, <https://doi.org/10.1088/0953-8984/2/7/001>
- [40] P. Schobinger-Papamantellos, K.H.J. Buschow, C. Ritter, Magnetic ordering and phase transitions of RFe₄Al₈ (R=La, Ce, Y, Lu) compounds by neutron diffraction, *J. Magn. Magn. Mater.* 186 (1) (1998) 21–32, [https://doi.org/10.1016/S0304-8853\(98\)00075-4](https://doi.org/10.1016/S0304-8853(98)00075-4)
- [41] K. Koepernik, H. Eschrig, Full-potential nonorthogonal local-orbital minimum-basis band-structure scheme, *Phys. Rev. B* 59 (3) (1999) 1743–1757, <https://doi.org/10.1103/PhysRevB.59.1743>
- [42] H. Eschrig, Chapter – 2 The essentials of density functional theory and the full-potential local-orbital approach, in: W. Hergert, M. Däne, A. Ernst (Eds.), *Computational Materials Science*, no. 642 in Lecture Notes in Physics, Springer Berlin Heidelberg, 2004, pp. 7–21, https://doi.org/10.1007/978-3-540-39915-5_2
- [43] J.P. Perdew, K. Burke, M. Ernzerhof, Generalized gradient approximation made simple, *Phys. Rev. Lett.* 77 (18) (1996) 3865–3868, <https://doi.org/10.1103/PhysRevLett.77.3865>
- [44] E.R. Ylvisaker, W.E. Pickett, K. Koepernik, Anisotropy and magnetism in the LSDA. U method, *Phys. Rev. B* 79 (3) (2009) 035103, <https://doi.org/10.1103/PhysRevB.79.035103>
- [45] M.T. Czyżyk, G.A. Sawatzky, Local-density functional and on-site correlations: the electronic structure of La₂CuO₄ and LaCuO₃, *Phys. Rev. B* 49 (20) (1994) 14211, <https://doi.org/10.1103/PhysRevB.49.14211>
- [46] W. Schnelle, A. Leithe-Jasper, M. Schmidt, H. Rosner, H. Borrmann, U. Burkhardt, J.A. Mydosh, Y. Grin, Itinerant iron magnetism in filled skutterudites CaFe₄Sb₁₂ and YbFe₄Sb₁₂: stable divalent state of ytterbium, *Phys. Rev. B* 72 (2005), <https://doi.org/10.1103/PhysRevB.72.020402>
- [47] J. Sichelschmidt, V. Voevodin, H.J. Im, S. Kimura, H. Rosner, A. Leithe-Jasper, W. Schnelle, U. Burkhardt, J.A. Mydosh, Y. Grin, F. Steglich, Optical pseudogap from iron states in filled skutterudites AFe₄Sb₁₂ (A = Yb, Ca, Ba), *Phys. Rev. Lett.* 96 (3) (2006) 037406, <https://doi.org/10.1103/PhysRevLett.96.037406>
- [48] J.A. Morkowski, G. Chetkowska, M. Werwiński, A. Szajek, R. Troć, C. Neise, X-ray photoemission spectrum, electronic structure, and magnetism of UCu₂Si₂, *J. Alloy. Compd.* 509 (25) (2011) 6994–6998, <https://doi.org/10.1016/j.jallcom.2011.04.026>
- [49] J. Skoryna, S. Pacanowski, A. Marczyńska, M. Werwiński, A. Rogowska, M. Wachowiak, L. Majchrzycki, R. Czajka, L. Smardz, XPS valence band studies of nanocrystalline ZrPd alloy thin films, *Surf. Coat. Technol.* 303 (2016) 125–130, <https://doi.org/10.1016/j.surfcoat.2016.03.030>
- [50] K. Momma, F. Izumi, VESTA: a three-dimensional visualization system for electronic and structural analysis, *J. Appl. Crystallogr.* 41 (3) (2008) 653–658, <https://doi.org/10.1107/S0021889808012016>
- [51] F. Gerken, Calculated photoemission spectra of the 4f states in the rare-earth metals, *J. Phys. F. Met. Phys.* 13 (3) (1983) 703–713, <https://doi.org/10.1088/0305-4608/13/3/021>
- [52] R. Eggenhöfner, Advances in the study of intermediate-valence and heavy-fermion effects in rare-earth and uranium systems, *Il Nuovo Cim. D.* 15 (2–3) (1993) 519–530, <https://doi.org/10.1007/BF02456935>
- [53] J.J. Yeh, I. Lindau, Atomic subshell photoionization cross sections and asymmetry parameters: 1 < Z <= 103, *At. Data Nucl. Data Tables* 32 (1) (1985) 1–155, [https://doi.org/10.1016/0092-640X\(85\)90016-6](https://doi.org/10.1016/0092-640X(85)90016-6)
- [54] T. Okane, S.-i. Fujimori, K. Mamiya, J. Okamoto, Y. Muramatsu, A. Fujimori, Y. Nagamoto, T. Koyanagi, Photoemission spectroscopy of the filled skutterudite compound YbFe₄Sb₁₂, *J. Phys. Condens. Matter* 15 (28) (2003) S2197–S2200, <https://doi.org/10.1088/0953-8984/15/28/351>
- [55] H. Ogasawara, A. Kotani, B.T. Thole, Lifetime effect on the multiplet structure of 4d x-ray-photoemission spectra in heavy rare-earth elements, *Phys. Rev. B* 50 (17) (1994) 12332–12341, <https://doi.org/10.1103/PhysRevB.50.12332>
- [56] S.B.M. Hagström, P.O. Hedén, H. Löfgren, Electron density of states in Yb metal as observed by X-ray photoemission, *Solid State Commun.* 8 (15) (1970) 1245–1248, [https://doi.org/10.1016/0038-1098\(70\)90369-8](https://doi.org/10.1016/0038-1098(70)90369-8)
- [57] A. Szytula, A. Jezierski, B. Penc, A. Winiarski, A. Leithe-Jasper, D. Kaczorowski, Electronic structure of YbTl compounds, *J. Alloy. Compd.* 360 (1) (2003) 41–46, [https://doi.org/10.1016/S0925-8388\(03\)00344-X](https://doi.org/10.1016/S0925-8388(03)00344-X)
- [58] B.K. Rai, E. Morosan, Intermediate valence in single crystals of (Lu_{1-x}Y_x)₃Rh₄Ge₁₃ (0 ≤ x ≤ 1), *APL Mater.* 3 (4) (2015) 041511, <https://doi.org/10.1063/1.4913742>
- [59] P.C. Graat, M.A. Somers, Simultaneous determination of composition and thickness of thin iron-oxide films from XPS Fe 2p spectra, *Appl. Surf. Sci.* 100–101 (1996) 36–40, [https://doi.org/10.1016/0169-4332\(96\)00252-8](https://doi.org/10.1016/0169-4332(96)00252-8)
- [60] T. Yamashita, P. Hayes, Analysis of XPS spectra of Fe₂ and Fe₃ ions in oxide materials, *Appl. Surf. Sci.* 254 (8) (2008) 2441–2449, <https://doi.org/10.1016/j.apusc.2007.09.063>
- [61] A. Svane, W.M. Temmerman, Z. Szotek, L. Petit, P. Strange, H. Winter, Ab Initio theory of valency in ytterbium compounds, *Phys. Rev. B* 62 (20) (2000) 13394–13399, <https://doi.org/10.1103/PhysRevB.62.13394>
- [62] E.R. Ylvisaker, J. Kuneš, A.K. McMahan, W.E. Pickett, Charge fluctuations and the valence transition in Yb under pressure, *Phys. Rev. Lett.* 102 (24) (2009) 246401, <https://doi.org/10.1103/PhysRevLett.102.246401>
- [63] T. Jeong, W.E. Pickett, First-principles study of the electronic structure of heavy fermion YbRh₂Si₂, *J. Phys. Condens. Matter* 18 (27) (2006) 6289–6297, <https://doi.org/10.1088/0953-8984/18/27/012>
- [64] A. Yasui, Y. Saitoh, S.-i. Fujimori, I. Kawasaki, T. Okane, Y. Takeda, G. Lapertot, G. Knebel, T.D. Matsuda, Y. Haga, H. Yamagami, Observation of bulk band dispersions of YbRh₂Si₂ using soft x-ray angle-resolved photoemission spectroscopy, *Phys. Rev. B* 87 (7) (2013) 075131, <https://doi.org/10.1103/PhysRevB.87.075131>
- [65] R. Wang, X. Tao, H. Chen, Y. Ouyang, Phase stability and mechanical properties of Al₃Fe₄RE via first-principle calculations, *Materials* 12 (5) (2019) 701, <https://doi.org/10.3390/ma12050701>
- [66] G.E. Grechnev, A.V. Logosha, A.A. Lyogenkaya, A.G. Grechnev, A.V. Fedorchenko, Electronic structure and properties of novel layered superconductors, *Ukr. J. Phys.* 59 (3) (2014), <https://doi.org/10.15407/ujpe.59.03.0284>
- [67] A.V. Logosha, G.E. Grechnev, A.A. Lyogenkaya, A.S. Panfilov, Features of the electronic structure of the layered superconductors RNi₂B₂C, RFe₄Al₈ and FeSe, *Low. Temp. Phys.* 40 (4) (2014) 311–317, <https://doi.org/10.1063/1.4871747>
- [68] I.P. Zhuravleva, G.E. Grechnev, A.S. Panfilov, A.A. Lyogenkaya, O.V. Kotlyar, A.V. Fedorchenko, A. Feher, Electronic structure and magnetic properties of RT₄Al₈ (R = Sc, Y, La, Lu; T = Fe, Mn, Cr) compounds. Hydrostatic pressure effects, *Low. Temp. Phys.* 42 (6) (2016) 458–465, <https://doi.org/10.1063/1.4954784>
- [69] V. Gvozdevskiy, A. Senyshyn, R. Gladyshevskii, V. Hlukhyy, Crystal and magnetic structures of the chain antiferromagnet CaFe₄Al₈, *Inorg. Chem.* 57 (10) (2018) 5820–5829, <https://doi.org/10.1021/acs.inorgchem.8b00208>
- [70] C. Fu, J. Zou, Site preference of ternary alloying additions in FeAl and NiAl by first-principles calculations, *Acta Mater.* 44 (4) (1996) 1471–1478, [https://doi.org/10.1016/1359-6454\(95\)00297-9](https://doi.org/10.1016/1359-6454(95)00297-9)
- [71] E. Gopal, *Specific Heats at Low Temperatures*, Springer Science & Business Media, 2012.
- [72] I. Hagmusa, E. Brück, F. de Boer, K. Buschow, Magnetic properties of RFe₄Al₈ compounds studied by specific heat measurements, *J. Alloy. Compd.* 278 (1–2) (1998) 80–82, [https://doi.org/10.1016/S0925-8388\(98\)00643-4](https://doi.org/10.1016/S0925-8388(98)00643-4)
- [73] S. Tanaka, H. Harima, Mass enhancement factor and fermi surface in YCo₂, *J. Phys. Soc. Jpn.* 67 (8) (1998) 2594–2597, <https://doi.org/10.1143/JPSJ.67.2594>

W. Marciniak, G. Chetkowska, A. Bajorek et al.

Journal of Alloys and Compounds 910 (2022) 164478

- [74] Z. Sniadecki, M. Werwiński, A. Szajek, U.K. Rößler, B. Idzikowski, Induced magnetic ordering in alloyed compounds based on Pauli paramagnet YCo₂, *J. Appl. Phys.* 115 (17) (2014) 17E129, <https://doi.org/10.1063/1.4866848>
- [75] I. Felner, I. Nowik, Crystal structure magnetic properties and hyperfine interactions in RFe₄Al₈ (R = rare earth) systems, *J. Phys. Chem. Solids* 39 (9) (1978) 951–956, [https://doi.org/10.1016/0022-3697\(78\)90109-9](https://doi.org/10.1016/0022-3697(78)90109-9)
- [76] R.S. Mulliken, Electronic population analysis on LCAO-MO molecular wave functions. I, *J. Chem. Phys.* 23 (10) (1955) 1833–1840, <https://doi.org/10.1063/1.1740588>
- [77] C.T. Chen, Y.U. Idzerda, H.-J. Lin, N.V. Smith, G. Meigs, E. Chaban, G.H. Ho, E. Pellegrin, F. Sette, Experimental confirmation of the X-ray magnetic circular dichroism sum rules for iron and cobalt, *Phys. Rev. Lett.* 75 (1) (1995) 152–155, <https://doi.org/10.1103/PhysRevLett.75.152>

Giant magnetocrystalline anisotropy energy in Fe–Co alloy under uniaxial compression: first-principles prediction

Wojciech Marciniak*

*Institute of Molecular Physics, Polish Academy of Sciences, M. Smoluchowskiego 17, 60-179 Poznań, Poland and
Institute of Physics, Poznan University of Technology, Piotrowo 3, 60-965 Poznań, Poland*

José Ángel Castellanos-Reyes

Department of Physics and Astronomy, Uppsala University, Box 516, 75120 Uppsala, Sweden

Joanna Marciniak and Mirosław Werwiński

Institute of Molecular Physics, Polish Academy of Sciences, M. Smoluchowskiego 17, 60-179 Poznań, Poland

Uniaxially strained Fe–Co disordered alloys have emerged as promising candidates for cost-effective rare-earth-free permanent magnets due to their high magnetocrystalline anisotropy energy (MAE). Using first-principles, fully relativistic calculations within the coherent potential approximation and PBE exchange-correlation potential, we explore the MAE of tetragonal Fe–Co alloys under uniaxial compression. Our results reveal a previously uncharted high-MAE (exceeding 3 MJ m^{-3}) region, distinct from known structures and accessible through uniaxial compression.

The 2011 *rare-earth crisis* highlighted the vulnerability of the rare-earth (RE) elements market and spurred efforts to identify cost-effective, RE-free permanent magnets [1]. This included a thorough revision of ideas proposed in the mid and late 20th century [2, 3]. In particular, the $\text{Fe}_{1-x}\text{Co}_x$ disordered alloy near 60 at% of cobalt, with uniaxial tetragonal strain close to 22%, emerged as a promising candidate for a rare-earth-free permanent magnet already in 2004. Virtual crystal approximation calculations predict for this alloy exceptional magnetic properties, including a giant magnetocrystalline anisotropy energy (MAE) of $\sim 800 \mu\text{eV atom}^{-1}$, a significant magnetic moment of $2.5 \mu_{\text{B}} \text{ atom}^{-1}$ [4], and a high Curie temperature (T_{C}) exceeding 1000°C [5, 6].

The synthesis of epitaxial films along Bain’s path [7] has been proposed as a viable fabrication route for this alloy [4], resulting in several experimental realizations in years 2006–2009 [8–11]. At the same time, progress was made towards obtaining bulk structures by stacking Fe–Co regions with precisely controlled lattice parameters using Pt interlayers [12, 13]. Another significant advance was the successful epitaxial growth of FeCo on AuCu substrate [14, 15]. Despite these efforts to precisely control the fabrication process, both ordered and disordered Fe–Co alloys tend to rapidly relax into the cubic bcc structure beyond a critical thickness of about 15 atomic monolayers ($\sim 2 \text{ nm}$) [16]. This abrupt structural relaxation can be mitigated by a second stabilization method consisting of interstitial doping with smaller atoms such as B, C, or N, as supported by both theoretical predictions [17, 18] and experimental evidence [14, 19–21].

Further theoretical studies, which were conducted between 2011 and 2016, explain this rapid relaxation and lower-than-expected measured MAE values. It has been shown that the virtual crystal approximation (VCA) applied in Ref. [4] to model chemical disorder tends to overestimate the MAE in Fe–Co systems. More advanced computational methods have demonstrated a significant reduction in MAE for optimized

bulk structures, with values approaching $200 \mu\text{eV atom}^{-1}$ ($\sim 2.5 \text{ MJ m}^{-3}$) for an optimal lattice parameters c/a ratio of 1.22 [17, 18, 22, 23]. Nonetheless, the Fe–Co system remains a valuable, cost-effective medium for exploring the mechanisms underlying itinerant hard magnetism.

The distinctive magnetic properties of Fe–Co alloy in the body-centered tetragonal (bct) structure, with c/a ratio close to 1.22, are attributed to symmetry changes in hybridized iron and cobalt orbitals [4]. Moreover, the magnetic behavior of these alloys is primarily driven by the strong Fe–Co exchange interactions [24]. Given that other symmetry changes can similarly alter the chemical environment, it is also important to investigate the magnetic properties of Fe–Co alloys along alternative lattice transformation pathways.

Thus, we complement the transformation along Bain’s path with a particular $\text{bcc} \leftrightarrow \text{hcp}$ martensitic phase transition pathway, first described by Burgers [25]. This process involves two steps: uniaxial compression along one of the main crystallographic axes, followed by the perpendicular slip of one of the two hexagonal atomic planes formed during such deformation. In general, incorporating hexagonal cell shear in addition to the plane slip allows the description of broader $\text{fcc} \leftrightarrow \text{hcp} \leftrightarrow \text{bcc} \leftrightarrow \text{fcc}$ transitions [26–28]. Simultaneous uniaxial deformation and shear (or atomic plane slip) is, however, currently considered the more likely transformation path [29, 30]. The described deformation essentially continues the well-known [31] tetragonal distortion along Bain’s path into the regime where $c/a < 1$. The resulting intermediate structure, for which the coordination number of the atoms changes to 10, is denoted further as bct_{10} and has been studied for various elements [32]. This structure forms through uniaxial deformation along the [001] direction of the tetragonal phase, transforming the bcc (110) into the hexagonal (0001) plane.

Firstly, we examined the $\text{Fe}_{1-x}\text{Co}_x$ system under uniaxial tetragonal distortion, ranging from ~ 1.41 (fcc struc-

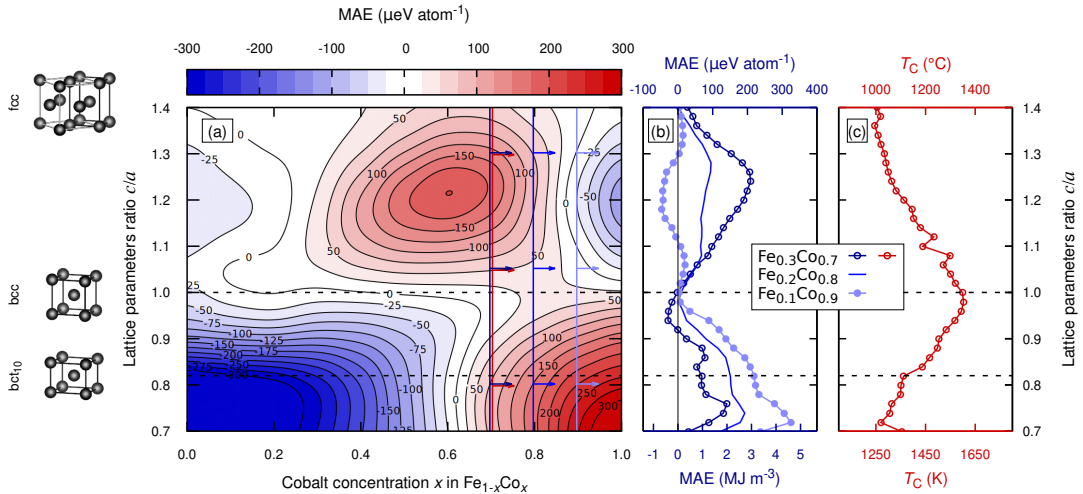


Figure 1. Magnetic properties of Fe_{1-x}Co_x alloy under tetragonal deformation. Icons on the left present the structure distortion, with light gray lines in the fcc structure depicting the conventional, 4-atom unit cell. Panel (a) presents a Gaussian-smoothed map of the magnetocrystalline anisotropy energy (MAE) calculated in the coherent potential approximation (CPA) chemical disorder treatment. Panel (b) displays the raw, non-approximated data for three different cobalt concentrations: $x = 0.7$ (dark blue, empty circles), $x = 0.8$ (blue, solid line), and $x = 0.9$ (light blue, filled circles). Panel (c) shows the Curie temperature (T_C) as obtained from Monte Carlo simulations for $x = 0.7$.

ture) through the intermediate bct₁₀ phase ($c/a = \sqrt{2/3} \approx 0.82$) in the Burgers transformation, down to $c/a \approx 0.7$. We employed the spin-polarized relativistic Korringa-Kohn-Rostoker method, implemented in SPR-KKR version 7.7.1 [33]. A 2-atom basis and space group $P4/mmm$ were used to ensure consistency in basis and symmetry across all structures. Each site was occupied evenly with the chemical disorder treated via coherent potential approximation (CPA). We began calculations with the experimental lattice parameter approximation for bcc iron (2.85 Å), followed by unit cell volume optimization for various cobalt concentrations, x , in Fe_{1-x}Co_x, with a step of 10%. The initial optimization indicated a requirement of at least 10,000 \mathbf{k} -points and an angular-momentum-expansion cutoff $l_{\max} = 4$ to properly capture the hybridization of Fe/Co 3d orbitals. This led to the characteristic Slater-Pauling-like shape in the unit cell volume *versus* x dependency (optimization results not shown). For the exchange-correlation potential, we used the generalized gradient approximation (GGA) with the Perdew, Burke, and Ernzerhof (PBE) parametrization [34], without shape approximation (full potential approach).

For the initial assessment of the MAE dependency on c/a and cobalt concentration x , we employed a constant volume approach, where the lattice parameters were rescaled to conserve the computational cell volume optimized previously for each cobalt concentration. We explored the entire Bain transition path between fcc and bcc structures along the z -axis distortion. The MAE of each structure was determined by calculating the energy difference between the [001] and [100] magnetization directions as follows:

$$\text{MAE} = E_{100} - E_{001}, \quad (1)$$

with the energies calculated in the four-component relativistic formalism, including the spin-orbit coupling.

The nonmagnetic global energy minimum of fcc iron has been thoroughly investigated in numerous works, including key Fe_{1-x}Co_x studies [22, 23, 31, 35]. Here, we aim to capture the behavior of the high-spin (HS) fcc iron phase [36], which has recently gained interest in layered systems [37, 38].

We began by comparing the MAE of the tetragonally strained structure, shown in Fig. 1(a), to the results of works by Burkert *et al.* [31], Turek *et al.* [22], Steiner *et al.* [23], and Neise *et al.* [35]. Our calculated MAE maximum – of about 200 μeV atom⁻¹ (2.5 MJ m⁻³) for $c/a = 1.22$ and $x = 0.6$ – is in good agreement with results obtained previously using CPA and explicit random alloy models. As expected, this value is about four times lower than the 800 μeV atom⁻¹, initially predicted by Burkert *et al.* The overall features, such as the observed uniaxial MAE maximum and the in-plane anisotropy region for the Co-rich system, are also consistent with previous findings. The noticeable difference is the complete vanishing of the MAE when considering the fcc iron HS phase, whereas prior studies reported a minor residual MAE. More importantly, we uncover a second, prominent MAE maximum for Fe_{1-x}Co_x under uniaxial compression, visible over a wide range of x on the Co-rich part of the plot. MAE value near this maximum easily exceeds 3 MJ m⁻³ and is an order of magnitude higher than that of the bulk hcp co [39, 40].

Qualitatively, the mutual part of our results (stoichiometric FeCo) aligns with the recent findings of Wolloch and Suess [41]. However, quantitative comparisons are limited due to our exclusion of surface effects and their use of an insubstantial quantity of special quasirandom structures (SQS) models. In Ref. [41], especially for stoichiometric FeCo, the in-plane anisotropy is strongly favored, particularly under uniaxial compression, behaving almost linearly. For $x = 0.9$, as presented in Fig. 1(b), we can compare only the system’s behavior under uniaxial strain, due to authors in Ref. [41] being unable to optimize the bcc SQS structure. The overall trend is the same, but -1.1 MJ m^{-3} (in-plane) MAE is not achievable in uniaxially strained systems.

We show that the MAE increases sharply with c/a decreasing to around 0.85 and remains stable over a wide range of lattice parameter ratios during further compression. It increases even further for c/a values below 0.8. Unfortunately, this extreme compression is accompanied by a rapid growth in system energy, as we will demonstrate later.

Considering lattice deformations more broadly, we find that for cobalt concentrations around 0.75, high uniaxial MAE in the strained structure is accompanied by similarly high MAE during equivalent compression. In other words, when the distance between neighboring atoms increases – due to, e.g., interstitial doping or finite-temperature lattice vibrations – the distance between those atoms and their respective neighbors on the other side decreases, further increasing MAE. This explains the appearance of a broader MAE maximum, shifted toward higher cobalt concentrations, as observed in studies using various configurational space sampling methods [17, 18, 35]. Moreover, phonon-induced magnetism enhancement has already been noted in cobalt-doped iron garnets [42].

Based on the self-consistently converged electron density, we calculated exchange integrals J_{ij} up to the 9th neighboring cell, corresponding to the 18th nearest neighbor, for $x = 0.7$. We applied the Lichtenstein *et al.* method for computing the exchange interaction coefficients [43] using the SPR-KKR package. The calculated parameters were subsequently used for Monte Carlo simulations in the Uppsala atomistic spin dynamics (UppASD) package [44]. The Curie temperature was determined using the Binder cumulant method, incorporating finite-size scaling [44–46].

Figure 1(c) shows the estimated T_C values derived from the intersection of the Binder cumulant *versus* temperature curves in two supercells – sized 25^3 and 30^3 – based on the methodology outlined in Ref. [46]. Our calculations suggest that for the bct₁₀ structure, composed predominantly of cobalt, the expected T_C ranges between 1250 and 1350 K, which is a highly suitable value for permanent magnet applications. These estimates align with prior results from the group of Blügel using mean-field theory [5, 47], which reported T_C values of 1550 K for bcc Fe_{0.3}Co_{0.7} and 1520 K for bcc Fe_{0.25}Co_{0.75}, with an approximate 20% T_C reduction under uniaxial compression. Additionally, we observe that the T_C *versus* c/a dependence is slightly asymmetric, favoring uniaxial compression over uni-

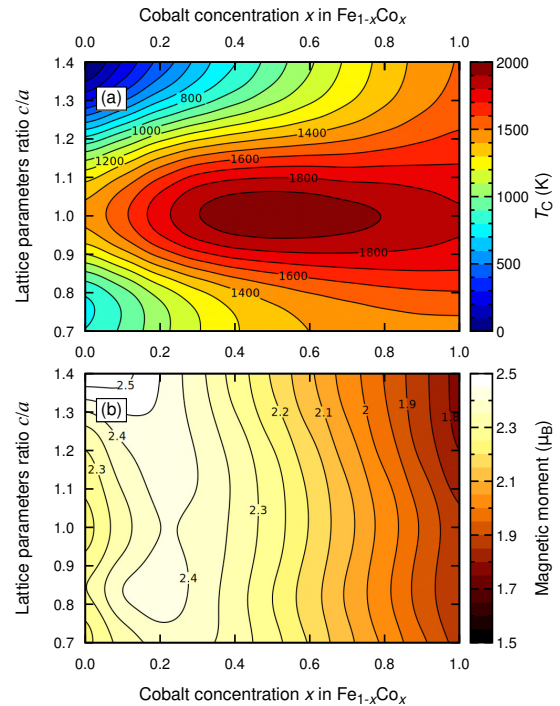


Figure 2. (a) Curie temperature (T_C) *versus* c/a lattice parameters ratio and cobalt concentration x for the $\text{Fe}_{1-x}\text{Co}_x$ alloy under tetragonal deformation. (b) Corresponding total (spin + orbital) magnetic moment map. Calculations were performed using the SPR-KKR 7.7.1 package, employing CPA for chemical disorder and the PBE exchange-correlation potential. T_C was estimated using the disordered local moments (DLM) method.

axial strain.

Due to computational limitations, we were restricted in performing high-accuracy Monte Carlo T_C calculations. Therefore, we employed the disordered local moments (DLM) method to derive a qualitative map of the critical temperature across the same c/a and x ranges. In this method, the material’s paramagnetic state is approximated as a CPA-like state, where each atomic site hosts mixed antiparallel magnetic moments (DLM state). The critical temperature of the ferromagnetic system can then be related to thermal energy and estimated approximately as follows [48, 49]:

$$T_{\text{critical}}^{\text{DLM}} = \frac{2}{3} \frac{E_{\text{DLM}} - E_{\text{FM}}}{k_B \cdot c}, \quad (2)$$

if the ferromagnetic state is energetically favorable, and:

$$T_{\text{critical}}^{\text{DLM}} = 0 \quad (3)$$

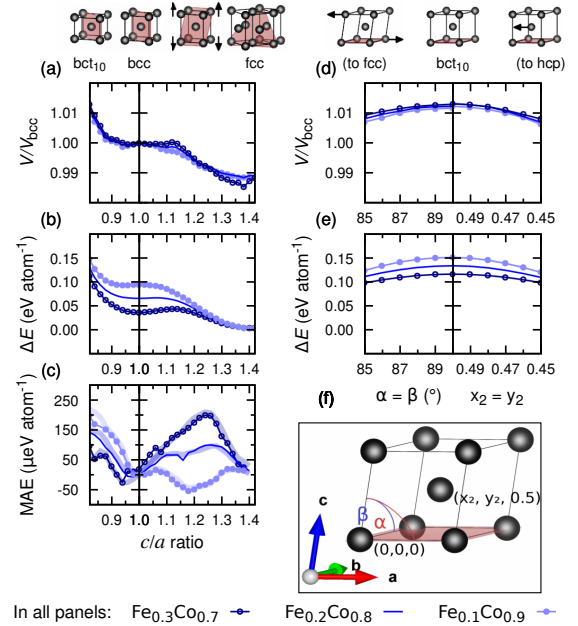
otherwise, where E_{DLM} and E_{FM} are the energies of the DLM and ferromagnetic states, respectively, c is the number of mag-

netic atoms in the system, and k_B is the Boltzmann constant. In Fig. 2, we present a calculated T_C^{DLM} map alongside the corresponding magnetic moments map.

Since the DLM state is fragile and susceptible to a collapse of the magnetic moment toward zero, we could not obtain a stable paramagnetic HS structure. Consequently, as shown in Fig. 2(a), T_C tends toward zero when approaching the iron fcc phase. In contrast, as depicted in Fig. 2(b), the ferromagnetic HS phase was successfully reproduced, with a magnetic moment value of $2.5 \mu_B \text{ atom}^{-1}$, consistent with previous studies [36, 38]. A key feature of the T_C and magnetic moment maps is the presence of Slater-Pauling-like maxima for cubic structures, observed at $x \approx 0.5$ for the T_C and at $x \approx 0.2$ for the magnetic moment. Both maps show promising results, with slightly asymmetric dependencies that favor the compressed structure across all cobalt concentrations. However, a clear minimum is observed in the magnetic moment versus c/a dependency at $c/a \approx 0.82$ and cobalt concentrations above $x = 0.4$. Given that the DLM method typically overestimates the critical temperature by approximately 30% [33, 50, 51], we estimate that for the bct_{10} structure – composed mainly of cobalt – T_C should lie between 1250 and 1350 K. We also expect the average magnetic moment in this structure to remain considerably high, between 1.8 and $2.2 \mu_B \text{ atom}^{-1}$. Additionally, in tetragonal structures, higher cobalt concentrations result in higher T_C . After accounting for the expected overestimation by the DLM method, our results are in agreement with both: our Monte Carlo calculations (shown in Fig. 1(c)) and previous work by the group of Blügel [5, 47]. Specifically, our findings align with the high T_C values predicted for body-centered tetragonal cobalt [5].

Two significant concerns arise. Firstly, the applied constant volume approximation may introduce certain distortions in the picture of such intricate value as MAE, and must impose inaccuracies in the magnetic moment description. Secondly, the bct_{10} system with $c/a \approx 0.82$ is a key intermediate structure along the Burgers transformation pathway. Developing a technological process to stabilize this phase may be possible, potentially making it easier to achieve experimentally than the phase in the MAE maximum proposed by Burkert *et al.* However, lattice vibrations could destabilize this structure. It is especially true for pure cobalt, as it is known to form hcp structure, although over 30 nm thick layers of bcc cobalt have been obtained [52] and tetragonal structure proven to be more stable [53]. Hence, in the last part of this work, we will focus on assessing the approximation accuracy and the structure’s stability.

To optimize the unit cell volume along the $\text{bcc} \leftrightarrow \text{fcc} \leftrightarrow \text{hcp}$ transformation path, we used the full-potential local-orbital (FPLO) code [54, 55], version 5.00-18, which features a localized basis. We applied the local density approximation (LDA) of exchange-correlation potential, based on the Perdew and Wang (PW92) parametrization [56], and used $P1$ symmetry. We sacrificed the accuracy of the PBE potential and fully relativistic approach – which was excessive for the geometry optimization – to adhere to the presumption of using CPA.



In all panels: $\text{Fe}_{0.3}\text{Co}_{0.7}$ — $\text{Fe}_{0.2}\text{Co}_{0.8}$ — $\text{Fe}_{0.1}\text{Co}_{0.9}$ —

Figure 3. Panels (a) and (d) depict the optimized cell volume ratio relative to the bcc structure. Panels (b) and (e) show the stability of the distorted $\text{Fe}_{1-x}\text{Co}_x$ alloy expressed in the form of transformation energy. Panel (c) presents the influence of geometry optimization on the MAE. The colors correspond to those in Fig. 1, with additional thick solid lines representing the unoptimized structure and thin lines with circles representing volume-optimized structures. Panels (a–c) depict the tetragonal structure under uniaxial distortion along the Bain path and beyond. Panels (d) and (e) show the skew and slip of hexagonal planes along the Burgers path. Panel (f) presents the $P1$ structure parameters that vary during the Burgers transformation. The atomic plane marked in red in the miniatures denotes the hexagonal plane: (101) in the bct_{10} structure, (111) in the fcc structure realized in $Pm\bar{3}m$ space group, and (001) in the structures along the Burgers path, realized in the $P1$ space group.

Although exact volume values differ between the LDA and GGA, we assumed that the volume ratios between any two structures would remain constant. Thus, we used the V/V_{bcc} profile to rescale the system volume for transformation energy (ΔE) and MAE calculations, which were carried out using the SPR-KKR/PBE framework described above. The results are presented in Fig. 3.

As expected, the unit cell volume decreases when approaching the fcc and hcp structures, both of which are close-packed phases. Overall, the optimized unit cell volume (Figs. 3(a) and 3(d)) remains within $\pm 1.25\%$ of the bcc unit cell volume. This is slightly lower than the $\sim 2\%$ value predicted by experiments but consistent with earlier density functional theory calculations [36, 57]. Our results indicate that full volume optimization does not significantly impact the MAE.

The energy profile for the tetragonal transformation (Fig. 3(b)) reveals a shallow minimum along the $\text{bcc} \leftrightarrow \text{bct}_{10}$ path, which forms when $x > 0.8$. At the same time, along the $\text{fcc} \leftrightarrow \text{bct}_{10} \leftrightarrow \text{hcp}$ transition path (Fig. 3(e)), the bct_{10} structure exhibits a local energy maximum. The two results taken together indicate a saddle point on the energy surface. While the minimum on the $\text{bcc} \leftrightarrow \text{bct}_{10}$ path is relatively shallow and close to more pronounced minima, we expect that the bct_{10} structure could be stabilized by combining interstitial doping with epitaxial growth on a suitable square lattice – a solution investigated by Mehl *et al.* [32]. It is primarily because the ΔE presented in Fig. 3(e) is almost flat in a wide range of transformations. We also expect the MAE in such epitaxial thin films to grow even further, especially made of pure Co [40].

In summary, we present a comprehensive study of magnetocrystalline anisotropy energies (MAE), magnetic moments, and Curie temperatures (T_C) of Fe–Co alloys across a wide range of tetragonal deformations. We also complete the investigation of the stability of the alloy by bridging the Bain and Burgers transformation pathways. While using state-of-the-art computational methods, this work covers a broader range of deformations than has been explored before. To validate the employed calculation techniques and their accuracy, we first reproduced key results from earlier studies, including the MAE and magnetic moment maps for body-centered tetragonal (bct) structures with $c/a > 1$, recreating the well-known Burkert *et al.* maximum in MAE. We then extended our study to Fe–Co alloys under uniaxial stress, a region that has rarely been investigated.

Our findings reveal a high-MAE region in uniaxially compressed Fe–Co alloys, particularly for alloys with high cobalt content. This region centers around an intermediate bct_{10} structure within the proposed Burgers $\text{bcc} \leftrightarrow \text{hcp} \leftrightarrow \text{fcc}$ transition pathway. We analyzed selected transformation energy profiles along the broader Burgers pathway, encompassing the transition to the fcc structure. The new structure is located at a saddle point of the energy surface, and consequently, it could be stabilized – by epitaxial growth on suitable square-lattice substrates or/and by interstitial doping, for example. This could lead to stable structures with much thicker layers than those previously reported for uniaxially strained Fe–Co alloys, potentially enabling bulk realizations. Monte Carlo simulations and DLM calculations indicate that this Co-rich structure under uniaxial tetragonal compression exhibits a higher T_C than under strain. Ultimately, our work broadens the range of stable, high-MAE structures available for various cobalt contents in tetragonal Fe–Co alloys. This now spans from ordered systems with cobalt concentrations as low as 25%, through stoichiometric FeCo, to nearly pure cobalt – as identified in this study.

ACKNOWLEDGEMENTS

We acknowledge the financial support of the National Science Centre Poland under the decision DEC-2018/30/E/ST3/00267. J. Á. C.-R. acknowledges the financial support from the Olle Engkvist Foundation and the Knut and Alice Wallenberg Foundation. The collaboration between W. M., J. M., and J. Á. C.-R. was possible thanks to the financial support of the Polish National Agency for Academic Exchange under the decision BPN/BEK/2022/1/00179/DEC/1. The main computational work was performed at the Poznan Supercomputing and Networking Centre (PSNC/PCSS). We are grateful to Paweł Leśniak and Daniel Depcik for their assistance with compiling and maintaining the computational codes. T_C calculations were enabled by resources provided by the National Academic Infrastructure for Supercomputing in Sweden (NAISS) at NSC Centre, partially funded by the Swedish Research Council through grant agreement no. 2022-06725. We thank Jan Ruzs for his valuable suggestions and discussions. We also thank Mateusz Kowacz, Zbigniew Śniadecki, Karol Synoradzki, and Justyn Snarski-Adamski for their comments on the manuscript. We thank Jan Martinek, whose insightful question inspired us to conduct this study.

* email: wojciech.marciniak@put.poznan.pl

- [1] R. Skomski, Permanent Magnets: History, Current Research, and Outlook, in *Novel Functional Magnetic Materials: Fundamentals and Applications*, edited by A. Zhukov (Springer International Publishing, Cham, 2016) pp. 359–395.
- [2] J. M. D. Coey, Perspective and Prospects for Rare Earth Permanent Magnets, *Engineering* **6**, 119 (2020).
- [3] R. Skomski and J. M. D. Coey, Magnetic anisotropy — How much is enough for a permanent magnet?, *Scr. Mater.* **112**, 3 (2016).
- [4] T. Burkert, L. Nordström, O. Eriksson, and O. Heinonen, Giant Magnetic Anisotropy in Tetragonal FeCo Alloys, *Phys. Rev. Lett.* **93**, 027203 (2004).
- [5] M. Ležaić, P. Mavropoulos, and S. Blügel, First-principles prediction of high Curie temperature for ferromagnetic bcc-Co and bcc-FeCo alloys and its relevance to tunneling magnetoresistance, *Appl. Phys. Lett.* **90**, 082504 (2007).
- [6] T. Hasegawa, Challenges toward development of rear-earth free FeCo based permanent magnet, *Electron. Comm. Jpn.* **104**, e12307 (2021).
- [7] P. Alippi, P. M. Marcus, and M. Scheffler, Strained Tetragonal States and Bain Paths in Metals, *Phys. Rev. Lett.* **78**, 3892 (1997).
- [8] A. Winkelmann, M. Przybylski, F. Luo, Y. Shi, and J. Barthel, Perpendicular Magnetic Anisotropy Induced by Tetragonal Distortion of FeCo Alloy Films Grown on Pd(001), *Phys. Rev. Lett.* **96**, 257205 (2006).
- [9] F. Yildiz, M. Przybylski, and J. Kirschner, Volume contribution to perpendicular anisotropy in $\text{Fe}_{0.5}\text{Co}_{0.5}$ alloy films on Pd(001), Ir(001), and Rh(001), *J. Appl. Phys.* **105**, 07E129 (2009).
- [10] F. Yildiz, M. Przybylski, X.-D. Ma, and J. Kirschner, Strong perpendicular anisotropy in $\text{Fe}_{1-x}\text{Co}_x$ alloy films epitaxially grown on mismatching Pd(001), Ir(001), and Rh(001) sub-

- strates, *Phys. Rev. B* **80**, 064415 (2009).
- [11] F. Luo, X. L. Fu, A. Winkelmann, and M. Przybylski, Tuning the perpendicular magnetic anisotropy in tetragonally distorted $\text{Fe}_x\text{Co}_{1-x}$ alloy films on Rh (001) by varying the alloy composition, *Appl. Phys. Lett.* **91**, 262512 (2007).
- [12] G. Andersson, T. Burkert, P. Warnicke, M. Björck, B. Sanyal, C. Chacon, C. Zlotea, L. Nordström, P. Nordblad, and O. Eriksson, Perpendicular Magnetocrystalline Anisotropy in Tetragonally Distorted Fe–Co Alloys, *Phys. Rev. Lett.* **96**, 037205 (2006).
- [13] P. Warnicke, G. Andersson, M. Björck, J. Ferré, and P. Nordblad, Magnetic anisotropy of tetragonal FeCo/Pt(001) superlattices, *J. Phys.: Condens. Matter* **19**, 226218 (2007).
- [14] G. Giannopoulos, R. Salikhov, B. Zingsem, A. Markou, I. Panagiotopoulos, V. Psycharis, M. Farle, and D. Niarchos, Large magnetic anisotropy in strained Fe/Co multilayers on AuCu and the effect of carbon doping, *APL Mater.* **3**, 041103 (2015).
- [15] M. Gong, A. Kirkemide, M. Wuttig, and S. Ren, Phase Transformation-Induced Tetragonal FeCo Nanostructures, *Nano Lett.* **14**, 6493 (2014).
- [16] L. Reichel, G. Giannopoulos, S. Kauffmann-Weiss, M. Hoffmann, D. Pohl, A. Edström, S. Oswald, D. Niarchos, J. Ruzs, L. Schultz, and S. Fähler, Increased magnetocrystalline anisotropy in epitaxial Fe–Co–C thin films with spontaneous strain, *J. Appl. Phys.* **116**, 213901 (2014).
- [17] E. K. Delczeg-Czirjak, A. Edström, M. Werwiński, J. Ruzs, N. V. Skorodumova, L. Vitos, and O. Eriksson, Stabilization of the tetragonal distortion of $\text{Fe}_x\text{Co}_{1-x}$ alloys by C impurities: A potential new permanent magnet, *Phys. Rev. B* **89**, 144403 (2014).
- [18] W. Marciniak and M. Werwiński, Structural and magnetic properties of Fe–Co–C alloys with tetragonal deformation: A first-principles study, *Phys. Rev. B* **108**, 214433 (2023).
- [19] G. Giannopoulos, R. Salikhov, G. Varvaro, V. Psycharis, A. M. Testa, M. Farle, and D. Niarchos, Coherently strained $[\text{Fe–Co(C)/Au–Cu}]_n$ multilayers: a path to induce magnetic anisotropy in Fe–Co films over large thicknesses, *J. Phys. D: Appl. Phys.* **51**, 055009 (2018).
- [20] L. Reichel, L. Schultz, D. Pohl, S. Oswald, S. Fähler, M. Werwiński, A. Edström, E. K. Delczeg-Czirjak, and J. Ruzs, From soft to hard magnetic Fe–Co–B by spontaneous strain: a combined first principles and thin film study, *J. Phys.: Condens. Matter* **27**, 476002 (2015).
- [21] L. Reichel, L. Schultz, and S. Fähler, Lattice relaxation studies in strained epitaxial Fe–Co–C films, *J. Appl. Phys.* **117**, 17C712 (2015).
- [22] I. Turek, J. Kudrnovský, and K. Carva, Magnetic anisotropy energy of disordered tetragonal Fe–Co systems from ab initio alloy theory, *Phys. Rev. B* **86**, 174430 (2012).
- [23] S. Steiner, S. Khmelevskiy, M. Marsmann, and G. Kresse, Calculation of the magnetic anisotropy with projected-augmented-wave methodology and the case study of disordered $\text{Fe}_{1-x}\text{Co}_x$ alloys, *Phys. Rev. B* **93**, 224425 (2016).
- [24] D. Odkhui and S. C. Hong, First-Principles Prediction of Possible Rare-Earth Free Permanent Magnet of Tetragonal fcco with Enhanced Magnetic Anisotropy and Energy Product through Interstitial Nitrogen, *Phys. Rev. Appl.* **11**, 054085 (2019).
- [25] W. G. Burgers, On the process of transition of the cubic-body-centered modification into the hexagonal-close-packed modification of zirconium, *Phys.* **1**, 561 (1934).
- [26] M. Ekman, B. Sadigh, K. Einarsdotter, and P. Blaha, Ab initio study of the martensitic bcc–hcp transformation in iron, *Phys. Rev. B* **58**, 5296 (1998).
- [27] F. M. Wang and R. Ingalls, Iron bcc–hcp transition: Local structure from x-ray-absorption fine structure, *Phys. Rev. B* **57**, 5647 (1998).
- [28] J. B. Liu and D. D. Johnson, bcc-to-hcp transformation pathways for iron versus hydrostatic pressure: Coupled shuffle and shear modes, *Phys. Rev. B* **79**, 134113 (2009).
- [29] Z. Lu, W. Zhu, T. Lu, and W. Wang, Does the fcc phase exist in the Fe bcc–hcp transition? A conclusion from first-principles studies, *Model. Simul. Mater. Sci. Eng.* **22**, 025007 (2014).
- [30] M. Friák and M. Šob, Ab initio study of the bcc–hcp transformation in iron, *Phys. Rev. B* **77**, 174117 (2008).
- [31] T. Burkert, O. Eriksson, P. James, S. I. Simak, B. Johansson, and L. Nordström, Calculation of uniaxial magnetic anisotropy energy of tetragonal and trigonal Fe, Co, and Ni, *Phys. Rev. B* **69**, 104426 (2004).
- [32] M. J. Mehl, A. Aguayo, L. L. Boyer, and R. de Coss, Absence of metastable states in strained monatomic cubic crystals, *Phys. Rev. B* **70**, 014105 (2004).
- [33] H. Ebert, D. Ködderitzsch, and J. Minár, Calculating condensed matter properties using the KKR–Green’s function method—recent developments and applications, *Rep. Prog. Phys.* **74**, 096501 (2011).
- [34] J. P. Perdew, K. Burke, and M. Ernzerhof, Generalized Gradient Approximation Made Simple, *Phys. Rev. Lett.* **77**, 3865 (1996).
- [35] C. Neise, S. Schönecker, M. Richter, K. Koepf, and H. Eschrig, The effect of chemical disorder on the magnetic anisotropy of strained Fe–Co films, *Phys. Status Solidi B* **248**, 2398 (2011).
- [36] V. L. Moruzzi, P. M. Marcus, K. Schwarz, and P. Mohn, Ferromagnetic phases of bcc and fcc Fe, Co, and Ni, *Phys. Rev. B* **34**, 1784 (1986).
- [37] Y. Liang, A. Gu, S. Wang, Y. He, S. Zheng, J. Guo, and F. S. Boi, Chemical vapour synthesis of carbon nano-onions filled with high-spin ferromagnetic $\gamma\text{-Fe}_{50}\text{Ni}_{50}$ nanocrystals: a structural and magnetic investigation, *CrystEngComm* **25**, 5382 (2023).
- [38] J. Meixner, J. Rychlý-Gruszecka, and M. Werwiński, Magnetic properties and structural phase transition in ultrathin fcc Fe(111) and bcc Fe(111) films: First-principles study, *J. Magn. Magn. Mater.* **589**, 171597 (2024).
- [39] C. J. Aas, L. Szunyogh, R. F. L. Evans, and R. W. Chantrell, Effect of stacking faults on the magnetocrystalline anisotropy of hcp Co: A first-principles study, *J. Phys.: Condens. Matter* **25**, 296006 (2013).
- [40] G. H. O. Daalderop, P. J. Kelly, and M. F. H. Schuurmans, First-principles calculation of the magnetocrystalline anisotropy energy of iron, cobalt, and nickel, *Phys. Rev. B* **41**, 11919 (1990).
- [41] M. Wolloch and D. Suess, Strain-induced control of magnetocrystalline anisotropy energy in FeCo thin films, *J. Magn. Magn. Mater.* **522**, 167542 (2021).
- [42] A. Frej, C. S. Davies, A. Kirilyuk, and A. Stupakiewicz, Phonon-induced magnetization dynamics in Co-doped iron garnets, *Appl. Phys. Lett.* **123**, 042401 (2023).
- [43] A. I. Liechtenstein, M. I. Katsnelson, and V. A. Gubanov, Exchange interactions and spin-wave stiffness in ferromagnetic metals, *J. Phys. F: Met. Phys.* **14**, L125 (1984).
- [44] O. Eriksson, A. Bergman, L. Bergqvist, and J. Hellsvik, *Atomistic Spin Dynamics: Foundations and Applications* (Oxford University Press, 2017).
- [45] D. Landau and K. Binder, *A Guide to Monte Carlo Simulations in Statistical Physics* (Cambridge University Press, 2021).
- [46] *Tutorial — UppASD Manual documentation*.
- [47] A. Jakobsson, E. Şaşıoğlu, P. Mavropoulos, M. Ležaić, B. Sanyal, G. Bihlmayer, and S. Blügel, Tuning the Curie temperature of FeCo compounds by tetragonal distortion, *Appl.*

- [Phys. Lett.](#) **103**, 102404 (2013).
- [48] B. L. Gyorffy, A. J. Pindor, J. Staunton, G. M. Stocks, and H. Winter, A first-principles theory of ferromagnetic phase transitions in metals, [J. Phys. F: Met. Phys.](#) **15**, 1337 (1985).
- [49] L. Bergqvist and P. H. Dederichs, A theoretical study of half-metallic antiferromagnetic diluted magnetic semiconductors, [J. Phys.: Condens. Matter](#) **19**, 216220 (2007).
- [50] L. Ke, K. D. Belashchenko, M. van Schilfgaarde, T. Kotani, and V. P. Antropov, Effects of alloying and strain on the magnetic properties of Fe_{16}N_2 , [Phys. Rev. B](#) **88**, 024404 (2013).
- [51] D. Hedlund, J. Cedervall, A. Edström, M. Werwiński, S. Kontos, O. Eriksson, J. Ruzs, P. Svedlindh, M. Sahlberg, and K. Gunnarsson, Magnetic properties of the $\text{Fe}_5\text{SiB}_2 - \text{Fe}_5\text{PB}_2$ system, [Phys. Rev. B](#) **96**, 094433 (2017).
- [52] G. A. Prinz, Stabilization of bcc Co via Epitaxial Growth on GaAs, [Phys. Rev. Lett.](#) **54**, 1051 (1985).
- [53] H. Giordano, A. Atrei, M. Torrini, U. Bardi, M. Gleeson, and C. Barnes, Evidence for a strain-stabilized bct phase of cobalt deposited on Pd{100}: An x-ray photoelectron diffraction study, [Phys. Rev. B](#) **54**, 11762 (1996).
- [54] K. Koepnick and H. Eschrig, Full-potential nonorthogonal local-orbital minimum-basis band-structure scheme, [Phys. Rev. B](#) **59**, 1743 (1999).
- [55] H. Eschrig, M. Richter, and I. Opahle, Chapter 12 - Relativistic Solid State Calculations, in *Theoretical and Computational Chemistry*, Relativistic Electronic Structure Theory, Vol. 14, edited by P. Schwerdtfeger (Elsevier, 2004) pp. 723–776.
- [56] J. P. Perdew and Y. Wang, Accurate and simple analytic representation of the electron-gas correlation energy, [Phys. Rev. B](#) **45**, 13244 (1992).
- [57] P. M. Marcus and V. L. Moruzzi, Equilibrium properties of the cubic phases of cobalt, [Solid State Commun.](#) **55**, 971 (1985).

Structural and magnetic properties of Fe-Co-C alloys with tetragonal deformation: A first-principles studyWojciech Marciniak^{1,2,*} and Mirosław Werwiński^{1,†}¹*Institute of Molecular Physics, Polish Academy of Sciences, M. Smoluchowskiego 17, 60-179 Poznań, Poland*²*Institute of Physics, Poznan University of Technology, Piotrowo 3, 60-965 Poznań, Poland*

(Received 16 July 2023; accepted 1 December 2023; published 29 December 2023)

Fe-Co alloys with induced tetragonal strain are promising materials for rare-earth-free permanent magnets. However, as ultrathin-film studies have shown, tetragonal Fe-Co structures tend to a rapid relaxation toward a cubic structure as the thickness of the deposited film increases. One of the main methods of inducing the stable strain in the bulk material is interstitial doping with small atoms, like B, C, or N. In this work, we present a full configuration-space analysis in the density functional theory approach for $(\text{Fe}_{1-x}\text{Co}_x)_{16}\text{C}$ supercells with a single C impurity in one of the octahedral interstitial positions and for the full range of Co concentrations x . We discuss all assumptions and considerations leading to calculated lattice parameters, mixing enthalpies, magnetic moments, and averaged magnetocrystalline anisotropy energies (MAE). We present a comprehensive qualitative analysis of the structural and magnetic properties' dependence on short- and long-range ordering parameters. We analyzed all unique Fe/Co atom occupancies at all stoichiometric concentrations possible in $2 \times 2 \times 2$ supercell based on two-atom tetragonal representation. We rely on the thermodynamic averaging method and large sample count to obtain accurate MAE values. We place the utilized method in the context of several chemical disorder approximation methods, including effective medium methods (virtual crystal approximation and coherent potential approximation) and special quasirandom structures method applied to Fe-Co-based alloys. We observe a structural phase transition from the body-centered-tetragonal structure above 70% Co concentration and confirm the structural stability of Fe-Co-C alloys in the tetragonal range. We show the presence of a broad MAE maximum around about 50% Co concentration and notably high MAE values for Co content x as low as 25%. In addition, we show the presence of a positive correlation between MAE and mixing enthalpy.

DOI: [10.1103/PhysRevB.108.214433](https://doi.org/10.1103/PhysRevB.108.214433)**I. INTRODUCTION**

Permanent magnets are an indispensable part of modern technology. Among their main characteristic parameters are the energy product $(BH)_{\text{max}}$ and coercive field H_C . $(BH)_{\text{max}}$ determines the efficiency of a permanent magnet and mainly depends on the saturation magnetization M_S and coercive field. Most of the current high-end magnets, with outstanding performance, contain rare-earth elements, such as samarium in SmCo_5 and neodymium in $\text{Nd}_2\text{Fe}_{14}\text{B}$. However, rare-earth-based magnets have limitations, such as the relatively low Curie temperature of neodymium magnets, which is insufficient for many applications. Moreover, concerns have risen recently about the rare-earth market fragility, which manifested in the so-called rare-earth crisis in 2011 [1,2]. Hence, intense research for rare-earth-free permanent magnets has been conducted in the following years. Many potential candidates have been discovered, including MnBi, MnAl, and

FeNi magnets [3,4]. Currently, rare-earth prices tend towards levels similar to those during the crisis period, encouraging further efforts towards developing efficient rare-earth-free permanent magnets.

One of the good alternatives are transition-metal-based (TM-based) magnets. Fe-Co alloys are especially promising in this category. Burkert *et al.* showed, using density functional theory (DFT) calculations, that in uniaxially strained body-centered-tetragonal (bct) disordered iron-cobalt $(\text{Fe}_{1-x}\text{Co}_x)$ alloys, giant magnetocrystalline anisotropy energy (MAE) of about $800 \mu\text{eV atom}^{-1}$ (over 10 MJ m^{-3}) can be achieved for Co concentration x close to 0.6 and lattice parameter ratio c/a close to 1.22 [5]. Such MAE value is comparable to properties observed for SmCo_5 , $\text{Nd}_2\text{Fe}_{14}\text{B}$, and FePt, while at the same time, the saturation magnetization of Fe-Co significantly exceeds the values observed for the aforementioned materials. Afterward, many systems have been synthesized following the epitaxial Bain path [6], including $\text{Fe}_{1-x}\text{Co}_x/\text{Pt}$ multilayers [7–9] and deposition of $\text{Fe}_{1-x}\text{Co}_x$ on Pd (001) [10–12], Ir (001) [11,12], and Rh (001) buffers [11–13]. However, the thin-film experiments showed MAE values lower than those predicted by Burkert *et al.*

Neise *et al.* [14] showed that the discrepancies between the theoretically predicted MAE and the measured values could be attributed to the virtual crystal approximation (VCA) utilized by Burkert *et al.* Using $2 \times 2 \times 2$ supercell approach with atom arrangements modeled according to randomized

*wojciech.robe.marciniak@doctorate.put.poznan.pl

†werwinski@ifmpan.poznan.pl

Published by the American Physical Society under the terms of the [Creative Commons Attribution 4.0 International license](https://creativecommons.org/licenses/by/4.0/). Further distribution of this work must maintain attribution to the author(s) and the published article's title, journal citation, and DOI.

nearest-neighbor pattern, they showed that ordered phases of $\text{Fe}_{1-x}\text{Co}_x$ have larger MAE than disordered ones, which was confirmed later by Turek *et al.* [15]. They also proposed the preparation of the $\text{Fe}_{1-x}\text{Co}_x$ epitaxial films along the Bain path [6], which has since been realized by Reichel *et al.* [16–18] on the $\text{Au}_x\text{Cu}_{1-x}$ buffer, offering a possibility to tailor the lattice parameter in a wide range [19].

Turek *et al.* further improved the theoretical prediction, ascribing again the calculated *versus* experimental MAE difference (of the order of 3–4) to the VCA. Utilizing a more sophisticated method of the chemical disorder approximation, namely, coherent potential approximation (CPA) [20], they obtained MAE of much lower and a less sharp maximum of $183 \mu\text{eV atom}^{-1}$ spanning a wider range between about 0.5 and 0.65 Co concentration for $c/a \approx 1.22$ [15]. They also showed that ordering of the $\text{Fe}_{1-x}\text{Co}_x$ alloys towards $L1_0$ phase (derived from B2 CsCl structure elongated along the z axis) could significantly increase the MAE (by a factor between 2 and 3) to $450 \mu\text{eV atom}^{-1}$ for $\text{Fe}_{0.4}\text{Co}_{0.6}$ and $580 \mu\text{eV atom}^{-1}$ for $L1_0 \text{Fe}_{0.5}\text{Co}_{0.5}$, corresponding well with theoretical K_u of $520 \mu\text{eV atom}^{-1}$ from Ref. [14]. Importantly, however, experiments and further calculations have shown that $\text{Fe}_{1-x}\text{Co}_x$ bct thin films are prone to a rapid relaxation towards the body-centered-cubic (bcc) structure above the critical thickness of about 15 monolayers (about 2 nm) [16,21].

Additions of small interstitial atoms such as B, C, and N were proposed to stabilize the necessary tetragonal distortion by the formation of $\text{Fe}_{1-x}\text{Co}_x$ martensite phase. Using special quasirandom structure (SQS) method [22] in $(\text{Fe}_{1-x}\text{Co}_x)_{16}\text{C}$ supercells, multiple authors obtained a bct structure with c/a lattice parameters ratio as high as 1.12–1.17 [23,24]. Several experimentally obtained systems have confirmed these predictions [16–18,25,26], although there is still plenty of room for further improvements. Two above-mentioned MAE enhancement methods, namely, (i) strain induced by a lattice mismatch between two epitaxially grown layers and (ii) spontaneous lattice distortion due to impurities, are summarized in the recent review by Hasegawa [3].

Steiner *et al.* performed an $\text{Fe}_{1-x}\text{Co}_x$ case study by averaging over completely random structures in a $2 \times 2 \times 2$ supercell [27]. They suggested that proper caution has to be placed on the averaging method since CPA and VCA are effective medium methods that do not describe local structure relaxation and reduced symmetry. Despite their concerns, they obtained MAE values similar to the CPA results reported previously by Turek *et al.* [15]. Since then, many papers have focused on a supercell approach applied to selected cases of $\text{Fe}_{1-x}\text{Co}_x$ doped with boron [28], carbon [29], and nitrogen [29–31], mostly regarding either (i) the $L1_0$ phase derived from B2 (CsCl) structure strained along the z axis, or (ii) the $\text{Fe}_{0.4}\text{Co}_{0.6}$ disordered alloy. An interesting new way of elucidating the interactions in $(\text{Fe}_{1-x}\text{Co}_x)_2\text{B}$ was proposed by Däne *et al.* They performed a sampling of the full configuration space of the 12-atom supercell, again using the argument that VCA and CPA do not correctly describe the distribution of possible values of MAE and the influence of chemical neighborhood and local geometry optimization. They observed a significant spread of the MAE values with an overall average in good agreement with the experiment. They

argue that treating a “true” disorder is certainly beneficial. They also noted that it is necessary to average over sufficiently large supercells, as the supercell size can significantly affect the MAE values obtained [32].

The discussion about configuration space analysis is connected with symmetry and ordering in the supercell. Given the vast data set regarding multiple structures in a single-crystal system, analysis of ordering towards specific structures is straightforward to implement; it provides more insight into physical phenomena occurring. Works on energy states of closely related structures reach the 1930s–1960s of the 20th century, including contributions from Bethe, Bragg, Williams, Warren, and Cowley in short- and long-range order analysis methods of that period [33–37]. Recently, a notable example of ordering effects analysis closely related to our work includes research on the FeNi ordering towards the $L1_0$ phase performed by Izardar, Ederer, and Si [38–40].

In this work, we aim at adding new involvement into the discussion about magnetism in $(\text{Fe}_{1-x}\text{Co}_x)_{16}\text{C}$ by implementing a similar method as used by Däne *et al.* It gives us the possibility to investigate more deeply the possible values of magnetic properties in the system, including dependencies on ordering and, broadly researched, the impurity first coordination shell occupancy. We present a complete analysis of all stoichiometric compositions modeled in a $2 \times 2 \times 2$ supercell. We consider all possible symmetrically inequivalent arrangements of Fe and Co atoms. The aim of the study is to predict the phase stability and intrinsic magnetic properties for the full range of concentrations of the $(\text{Fe}_{1-x}\text{Co}_x)_{16}\text{C}$ system and place it in the frame of works on Fe-Co, Fe-Co-B, Fe-Co-N, and Fe-Co-C alloys. To achieve it, we study the full configuration space of the 17-atom representation of the Fe-Co-C system and explore this approach to crystallize the most effective method of similar analyses for future applications. Taking advantage of the opportunity to analyze a significant portion of the configuration space of this alloy, we start with the analysis of the entropic and enthalpic contribution towards the system energy. Selected computational cell size is currently the practical limit due to the computational cost.

II. CALCULATION DETAILS

A. System preparation

We used the full-potential local-orbital (FPLO18.00) code [41,42] with the generalized gradient approximation (GGA) exchange-correlation functional in the Perdew, Burke, and Ernzerhof (PBE) [43] parametrization for all calculations. The use of FPLO was dictated by, *inter alia*, the inherent implementation of the full-potential approach (i.e., omitting the crystalline potential shape approximation), and the expansion of the extended states in terms of localized atomic-like numerical orbital basis [41,42]. The full-potential approach is particularly essential for accurately determining a subtle quantity such as MAE. Another important factor in choosing FPLO is the very high performance of the code, at the expense of the lack of multithreading. In our approach, scaling multiple single-thread calculations up in an embarrassingly parallel manner is the optimal solution.

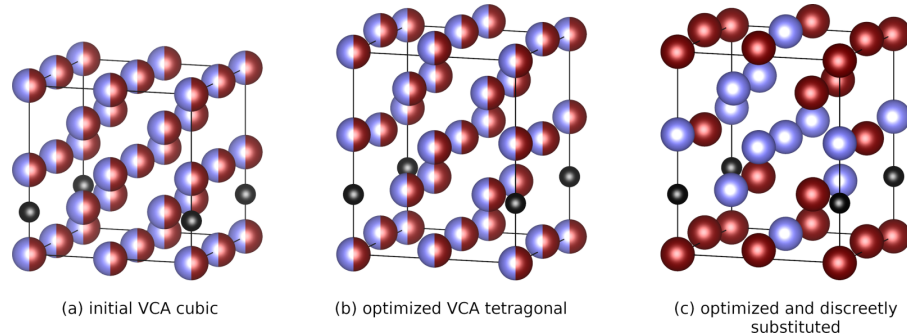


FIG. 1. Examples of prepared and obtained crystal structures of $\text{Fe}_8\text{Co}_8\text{C}$. Initial cubic supercell: input to virtual crystal approximation (VCA) relaxation (a), structure resultant from VCA geometry optimization (b), and one of the final structures with VCA atoms substituted by Fe and Co atoms (c). Iron, cobalt, and carbon atoms are presented in dark red, light blue, and black, respectively.

Initially, we built a $2 \times 2 \times 2$ supercell of the two-atom $\text{Fe}_{1-x}\text{Co}_x$ body-centered system representation in the $P4/mmm$ space group (s.g. 123). The result is a computational cell containing a total of 16 Fe/Co atoms. Initial atomic positions were assumed to be perfect $(0, 0, 0)$ and $(\frac{1}{2}, \frac{1}{2}, \frac{1}{2})$ in each unit cell, and a single C atom was introduced as an octahedral interstitial dopant on the $(0, 0, \frac{1}{4})$ site in the supercell. The resultant structure is shown in Fig. 1(a). Structure visualizations were prepared in VESTA software [44]. The carbon concentration in the prepared models is about 6 at.% and 1.25 wt.% (1 C atom per 16 TM atoms). Initial atomic positions were optimized for Co concentrations equivalent to all stoichiometric cases in the 17-atom supercell (Fe_{16}C , Fe_{15}CoC , $\text{Fe}_{14}\text{Co}_2\text{C}$, ..., Co_{16}C). At this stage, we used VCA for the disorder treatment, $6 \times 6 \times 6$ \mathbf{k} -point mesh, 10^{-5} density and 10^{-7} Ha ($\sim 2.72 \cdot 10^{-5}$ eV) energy convergence criteria and 10^{-3} eV \AA^{-1} force tolerance for initial optimization. Cell volume and c/a optimization were performed based on a third-order surface fit to energy *versus* computational cell volume in the 160–208 \AA^3 range, incremented by 4 \AA^3 and c/a ratios in the 1.05–1.16 range, incremented by 0.01. Uniaxial elongation of the cell was assumed after Reichel *et al.* [24]. The preparation of the VCA system ended with a full optimization of atomic positions for the minimum of the mentioned fit. We used a scalar-relativistic approach with the same parameters as before. An exemplary resultant structure for the $\text{Fe}_8\text{Co}_8\text{C}$ system is shown in Fig. 1(b).

In the final step of structures' preparation, atomic sites were populated with all possible discrete, stoichiometric, geometrically inequivalent Fe/Co occupations. The equivalency was determined based on the initial, perfect body-centered-tetragonal geometry with a single octahedral dopant. 4394 unique combinations were obtained out of 65 536 total combinations without repetitions, including 748 unique combinations out of 12 870 for the $\text{Fe}_8\text{Co}_8\text{C}$ case alone. The detailed presentation of the number of unique atomic arrangements in a 16-atom $2 \times 2 \times 2$ supercell on a bcc, bct, and octahedrally doped bct lattice are presented in Table I. The criterion of identity between the combinations was the equity of all interatomic distances between all atom types,

i.e., Fe-Fe, Co-Co, Fe-Co, Fe-C, and Co-C in the initial, perfect supercell. It can be proven that it is unambiguous and directly couples each combination with the distribution of minority atoms in the supercell, such as the short-range ordering parameter described later. This approach provided us with a relatively simple method for preliminary analysis. Electron density was then converged in the scalar-relativistic mode, using $9 \times 9 \times 9$ \mathbf{k} points over the entire Brillouin zone, following five additional force optimization steps for every structure to prevent numerical artifacts. For this step of the calculations, convergence criteria were set at 10^{-6} density and 10^{-8} Ha ($\sim 2.72 \cdot 10^{-6}$ eV). One of the final $\text{Fe}_8\text{Co}_8\text{C}$ structures is presented in Fig. 1(c).

In the end, we performed a single step of fully relativistic calculations with magnetization direction aligned in two orthogonal directions, $[1 0 0]$ and $[0 0 1]$, over a charge density self-consistently converged in the scalar-relativistic approach [45], a method proven previously to be both accurate and effective [46,47]. Based on the resultant charge density and system energies, we derived relevant magnetic and structural parameters per configuration. Those include magnetocrystalline anisotropy energies (MAE), mixing enthalpies (ΔH_{mix}), magnetic hardness parameter (κ), Bethe short-range order parameter (σ), Warren-Cowley short-range

TABLE I. Number of possible structures in $2 \times 2 \times 2$ supercell of AB binary alloy in different representations.

Minority atoms in AB $2 \times 2 \times 2$ supercell	bcc symmetry unique	bct symmetry unique	bct symmetry (octahedrally doped) unique	All possible
0	1	1	1	1
1	1	1	5	16
2	4	6	24	120
3	6	10	69	560
4	15	30	174	1820
5	17	39	330	4368
6	24	67	526	8008
7	27	77	694	11440
8	32	84	748	12870

order parameter (α^{XY}) for first coordination shell, and long-range ordering parameter towards B2 phase (S). Specific equations and methods relevant to detailed parts of the presented work are introduced further alongside the results.

B. Assumptions and ensemble-averaging methods

We estimate our MAE results for each data point to be within 15% relative error due to relatively low \mathbf{k} -point mesh. Obviously, obtaining accuracy within 1% for each considered structure would be highly valuable. However, raising the accuracy would greatly increase the computational cost beyond current capabilities. Obtained system energies and the mixing enthalpies are much more accurate. Bound by this limitation, we focus on qualitative trends and averages in more subtle values, such as MAE. We assume the error imposed by the low \mathbf{k} -point mesh for each data point is random and noncumulative.

We utilize thermal averaging after Däne *et al.* [32] to include influence of nonoptimal ground-level energy states:

$$\text{MAE}(T) \equiv \frac{\sum_{\nu} [\text{MAE}_{\nu} \exp(-E_{\nu}/k_{\text{B}}T) n_{\nu}]}{\sum_{\nu} [\exp(-E_{\nu}/k_{\text{B}}T) n_{\nu}]}, \quad (1)$$

where E_{ν} denotes the total energy of a unique atomic arrangement combination ν , MAE_{ν} represents its magnetocrystalline anisotropy energy, and n_{ν} is the number of geometrically equivalent configurations.

An important part of the discussion is whether the averaging assumed in Eq. (1) is proper. Foremost, we acknowledge the fact that at room temperature, a vast part of the system does not occupy the ground state, which is calculated in plain DFT. It results, e.g., in the real magnetic moments being lower than predicted. A fact more important for us is that Eq. (1) does not count factors such as the energy barrier height between atom arrangements in the cell. In fact, if the energy barrier is high enough, simple arithmetic averaging should be more appropriate. The height of the energy barrier between the conformations could be obtained by, for example, the nudged elastic band (NEB) method [48,49]. However, it would be computationally not yet feasible to obtain heights of all possible transitions [50]. Obtaining at least a few values of the barriers in the near future could be beneficial. The solution is, however, not compatible with our methods. Less accurate but less costly linear scaling DFT methods could be utilized to obtain rough values of the barriers. Moreover, this thermodynamic approach results in the configurations' statistical distribution corresponding to slow cooling. Overall, despite the obtained results do not rely solely on the most optimal atomic arrangements, the lowest-energy structures vastly contribute to the overall MAE. Equation (1) certainly works for situations corresponding to slow cooling of the alloy. Hence, it is another assumption in our work that applies to thermal averages.

Apart from the assumptions, an important factor to note is the notation we use to describe various C impurity nearest-neighbor patterns. Those designations (Fe–C–Fe, Co–C–Co, and especially Fe–C–Co) should not be mistaken with the common Fe–Co–C system designation, which we also utilize in this work.

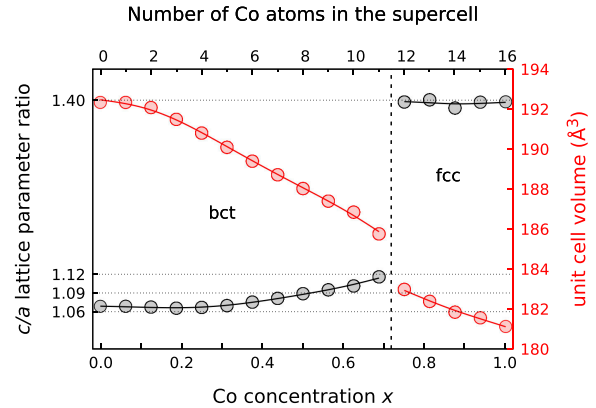


FIG. 2. Dependency of lattice parameters (c/a) ratio (black) and unit cell volume (red) on Co concentration x in $(\text{Fe}_{1-x}\text{Co}_x)_{16}\text{C}$ system, calculated with FPLO18 in virtual crystal approximation (VCA) with PBE exchange-correlation potential. The dashed line denotes the structural phase transition between body-centered-tetragonal (bct) and face-centered-cubic (fcc) structures.

III. RESULTS AND DISCUSSION

A. Structural properties

We will first discuss the structural parameters of the alloys under consideration. During the VCA geometry optimization, we observed a structural phase transition from body-centered tetragonal (bct) to face-centered cubic (fcc) structure, which occurs between 11 and 12 Co atoms in the supercell (between 69% and 75% Co concentration) (see Fig. 2). It corresponds to the well-known phase transition towards hexagonal close-packed structure for high-Co concentration in $\text{Fe}_{1-x}\text{Co}_x$. The fcc structure is the closest to the hcp structure we can obtain under the assumed constraints. Although unstable at the standard conditions, the fcc structure for pure Co has been obtained in the high-pressure regime by Yoo *et al.* [51].

Unit cell volume decreases monotonically with Co concentration after a weak peak for a single Co atom in the supercell, with a significant drop with the transition from bct to fcc structure. Distinct maximum in unit cell volume has been argued by Pauling and other authors, as brought recently by Díaz-Ortiz *et al.*, to be of the same nature as a peak in magnetization (Slater-Pauling curve) [52,53]. The weak maximum we obtained stays in contradiction with the expected, Slater-Pauling-type shape of the curve brought to attention by Prinz [54] and successfully reproduced in calculations, e.g., by Díaz-Ortiz *et al.* [53] and Steiner *et al.* [27], with a distinct maximum at around 20%–30% Co in $\text{Fe}_{1-x}\text{Co}_x$. We ascribe this discrepancy to the presence of the dopant atom in the unit cell. Nevertheless, a noticeable positive deviation from Vegard's law is apparent. A similar influence of the small interstitial dopant on the structural (and magnetic) parameters of the system has been observed by Chandran *et al.* for the $(\text{Fe}_{1-x}\text{Co}_x)_{16}\text{N}_2$ system [30].

The exact lattice parameters obtained using the VCA in the bct regime are a ranging from 2.75 Å for $\text{Fe}_5\text{Co}_{11}\text{C}$ to 2.82 Å for $\text{Fe}_{15}\text{Co}_1\text{C}$, and c ranging from 3.01 Å for

$\text{Fe}_5\text{Co}_{11}\text{C}$ to 3.07 \AA for $\text{Fe}_{12}\text{Co}_4\text{C}$. Resultant optimized volume of the bct systems ranges from 185.8 \AA^3 for $\text{Fe}_5\text{Co}_{11}\text{C}$ to 192.3 \AA^3 for $\text{Fe}_{15}\text{Co}_1\text{C}$. Consistency with Fe_{16}C supercell volume obtained by Delczeg-Czirjak *et al.* [23] in VASP code (about 196 \AA^3) is good, as well as comparison to experimental value (about 183 \AA^3) obtained by Reichel *et al.* for $(\text{Fe}_{0.4}\text{Co}_{0.6})_{0.98}\text{C}_{0.02}$ [16]. The result for equiatomic $(\text{Fe}_{0.5}\text{Co}_{0.5})_{16}\text{C}$ (188 \AA^3) is close to values obtained by Khan and Hong in equiatomic $(\text{Fe}_{0.5}\text{Co}_{0.5})_{32}\text{C}$ (about 187 \AA^3) [29] and $(\text{Fe}_{0.5}\text{Co}_{0.5})_{32}\text{N}$ (about 188 \AA^3) [28]. It is also close to the result by Odkhuu and Hong for $(\text{Fe}_{0.5}\text{Co}_{0.5})_{16}\text{N}$ (about 190 \AA^3) [31]. Similar values have also been presented for B-doped $\text{Fe}_{1-x}\text{Co}_x$ alloys by Reichel *et al.* [24]. This slight overestimation of the transition metal alloy lattice parameter is an expected behavior of the applied PBE exchange-correlation functional. Diaz-Ortiz *et al.* provided an excellent review of structural parameters, magnetic moments, and stabilities of $\text{Fe}_{1-x}\text{Co}_x$ alloys calculated from first principles. They listed several other results of unit cell volume for $\text{Fe}_{1-x}\text{Co}_x$, ranging from 180 to 190 \AA^3 per 16-atom cell [53]. Most importantly, Delczeg-Czirjak *et al.* showed that lattice parameters do not exhibit any significant dependency on the atomic configuration exemplified by the C impurity nearest neighbors [23]. We followed the assumption of not optimizing lattice parameters for every configuration, as it would be too computationally demanding.

Derived lattice parameters lead to the c/a ratio in the bct regime rising from 1.07 in the case of Fe_{16}C to 1.12 for $\text{Fe}_5\text{Co}_{11}\text{C}$. It is in agreement with the initial assumption of Burkert *et al.* [5] and following theoretical estimations of uniaxial strain induction by interstitial impurities [23,24]. Reichel *et al.* presented experimental c/a value of 1.05 for B-doped $\text{Fe}_{0.38}\text{Co}_{0.62}$, and c/a for $(\text{Fe}_{0.4}\text{Co}_{0.6})_{16}\text{C}$ equal 1.03 – 1.04 , which is lower than the value of approximately 1.10 close to earlier calculation results present in the literature, and also predicted by us. They provided several possible reasons for the observed difference in their work [24]. The phase transition from bct to fcc for $(\text{Fe}_{1-x}\text{Co}_x)_{16}\text{C}$ has been also previously reproduced computationally by Delczeg-Czirjak *et al.* for Co concentration around 65 at.% [23]. Uniaxial strain in the order of a few percent has been numerously shown to lead to reasonable MAE values [5,14,15,27], which can be further improved, e.g., by buffer-induced effects in thin-film applications [16,18,24,50].

B. Mixing entropy

Considering configuration space analysis, an interesting insight can be provided by investigating the enthalpic and entropic contributions to the system energy. The entropy of mixing (also called configurational entropy) is a statistical parameter describing the system configuration (or conformation) space quantitatively and, in a basic Boltzmann formulation, takes the form

$$\Delta S_{\text{conf}} = -k_B \ln \omega, \quad (2)$$

where k_B is Boltzmann constant and ω is the total number of possible arrangements of the system. Then, for a finite computational supercell of binary alloy, the atomic contribution to configurational entropy can be calculated from the

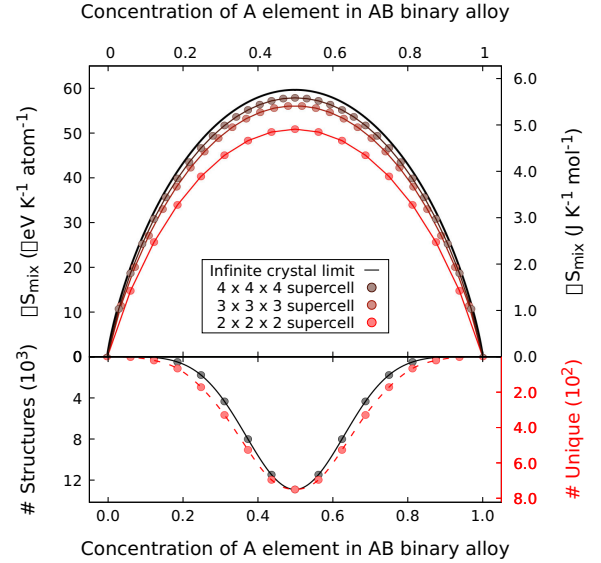


FIG. 3. Configurational entropy for binary alloys calculated for several supercells of different sizes and the number of all obtainable structures in $2 \times 2 \times 2$ supercells (black). With the dashed red line, we denote the number of symmetrically inequivalent structures in the bct representation with the symmetry broken by an octahedral impurity.

equation [55]

$$\Delta S_{\text{conf}}(x, N) = -\frac{1}{N} k_B \ln \frac{N!}{[Nx]![N(1-x)]!}, \quad (3)$$

where x is the concentration of a selected element in the alloy and N is the number of atomic sites occupied by mixed elements in the supercell. It can be also expressed in the shortened form

$$\Delta S_{\text{conf}}(x, N) = -\frac{1}{N} k_B \ln \binom{N}{Nx}, \quad (4)$$

where $\binom{n}{k} = \frac{n!}{k!(n-k)!}$ is the binomial coefficient. Independently of the exact transcription of the above formula, the equation for the ideal ΔS value for an infinitely large supercell takes the form

$$\begin{aligned} \Delta S_{\text{conf-ideal}}(x) &= \lim_{N \rightarrow \infty} \Delta S_{\text{conf}}(x, N) \\ &= -k_B [x \ln x + (1-x) \ln(1-x)]. \end{aligned} \quad (5)$$

For the purposes of our analysis, we consider the configurational entropy of a binary alloy, even though our supercells contain three elements (Fe, Co, and C). We motivate this approximation by the C atom fixing in the interstitial position so that only Fe and Co atoms are mixed in common sites.

Figure 3 shows the determination of Eqs. (3) and (5) for several selected supercell sizes and the full range of concentrations, as well as total and reduced number of configurations for the $2 \times 2 \times 2$ supercell with the symmetry reduced by a single octahedral interstitial dopant. The highest configurational entropy value occurs at the equilibrium concentration ($x = 0.5$), and a $2 \times 2 \times 2$ supercell, such as the one we used in this study, leads to an entropy underestimation of about 15%

compared to the ideal result. The error due to the finite size of supercells decreases quite quickly as their size increases. The obtained $\Delta S(x)$ relationship can be compared with the previously determined mixing enthalpy values for $(\text{Fe}, \text{Co})_{16}\text{C}$ alloys. As we can read from Fig. 3, the highest value of $T\Delta S$ at 1000 K for equiatomic concentration would be equal to 60 meV atom⁻¹, which in absolute terms is less than the highest value of mixing enthalpy calculated as equal to about 100 meV, for $\text{Fe}_8\text{Co}_8\text{C}$ composition. This means that below 1000 K, there is a high probability that ordered Fe-Co intermetallic compounds will be thermodynamically more favored than solid solutions [56]. The estimated gain from considering structure degeneracy was described in the previous sections.

C. Mixing enthalpy and basic magnetic properties *versus* Co concentration

A basic energetic parameter describing the system is the mixing enthalpy. It provides information about the tendency towards the formation of respective structures instead of separation into their constituent phases (in this case, pure Fe- and Co-based phases). For each structure, we calculated mixing enthalpy ΔH_{mix} between bct Fe_{16}C and fcc Co_{16}C using an equation analogous to the one used by Díaz-Ortiz *et al.*, for convenient comparison with their results [53]:

$$\Delta H_{\text{mix}}(x) = E_{(\text{Fe}_{1-x}\text{Co}_x)_{16}\text{C}} - xE_{\text{Co}_{16}\text{C}} - (1-x)E_{\text{Fe}_{16}\text{C}}, \quad (6)$$

as it, in fact, is the same quantity they calculated for ordered $\text{Fe}_{1-x}\text{Co}_x$ structures in $2 \times 2 \times 2$ supercells. The results, presented in Fig. 4(a), correspond well with the aforementioned data for $\text{Fe}_{1-x}\text{Co}_x$. The absolute values of ΔH_{mix} (up to 8 mRy atom⁻¹) are only slightly lower in comparison with up to 9 mRy atom⁻¹ calculated by Díaz-Ortiz *et al.* [53]. It indicates the stability of both disordered and ordered $(\text{Fe}_{1-x}\text{Co}_x)_{16}\text{C}$ alloys with a minor structure destabilization by the dopant. Overall, the magnitude of mixing enthalpies suggests good mixing potential, comparable to both TM alloys and steels. Moreover, the shape of the curve suggests the stability of each of the structures relative to neighboring ones, up to 11 Co atoms in the system, or up to the calculated bct-fcc transition. Furthermore, a slight asymmetry in the dependence of mixing enthalpy on x can be observed. On average, the systems closer to the Co side have lower energies, especially for Co-C-Co systems. However, the absolute minimum for Co-C-Co systems occurs for $\text{Fe}_8\text{Co}_8\text{C}$. For Fe-C-Co, and especially Fe-C-Fe systems, the minimum is moved to the left. The effect of ordering on the mixing enthalpy will be discussed in the following sections. On average, for the region around the equiatomic $\text{Fe}_8\text{Co}_8\text{C}$, the energy of the systems with C impurity neighbored by two Co atoms is lower compared to systems with the C atom adjacent to two Fe atoms or one Fe and one Co atom. This is consistent with the observation by Delczeg-Czirjak *et al.* [23] that the energy of Fe-Co-C systems depends mainly on the direct chemical neighborhood of the impurity atom, with a preference towards Co-C-Co nearest-neighbor sequence. A similar effect has been calculated by Chandran *et al.* for N-doped Fe and $\text{Fe}_{1-x}\text{Co}_x$ [30]. Such behavior contradicts the negligence of the direct chemical neighborhood of the impurity atom in

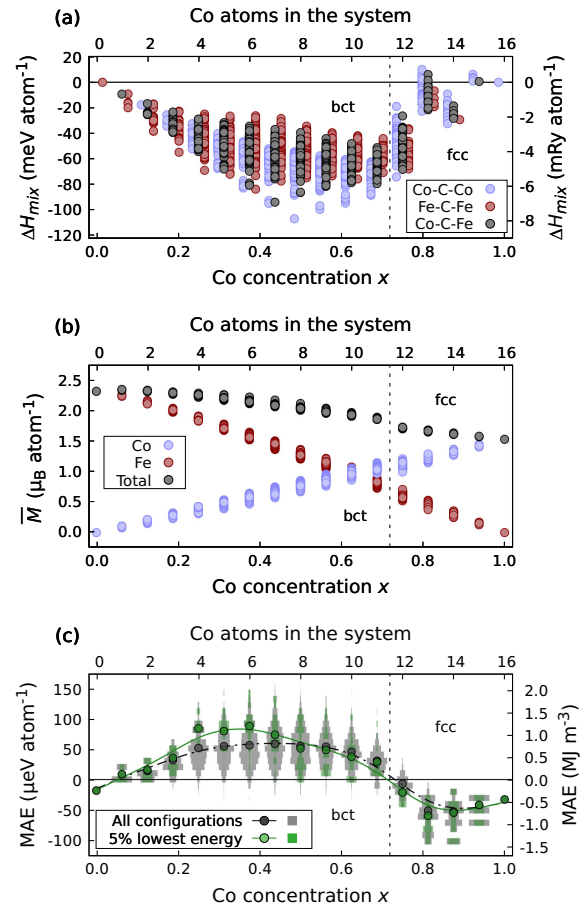


FIG. 4. Mixing enthalpy (ΔH_{mix}), average spin magnetic moments per transition metal atom (\bar{M}), and magnetocrystalline anisotropy energy (MAE) per transition metal atom *versus* Co concentration x in $(\text{Fe}_{1-x}\text{Co}_x)_{16}\text{C}$ system, as calculated using FPLO18 and PBE exchange-correlation potential for all nonequivalent Fe/Co site occupancies in a $2 \times 2 \times 2$ supercell. In (a), the light blue and dark red colors represent systems with, respectively, two Co and two Fe atoms neighboring the C impurity. Dark gray represents systems with one Fe and one Co atom neighboring the dopant. For readability, the plotted points are slightly shifted for Co-C-Co and Fe-C-Co configurations. The light blue and dark red colors in (b) represent the average contribution of Co and Fe magnetic moments, respectively. Dark gray is the sum of both. Gray histogram (c) represents the aggregation of all results, while the green one represents 5% of the most energetically favorable atomic arrangements. The circles represent respective average values, and the lines are averaged splines to guide the eye. Vertical dashed lines indicate the structural phase transition between bct and fcc structures.

earlier works of Khan and Hong [28,29,57]. However, we will try to show that despite notable influence on exact quantitative results, negligence of the direct C neighborhood does not alter the qualitative trends in the $(\text{Fe}_{1-x}\text{Co}_x)_{16}\text{C}$ system and possibly in other interstitially doped $\text{Fe}_{1-x}\text{Co}_x$ systems. Surprisingly, we can observe a tendency towards the energetic preference of systems containing Fe-C-Fe nearest-neighbor

sequence for low-Co concentrations. The rapid increase in mixing enthalpy for Co-rich systems is consistent with mixing enthalpies calculated by Díaz-Ortiz *et al.* and instability of Co-rich bct alloys observed in experiments [53]. Meanwhile, in the bct range, the maximum drop in ΔH_{mix} for any single structure is by a factor of 2, and there are no positive-enthalpy (unstable) structures. It indicates that C doping does not destabilize the system, regardless of the atomic configuration.

In Fig. 4(b), we see a decrease in average spin magnetic moments per TM atom with increasing Co concentration. The average magnetic moment on an Fe atom in Fe_{16}C is $2.38 \mu_{\text{B}}$, and the average magnetic moment on a Co atom in Co_{16}C is $1.53 \mu_{\text{B}}$. There is a positive deviation from a linear change with x , similar to the Slater-Pauling-type characteristics of unit cell volume *versus* x dependency. As seen in partial Fe and Co contributions to the average spin magnetic moment, this deviation from a linear trend stems from the Fe contribution. The partial contribution from Co magnetic moments increases linearly. However, as opposed to pure $\text{Fe}_{1-x}\text{Co}_x$ results reported by Bardos [58], we do not observe a characteristic, sharp maximum related to Slater-Pauling behavior. There is a considerably low deviation in average Fe, Co, and total TM magnetic moments across different configurations. The structural phase transition, between 11 and 12 Co atoms, affects magnetic moments on both Fe and Co atoms, but the change from 2.55 to $2.48 \mu_{\text{B}}$ in the average spin magnetic moment on Fe and from 1.56 to $1.46 \mu_{\text{B}}$ in the average spin magnetic moment on Co, is minimal.

Giannopoulos *et al.* found magnetization in thin films of $(\text{Fe}_{0.45}\text{Co}_{0.55})\text{-C}$ with 20 at.% C to be in range of 1600 emu cc^{-1} [59], which translates to about $2.05 \mu_{\text{B}} \text{ atom}^{-1}$. In the literature review performed by Díaz-Ortiz *et al.*, as well as in their own results, we can find average magnetic moments in bcc Fe and bcc Co ranging from 2.13 to $2.35 \mu_{\text{B}}$ on Fe atoms and from 1.53 to $1.77 \mu_{\text{B}}$ on Co atoms. Their MBPP/PBE (mixed-basis pseudopotential code) calculations for ordered Fe-Co phases yield a total magnetic moment of $2.36 \mu_{\text{B}} \text{ atom}^{-1}$ for $\text{Fe}_3\text{Co D0}_3$ phase, $2.29 \mu_{\text{B}} \text{ atom}^{-1}$ for Fe-Co B2 phase, and $2.00 \mu_{\text{B}} \text{ atom}^{-1}$ for $\text{FeCo}_3 \text{ D0}_3$ phase [53]. Similarly, Chandran *et al.* reported from VASP/GGA that Fe bcc has a magnetic moment of $2.22 \mu_{\text{B}} \text{ atom}^{-1}$, and Co bcc has a magnetic moment of $1.59 \mu_{\text{B}} \text{ atom}^{-1}$, not counting for the orbital moment contribution, which for both systems should be around $0.10\text{--}0.15 \mu_{\text{B}} \text{ atom}^{-1}$ [30]. For C-doped systems, Delczeg-Czirjak *et al.* found in SPR-KKR/PBE (spin-polarized relativistic Korringa-Kohn-Rostoker) with CPA that the average magnetic moment drops from $2.2 \mu_{\text{B}} \text{ atom}^{-1}$ in systems with the composition close to $\text{Fe}_{0.4}\text{Co}_{0.6}$ to around $1.8 \mu_{\text{B}} \text{ atom}^{-1}$ in systems with the compositions close to $(\text{Fe}_{0.4}\text{Co}_{0.6})_{16}\text{C}$ [23].

Possible giant MAE values are the property that initially brought attention to the $\text{Fe}_{1-x}\text{Co}_x$ system. Hence, MAE is among the first characteristics of the system to consider. We calculated MAE according to the formula

$$\text{MAE} = E_{100} - E_{001}, \quad (7)$$

where E_{100} and E_{001} denote the system's energies in the $[100]$ and $[001]$ magnetization axis directions (hard and easy axis in the bct structure, respectively).

Figure 4(c) presents MAE *versus* x for all configurations, as well as thermodynamical averages according to Eq. (1) and assuming $T = 300 \text{ K}$ for each Co concentration. We provide an approximate MAE scale¹ in MJ m^{-3} . Vertical histograms are scaled to fit the width between points and represent the data spread (i.e., represent the probability distribution). There is apparently a unimodal distribution of all MAE results for the whole x range among all configurations. A bimodal distribution can be observed in the results obtained for the lowest-energy configurations, with MAE values being either very high or near zero. We observe that MAE varies hugely between configurations, with the absolute maximum for 7 Co atoms in the 16 TM-atom supercell. With more than 11 Co atoms in the system, we observe a rapid decrease and change in the sign of MAE, associated with the phase transition. The high difference in MAE between individual configurations is consistent with similar results for ordering towards L1_0 phase in equiatomic FeNi obtained by Izardar, Ederer, and Si. Although we focus on qualitative trends with low convergence criteria for each data point, they conducted a full convergence for several dozen structures [38,40].

Closer inspection of Fig. 4(c), especially the lowest-energy-configurations-resolved thermal averages (green points connected with the solid green line), leads to observation that the averages lie much higher than the most probable MAE in terms of the presented histograms, especially for $\text{Fe}_{12}\text{Co}_4\text{C}$, $\text{Fe}_{11}\text{Co}_5\text{C}$, and $\text{Fe}_{10}\text{Co}_6\text{C}$. In the case of those concentrations, considering only 5% of the most energetically favorable structures leads to the overestimation of the MAE by almost a factor of 2. The conclusion is twofold. First, the overestimation by a factor of 2 is better than the overestimation by a factor of 4, known for the VCA method and $\text{Fe}_{1-x}\text{Co}_x$ system [5,15]. It is, however, still significant, and the care should be ensured to include enough samples in the statistics. We took a certain fixed percentage of the lowest-energy unique configurations, with a minimum of 10 (as a minimal statistically significant amount), which leads to a substantial influence of entropic effects. This approach is open for future improvements in the relation between sampled configurations and the configurational entropy of the system, but such enhancements are beyond the scope of this work. Second, the number of ways in which certain configurations can be achieved, configuration degeneracy due to the resultant structure symmetry, cannot be the only culprit beyond the discrepancies between the full and partial configuration space sampling.

To investigate the discrepancy between full and reduced statistics, we plotted structure occurrence probability distribution for different mixing enthalpies, and present it in Fig. 5. Since the formation enthalpy can be derived in a similar way, with a reference point leading to a shift in values, the distribution is representative of this quantity, too. An expected feature of the plot would be following the Gaussian distribution, with the vast majority of the systems possessing medium mixing

¹To provide an approximate scale in MJ m^{-3} , we assume a uniform, average cell volume of 189 \AA^3 across all Co concentrations and TM atom configurations. The approximate scale can yield values with uncertainty up to 1.5% for the bct region.

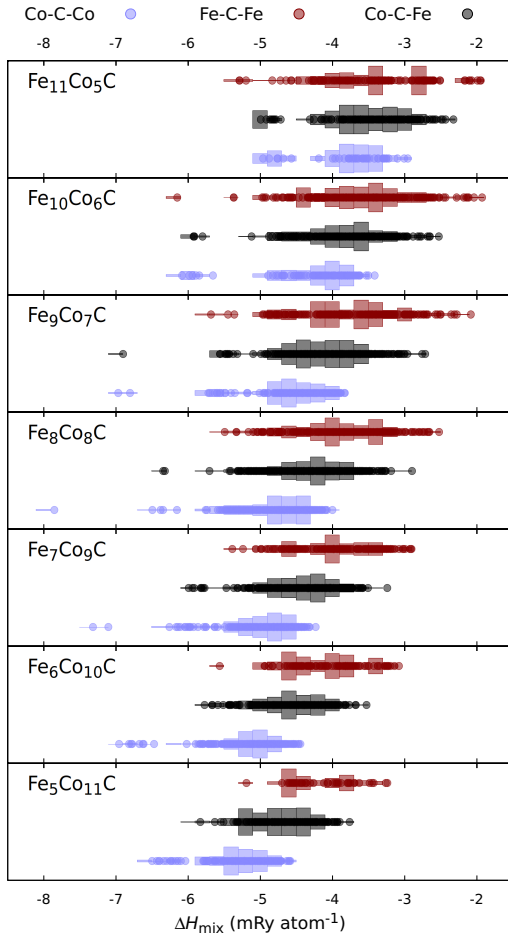


FIG. 5. Mixing enthalpies probability distribution across all configurations for intermediate Co contents in the $2 \times 2 \times 2$ supercell of $(\text{Fe}_{1-x}\text{Co}_x)_6\text{C}$. The light blue and dark red colors represent systems with, respectively, two Co and two Fe atoms neighboring the C impurity. Dark gray represents systems with one Fe and one Co atom neighboring the dopant. Points along the histograms present the distribution of geometrically inequivalent structures and are horizontal representations of data presented in vertical series in Fig. 4(a).

enthalpy, and only a few of really preferable (or unpreferable) structures, with possible addition of ordering effects, leading to a slight change in the curve shape. Clearly, that is not the case. Although we can observe such features for the Fe-C-Co structures, and to some extent Co-C-Co structures, the distribution for the Fe-C-Fe structures is definitely not unimodal. In the case of $\text{Fe}_{11}\text{Co}_5\text{C}$ or $\text{Fe}_5\text{Co}_{11}\text{C}$ one could argue that some discrepancies may stem from the relatively low number of samples, but we remind that we got 748 unique structures for the $\text{Fe}_8\text{Co}_8\text{C}$ system, out of which over 200 contain Fe-C-Fe nearest-neighbor sequence. Each of those configurations can be realized in multiple ways, which were included in the histograms. We ascribe this behavior to various ordering effects influencing the systems' energy. Nevertheless, the most energetically preferable system can have much lower mixing

enthalpy (enthalpy of formation²) than the vast majority of the structures. It leads to its weight in Boltzmann averaging being a few orders of magnitude higher, though the number of systems with the mixing (formation) enthalpy closer to the most probable one can outweigh the contribution from the most energetically preferable configuration. Hence, regardless of the undoubted usefulness of effective medium-based methods such as VCA and CPA, taking into account the effects of the system's ordering can be necessary for the proper description of the sensitive electronic properties.

Focusing on qualitative trends, in Fig. 4(c), we see a broad maximum for $x \simeq 0.25$ – 0.75 . According to Eq. (1), we obtained an average MAE of 0.87 MJ m^{-3} for $\text{Fe}_8\text{Co}_8\text{C}$. MAE decreases by around 20% between $x = 0.5$ and $x \simeq 0.3$. It is in contrast to a rapid drop in MAE for low-Co concentrations reported by Delczeg-Czirjak *et al.* (65% drop between $x = 0.6$ and 0.3). We obtained nearly the same MAE values for $x \simeq 0.6$ and $x \simeq 0.3$. Intriguingly, we observe several configurations with relatively high MAE values for Co concentration as low as 0.25. Our findings of notable, positive MAE for low-Co concentrations contradict earlier results obtained with effective medium methods. VCA and CPA reported negative MAE for low-Co concentrations Fe-Co alloy, as seen on MAE versus c/a versus x maps by Burkert *et al.* and Turek *et al.* [5,15]. On the other hand, it is consistent with the findings of Steiner *et al.*, who reported positive MAE for $\text{Fe}_{1-x}\text{Co}_x$ supercells in a much wider Co concentration range, and Wu *et al.*, who reported high MAE for $\text{Fe}_{12}\text{Co}_4\text{C}$ and $\text{Fe}_{11}\text{Co}_5\text{C}$ [27,60]. Moreover, we observe a few high-MAE configurations among the 5% most preferable ones [see green histograms in Fig. 4(c)]. The thermodynamically averaged MAE values over 5% of the lowest-energy configurations overestimate averages of all symmetrically nonequivalent configurations. It suggests the non-negligible influence of high-energy (and hence low-probability) structures stemming from their quantity.

Our quantitative MAE results can be placed in the context of numerous works describing selected atomic configurations in pure Fe-Co, as well as B-, C-, and N-doped systems, realized both experimentally and by DFT calculations to date. For comparison, in Table II, we present our thermally averaged MAEs along with selected results from the literature. Data for cross reference are chosen to resemble our setup (c/a ratio, and TM and dopant concentration) as closely as possible. At the beginning, we want to point out a few noticeable general features of some of the results we are comparing our results to. First, some of the samples analyzed in experiments, i.e., Refs. [26] and [18], were prepared as layered systems with various content of Au-Cu interlayer buffers. Hence, the results of those experiments can serve as a lower boundary of technologically possible MAE. Second, in multiple of the cited articles, VCA is proven to overestimate the MAE [15,16,23]. Third, highly ordered structures, like the one calculated by Odkhuu and Hong [31], can present heightened MAE, as shown by Turek *et al.* [15] and as we prove in this work. Going into the more precise description, Giannopoulos *et al.* found experimentally K_u

²In the bct region those two quantities are equivalent.

TABLE II. Magnetocrystalline anisotropy energy of selected $(\text{Fe}_{1-x}\text{Co}_x)_{16}\text{C}$ systems, resultant from the averaging proposed in Eq. (1) and calculated in FPLO18 with PBE exchange-correlation functional, compared to selected other computational and experimental results. Reference results were chosen to resemble our setup as closely as possible.

Source	Compound	Method	MAE ($\mu\text{eV atom}^{-1}$)	MAE (MJ m^{-3})
This work	$\text{Fe}_{11}\text{Co}_5\text{C}$	Calc. supercells (FPLO)	51	0.69
This work	$\text{Fe}_8\text{Co}_8\text{C}$	Calc. supercells (FPLO)	64	0.87
This work	$\text{Fe}_5\text{Co}_{11}\text{C}$	Calc. supercells (FPLO)	40	0.55
Giannopoulos <i>et al.</i> [59]	$(\text{Fe}_{0.45}\text{Co}_{0.55})_{0.8}\text{C}_{0.2}$	Expt. SQUID/EMCD, thin film on Au-Cu		~ 0.8
Giannopoulos <i>et al.</i> [25]	$\text{Fe}_{0.8}\text{C}_{0.2}/\text{Co}$, $\text{Fe}/\text{Co}_{0.8}\text{C}_{0.2}$	Expt. SQUID, thin film on Au-Cu		~ 1
Giannopoulos <i>et al.</i> [26]	$(\text{Fe}_{0.45}\text{Co}_{0.55})_{0.9}\text{C}_{0.1}$	Expt. FMR, FeCo-C 3nm/Au-Cu 1nm layers		up to 0.4
Reichel <i>et al.</i> [17]	$(\text{Fe}_{0.4}\text{Co}_{0.6})_{0.98}\text{C}_{0.02}$	Expt. VSM, thin films on Au-Cu		0.8 ± 0.15
Reichel <i>et al.</i> [16]	$(\text{Fe}_{0.4}\text{Co}_{0.6})_{0.98}\text{C}_{0.02}$	Expt. VSM, thin films on Au-Cu		0.44 ± 0.14
Reichel <i>et al.</i> [16]	$(\text{Fe}_{0.4}\text{Co}_{0.6})_{32}\text{C}$	Calc. VCA (WIEN2k) /CPA (SPR-KKR)		$0.51 / 0.224$
Reichel <i>et al.</i> [24]	$\text{Fe}_{0.38}\text{Co}_{0.62}\text{-B}$	Expt. VSM, thin films on Au-Cu		$0.4\text{-}0.55$
Reichel <i>et al.</i> [24]	$(\text{Fe}_{0.5}\text{Co}_{0.5})_{16}\text{B}$	Calc. CPA (SPR-KKR)	46	0.62
Reichel <i>et al.</i> [24]	$(\text{Fe}_{0.4}\text{Co}_{0.6})_{16}\text{B}$	Calc. CPA (SPR-KKR)	52	0.69
Reichel <i>et al.</i> [18]	$(\text{Fe}_{0.4}\text{Co}_{0.6})_{0.98}\text{C}/\text{B}_{0.02}$	Expt. FeCo-C/B 4nm/Au-Cu 4nm layers		~ 0.5
Delczeg-Czirjak <i>et al.</i> [23]	$(\text{Fe}_{0.4}\text{Co}_{0.6})_{16}\text{C}$	Calc. VCA (WIEN2k)	90	1.29
Delczeg-Czirjak <i>et al.</i> [23]	$(\text{Fe}_{0.4}\text{Co}_{0.6})_{16}\text{C}$	Calc. CPA (SPR-KKR)	42	0.59
Delczeg-Czirjak <i>et al.</i> [23]	$\text{Fe}_6\text{Co}_{10}\text{C}$	Calc. SQS (VASP)	51 ± 9	0.75 ± 0.13
Odkhuu and Hong [31]	$\text{Fe}_{27}\text{Co}_{27}\text{N}_2$	Calc. ordered supercells (VASP)	~ 100	–
Khan and Hong [29]	$\text{Fe}_{64}\text{Co}_{64}\text{C}_4$	Calc. ordered supercells (FLAPW+VASP)	47	0.62
Khan and Hong [29]	$\text{Fe}_{64}\text{Co}_{64}\text{N}_4$	Calc. ordered supercells (FLAPW+VASP)	42	0.58
Khan and Hong [28]	$\text{Fe}_{64}\text{Co}_{64}\text{N}_4$	Calc. ordered supercells (FLAPW+VASP)	59	0.8

for C-doped $\text{Fe}_{0.45}\text{Co}_{0.55}$ thin films to be in order of 0.8 MJ m^{-3} [59], exact same value as obtained by Reichel *et al.* for $(\text{Fe}_{0.4}\text{Co}_{0.6})_{0.98}\text{C}_{0.02}$ thin films [17]. Reichel *et al.* have also shown from combined DFT and experimental analysis that the $(\text{Fe}_{0.4}\text{Co}_{0.6})_{32}\text{C}$ system possesses slightly lower MAE of the order of 0.5 MJ m^{-3} and much higher stability for relatively thick films [16]. They also reported B-doped $\text{Fe}_{1-x}\text{Co}_x$ alloys to behave similarly, with a little higher MAE than C-doped system [24]. Odkhuu and Hong provide similar results for $(\text{Fe}_{1-x}\text{Co}_x)_{16}\text{N}_2$ [31]. Delczeg-Czirjak *et al.* found MAE for $\text{Fe}_6\text{Co}_{10}\text{C}$ to be in the order of $51 \mu\text{eV atom}^{-1}$ or 0.75 MJ m^{-3} as calculated in WIEN2K/SQS, higher than their SPR-KKR/CPA calculations ($41.6 \mu\text{eV atom}^{-1}$) [23]. For B2 Fe-Co-C and Fe-Co-N systems, Khan and Hong reported MAE values of 0.65 and 0.58 MJ m^{-3} , respectively [29].

Overall, our results agree well with previous calculations and experiments wherever direct comparison is possible. Qualitative trends among major magnetic properties are similar, and quantitative results lie close to previous DFT data. However, the data set we provide is vastly greater than anything currently available in the literature. The method implemented in our work is slightly more computationally expensive than the CPA method while yielding MAE results with a similar accuracy. On the other hand, it allows us to provide a more detailed analysis of aspects other than the basic magnetic properties. In particular, it enables us to interpret ordering dependencies, which we will present in the following sections.

D. Magnetocrystalline anisotropy energy and magnetic hardness in relation to the mixing enthalpy

To systematize the data set, we first analyze the dependency of MAE on the mixing enthalpy. This dependency for

all configurations is shown in Fig. 6(a). We see an increase of MAE with lowering the system enthalpy, indicating the preference towards high-MAE structures. There is a significant scatter of values for separate systems around the average. Systems with the dopant atom neighbored by two Co atoms have noticeably larger MAE and lower mixing enthalpy relative to the systems with Fe-C-Fe and Fe-C-Co nearest-neighbor (NN) sequence.

To further explore the usefulness of investigated structures, we calculate magnetic hardness. It is a parameter describing the system resistance towards spontaneous self-demagnetization and can be defined as [4]

$$\kappa = \sqrt{\frac{K_1}{\mu_0 M_S^2}}, \quad (8)$$

where K_1 is the magnetic anisotropy constant, M_S is the saturation magnetization, and μ_0 is the vacuum permeability. A simple empirical rule is that a permanent magnet candidate needs κ greater than 1 to resist self-demagnetization. κ is a useful technical value, as plenty of magnets with relatively low MAE values are manufactured widely due to their high magnetic hardness and low materials cost.

In the case of the Fe-Co-C system, numerous experimental realizations showed a possibility of further amendment of the system to at least double its MAE by tuning the c/a ratio, where interstitial doping can be combined with growth on specifically tailored substrates [17,23,24,26]. We also previously showed the positive effect of $5d$ doping of a similar system [47]. Hence, we are interested in promising compositions showing at least semihard magnetic properties due to C-doping alone. Skomski and Coey described systems with κ around 0.5 as semihard [4]. We mark the $\kappa = 0.5$ value in Fig. 6(b) with dashed lines. In our estimation, we assume K_1

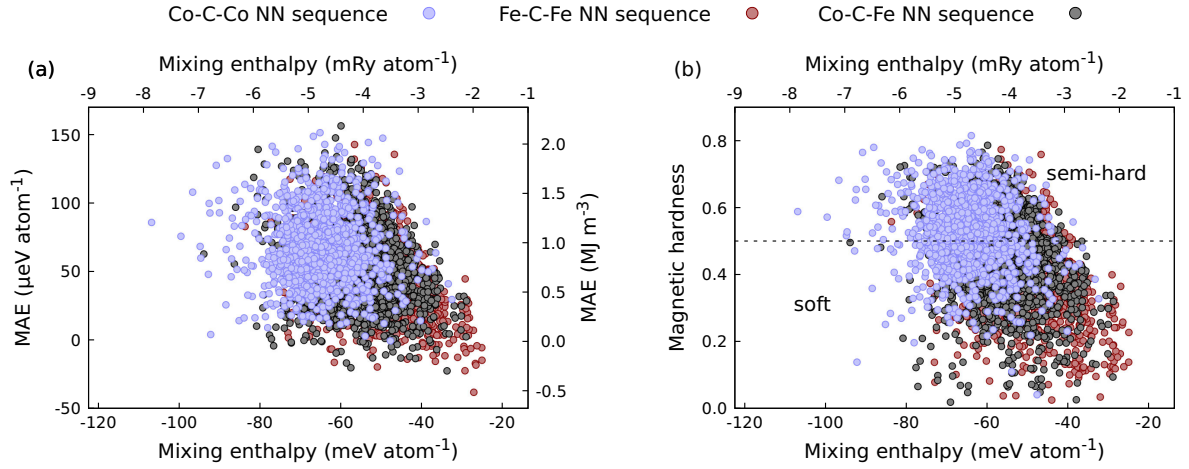


FIG. 6. Magnetocrystalline anisotropy energy (MAE) (a), and magnetic hardness (b) versus Fe₁₆C and Co₁₆C mixing enthalpy in the (Fe_{1-x}Co_x)₁₆C system (from 3 to 11 Co atoms in the supercell). The light blue color denotes systems with two Co atoms neighboring the C dopant, the dark red color denotes systems with two Fe atoms neighboring the impurity, and the black color denotes systems with the C atom neighbored by one Fe and one Co atom. In (b), the dashed line for hardness equal to 0.5 indicates a semihard magnetic material threshold. The results were obtained in FPLO18 with the PBE exchange-correlation potential.

equals MAE, as defined before. Saturation magnetization is derived from the calculated total magnetic moment and cell volume. Thus, we can expand Eq. (8) to the form

$$\kappa = \sqrt{\frac{E_{100} - E_{001}}{\mu_0 \left[\frac{\sum_i M_i}{V} \right]^2}}, \quad (9)$$

where i is the atomic site in the computational cell, M_i is the total magnetic moment of the atom occupying site i , and V is the computational cell volume.

Figure 6(b) presents the resultant magnetic hardness versus mixing enthalpy relation. It is similar to the MAE dependency on the mixing enthalpy, presented in Fig. 6(a). The magnetic hardness of many configurations exceeds the conventional limit of 0.5 for semihard magnetic materials but does not exceed 0.9, remaining below the limit for hard magnetic materials. Odkhuu and Hong reported similar values of κ , ranging from 0.5 to 1 for the (Fe_{1-x}Co_x)₁₆N₂ system [31]. From Eq. (9), we can see that there are two main ways to improve the magnetic hardness of the sample. We can either improve MAE or reduce magnetic moment. For permanent magnet applications, we are at the same time interested in as high saturation magnetization as possible. It implies that improving magnetic anisotropy while maintaining relatively high magnetic moments is of interest. Alternatively, achieving high magnetic hardness at the cost of magnetic moment can be beneficial in case of sufficient economic advantage. Relatively negligible changes in total magnetic moment across configurations with the same Co content suggest that, in our case, the MAE changes are a decisive factor in the magnetic hardness variations for different configurations. Either way, both pathways for MAE improvements are feasible in the Fe-Co-C system.

E. Magnetic moments

Looking into the dataset, we focus on average magnetic moments per TM atom in the system, along with the spread of the values in different atomic configurations. Figure 7 summarizes results for exemplary Co concentrations x , 25%, 50%, and 75%. Presented trends in average Fe, Co, and total spin magnetic moments (dependencies on mixing enthalpy and short-range ordering, and their distribution) are representative. Similar results in the literature are scarce, in contrast to analyses of TM magnetic moments on different impurity atom coordination shells, performed by, e.g., Delczeg-Czirjak *et al.* and Khan *et al.* [23,28,29,57].

As presented in Fig. 7(a), for low Co concentration, the low-enthalpy configurations are particularly associated with high average magnetic moment on Co atoms. It can be explained by the preferred Fe-C-Fe neighborhood, as the dopant atom tends to lower magnetic moments on neighboring atoms. Delczeg-Czirjak *et al.* shown that TM atoms adjacent to the C impurity in the (Fe_{1-x}Co_x)₁₆C system have significantly reduced magnetic moments [23]. For intermediate Co content (exemplified by the Fe₈Co₈C system), there is no significant correlation between the average total magnetic moment and mixing enthalpy neither on Fe nor on Co atoms in the bct range. For $x = 0.75$ (in the fcc range), a preference towards higher Fe and lower Co magnetic moments emerges. We can observe that despite the average total spin magnetic moment on Fe and Co atoms varying considerably between configurations, the average total spin magnetic moment per atom remains almost constant. Spin magnetic moment on Co atoms remains close to $1.5 \mu_B \text{ atom}^{-1}$, as predicted by linearity in its partial contribution to the total average spin magnetic moment in the supercell.

The trend can be seen more clearly in Figs. 7(d)–7(f) where we present histograms of the average Fe, Co, and total magnetic moments in the structures. In general, the magnetic

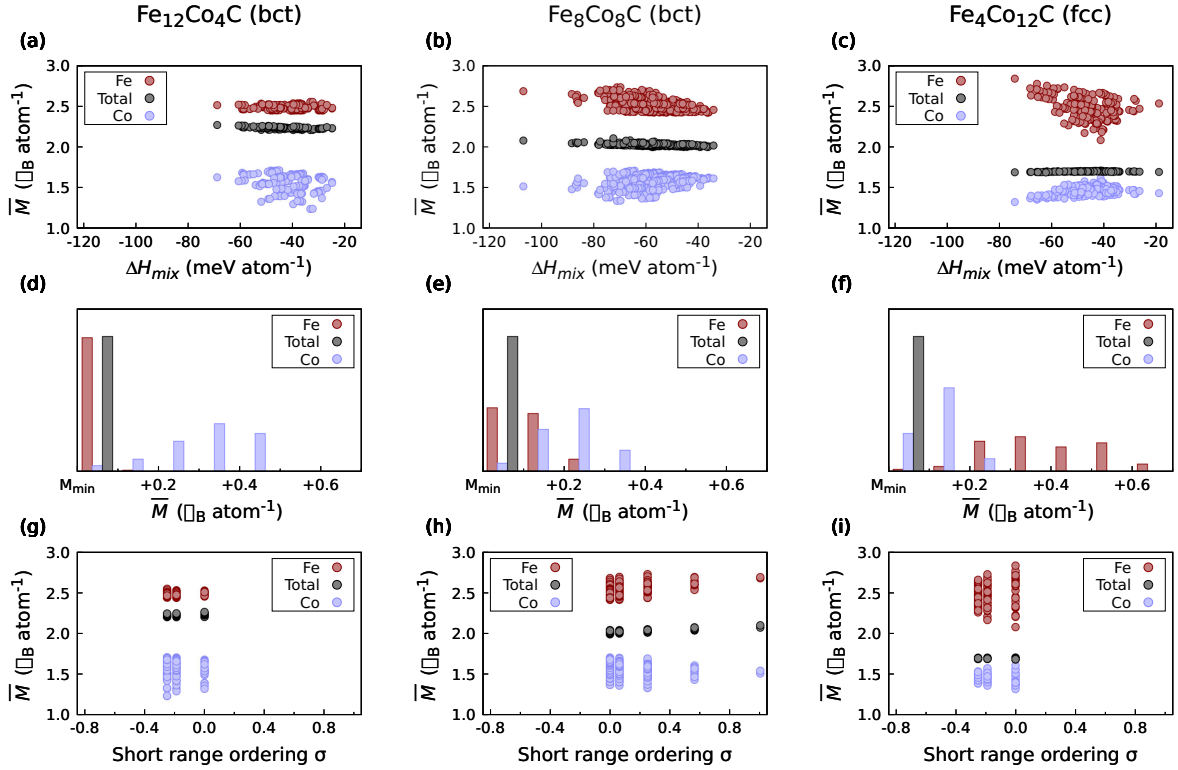


FIG. 7. The average spin magnetic moment per atom *versus* the mixing enthalpy of Fe_{16}C and Co_{16}C (a)–(c), the same value presented as a histogram (d)–(f), and *versus* Bethe short-range ordering (g)–(i), obtained for all geometrically inequivalent Fe/Co arrangements in a $2 \times 2 \times 2$ supercells of $(\text{Fe}_{1-x}\text{Co}_x)_{16}\text{C}$, calculated with FPLO18 code and PBE exchange–correlation potential. Results are presented for 4, 8, and 12 Co atoms in the supercell. The $\text{Fe}_4\text{Co}_{12}\text{C}$ fcc structure is metastable.

moment on Fe atoms depends much more on their chemical neighborhood than the magnetic moment on Co atoms. In Fig. 7(d), we see that on the Fe-rich side of the concentration range, for $\text{Fe}_{12}\text{Co}_4\text{C}$, the total magnetic moment in the system, $2.23 \mu_{\text{B}}$, remains almost constant across all configurations with a triple standard deviation of $0.03 \mu_{\text{B}}$. A similar trend can be observed for the average Fe magnetic moment ($2.48 \pm 0.08 \mu_{\text{B}} \text{ atom}^{-1}$). However, for average Co magnetic moments ($1.57 \mu_{\text{B}} \text{ atom}^{-1}$), we can see that the triple standard deviation is relatively high and equals $0.31 \mu_{\text{B}} \text{ atom}^{-1}$. On the Co-rich side, for $\text{Fe}_4\text{Co}_{12}\text{C}$ alloy [see Fig. 7(f)], we notice that the total magnetic moment in the system also remains almost constant ($1.70 \pm 0.02 \mu_{\text{B}} \text{ atom}^{-1}$). Still, we observe a noticeable variation of $0.16 \mu_{\text{B}} \text{ atom}^{-1}$ around the average value of Co magnetic moments ($1.45 \mu_{\text{B}} \text{ atom}^{-1}$). However, average magnetic moments on Fe atoms, $2.48 \mu_{\text{B}} \text{ atom}^{-1}$, vary considerably across different configurations, in the range of $\pm 0.42 \mu_{\text{B}} \text{ atom}^{-1}$, which yields almost 34% relative variability between lowest and highest Fe magnetic moment value. In Fig. 7(e), presenting results for $\text{Fe}_8\text{Co}_8\text{C}$, we observe moderate variation in average magnetic moments on both Fe and Co atoms, in the range of $2.53 \pm 0.20 \mu_{\text{B}} \text{ atom}^{-1}$ on Fe, $1.56 \pm 0.22 \mu_{\text{B}} \text{ atom}^{-1}$ on Co, and a total magnetic moment in the system of $2.03 \pm 0.05 \mu_{\text{B}} \text{ atom}^{-1}$.

Again, a major driving factor in the spread of magnetic moments across all structures can be the magnetic moment lowering by the neighboring C impurity, which is most prominent on Co atoms, as presented for numerous Fe-Co-based systems by Khan *et al.* [28,29,57]. Moreover, a similar result for N-doped B2 Fe-Co was obtained by Chandran *et al.* They obtained magnetic moments being reduced from $2.78 \mu_{\text{B}}$ to $2.09 \mu_{\text{B}}$ between next-nearest and nearest neighbors of the dopant for Fe atoms and from $1.76 \mu_{\text{B}}$ to $1.12 \mu_{\text{B}}$ for Co atoms, with magnetic moment fluctuations propagating into next-nearest neighbors [30].

To explore other factors influencing magnetic moments in the system, we can use a local neighborhood-based order parameter σ of Bethe, which can be defined for a binary alloy as [35]

$$\sigma = p_{AB} - (p_{AA} + p_{BB}) = 2p_{AB} - 1, \quad (10)$$

where p_{XY} denotes the probability of finding an XY nearest-neighbor pair.

Although developed for equiatomic systems, σ derived from Eq. 10 also provides useful information for nonequiatomic binary systems, as it depicts changes in the system with increasing content of NN pairs of nonsimilar atoms. In that case, σ generally takes values between -1 and

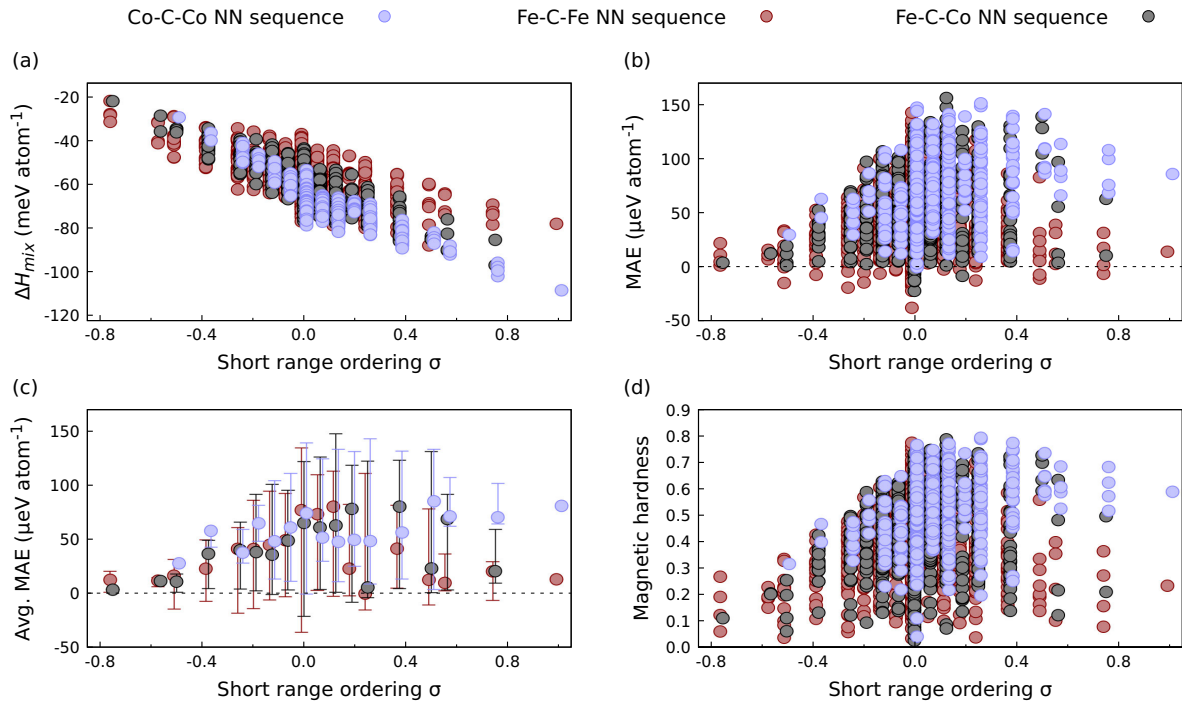


FIG. 8. Dependence of mixing enthalpy (a), magnetocrystalline anisotropy energy (b), (c), and magnetic hardness (d) on short-range ordering parameter σ in $(\text{Fe}_{1-x}\text{Co}_x)_{16}\text{C}$ structures with from 3 to 11 Co atoms in the supercell. The light blue color denotes systems with two Co atoms neighboring the C dopant, the dark red color indicates systems with two Fe atoms neighboring the impurity, and the black color denotes systems with the C atom neighbored by one Fe and one Co atom. Results were obtained using the FPLO18 code with PBE exchange-correlation potential. Fe-C-Fe and Co-C-Co data points are slightly shifted for better readability. (c) Presents thermodynamic averages according to Eq. (1), and error bars denote the maximum and minimum calculated values.

1, with positive values indicating preference towards dislike (in our case, Fe-Co) atomic pairs in the structure and negative values indicating preference towards same-atom type pair (Fe-Fe and Co-Co). However, both minimum and maximum achievable σ changes with the system composition and supercell size, σ_{min} being in $(-1, 0)$ range (likewise atom pair affinity) and σ_{max} in $(0, 1)$ range (dislike atom pair affinity).

Considering different atomic configurations for particular Co concentrations makes it possible to determine the effect of the former on the values of magnetic moments on individual atoms. Díaz-Ortiz *et al.* showed for $\text{Fe}_{1-x}\text{Co}_x$ that the average magnetic moment does not change significantly with ordering [53]. Similarly, for special quasirandom structures (SQS), comparing C impurity local neighborhood, Delczeg-Czirjak *et al.* did not find any relevant change of total magnetic moment in the Fe-Co-C system. The magnetic moment for the $(\text{Fe}_{0.5}\text{Co}_{0.5})_4\text{C}$ in their work remained at around $1.8 \mu_{\text{B}} \text{ atom}^{-1}$ [23]. Indeed, for $(\text{Fe}_{1-x}\text{Co}_x)_{16}\text{C}$, we do not see any significant change in the average spin magnetic moment with the local chemical neighborhood, as shown in Figs. 7(g)–7(i). Only a slight increase in the average spin magnetic moment with short-range ordering can be observed for the $\text{Fe}_8\text{Co}_8\text{C}$ system, presented in Fig. 7(h). It validates effective medium approaches, such as VCA and CPA, to work for disordered $(\text{Fe}_{1-x}\text{Co}_x)_{16}\text{C}$, similarly to $\text{Fe}_{1-x}\text{Co}_x$, the latter pointed by Díaz-Ortiz *et al.* [53]. As for the average Fe and Co magnetic

moments, we can see the variation across different structures drops with short-range ordering, indicating a strong contribution from Fe-Co NN interaction. It is consistent with a known strong Fe-Co d orbital hybridization and exchange interaction [31]. For any specific minority atom concentration in our computational cell, the σ range is restricted due to limitations induced by the composition and system size, as described above.

F. Ordering and its influence on magnetic properties

Apart from average magnetic moment dependence on the short-range ordering, we can explore the ordering effect on other important system properties, including mixing enthalpy, magnetocrystalline anisotropy energy, and magnetic hardness. Figure 8 presents aggregated results for Co content between 3 and 11 atoms in the system, in the bct region. We do not present results for lower Co concentrations because they cover only a small number of configurations and do not have reasonable statistics.

Figure 8(a) shows mixing enthalpy decrease with the increase of short-range Fe-Co ordering, i.e., the fraction of Fe-Co pairs among all NN pairs. It might indicate system stabilization by Fe-Co nearest-neighbor and Co-Co or Fe-Fe next-nearest-neighbor interaction. As previous studies have shown, in the case of the N-doped B2 phase, nearest-neighbor

Fe-Co exchange integral and next-nearest-neighbor Co-Co integral calculated by Odkhuu and Hong contribute the most to magnetic ordering [31]. Hence, we ascribe the system stabilization to the same interactions.

Figure 8(b) shows the distribution of MAE in structures with different atomic configurations. Both the highest and lowest MAE for a single configuration can be observed for σ equal to 0. For the highest σ values, MAE converges to around $85 \mu\text{eV atom}^{-1}$ for the Co-C-Co NN sequence and to around $10 \mu\text{eV atom}^{-1}$ for the Fe-C-Fe NN sequence. For negative σ values, which can be associated with low Co concentrations, the uniaxial MAE vanishes. It can be deduced that the NN ordering influences the MAE by strong Fe-Co interplay. Nevertheless, the factor that contributes most to the overall behavior of the MAE relative to order is the direct immediate chemical neighborhood of the impurity atom. In Fig. 8(c), we present thermodynamic averages, according to Eq. (1). Bars represent the range of MAE values obtained in calculations. We observe no significant correlation between average MAE and atom distribution for $\sigma > 0$. The most probable MAE for σ equal to 0 is quite high regardless of the dopant neighborhood. The changes in MAE described above are clear, though the scatter of MAE values for various individual structures is substantial.

Taking all the above into account, the configuration space of Fe-Co-C alloys can be somewhat effectively reduced to random nearest-neighbor patterns. Still, it should be done cautiously and can lead to substantial errors, though any anomalies should be evident in the results. Along with the low average magnetic moment dependence discussed above, the lack of strong MAE dependence on the short-range ordering implies that Fe-Co-C retains the properties of a random alloy, similarly to pure Fe-Co. Thus, methods relying on conformational space reduction by neighbor patterns analysis, such as SQS, yield a non-negligible error, similar to effective medium methods, as noted before by Díaz-Ortiz *et al.* [53]. In future studies, it should be decided on a case-by-case basis whether the tradeoff between the significant reduction in computation time in approximate (SQS-type) methods and the accuracy and ability to obtain a complete picture of the system in methods that allow order-dependence analysis is justified.

Figure 8(d) presents a similar picture for magnetic hardness. We can see that practical magnetic hardness can be obtained for systems around and above $\sigma = 0$. For highly ordered systems, the first coordination shell of the dopant plays a key part. Above $\sigma = 0.4$, only Co-C-Co and part of Fe-C-Co systems retain magnetic hardness in the semihard region. The interesting part is the negative- σ side of Figs. 8(b)–8(d). We observe that where Fe-Fe and Co-Co interactions dominate, MAE and hence the magnetic hardness drops.

Although the σ is a convenient and effective parameter in analyzing the aggregated results, especially showing the linear decrease of mixing enthalpy with increasing dislike atom pairs content in the supercells, it lacks one property necessary to conduct a complete analysis. It conveys a strict order-parameter definition only for equiatomic binary alloy. Namely, its expected value, the same as the value for a completely disordered alloy, is not always equal to zero and depends on minority atom concentration c_m as $4(c_m - c_m^2)$. For equiatomic alloy, σ equals 0 for completely disordered

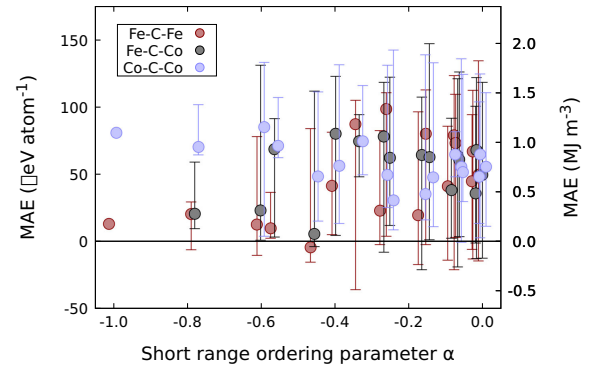


FIG. 9. Magnetocrystalline anisotropy energy *versus* Warren-Cowley short-range order parameter for the first coordination shell of transition metal atoms in $(\text{Fe}_{1-x}\text{Co}_x)_{16}\text{C}$ (from 3 to 11 Co atoms in the supercell). Points represent 300 K thermodynamical averages according to Eq. (1). Results were obtained using the FPLO18 code with PBE exchange-correlation potential. Fe-C-Fe and Co-C-Co data points are slightly shifted for better readability. Bars denote the minimum and maximum values obtained in calculations.

alloy and takes values up to 1 (or -1) for completely ordered alloys.

To investigate the properties of disordered alloys in a broad concentration range, we use Warren-Cowley short-range order parameter α [36,37], which for the first coordination shell ($\alpha_i^{\text{Fe,Co}}$ shortened further to α) can be simplified as

$$\alpha_i^{AB} = 1 - \frac{P_{AB}}{2c_Ac_B}, \quad (11)$$

where c_A denotes the concentration of atom type A , $P_{AB}/2c_B = P_{AB}$ equals the conditional probability of finding an atom of type B at the first coordination shell of the randomly selected atom of type A , and when substituted, gives the exact Warren-Cowley formulation. Structures with all α parameters (for different coordination shells) equal to 0 are disordered, and structures with α_i equal to 1 (or -1) are perfectly ordered on coordination shell i . For simplicity, in Fig. 9, we present only MAE *versus* α dependency. Generally, in an infinite crystal, α takes values between $\frac{2c_Ac_B-1}{2c_Ac_B}$ and 1 [61]. We get only zero to negative α values due to the small computational cell size. Overall, the plot is similar to the positive σ part of Figs. 8(b) and 8(c) taking into account that preferred dislike atom type coordination is associated with positive σ , but negative α . The most probable MAE value is proportional to the ordering for Co-C-Co systems and, to some extent, for others. Apart from that, we want to highlight three main observations. First, there is a considerable spread in values for random alloys (for $\alpha = 0$). It is further indicator implying that certain methods of configurational space reduction, like SQS, are inherently predestined to fail in proper $\text{Fe}_{1-x}\text{Co}_x$ -based alloys MAE predictions, and the uncertainty of such results can be, in fact, substantial. Second, same as for σ and similarly to order parameters in recent works by Izardar and Ederer for L_{10} FeNi [38,39], the MAE value converges towards a reasonably high MAE value for perfectly ordered systems. Lastly, in all (Fe-C-Fe, Fe-C-Co,

and Co–C–Co systems, there is a group of configurations that possess high MAE, increasing with ordering. We remind here that $\alpha = -1$ structures are ordered. For Fe–C–Fe and Fe–C–Co systems, the average MAE value diverges and eventually suddenly drops for high-order structures, a behavior described above for Bethe σ dependencies.

From the comparison of high-order structure calculations to the random $\text{Fe}_{1-x}\text{Co}_x$ alloy, Díaz-Ortiz *et al.* deduced that ordered structures are stable, with B2 phase among them [53]. Structures predicted by them, namely, D0_3 , L6_0 , and B2, as well as similar phases such as L1_2 exhibit a high degree of short-range σ and α ordering, as calculated according to Eqs. (10) and (11). Wu *et al.* have, similarly, reported stability of Fe-rich D0_3 , and equiatomic B2 phases [60], and Odkhuu and Hong postulated B2 Fe–Co to be a good matrix for low-energy high-MAE N-doped phases [31]. One of the very first works on the topic of strained $\text{Fe}_{1-x}\text{Co}_x$ system treated with CPA effective medium approximation by Turek *et al.* researched L1_0 ordering influence on MAE in the system [15]. L1_0 and B2 phases differ only by lattice parameters c/a ratio, where L1_0 is an fcc-like structure and B2 is close to bcc. As such, we also checked specifically the B2 ordering in the low c/a regime for the C-doped $\text{Fe}_{1-x}\text{Co}_x$ alloy.

For this purpose, we use the long-range order parameter S of a binary alloy, which is defined in relation to a specific structure, in our case, B2-like $\text{Fe}_8\text{Co}_8\text{C}$. Ordering towards B2 and its equivalent L1_0 phase has been studied in VCA and CPA approaches in several works to date, including one by Turek *et al.* [15]. The parameter S value equal to 1 is associated with a perfect ordering towards the chosen structure (in our case, an ideal crystal in the B2 type), and S equal to 0 represents an absolute lack of the ordering of the given type. Importantly, a system without ordering towards one structure can be perfectly ordered towards another structure, such as L1_2 structure having a zero S towards L1_0 , both being highly ordered fcc-like structures and having a high degree of nearest-neighbor ordering. Long-range ordering parameter S can be represented in general as follows [33–35,62]:

$$S = \frac{p - p(S=0)}{p(S=1) - p(S=0)}, \quad (12)$$

where p denotes the probability of finding an atom of a given type on the expected atomic site. For two-atom type $2 \times 2 \times 2$ supercell and B2 ordering we expand it as

$$S = \frac{|N_I - N_{II}|}{N}, \quad (13)$$

where N_I denotes the number of minority atoms close to $z = 0$ or $0.5c$ plane, N_{II} denotes the number of minority atoms close to $z = 0.25c$ or $0.75c$ plane, and N is the sum of minority atoms in the system. The sites are visualized in Fig. 10. An effectively similar approach has been used recently by Izardar *et al.* studying equiatomic FeNi L1_0 binary phase [38,39]. Parameter S provides a linear scale, similar to one applied by Turek *et al.* [15].

In Fig. 11, we show ordering towards B2 structure dependencies analogous to Fig. 8, presenting results for short-range ordering parameter σ . As the S parameter towards B2 considers only equiatomic systems, the results aggregated are for $\text{Fe}_8\text{Co}_8\text{C}$ only. Similarly to σ dependency, Fig. 11(a)

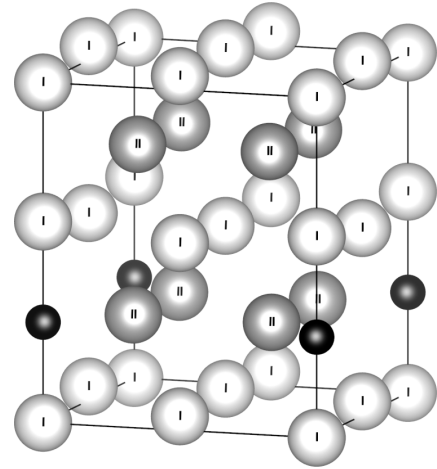


FIG. 10. Graphical representation of atomic sites relevant in Eq. (13). The presented structure is a $2 \times 2 \times 2$ supercell with a single octahedral C atom (black). Sites I are located close to $z = 0$ or $0.5c$ plane, and sites II lie close to $z = 0.25c$ or $0.75c$ plane.

presents a monotonic decrease in mixing enthalpy with B2 ordering in $\text{Fe}_8\text{Co}_8\text{C}$. The energy of configurations with the Co–C–Co NN sequence is, on average, significantly lower than the energy of configurations with the Fe–C–Co NN sequence, which is, in turn, lower than the energy of Fe–C–Fe systems. This fact is independent of the ordering. Perfectly ordered B2 structure with C dopant between two Co atoms possesses the lowest energy.

In Fig. 11(b), we see multiple atomic configurations deviating vastly from the average. In fact, the single highest MAE value, which is twice the average, can be observed for $S = 0.5$. The associated structure is presented in Fig. 12(c). The qualitative agreement of MAE averages, presented in Fig. 11(c), with the work of Turek *et al.* is good. We can see that MAE does not follow any specific trend with B2 ordering. For low ordering towards the B2 phase, we can see both very high and very low MAE values. MAE value converges towards a reasonably high $85 \mu\text{eV atom}^{-1}$ for perfect B2 order and Co–C–Co configuration. Conversely, for C impurity in the Co plane (neighbored by two Fe atoms), MAE converges towards a low value of approximately $10 \mu\text{eV atom}^{-1}$. These are exactly the same MAE values as for most positive sigma and most negative alpha parameters (see Figs. 8 and 9). It is, in fact, the same structure, visualized further in Fig. 12. Magnetic hardness versus B2 ordering, shown in Fig. 11(d), has to be similar to MAE since the system magnetization has been shown above to not depend on the ordering. The main conclusion is that for higher ordering, only systems with Co–C–Co and Fe–C–Co NN sequences possess practical magnetic hardness. Similarly to σ , for low B2 ordering, we can still observe many individual atomic arrangements with hardness above 0.5.

It might be tempting to dive more deeply into the evaluated atomic occupation configurations individually, with particular emphasis on the high-symmetry structures. However, such analysis is beyond the scope of this work, as we rely on

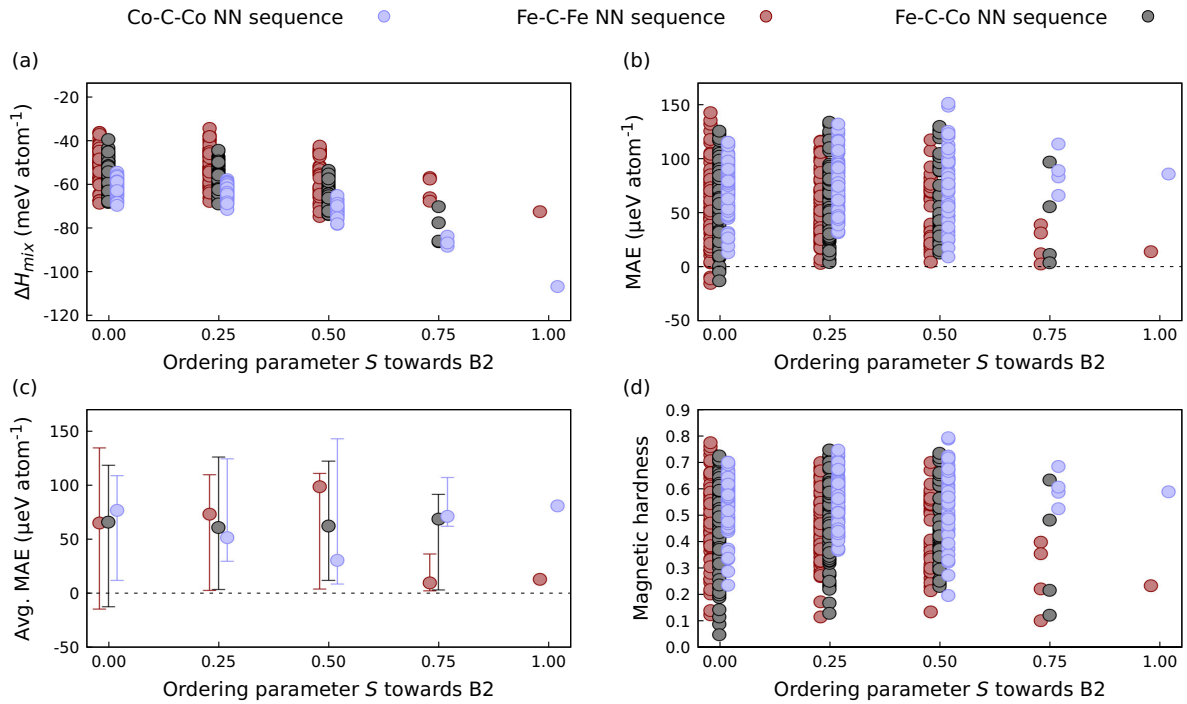


FIG. 11. Dependence of mixing enthalpy (a), magnetocrystalline anisotropy energy (b), (c), and magnetic hardness (d) on long-range ordering parameter S in $\text{Fe}_8\text{Co}_8\text{C}$. The light blue color denotes systems with two Co atoms neighboring the C dopant, the dark red color indicates systems with two Fe atoms neighboring the impurity, and the black color denotes systems with the C atom neighbored by one Fe and one Co atom. Results were obtained using the FPLO18 code with PBE exchange-correlation potential. Fe-C-Fe and Co-C-Co data points are slightly shifted for better readability. Error bars on (c) denote maximum and minimum calculated values.

error cancellation due to the high sample count. A detailed look at the specific structures would require a much finer \mathbf{k} -point mesh and fine atomic positions optimization of such atomic arrangements. Nevertheless, to emphasize possible further paths of Fe-Co-C system investigation, we present in Fig. 12 four selected low-energy, high-MAE structures [Figs. 12(a)–12(c), and 12(e)], as well as a high-energy, low-

MAE, perfectly ordered B2 structure [Fig. 12(d)]. We found that high-order structures for as low as 25% Co concentration can indicate practical magnetic properties. Interestingly, the lowest-energy structure for $\text{Fe}_{12}\text{Co}_4\text{C}$ is the Co interlayer in the plane farthest away from the C impurity. These structures can be promising candidates for future permanent magnets since the price of Fe is negligible in the overall price of an

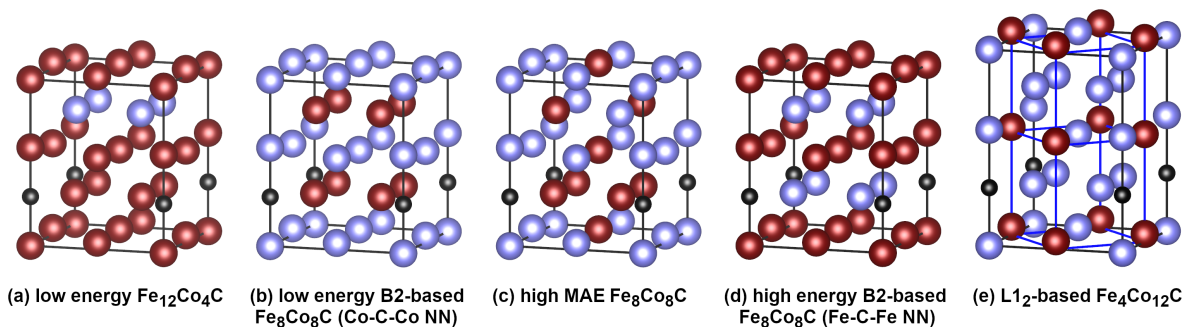


FIG. 12. (a)–(c) Present exemplary obtained low-energy, high-MAE, and high-symmetry supercells: Co interlayer separated from C impurity by half of the supercell (a), Co-C-Co B2 (b), and highest MAE $\text{Fe}_8\text{Co}_8\text{C}$ (c). (d) Presents the high-energy Fe-C-Fe B2 structure, and (e) presents low-energy, high-MAE $\text{Fe}_4\text{Co}_{12}\text{C}$ L_{12} . In (e), the alternative fcc representation of the L_{12} structure is presented with blue lines. Supercell lattice parameters were optimized in FPLO/PBE with virtual crystal approximation, and atomic positions were optimized for a few steps in every atomic position occupancy.

Fe-Co alloy. As for qualitative trends, we observe the L1₂ structure among the lowest-energy systems for high-Co concentrations in the fcc regime. Despite the structure changes towards bct with lowering of the Co content, the atomic occupations for low-energy Fe₁₂Co₄C remain the same as in the high-Co L1₂ phase, presented in Fig. 12(e).

IV. SUMMARY AND CONCLUSIONS

We conducted a full configuration-space analysis for $2 \times 2 \times 2$ (Fe_{1-x}Co_x)₁₆C supercell based on a two-atom body-centered-tetragonal unit cell, with a single C impurity at one of the octahedral interstitial positions in the supercell. The calculations were performed using density functional theory (DFT) with the generalized gradient approximation (GGA) using the full-potential local-orbit scheme (FPLO18).

In our tetragonal (Fe_{1-x}Co_x)₁₆C supercells, we observe a structural phase transition from a body-centered-tetragonal (bct) to a face-centered-cubic (fcc) structure at a Co concentration of about 70 at.%. The lattice parameter c/a ratio in the bct region ranges from 1.07 to 1.12. We calculated relevant magnetic properties for all nonequivalent Fe/Co atom arrangements in the computational cell. Since DFT calculations are, by definition, performed for a temperature of 0 K (for the ground state), we used thermodynamic averaging with an assumed temperature of 300 K in determining the average magnetocrystalline anisotropy energy (MAE) values. Although, as previous experiments have shown, the structure expected above the critical Co concentration ($x \simeq 0.7$) is hexagonal, the assumed tetragonal geometry of the supercell does not allow this and leads to an fcc structure.

One of the basic features of the supercell geometry we analyzed is the first coordination shell of the C dopant atom. The C atom has two nearest-neighboring sites, which can be occupied by two Fe atoms, two Co atoms, or one Fe and one Co atom. We found that for low-Co concentrations, structures with impurities adjacent to two Fe atoms become more stable. The expected result of the stabilization of the (Fe_{0.5}Co_{0.5})_xC alloys by the Co-C-Co nearest-neighbor sequence for medium- to high-Co concentrations is also confirmed in our results.

Although we observe a rather large spread of magnetic moments for different configurations on both Fe and Co atoms, the total magnetic moment in the supercell remains more or less constant. Average (spin) magnetic moments decrease with increasing Co content, without a clear maximum for intermediate concentrations.

Positive MAE values in the bct region indicate a uniaxial magnetocrystalline anisotropy and show a broad maximum around medium-Co concentration ($x \simeq 0.5$). The calculated course of MAE as a function of Co concentration is in very good quantitative agreement with experimental data, which is a noteworthy improvement over effective medium methods. The magnetic hardness of many configurations exceeds the conventional limit of 0.5 for magnetically semihard materials but does not exceed 0.9, remaining below the limit for hard magnetic materials. In addition, for relatively low-Co concentrations, on the order of 25%, we have identified a number of energetically stable structures with high MAE values and potential economic significance.

The calculated mixing enthalpy of considered Fe-Co-C alloys is the lowest at around 50% Co concentration. Moreover, the general trends indicate that higher values of MAE (and magnetic hardness) correlate with more negative values of mixing enthalpy. It shows that better structural stability coincides with high MAE. Magnetocrystalline anisotropy energy values we obtain are comparable to the computationally derived MAE values of other C-, B-, and N-doped Fe_{1-x}Co_x systems, and slightly lower than both, experimentally and computationally obtained values for tetragonally strained undoped Fe_{1-x}Co_x. Energywise, the C doping only slightly shifts mixing enthalpy towards less preferable values, and the energetically worst-case atomic arrangements decrease mixing enthalpy maximally by a factor of 2. It indicates maintaining relatively good structure stability and magnetic properties regardless of the atomic configuration.

A significant part of the discussion is devoted to determining the effect of ordering on the magnetic properties of the compositions under consideration. We focus on the Bethe and Warren-Cowley short-range ordering parameters and the ordering parameter towards the arbitrarily chosen B2 (CsCl) structure. In the largest range of values of the Bethe short-range ordering parameter, its increase correlates with an increase in MAE, while for the highest values of the parameter (above 0.2), we no longer track correlation. Furthermore, we observe no significant correlation between MAE and the value of the Warren-Cowley short-range ordering parameter and the ordering parameter towards the B2 structure. The direct neighborhood of the impurity dominates MAE value dependencies. On the contrary, we see a clear decrease in the value of the enthalpy of mixing (higher stability) as short-range and long-range ordering parameters increase.

In summary, we present a relatively simple and effective method for averaging multiple configurations to predict accurate MAE values for the Fe-Co-C system. We show that the method can be made even more efficient by averaging a few percent of the most energetically favorable structures, with little loss in accuracy. In addition, the Fe-Co-C system is a good matrix for further modifications (e.g., induction of additional stresses) stabilized by the Fe-Co nearest-neighbor interactions. Considering that B-, C-, and N-doped Fe-Co alloys possess similar structural and magnetic properties, further research of Fe/Co ordering in interstitially doped Fe-Co can provide much-needed insight towards efficient, rare-earth-free permanent magnet development. The utilized method allowed us, at a computational cost slightly exceeding that of the CPA method, to obtain basic magnetic characteristics with similar accuracy and, moreover, provided valuable information about the magnetic properties' dependence on the internal structure of the alloy.

ACKNOWLEDGMENTS

We acknowledge the financial support of the National Science Centre Poland under the Grant No. DEC-2018/30/E/ST3/00267. The work on the conformation-picking scheme development has been financed by the Polish Ministry of Science and Higher Education under the Grant No. DI2017/007947. Calculations were made in the Poznan Supercomputing and Networking Centre (PSNC/PCSS).

We acknowledge P. Leśniak for his help in compiling and maintaining the computational codes utilized. We thank J. Marciniak and J. Ruzs for their valuable discussion and sug-

gestions. We also want to thank L. Baldo, K. Olszewska, J. Rychły-Gruszecka, J. Snarski-Adamski, M. Szary, and J. Raczyński for the valuable feedback on the manuscript.

- [1] J. M. D. Coey, Permanent magnets: Plugging the gap, *Scr. Mater.* **67**, 524 (2012).
- [2] O. Gutfleisch, M. A. Willard, E. Brück, C. H. Chen, S. G. Sankar, and J. P. Liu, Magnetic materials and devices for the 21st Century: Stronger, lighter, and more energy efficient, *Adv. Mater.* **23**, 821 (2011).
- [3] T. Hasegawa, Challenges toward development of rear-earth free FeCo based permanent magnet, *Electron. Commun. Jpn.* **104**, e12307 (2021).
- [4] R. Skomski and J. M. D. Coey, Magnetic anisotropy — How much is enough for a permanent magnet? *Scr. Mater.* **112**, 3 (2016).
- [5] T. Burkert, L. Nordström, O. Eriksson, and O. Heinonen, Giant magnetic anisotropy in tetragonal FeCo alloys, *Phys. Rev. Lett.* **93**, 027203 (2004).
- [6] P. Alippi, P. M. Marcus, and M. Scheffler, Strained tetragonal states and bain paths in metals, *Phys. Rev. Lett.* **78**, 3892 (1997).
- [7] G. Andersson, T. Burkert, P. Warnicke, M. Björck, B. Sanyal, C. Chacon, C. Zlotea, L. Nordström, P. Nordblad, and O. Eriksson, Perpendicular magnetocrystalline anisotropy in tetragonally distorted Fe-Co alloys, *Phys. Rev. Lett.* **96**, 037205 (2006).
- [8] P. Warnicke, G. Andersson, M. Björck, J. Ferré, and P. Nordblad, Magnetic anisotropy of tetragonal FeCo/Pt(001) superlattices, *J. Phys.: Condens. Matter* **19**, 226218 (2007).
- [9] G. Andersson, M. Björck, H. Lidbaum, B. Sanyal, C. Chacon, C. Zlotea, and S. Valizadeh, Structure of Fe–Co/Pt(001) superlattices: A realization of tetragonal Fe–Co alloys, *J. Phys.: Condens. Matter* **19**, 016008 (2007).
- [10] A. Winkelmann, M. Przybylski, F. Luo, Y. Shi, and J. Barthel, Perpendicular magnetic anisotropy induced by tetragonal distortion of FeCo alloy films grown on Pd(001), *Phys. Rev. Lett.* **96**, 257205 (2006).
- [11] F. Yildiz, M. Przybylski, and J. Kirschner, Volume contribution to perpendicular anisotropy in Fe_{0.5}Co_{0.5} alloy films on Pd(001), Ir(001), and Rh(001), *J. Appl. Phys.* **105**, 07E129 (2009).
- [12] F. Yildiz, M. Przybylski, X.-D. Ma, and J. Kirschner, Strong perpendicular anisotropy Fe_{1-x}Co_x alloy films epitaxially grown on mismatching Pd(001), Ir(001), and Rh(001) substrates, *Phys. Rev. B* **80**, 064415 (2009).
- [13] F. Luo, X. L. Fu, A. Winkelmann, and M. Przybylski, Tuning the perpendicular magnetic anisotropy in tetragonally distorted Fe_xCo_{1-x} alloy films on Rh (001) by varying the alloy composition, *Appl. Phys. Lett.* **91**, 262512 (2007).
- [14] C. Neise, S. Schönecker, M. Richter, K. Koepf, and H. Eschrig, The effect of chemical disorder on the magnetic anisotropy of strained Fe–Co films, *Phys. Status Solidi B* **248**, 2398 (2011).
- [15] I. Turek, J. Kudrnovský, and K. Carva, Magnetic anisotropy energy of disordered tetragonal Fe–Co systems from ab initio alloy theory, *Phys. Rev. B* **86**, 174430 (2012).
- [16] L. Reichel, G. Giannopoulos, S. Kauffmann-Weiss, M. Hoffmann, D. Pohl, A. Edström, S. Oswald, D. Niarchos, J. Ruzs, L. Schultz, and S. Fähler, Increased magnetocrystalline anisotropy in epitaxial Fe-Co-C thin films with spontaneous strain, *J. Appl. Phys.* **116**, 213901 (2014).
- [17] L. Reichel, L. Schultz, and S. Fähler, Lattice relaxation studies in strained epitaxial Fe-Co-C films, *J. Appl. Phys.* **117**, 17C712 (2015).
- [18] L. Reichel, A. Edström, D. Pohl, J. Ruzs, O. Eriksson, L. Schultz, and S. Fähler, On the origin of perpendicular magnetic anisotropy in strained Fe–Co(–X) films, *J. Phys. D: Appl. Phys.* **50**, 045003 (2017).
- [19] S. Kauffmann-Weiss, S. Hamann, L. Reichel, A. Siegel, V. Alexandrakis, R. Heller, L. Schultz, A. Ludwig, and S. Fähler, The Bain library: A Cu-Au buffer template for a continuous variation of lattice parameters in epitaxial films, *APL Mater.* **2**, 046107 (2014).
- [20] P. Soven, Coherent-potential model of substitutional disordered alloys, *Phys. Rev.* **156**, 809 (1967).
- [21] D. Kim and J. Hong, Origin of thickness dependent spin reorientation transition of B2 type FeCo alloy films, *J. Appl. Phys.* **114**, 213911 (2013).
- [22] A. Zunger, S.-H. Wei, L. G. Ferreira, and J. E. Bernard, Special quasirandom structures, *Phys. Rev. Lett.* **65**, 353 (1990).
- [23] E. K. Delczeg-Czirjak, A. Edström, M. Werwiński, J. Ruzs, N. V. Skorodumova, L. Vitos, and O. Eriksson, Stabilization of the tetragonal distortion of Fe_xCo_{1-x} alloys by C impurities: A potential new permanent magnet, *Phys. Rev. B* **89**, 144403 (2014).
- [24] L. Reichel, L. Schultz, D. Pohl, S. Oswald, S. Fähler, M. Werwiński, A. Edström, E. K. Delczeg-Czirjak, and J. Ruzs, From soft to hard magnetic Fe–Co–B by spontaneous strain: A combined first principles and thin film study, *J. Phys.: Condens. Matter* **27**, 476002 (2015).
- [25] G. Giannopoulos, R. Salikhov, B. Zingsem, A. Markou, I. Panagiotopoulos, V. Psycharis, M. Farle, and D. Niarchos, Large magnetic anisotropy in strained Fe/Co multilayers on AuCu and the effect of carbon doping, *APL Mater.* **3**, 041103 (2015).
- [26] G. Giannopoulos, R. Salikhov, G. Varvaro, V. Psycharis, A. M. Testa, M. Farle, and D. Niarchos, Coherently strained [Fe–Co(C)/Au–Cu]_n multilayers: A path to induce magnetic anisotropy in Fe–Co films over large thicknesses, *J. Phys. D: Appl. Phys.* **51**, 055009 (2018).
- [27] S. Steiner, S. Khmelevskiy, M. Marsmann, and G. Kresse, Calculation of the magnetic anisotropy with projected-augmented-wave methodology and the case study of disordered Fe_{1-x}Co_x alloys, *Phys. Rev. B* **93**, 224425 (2016).
- [28] I. Khan and J. Hong, Potential rare earth free permanent magnet: Interstitial boron doped FeCo, *J. Phys. D: Appl. Phys.* **47**, 415002 (2014).
- [29] I. Khan and J. Hong, Magnetic anisotropy of C and N doped bulk FeCo alloy: A first principles study, *J. Magn. Magn. Mater.* **388**, 101 (2015).
- [30] M. Chandran, L. E. Iorio, and P. R. Subramanian, Effect of nitrogen on the magnetic moment of α-Fe and FeCo alloys from first-principle calculations, *J. Appl. Phys.* **101**, 033912 (2007).

- [31] D. Odkhuu and S. C. Hong, First-principles prediction of possible rare-earth free permanent magnet of tetragonal FeCo with enhanced magnetic anisotropy and energy product through interstitial nitrogen, *Phys. Rev. Appl.* **11**, 054085 (2019).
- [32] M. Däne, S. K. Kim, M. P. Surh, D. Åberg, and L. X. Benedict, Density functional theory calculations of magnetocrystalline anisotropy energies for $(\text{Fe}_{1-x}\text{Co}_x)_2\text{B}$, *J. Phys.: Condens. Matter* **27**, 266002 (2015).
- [33] W. L. Bragg and E. J. Williams, The effect of thermal agitation on atomic arrangement in alloys, *Proc. R. Soc. London A* **145**, 699 (1934).
- [34] W. L. Bragg and E. J. Williams, The effect of thermal agitaion on atomic arrangement in alloys—II, *Proc. R. Soc. London A* **151**, 540 (1935).
- [35] H. A. Bethe and W. L. Bragg, Statistical theory of superlattices, *Proc. R. Soc. London A* **150**, 552 (1935).
- [36] J. M. Cowley, An approximate theory of order in alloys, *Phys. Rev.* **77**, 669 (1950).
- [37] J. M. Cowley, Short-range order and long-range order parameters, *Phys. Rev.* **138**, A1384 (1965).
- [38] A. Izardar and C. Ederer, Impact of chemical disorder on magnetic exchange interactions in L1_0 FeNi, *Phys. Rev. B* **105**, 134428 (2022).
- [39] A. Izardar and C. Ederer, Interplay between chemical order and magnetic properties in L1_0 FeNi (tetrataenite): A first-principles study, *Phys. Rev. Mater.* **4**, 054418 (2020).
- [40] M. Si, A. Izardar, and C. Ederer, Effect of chemical disorder on the magnetic anisotropy in L1_0 FeNi from first-principles calculations, *Phys. Rev. Res.* **4**, 033161 (2022).
- [41] K. Koepernik and H. Eschrig, Full-potential nonorthogonal local-orbital minimum-basis band-structure scheme, *Phys. Rev. B* **59**, 1743 (1999).
- [42] H. Eschrig, M. Richter, and I. Opahle, Relativistic solid state calculations, in *Theoretical and Computational Chemistry, Relativistic Electronic Structure Theory Vol. 14*, edited by P. Schwerdtfeger (Elsevier, Amsterdam, 2004), Chap. 12, pp. 723–776.
- [43] J. P. Perdew, K. Burke, and M. Ernzerhof, Generalized gradient approximation made simple, *Phys. Rev. Lett.* **77**, 3865 (1996).
- [44] K. Momma and F. Izumi, VESTA: A three-dimensional visualization system for electronic and structural analysis, *J. Appl. Crystallogr.* **41**, 653 (2008).
- [45] G. H. O. Daalderop, P. J. Kelly, and M. F. H. Schuurmans, Magnetocrystalline anisotropy and orbital moments in transition-metal compounds, *Phys. Rev. B* **44**, 12054 (1991).
- [46] M. Werwiński and W. Marciniak, Ab initio study of magnetocrystalline anisotropy, magnetostriction, and Fermi surface of L1_0 FeNi (tetrataenite), *J. Phys. D: Appl. Phys.* **50**, 495008 (2017).
- [47] A. Musiał, W. Marciniak, Z. Śniadecki, M. Werwiński, P. Kuświk, B. Idzikowski, M. Kołodziej, A. Grabias, M. Kopcewicz, J. Marcin, and J. Kováč, Structural transformation and magnetic properties of $(\text{Fe}_{0.7}\text{Co}_{0.3})_2\text{B}$ alloys doped with 5d elements: A combined first-principles and experimental study, *J. Alloys Compd.* **921**, 166047 (2022).
- [48] G. Henkelman, B. P. Uberuaga, and H. Jónsson, A climbing image nudged elastic band method for finding saddle points and minimum energy paths, *J. Chem. Phys.* **113**, 9901 (2000).
- [49] G. Henkelman and H. Jónsson, Improved tangent estimate in the nudged elastic band method for finding minimum energy paths and saddle points, *J. Chem. Phys.* **113**, 9978 (2000).
- [50] Z. Rong, D. Kitchaev, P. Canepa, W. Huang, and G. Ceder, An efficient algorithm for finding the minimum energy path for cation migration in ionic materials, *J. Chem. Phys.* **145**, 074112 (2016).
- [51] C. S. Yoo, H. Cynn, P. Söderlind, and V. Iota, New β (fcc)-cobalt to 210 GPa, *Phys. Rev. Lett.* **84**, 4132 (2000).
- [52] L. Pauling, The nature of the interatomic forces in metals, *Phys. Rev.* **54**, 899 (1938).
- [53] A. Díaz-Ortiz, R. Drautz, M. Fähnle, H. Dosch, and J. M. Sanchez, Structure and magnetism in bcc-based iron-cobalt alloys, *Phys. Rev. B* **73**, 224208 (2006).
- [54] G. A. Prinz, Stabilization of bcc Co via epitaxial growth on GaAs, *Phys. Rev. Lett.* **54**, 1051 (1985).
- [55] Q. Wang, R. Grau-Crespo, and N. H. de Leeuw, Mixing thermodynamics of the calcite-structured $(\text{Mn,Ca})\text{CO}_3$ solid solution: A computer simulation study, *J. Phys. Chem. B* **115**, 13854 (2011).
- [56] D. Evans, J. Chen, G. Bokas, W. Chen, G. Hautier, and W. Sun, Visualizing temperature-dependent phase stability in high entropy alloys, *npj Comput. Mater.* **7**, 151 (2021).
- [57] I. Khan, S. Park, and J. Hong, Temperature dependent magnetic properties of Dy-doped Fe_{16}N_2 : Potential rare-earth-lean permanent magnet, *Intermetallics* **108**, 25 (2019).
- [58] D. I. Bardos, Mean magnetic moments in bcc Fe–Co alloys, *J. Appl. Phys.* **40**, 1371 (1969).
- [59] G. Giannopoulos, L. Reichel, A. Markou, W. Wallisch, M. Stöger-Pollach, I. Panagiotopoulos, V. Psycharis, S. Fähler, J. Fidler, and D. Niarchos, Structural and magnetic properties of strongly carbon doped Fe-Co thin films, *J. Magn. Magn. Mater.* **393**, 479 (2015).
- [60] D. Wu, Q. Zhang, J. P. Liu, D. Yuan, and R. Wu, First-principles prediction of enhanced magnetic anisotropy in FeCo alloys, *Appl. Phys. Lett.* **92**, 052503 (2008).
- [61] L. R. Owen, H. Y. Playford, H. J. Stone, and M. G. Tucker, A new approach to the analysis of short-range order in alloys using total scattering, *Acta Mater.* **115**, 155 (2016).
- [62] E. J. Williams and W. L. Bragg, The effect of thermal agitation on atomic arrangement in alloys-III, *Proc. R. Soc. London A* **152**, 231 (1935).



Structural transformation and magnetic properties of $(\text{Fe}_{0.7}\text{Co}_{0.3})_2\text{B}$ alloys doped with 5d elements: A combined first-principles and experimental study



A. Musiał^{a,b,*}, W. Marciniak^{a,c}, Z. Śniadecki^a, M. Werwiński^a, P. Kuświk^a, B. Idzikowski^a, M. Kołodziej^{a,d}, A. Grabias^{e,f}, M. Kopcewicz^{e,f}, J. Marcin^g, J. Kováč^g

^a Institute of Molecular Physics, Polish Academy of Sciences, M. Smoluchowskiego 17, Poznań 60-179, Poland

^b Center for Advanced Technologies, Adam Mickiewicz University, Uniwersytetu Poznańskiego 10, Poznań 61-614, Poland

^c Institute of Physics, Faculty of Technical Physics, Poznań University of Technology, Piotrowo 3, Poznań 61-138, Poland

^d NanoBioMedical Centre, Adam Mickiewicz University in Poznań, Wszechnicy Piastowskiej 3, Poznań 61-614, Poland

^e Łukasiewicz - Institute of Microelectronics and Photonics, Lotników 32/46, Warsaw 02-668, Poland

^f Center of Electronic Materials Technology, Wólczyńska 133, Warsaw 01-919, Poland

^g Institute of Experimental Physics, Slovak Academy of Sciences, Watsonova 47, Košice 040 01, Slovakia

ARTICLE INFO

Article history:

Received 25 June 2021

Received in revised form 10 June 2022

Accepted 25 June 2022

Available online 28 June 2022

Keywords:

Amorphous alloy

Magnetic properties

Magnetocrystalline anisotropy energy

Crystal structure

Radio-frequency Mössbauer spectroscopy

ABSTRACT

$(\text{Fe,Co})_2\text{B}$ -based compounds with specific 5d substitutions are considered as promising materials for permanent magnets without rare-earth elements. We conducted a combined first-principles and experimental study focused on $(\text{Fe}_{0.7}\text{Co}_{0.3})_2\text{B}$ alloys doped with W and Re. First, we used full-potential local-orbital scheme to systematically investigate $(\text{Fe,Co})_2\text{B}$ alloys with 3d, 4d, and 5d substitutions. Computational analyses showed a significant increase in magnetocrystalline anisotropy only for the Re doped sample. Simultaneously, the structural and magnetic properties of the $(\text{Fe}_{0.7-x}\text{Co}_{0.3-x}\text{M}_{2x})_2\text{B}$ ($M = \text{W, Re}; x = 0, 0.025$) alloys were investigated experimentally. The desired $(\text{Fe,Co})_2\text{B}$ tetragonal phase was synthesized by heat treatment of amorphous precursors. We observed that isothermal annealing increases the coercive field of all samples. However, the obtained values, without further optimization, are well below the threshold for permanent magnet applications. Nevertheless, annealing of substituted samples at 750°C significantly improves saturation magnetization values. Furthermore, Mössbauer spectroscopy revealed a reduction of the hyperfine field due to the presence of Co atoms in the $(\text{Fe,Co})_2\text{B}$ phase, where additional defect positions are formed by Re and W. Radio-frequency Mössbauer studies showed that $(\text{Fe}_{0.7}\text{Co}_{0.3})_2\text{B}$ and the W-substituted sample began to crystallize when exposed to a radio frequency field of 12 Oe, indicating that the amorphous phase is stabilized by Re substitution. Improvement of thermal stability of $(\text{Fe}_{0.675}\text{Co}_{0.275}\text{Re}_{0.05})_2\text{B}$ alloy is consistent with the results of differential scanning calorimetry and thermomagnetic measurements.

© 2022 Published by Elsevier B.V.

1. Introduction

Permanent magnets are one of the most important materials used in modern technology. The best known and widely used permanent magnets are characterized by high T_c values, such as SmCo_5 alloys [1], and high energy product (BH), where the most obvious example is $\text{Nd}_2\text{Fe}_{14}\text{B}$ [2]. As rare earth prices have shown high volatility over the past decade, the search for high-energy product magnets with limited content of elements such as Sm or Nd has

intensified [3–5]. Currently, candidates for rare-earth-free permanent magnets include for example: FeNi compounds [6], $\text{Fe}_{16-x}\text{Co}_x\text{N}_2$ alloys [7], and manganese-based materials such as MnBi, MnAl, and MnGa [8,9]. Promising candidates, recently predicted from data-mining approach, are also Pt_2FeNi , Pt_2FeCu , and W_2FeB_2 [10]. The prospect of use as rare-earth-free permanent magnets has also sparked interest in $(\text{Fe}_{1-x}\text{Co}_x)_2\text{B}$ alloys. Experimental studies of these alloys include, for example, analyses of the full range of cobalt concentration [11–13] along with reinvestigation of their intrinsic magnetic properties [14]. Other experiments involved characterization of $(\text{Fe}_{0.7}\text{Co}_{0.3})_2\text{B}$ single crystal [15] and mechanically milled $(\text{Fe}_{0.675}\text{Co}_{0.3}\text{Re}_{0.025})_2\text{B}$ [16]. Experimental efforts were also supported by numerous first-principles calculations. For example, the calculations have helped to explain the origin of spin-reorientation

* Corresponding author at: Institute of Molecular Physics, Polish Academy of Sciences, M. Smoluchowskiego 17, Poznań 60-179, Poland.
E-mail address: musial@ifmpan.poznan.pl (A. Musiał).

transitions in $(\text{Fe}_{1-x}\text{Co}_x)_2\text{B}$ alloys [12] and spin-fluctuation mechanism of the temperature dependence of the magnetocrystalline anisotropy of $(\text{Fe}_{1-x}\text{Co}_x)_2\text{B}$ [17]. The calculations also predict a high-pressure induced magnetic moment collapse [18]. Moreover, some groups have investigated the effect of doping with $3d$ [19] and $5d$ [11] elements. Another computational work involved accurate estimation of the magnetocrystalline anisotropy energies for $(\text{Fe}_{1-x}\text{Co}_x)_2\text{B}$ alloys [20]. In several cases, the results on $(\text{Fe}_{1-x}\text{Co}_x)_2\text{B}$ alloys were the effect of synergy between experiment and theory [11,12,15]. Furthermore, also a number of related boride phases, such as $\text{Co}_{2-x}\text{Mn}_x\text{B}$, $(\text{Fe}_x\text{Co}_{1-x})_3\text{B}$, and $\text{Mn}_{0.95-x}\text{Fe}_{1.05-x}\text{Co}_x\text{B}$ [21–23], have been studied recently to tune their magnetic properties. In this work, we investigate the rare-earth-free magnet $(\text{Fe}_{0.7}\text{Co}_{0.3})_2\text{B}$ and its alloys substituted with Re and W. The Co content and the type of dopant elements were predicted in a previous study [11] in which one of us participated. The purpose of this work is to verify the previous predictions using a more advanced computational method based on a full-potential approach and to experimentally characterize the structural and magnetic properties of the alloys. Density functional theory along with X-ray diffraction, differential scanning calorimetry, macroscopic magnetic measurements, and Mössbauer spectroscopy were utilized to reach this aim. Based on the experimental work mentioned above, we will present the basic physical properties of Fe_2B , Co_2B , $(\text{Fe}_{0.7}\text{Co}_{0.3})_2\text{B}$, and W- and Re-substituted alloys. Fe_2B and Co_2B crystallize in a tetragonal structure with space group $I4/mcm$ [11]. The experimental value of the magnetic anisotropy constant K_1 is equal to -0.80 MJ m^{-3} for Fe_2B and 0.10 MJ m^{-3} for Co_2B [24]. The total magnetic moment drops from about $1.9 \mu_B/3d$ atom for Fe_2B to $0.8 \mu_B/3d$ atom for Co_2B [25]. The Curie temperature for Fe_2B is above 1000 K [11], while that for Co_2B is equal to 433 K [25]. The $(\text{Fe}_{0.7}\text{Co}_{0.3})_2\text{B}$ alloy shows the highest value of magnetocrystalline anisotropy constant among the alloys containing tetragonal $(\text{Fe},\text{Co})_2\text{B}$ phase [11,24] and one of the highest values of magnetic moment. Its Curie temperature is relatively high and equal to above 800 K [11]. The addition of 2.5 at% Re in place of the $3d$ elements results in an increase in the magnetocrystalline anisotropy constant of the alloy $(\text{Fe}_{0.7}\text{Co}_{0.3})_2\text{B}$ from 0.42 to 0.63 MJ m^{-3} (at room temperature) and an increase of anisotropy field from 1 T to 1.6 T . At the same time, the saturation magnetization (at 2 T) decreases from 143.3 to $122.2 \text{ A m}^2 \text{ kg}^{-1}$ [11].

2. Computational and experimental details

2.1. Computational details

Calculations of the electronic band structure were carried out using the full-potential local-orbital electronic structure code FPLO18.00–52 [26] employing a fixed atomic-like basis set. FPLO was the choice for accurate magnetocrystalline anisotropy energy (MAE) calculations due to the full potential and fully-relativistic implementation of the code. For the exchange-correlation potential, we used the generalized gradient approximation (GGA) in the Perdew-Burke-Ernzerhof (PBE) form [27]. For the scalar-relativistic calculations, we used the criterion of the convergence of charge density equal to 10^{-6} . MAE was evaluated as the difference between fully-relativistic total energies calculated in one iteration for the quantization axes $[001]$ and $[100]$. We confirmed the reliability of such a procedure by performing the full self-consistent calculations for selected cases. The positive MAE sign corresponds to the axis of easy magnetization along the direction $[001]$ (c axis), see Fig. 1. For a selected alloy doped with Re, we examined the MAE as a function of spin magnetic moment (m_s) using the fully-relativistic version of the fixed spin moment (FSM) approach [28,29]. For the supercell models under consideration, the energy convergence with the number of \mathbf{k} -points was thoroughly tested. We found that a $12 \times 12 \times 12$ \mathbf{k} -mesh leads to the well converged MAE results.

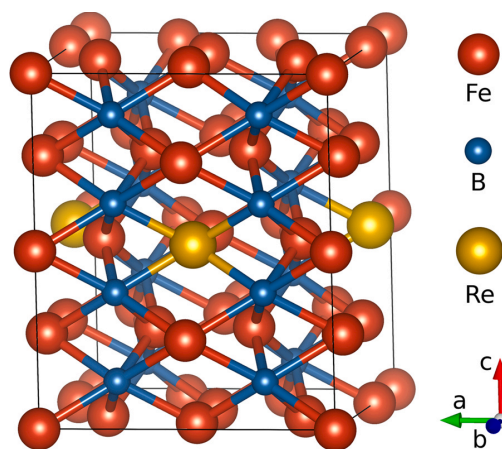


Fig. 1. Supercell of $\text{Fe}_{15}\text{ReB}_8$ (based on tetragonal Fe_2B structure) with space group $I4/mcm$ ($a = 7.116 \text{ \AA}$, $c = 8.482 \text{ \AA}$). The presented model consists of sixteen formulas of Fe_2B .

The exemplary model of $(\text{Fe}_{0.66}\text{Co}_{0.28}\text{Re}_{0.06})_2\text{B}$ is obtained by combining a supercell approach with virtual crystal approximation (VCA). First, based on the tetragonal Fe_2B unit cell, we prepared the $\text{Fe}_{15}\text{ReB}_8$ supercell consisting of eight Fe_2B formulas and with a single Fe atom replaced by Re, see Fig. 1. This procedure leads to a crystalline structure containing 11 nonequivalent atomic positions (8 Fe, 2 B, and 1 Re). Next, in place of the remaining Fe atoms, we introduced the virtual atoms with a fractional atomic number 26.3, in order to mimic the 70% concentration of Fe (with atomic number $Z = 26$) and 30% concentration of Co (with atomic number $Z = 27$). Because one Fe atom from the supercell was previously replaced by Re, the final composition can be written as $(\text{Fe}_{0.66}\text{Co}_{0.28}\text{Re}_{0.06})_2\text{B}$. Subsequently, by replacing the Re atoms with other transition metals, we prepared the models containing $3d$, $4d$, and $5d$ elements. The crystallographic parameters for $(\text{Fe}_{0.7}\text{Co}_{0.3})_{15}\text{MB}_8$ supercells ($a = 7.116 \text{ \AA}$, $c = 8.482 \text{ \AA}$) were based on the parameters for $(\text{Fe}_{0.7}\text{Co}_{0.3})_2\text{B}$ ($a = 5.032 \text{ \AA}$, $c = 4.241 \text{ \AA}$), which in turn were interpolated based on the theoretically predicted parameters of Fe_2B ($a = 5.059 \text{ \AA}$, $c = 4.239 \text{ \AA}$) and Co_2B ($a = 4.969 \text{ \AA}$, $c = 4.244 \text{ \AA}$). The VESTA code was used for visualization of the crystal structure [30] presented in Fig. 1.

2.2. Experimental details

Master alloys of $(\text{Fe}_{0.7-x}\text{Co}_{0.3-x}\text{M}_{2x})_2\text{B}$ ($M = \text{W}, \text{Re}; x = 0, 0.025$) were prepared by arc-melting technique. High purity elements Fe, Co, and B (3 N or more) were re-melted several times in the argon atmosphere to obtain full homogeneity. The mass of ingots was controlled at each step of the synthesis in order to maintain the nominal composition. The alloys were subsequently injected on the copper wheel rotating with the surface velocity of 30 ms^{-1} in an argon atmosphere. The melt-spun ribbons were $30 \mu\text{m}$ thick. Densities of the alloys were calculated assuming the density of $\text{Co}_{53}\text{B}_{27}$ equal to 8.08 g cm^{-3} [31]. Calculated densities are 7.53 , 7.97 , and 8.04 g cm^{-3} for $(\text{Fe}_{0.7}\text{Co}_{0.3})_2\text{B}$, $(\text{Fe}_{0.675}\text{Co}_{0.275}\text{W}_{0.05})_2\text{B}$, and $(\text{Fe}_{0.675}\text{Co}_{0.275}\text{Re}_{0.05})_2\text{B}$, respectively. Structural information was obtained by X-ray diffraction (XRD) with the use of TUR-M62 diffractometer (HZG4 goniometer) with $\text{CoK}\alpha$ radiation ($\lambda = 1.7889 \text{ \AA}$) in Bragg-Brentano geometry. The thermal stability of as-quenched samples was investigated by differential scanning calorimetry (DSC), in the temperature range from 100 to 850°C , at a heating rate of 10 K min^{-1} , using Netzsch DSC 404 apparatus. Magnetic hysteresis loops were measured using a vibrating sample magnetometer (VSM) option in the Quantum Design Physical Property Measurement

System (PPMS). Magnetization measurements at high temperatures were collected using a homemade VSM. In order to obtain information on the local ^{57}Fe environment, ^{57}Fe Mössbauer spectroscopy measurements were made at room temperature. The hyperfine structure was modeled by least-square fitting using NORMOS program [32]. An unconventional radio-frequency-Mössbauer technique was used to study the effect of the chemical composition on the physical properties of amorphous alloys. The spectra were measured when the samples were exposed to a radio-frequency magnetic field from 0 to 18 Oe at 61.8 MHz.

3. Results and discussion

3.1. Density functional theory calculations

$(\text{Fe}_{0.7}\text{Co}_{0.3})_2\text{B}$ shows the highest value of magnetocrystalline anisotropy among the $(\text{Fe},\text{Co})_2\text{B}$ tetragonal alloys [11,24]. To further increase the MAE of this material, one strategy is to combine it with elements from the d -block, particularly from $5d$ -series [11]. Previously, when examining the impact of the $5d$ substitutions from the first principles, by applying atomic sphere approximation (ASA), Edström and coworkers [11] stated that the positive effect on the MAE of $(\text{Fe}_{0.7}\text{Co}_{0.3})_2\text{B}$ should be due to the doping of W and Re. While the growth of MAE due to the alloying with Re was confirmed experimentally, problems with the preparation of single-phase samples with W prevented from evaluating this prediction [11]. In this work, we perform similar calculations, but using the full-potential approach instead atomic sphere approximation and extending the range of dopants tested. Moreover, we were successful in synthesis of single phase W-containing alloy, what enabled us to make comprehensive analysis. Fig. 2 shows the results of our calculations of the influence of $3d$ -, $4d$ -, and $5d$ -substitutions on the MAE of $(\text{Fe}_{0.7}\text{Co}_{0.3})_2\text{B}$. We see a maximum of MAE in the middle of each series, but a significant increase in MAE was observed only for $(\text{Fe}_{0.66}\text{Co}_{0.28}\text{Re}_{0.06})_2\text{B}$. However, given the above arguments, we decided that both compositions, with W and with Re, would be subjected to thorough theoretical and experimental analysis.

It has been shown previously, that the growth in the MAE seen for W and Re dopants is primarily due to the strong spin-orbit coupling of $5d$ element. However, other changes in the electronic structure also have an impact on MAE [11,33]. The calculations from this work predict that the MAE increases from 1.17 MJ m^{-3} for $(\text{Fe}_{0.7}\text{Co}_{0.3})_2\text{B}$ to about 2.34 MJ m^{-3} for $(\text{Fe}_{0.66}\text{Co}_{0.28}\text{Re}_{0.06})_2\text{B}$. Although the qualitative results obtained are reliable, the exact values we have determined are subject to a known error of the virtual

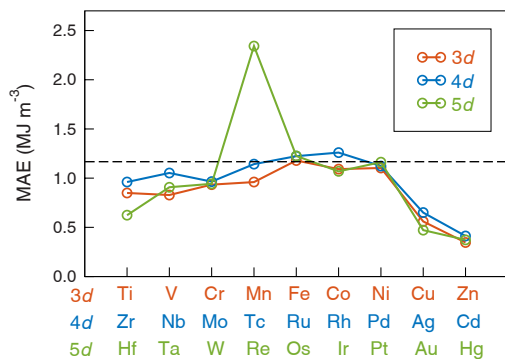


Fig. 2. Magnetocrystalline anisotropy energy (MAE) for $(\text{Fe}_{0.66}\text{Co}_{0.28}\text{M}_{0.06})_2\text{B}$ alloys, where M stands for $3d$, $4d$, and $5d$ elements. The calculation was performed using FPLO18 code with PBE functional. The dashed line means the calculated MAE of $(\text{Fe}_{0.7}\text{Co}_{0.3})_2\text{B}$ (1.17 MJ m^{-3}). The alloy model is prepared using a supercell combined with a virtual crystal approximation (VCA).

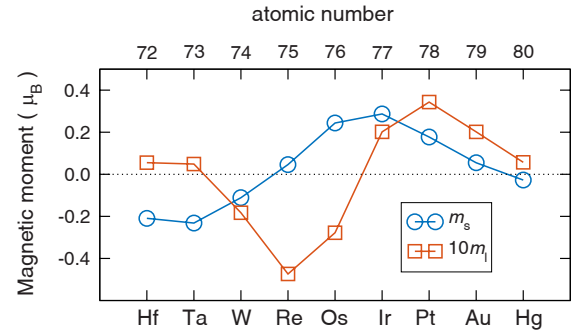


Fig. 3. Spin (m_s) and orbital (m_l) magnetic moments of $5d$ transition metal impurities M in $(\text{Fe}_{0.66}\text{Co}_{0.28}\text{M}_{0.06})_2\text{B}$ alloys as calculated for spin quantization axis along c -axis. The calculation was performed using FPLO18 code with PBE functional.

crystal approximation (VCA). Thus, we estimate that the exact MAE values are overestimated by about 2–4 times compared to experiment [11]. Before we proceed to a detailed analysis of the compositions with W and Re, we would like to present how the magnetic moments induced on $5d$ dopants change along the $5d$ -series. Fig. 3 shows the calculated spin and orbital magnetic moments on $5d$ transition metal impurities M in $(\text{Fe}_{0.66}\text{Co}_{0.28}\text{M}_{0.06})_2\text{B}$ alloys. The spin magnetic moments of the early $5d$ impurities (Hf, Ta, W) are coupled antiferromagnetically to the Fe/Co moments, while the moments of the late $5d$ elements are coupled to Fe/Co ferromagnetically, except Hg. The calculated spin moments take values between approximately -0.2 and $0.3 \mu_B \text{ atom}^{-1}$. The above results can be compared with the previously studied behavior of the $5d$ impurities in the Fe matrix [34]. The measured local magnetic moments of $5d$ impurities in the Fe matrix show a similar trend along the series as the calculated spin moments, with a transition between antiferromagnetic and ferromagnetic coupling located between Os and Ir, and with magnetic moment values ranging from -0.4 – $0.5 \mu_B \text{ atom}^{-1}$ [34]. The shift of the transition point between antiferromagnetic and ferromagnetic coupling, observed in our system between W and Re, in relation to the pure Fe matrix, is due to the presence of Co, causing an increase in the number of electrons in our alloy and results from comparing the calculated spin magnetic moment with the measured total moment. Simultaneously, the decrease of magnetic moment values in respect to the Fe matrix most probably results from the relatively high share of non-magnetic B atoms in the alloy, leading to the reduction of magnetic moments on Fe/Co atoms. The discussed above results of measurements for $5d$ impurities in the Fe matrix were initially theoretically predicted using the first-principles methods [35,36]. Returning to the results shown in Fig. 3, we further notice that the function of orbital moment dependence on the type of $5d$ impurity resembles the course of the sinus function with a minimum and maximum on the negative and positive side of the value range. Very similar behavior for $5d$ impurities in Fe matrix has been predicted previously, with the minimum for Os and maximum for Pt [36]. We have also presented similar results for $5d$ impurities in Fe_5P_2 compound [33].

Table 1 presents the spin (m_s) and orbital (m_l) magnetic moments of considered compositions: $(\text{Fe}_{0.66}\text{Co}_{0.28}\text{W}_{0.06})_2\text{B}$, $(\text{Fe}_{0.66}\text{Co}_{0.28}\text{Re}_{0.06})_2\text{B}$, and $(\text{Fe}_{0.7}\text{Co}_{0.3})_2\text{B}$. The m_l on the virtual Fe/Co atom is relatively low and underestimated by application of PBE approximation. For $(\text{Fe}_{0.7}\text{Co}_{0.3})_2\text{B}$ the m_s on virtual Fe/Co atom is equal to $1.81 \mu_B$ and the induced m_s on B is equal to $-0.22 \mu_B$. The substitution of the considered alloy with W and Re leads to a reduction of several percent of m_s on both virtual Fe/Co atom and B, whereas the small induced magnetic moments on W and Re have been discussed before. In summary, the admixture of W and Re leads

Table 1

Spin (m_s) and orbital (m_l) magnetic moments [μ_B (atom or formula unit) $^{-1}$] of $(\text{Fe}_{0.66}\text{Co}_{0.28}\text{W}_{0.06})_2\text{B}$, $(\text{Fe}_{0.66}\text{Co}_{0.28}\text{Re}_{0.06})_2\text{B}$, and $(\text{Fe}_{0.7}\text{Co}_{0.3})_2\text{B}$ as calculated for spin quantization axis along the c -axis. The calculation was performed using fully-relativistic FPLO18 code with PBE functional.

	$(\text{Fe}_{0.66}\text{Co}_{0.28}\text{W}_{0.06})_2\text{B}$		$(\text{Fe}_{0.66}\text{Co}_{0.28}\text{Re}_{0.06})_2\text{B}$		$(\text{Fe}_{0.7}\text{Co}_{0.3})_2\text{B}$	
	m_s	m_l	m_s	m_l	m_s	m_l
Fe/Co	1.67	0.04	1.69	0.05	1.81	0.04
B	-0.18	0.00	-0.18	0.00	-0.22	0.00
M	-0.11	-0.02	0.05	-0.05	-	-
total	2.93	0.08	2.99	0.08	3.41	0.09

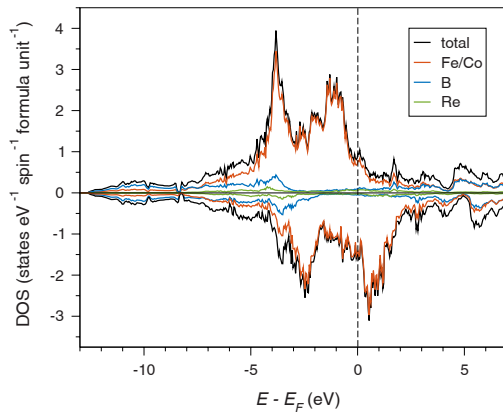


Fig. 4. Densities of states (DOS) of $(\text{Fe}_{0.66}\text{Co}_{0.28}\text{Re}_{0.06})_2\text{B}$ alloy. The model is combined of supercell and virtual crystal approximation (VCA). The calculation was performed using FPLO18 code with PBE functional.

to a total moment per formula unit of $2.93 \mu_B$ for $(\text{Fe}_{0.66}\text{Co}_{0.28}\text{W}_{0.06})_2\text{B}$ and $2.99 \mu_B$ for $(\text{Fe}_{0.66}\text{Co}_{0.28}\text{Re}_{0.06})_2\text{B}$, as compared to $3.41 \mu_B$ for $(\text{Fe}_{0.7}\text{Co}_{0.3})_2\text{B}$.

The discussed spin polarization is clearly visible on the plot of spin-polarized densities of states (DOS) of $(\text{Fe}_{0.66}\text{Co}_{0.28}\text{Re}_{0.06})_2\text{B}$, see Fig. 4. The plot covers the range of the valence band of several eV's around the Fermi level. The main contribution comes from Fe/Co $3d$ orbitals. Contribution from Re, although noticeably small, leads to changes in the band structure leading to the doubling of the MAE. These changes are barely visible in this scale, but can be traced on a scale of tenths of eV around the Fermi level [11].

The experiments have shown that the magnetic anisotropy constants of some $(\text{Fe},\text{Co})_2\text{B}$ alloys change significantly with temperature [24]. However, for Co concentration $x = 0.3$ it behaves rather conventional, monotonically decreasing with temperature [24]. The question arises, whether this behavior will also be true for the $(\text{Fe}_{0.7}\text{Co}_{0.3})_2\text{B}$ sample doped with Re? To answer it, we calculate how the MAE changes with the reduction of the spin magnetic moment. Our conclusion is based on the expected relationship, that an increase in temperature causes a decrease in a magnetic moment [11]. In this way, by studying magnetic moment reduction, we gain insight into the behavior of MAE with temperature. In Fig. 5 we present the plot of MAE as a function of the fixed spin magnetic moment for $(\text{Fe}_{0.66}\text{Co}_{0.28}\text{Re}_{0.06})_2\text{B}$ alloy. As the magnetic moment decreases, the MAE first increases to about 2.9 MJ m^{-3} and then begins to decrease, reaching its initial value of about 2.4 MJ m^{-3} at about 25% of the moment decrease ($m_s = 2.3 \mu_B \text{ f.u.}^{-1}$). As it has been shown experimentally for similar alloy $(\text{Fe}_{0.75}\text{Co}_{0.25})_2\text{B}$ [11], a decrease in magnetization of about 25% occurs at about 700 K. Thus we would expect that the predicted large MAE of $(\text{Fe}_{0.66}\text{Co}_{0.28}\text{Re}_{0.06})_2\text{B}$ will be stable up to relatively high temperatures. However, thermal effects can also affect the electronic structure in other ways than just

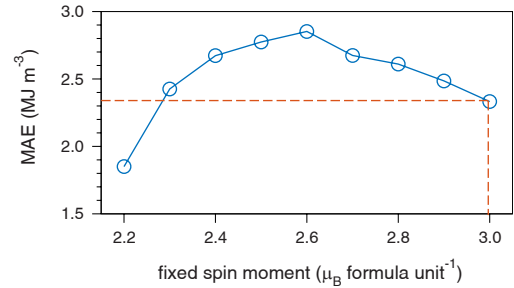


Fig. 5. Magnetocrystalline anisotropy energy (MAE) of $(\text{Fe}_{0.66}\text{Co}_{0.28}\text{Re}_{0.06})_2\text{B}$ alloy as a function of the fixed spin magnetic moment. The dashed line means MAE equal to 2.34 MJ m^{-3} for equilibrium spin magnetic moment $2.99 \mu_B \text{ f.u.}^{-1}$. The calculation was performed using FPLO18 code with PBE functional. The model is combined of supercell and virtual crystal approximation (VCA).

destabilizing magnetic interactions, leading to a subsequent decrease in MAE.

3.2. Structural characterization

X-ray diffraction measurements were performed mainly to characterize as-quenched samples, their transformation route during heat treatment, and to confirm single phase character of annealed samples. Results for as-quenched and annealed $(\text{Fe}_{0.7}\text{Co}_{0.3})_2\text{B}$, $(\text{Fe}_{0.675}\text{Co}_{0.275}\text{W}_{0.05})_2\text{B}$, and $(\text{Fe}_{0.675}\text{Co}_{0.275}\text{Re}_{0.05})_2\text{B}$ alloys are shown in Fig. 6. All samples are amorphous in the as-quenched state and crystallize into tetragonal $(\text{Fe},\text{Co})_2\text{B}$ structure (CuAl₂-type with the $I4/mcm$ space group) [37] after annealing. A similar situation has already been reported for Co-B systems [31]. The shortest interatomic distances R are equal to 2.44, 2.42, and 2.45 Å for $(\text{Fe}_{0.7}\text{Co}_{0.3})_2\text{B}$, $(\text{Fe}_{0.675}\text{Co}_{0.275}\text{W}_{0.05})_2\text{B}$, and $(\text{Fe}_{0.675}\text{Co}_{0.275}\text{Re}_{0.05})_2\text{B}$, respectively. These values are slightly larger than the average of interatomic distances between different atoms in the calculated FeCoB relaxed tetragonal structure, where R is equal to 2.35 Å [38]. Comparable results have been also obtained for amorphous alloy $\text{Fe}_8\text{Co}_{80}\text{Zr}_7\text{B}_4\text{Cu}_1$ ($R = 2.53 \text{ Å}$) [39]. The position $8h$ of Co atoms in tetragonal Co_2B phase [40] and Fe atoms in Fe_2B phase are slightly different. With the increase of annealing temperature, some peaks (68° , 97° , and 116°) split into two independent reflections. Moreover, alteration of the intensity ratio of (002) and (211) reflections is observed after isothermal annealing at 750°C and already at 600°C for $(\text{Fe}_{0.675}\text{Co}_{0.275}\text{W}_{0.05})_2\text{B}$. The (200) reflection appeared only after annealing at 750°C and its intensity is relatively low. Lattice parameters were calculated by the use of the Rietveld method and are in agreement with values used for theoretical calculation and also similar to those reported before [11,41]. Lattice parameters strongly depend on the annealing temperature and chemical composition of the alloys, as shown in Table 2. With the increasing annealing temperature, lattice parameter a decreases and c increases, as in Ref. [24].

3.3. Thermal stability

Calorimetric measurements were performed to determine thermal stability of amorphous phase and characteristic temperatures of crystallization of tetragonal phase, see Fig. 7. For each case, one distinct exothermic reaction is observed between 500 and 600°C . Small exothermic effects were also detected at around 800°C for $(\text{Fe}_{0.7}\text{Co}_{0.3})_2\text{B}$ and $(\text{Fe}_{0.675}\text{Co}_{0.275}\text{Re}_{0.05})_2\text{B}$. The onset temperature of crystallization (T_{onset}) for $(\text{Fe}_{0.7}\text{Co}_{0.3})_2\text{B}$ sample is equal to 536°C , with maxima of phase transitions for the first and the second process at $T_{p1} = 551^\circ\text{C}$ and $T_{p2} = 780^\circ\text{C}$. Their enthalpies are equal to $\Delta H_1 \approx 109 \text{ J g}^{-1}$ and $\Delta H_2 \approx 4 \text{ J g}^{-1}$. T_{onset} for $(\text{Fe}_{0.675}\text{Co}_{0.275}\text{W}_{0.05})_2\text{B}$

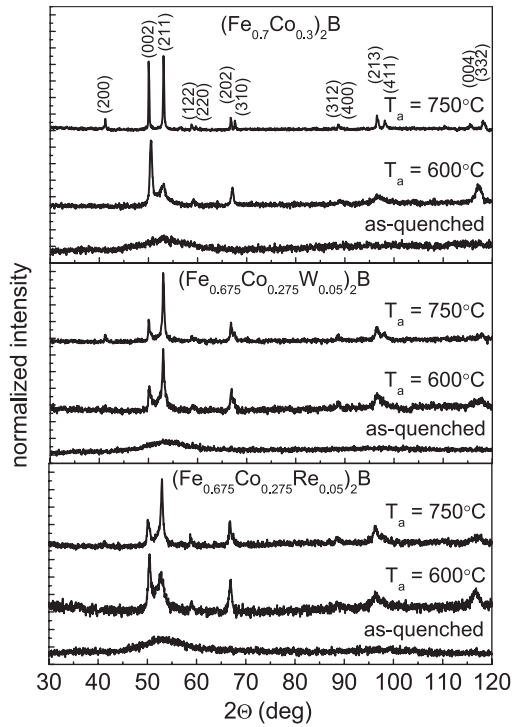


Fig. 6. X-ray diffraction patterns of $(\text{Fe}_{0.7}\text{Co}_{0.3})_2\text{B}$, $(\text{Fe}_{0.675}\text{Co}_{0.275}\text{W}_{0.05})_2\text{B}$, and $(\text{Fe}_{0.675}\text{Co}_{0.275}\text{Re}_{0.05})_2\text{B}$ alloys in as-quenched state and annealed at $T_a = 600$ and 750°C for 60 min. Miller indexes of CuAl_2 -type structure are assigned.

Table 2

Lattice parameters and their ratio determined from X-ray diffraction analysis for $(\text{Fe}_{0.7}\text{Co}_{0.3})_2\text{B}$, $(\text{Fe}_{0.675}\text{Co}_{0.275}\text{W}_{0.05})_2\text{B}$, and $(\text{Fe}_{0.675}\text{Co}_{0.275}\text{Re}_{0.05})_2\text{B}$ alloys after isothermal annealing at annealing temperature T_a equal to 600 and 750°C for 60 min.

alloy	T_a [$^\circ\text{C}$]	a [\AA]	c [\AA]	c/a
$(\text{Fe}_{0.7}\text{Co}_{0.3})_2\text{B}$	600	5.128	4.192	0.817
	750	5.084	4.228	0.831
$(\text{Fe}_{0.675}\text{Co}_{0.275}\text{W}_{0.05})_2\text{B}$	600	5.100	4.214	0.826
	750	5.092	4.224	0.829
$(\text{Fe}_{0.675}\text{Co}_{0.275}\text{Re}_{0.05})_2\text{B}$	600	5.150	4.199	0.815
	750	5.107	4.222	0.826

decreases to 503°C , indicating lower thermal stability than for the $(\text{Fe}_{0.7}\text{Co}_{0.3})_2\text{B}$ alloy ($T_{p1} = 510^\circ\text{C}$ and $\Delta H_1 \approx 121 \text{ J g}^{-1}$). In the case of Re substitution $T_{onset} = 560^\circ\text{C}$ indicates higher thermal stability in comparison to $(\text{Fe}_{0.7}\text{Co}_{0.3})_2\text{B}$. As mentioned above, two-phase transitions were detected in Re-doped alloy, where $T_{p1} = 574^\circ\text{C}$, $T_{p2} = 815^\circ\text{C}$, and $\Delta H_1 \approx 112 \text{ J g}^{-1}$, $\Delta H_2 \approx 3 \text{ J g}^{-1}$, respectively. In all the investigated alloys, the first crystallization peak occurs at higher temperatures than determined previously by Spassov and Diakovich for amorphous $\text{Fe}_{76}\text{Co}_{4}\text{B}_{20}$ alloy [42]. It can be associated with higher boron content as has been shown by Fukamichi et al. [43]. Authors have proposed that an increase of boron content in amorphous Fe-B alloys leads to enhancement of crystallization temperature. Differences in T_{onset} are governed by changing atomic packing, which in turn is related to the shortest interatomic distances. T_{onset} for $(\text{Fe}_{0.675}\text{Co}_{0.275}\text{W}_{0.05})_2\text{B}$ alloy is the lowest and coincides with the lowest calculated R value. Table 3.

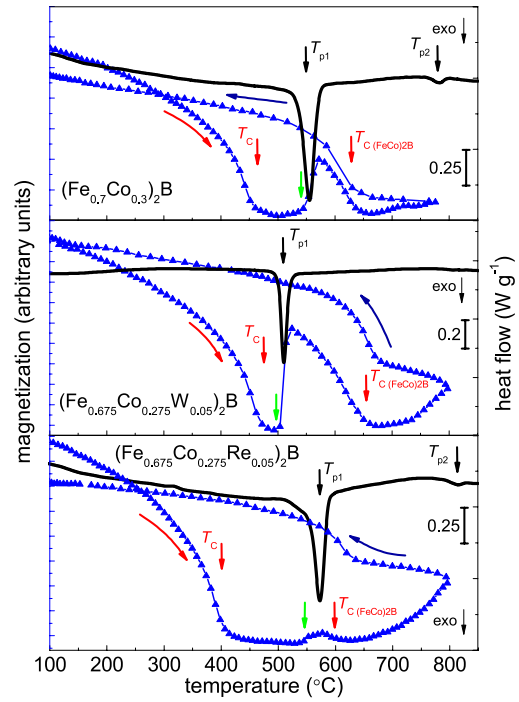


Fig. 7. Thermomagnetic curves (blue points) set with differential scanning calorimetry traces (black line) for $(\text{Fe}_{0.7}\text{Co}_{0.3})_2\text{B}$, $(\text{Fe}_{0.675}\text{Co}_{0.275}\text{W}_{0.05})_2\text{B}$, and $(\text{Fe}_{0.675}\text{Co}_{0.275}\text{Re}_{0.05})_2\text{B}$ alloys in the as-quenched state, measured at heating and cooling rates of 10 K min^{-1} . Thermomagnetic curves were collected in a magnetic field of 2.5 kOe .

Table 3

Thermal properties as maxima of phase transitions for the first and the second process (T_{p1} and T_{p2}), enthalpies of phase transition for the first and the second process ΔH_1 and ΔH_2 of $(\text{Fe}_{0.7}\text{Co}_{0.3})_2\text{B}$, $(\text{Fe}_{0.675}\text{Co}_{0.275}\text{W}_{0.05})_2\text{B}$, and $(\text{Fe}_{0.675}\text{Co}_{0.275}\text{Re}_{0.05})_2\text{B}$ alloys in as-quenched state.

alloy	T_{p1} [$^\circ\text{C}$]	T_{p2} [$^\circ\text{C}$]	ΔH_1 [J g^{-1}]	ΔH_2 [J g^{-1}]
$(\text{Fe}_{0.7}\text{Co}_{0.3})_2\text{B}$	551	780	109	4
$(\text{Fe}_{0.675}\text{Co}_{0.275}\text{W}_{0.05})_2\text{B}$	510	-	121	-
$(\text{Fe}_{0.675}\text{Co}_{0.275}\text{Re}_{0.05})_2\text{B}$	574	815	112	3

3.4. Magnetic properties

The magnetic properties of as-quenched and annealed samples were measured especially to determine the influence of $5d$ elements (to make a firm comparison with DFT results), especially for W-containing sample, which was synthesized in single phase tetragonal structure for the first time. Thermomagnetic measurements (performed in an external magnetic field of 2.5 kOe , with a heating and cooling rate of 10 K min^{-1}) play a key role, when compared with X-ray diffraction and calorimetric data. Thermomagnetic and differential scanning calorimetry curves for the amorphous alloys are shown in Fig. 7. Curie temperatures for $(\text{Fe}_{0.7}\text{Co}_{0.3})_2\text{B}$ and $(\text{Fe}_{0.675}\text{Co}_{0.275}\text{W}_{0.05})_2\text{B}$ are equal to 444 and 456°C , respectively. $(\text{Fe}_{0.675}\text{Co}_{0.275}\text{Re}_{0.05})_2\text{B}$ alloy has the lowest $T_C = 391^\circ\text{C}$, which may be related to higher boron content [43]. Above T_C , at about 550°C , the thermomagnetic curve rises as a result of crystallization of $(\text{Fe,Co})_2\text{B}$ phase for $(\text{Fe}_{0.7}\text{Co}_{0.3})_2\text{B}$ alloy. Similar behavior is observed in the $(\text{Fe}_{0.675}\text{Co}_{0.275}\text{W}_{0.05})_2\text{B}$ ribbon, where magnetization rises at about 500°C , but with a further decrease of magnetization to zero due to ferromagnetic-paramagnetic transition of $(\text{Fe,Co})_2\text{B}$

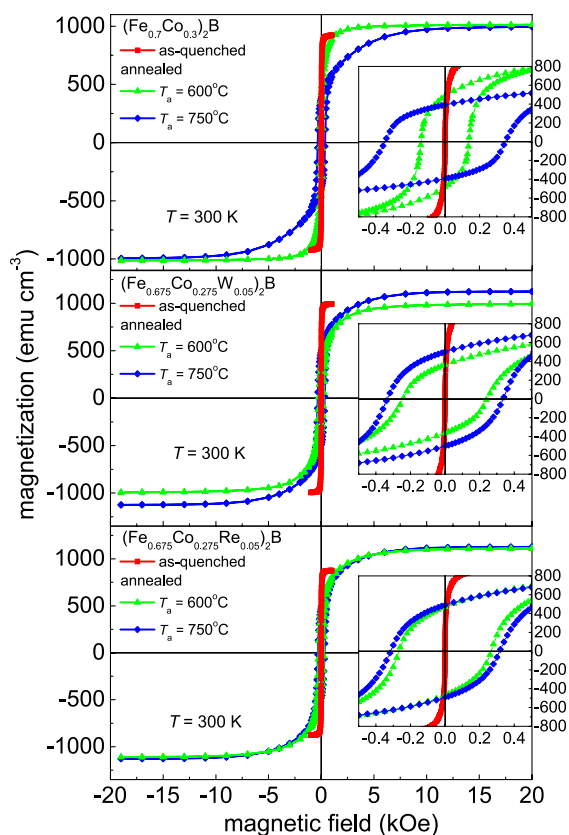


Fig. 8. Magnetic hysteresis loops measured at room temperature for $(\text{Fe}_{0.7}\text{Co}_{0.3})_2\text{B}$, $(\text{Fe}_{0.675}\text{Co}_{0.275}\text{W}_{0.05})_2\text{B}$, and $(\text{Fe}_{0.675}\text{Co}_{0.275}\text{Re}_{0.05})_2\text{B}$ alloys in as-quenched state and after annealing at T_a equal to 600 and 750°C for 60 min.

phase at 634°C. The determined T_C is lower than 662°C reported before for this compound [41]. As expected, magnetization increases at T_C during cooling. The crystallization temperature of $(\text{Fe}_{0.675}\text{Co}_{0.275}\text{Re}_{0.05})_2\text{B}$ is equal to about 550°C, which is close to Curie temperature for the $(\text{Fe},\text{Co})_2\text{B}$ phase. Thus, the crystallization process induces only a slight increase in magnetization.

Since the ribbons in the as-quenched state reached magnetization saturation (M_s) in a magnetic field of 0.5 kOe, the measurements for these alloys were performed up to the magnetic field of 20 kOe, see Fig. 8. M_s is equal to 922, 993, and 876 emu cm^{-3} for $(\text{Fe}_{0.7}\text{Co}_{0.3})_2\text{B}$, $(\text{Fe}_{0.675}\text{Co}_{0.275}\text{W}_{0.05})_2\text{B}$, and $(\text{Fe}_{0.675}\text{Co}_{0.275}\text{Re}_{0.05})_2\text{B}$, respectively. Magnetization saturation is reached at about 15 kOe for all three ribbons after annealing and is higher than for the as-quenched samples. For alloys with W and Re substitutions, magnetization saturation increases with isothermal annealing temperature and for $T_a = 750^\circ\text{C}$ is equal to 1124 and 1126 emu cm^{-3} for alloys with W and Re atoms, respectively. In the case of $(\text{Fe}_{0.7}\text{Co}_{0.3})_2\text{B}$ alloy, M_s after isothermal annealing at 750°C is equal to 995 emu cm^{-3} and is lower than for the sample annealed at 600°C ($M_s = 1012 \text{emu cm}^{-3}$). The value of magnetic moment is higher for the substituted samples than for the parent $(\text{Fe}_{0.7}\text{Co}_{0.3})_2\text{B}$ alloy, see Table 4, which contradicts our calculations in which we observed inverse relation.

This discrepancy can be connected with samples' microstructure, crystallinity, crystallite size, morphology. These factors are not taken into account in conducted calculations. According to this additional scanning electron microscopy (SEM) and energy-dispersive X-ray spectroscopy (EDX) measurements were made for the alloys

Table 4

Magnetic properties such as Curie temperature (T_C), saturation magnetization (M_s), coercive field (H_c), and magnetic moment per formula unit (m) of $(\text{Fe}_{0.7}\text{Co}_{0.3})_2\text{B}$, $(\text{Fe}_{0.675}\text{Co}_{0.275}\text{W}_{0.05})_2\text{B}$, and $(\text{Fe}_{0.675}\text{Co}_{0.275}\text{Re}_{0.05})_2\text{B}$ alloys in as-quenched state and after isothermal annealing at temperatures (T_a) equal to 600 and 750°C for 60 min.

alloy	T_a [°C]	T_C [°C]	M_s [emu cm^{-3}]	H_c [Oe]	m [μB f.u. ⁻¹]
$(\text{Fe}_{0.7}\text{Co}_{0.3})_2\text{B}$	as-quenched	458	922	10	
	600		1012	138	2.99
	750		995	348	2.94
$(\text{Fe}_{0.675}\text{Co}_{0.275}\text{W}_{0.05})_2\text{B}$	as-quenched	456	993	10	
	600		994	243	3.06
	750		1124	335	3.46
$(\text{Fe}_{0.675}\text{Co}_{0.275}\text{Re}_{0.05})_2\text{B}$	as-quenched	391	876	10	
	600		1111	267	3.39
	750		1126	315	3.44

Table 5

The average crystallite size (D) and lattice strain (ϵ) determined on the basis of Williamson-Hall method for $(\text{Fe}_{0.7}\text{Co}_{0.3})_2\text{B}$, $(\text{Fe}_{0.675}\text{Co}_{0.275}\text{W}_{0.05})_2\text{B}$, and $(\text{Fe}_{0.675}\text{Co}_{0.275}\text{Re}_{0.05})_2\text{B}$ alloys after isothermal annealing at annealing temperature T_a equal to 600 and 750°C for 60 min [46].

alloy	T_a [°C]	D [nm]	$\epsilon \times 10^{-3}$
$(\text{Fe}_{0.7}\text{Co}_{0.3})_2\text{B}$	600	30 ± 25	2.2 ± 2.0
	750	150 ± 61	1.1 ± 0.2
$(\text{Fe}_{0.675}\text{Co}_{0.275}\text{W}_{0.05})_2\text{B}$	600	32 ± 17	1.5 ± 1.4
	750	45 ± 29	1.3 ± 1.2
$(\text{Fe}_{0.675}\text{Co}_{0.275}\text{Re}_{0.05})_2\text{B}$	600	30 ± 25	3.6 ± 2.8
	750	24 ± 17	2.6 ± 2.2

annealed at 750°C (see Supplementary Fig. S1-S3). SEM micrographs and elemental maps show quite uniform microstructure and uniform distribution of elements in a microscale. Moreover, Williamson-Hall analysis was performed to determine changes in average crystallite size and lattice strain in annealed samples (see Table 5). Due to rather large uncertainties we are able to comment on some general trends. At first, the values of lattice strain are similar for analysed samples. Therefore, narrowing of X-ray diffraction peaks after annealing at 750°C can be ascribed to the increase of average crystallite size mostly. Even though the onset of crystallization of $(\text{Fe}_{0.7}\text{Co}_{0.3})_2\text{B}$ is higher than that determined for $(\text{Fe}_{0.675}\text{Co}_{0.275}\text{W}_{0.05})_2\text{B}$ and similar to the onset temperature of $(\text{Fe}_{0.675}\text{Co}_{0.275}\text{Re}_{0.05})_2\text{B}$, we observe significant increase of average crystallite size for the parent alloy. It suggests that the presence of Re and W restrains the growth of crystallites. Such effect and differences in crystallite size and morphology of annealed samples are surely responsible for observed discrepancies in magnetic properties. A low coercive fields (H_c), on the order of a few Oe, were obtained for as-quenched alloys, which is typical for amorphous materials. Isothermal annealing at 600°C leads to an increase of coercive field values up to 138, 243, and 267 Oe for $(\text{Fe}_{0.7}\text{Co}_{0.3})_2\text{B}$, $(\text{Fe}_{0.675}\text{Co}_{0.275}\text{W}_{0.05})_2\text{B}$, and $(\text{Fe}_{0.675}\text{Co}_{0.275}\text{Re}_{0.05})_2\text{B}$, respectively. H_c 's for substituted samples confirmed previous theoretical results obtained by Edström and coworkers [11]. Annealing at $T_a = 750^\circ\text{C}$ improves the coercive field to the range of 315–348 Oe. The values obtained are still below the threshold of permanent magnets applications, but one has to bear in mind that these values can be maximized by further processing e.g. by magnetic field annealing or combined high pressure torsion and heat treatment [45].

3.5. Mössbauer spectroscopy

3.5.1. Transmission Mössbauer spectroscopy

Transmission and rf-Mössbauer spectroscopy studies were performed to confirm conclusions drawn on the basis of structural and magnetic measurements and to determine microscopic mechanisms underlying the effect of 5d elements substitution. Mössbauer spectra

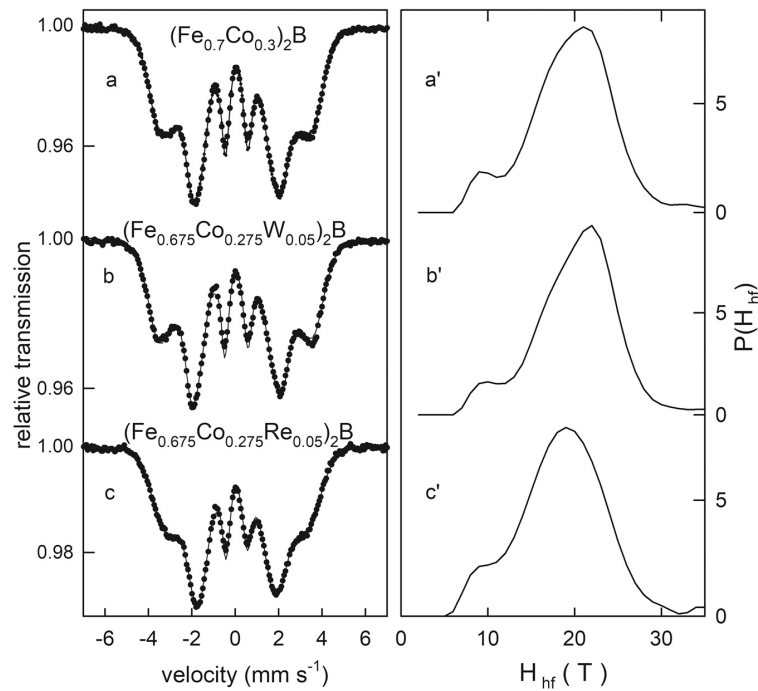


Fig. 9. Mössbauer spectra and hyperfine field (H_{hf}) distributions of (a) and (a') $(\text{Fe}_{0.7}\text{Co}_{0.3})_2\text{B}$, (b) and (b') $(\text{Fe}_{0.675}\text{Co}_{0.275}\text{W}_{0.05})_2\text{B}$, and (c), (c') $(\text{Fe}_{0.675}\text{Co}_{0.275}\text{Re}_{0.05})_2\text{B}$ alloys in as-quenched state.

shown in Fig. 9 confirmed the amorphous structure for all three alloys in the as-quenched state. The spectra reveal unresolved magnetic hyperfine structures due to the lack of long-range order. The diversity of atomic environments around Fe nuclei in the amorphous phase is clearly visible in the broad hyperfine field distributions extracted from the spectra, see Fig. 9. The dominating broad peak at about 20 T is accompanied by a small one at a reduced hyperfine field of about 9 T, related to minor Fe-depleted regions. The average magnetic hyperfine field determined for the as-quenched $(\text{Fe}_{0.7}\text{Co}_{0.3})_2\text{B}$ alloy is 20.1 T. For the alloy with W substitution this value is somewhat larger (20.6 T), while for the alloy with Re it is smaller and equals about 19 T. A similar trend is observed for saturation magnetization, see Table 4. The value of M_s was significantly higher for $(\text{Fe}_{0.675}\text{Co}_{0.275}\text{W}_{0.05})_2\text{B}$ as compared with the non-substituted and Re-substituted alloys.

Mössbauer spectra obtained for alloys annealed at 600°C and 750°C showed a complete crystallization of the amorphous phase. The spectra collected for the alloys after annealing at 600°C for 60 min are shown in Fig. 10. The Mössbauer spectrum for the $(\text{Fe}_{0.7}\text{Co}_{0.3})_2\text{B}$ alloy consists of two sextets, which is due to the Fe atoms occupying two magnetically inequivalent positions in the Fe_2B tetragonal structure. These sextets have slightly broadened lines due to incomplete crystalline order. The parameters of the hyperfine interactions related to these sextets are as follows: (1) hyperfine field $H_{hf1} = 23.7$ T, isomer shift $IS_1 = +0.12$ mm s⁻¹, the relative spectral fraction $A_1 = 38\%$ and (2) $H_{hf2} = 22.3$ T, $IS_2 = +0.11$ mm s⁻¹, $A_2 = 62\%$. Typical hyperfine parameters for the Fe_2B crystal phase are $H_{hf1} = 24.0$ T, $H_{hf2} = 23.2$ T, and the isomer shift of $+0.17$ mm s⁻¹ for both spectral components [47,48]. Thus, substitution of Co for Fe reduces the value of the hyperfine field in the alloy, which was also observed for the $(\text{Fe,Co})_2\text{B}$ phase formed in the $(\text{Fe,Co})\text{-Pt-B}$ alloys [49]. For the substituted alloys, three sextets were

fitted in the Mössbauer spectra, see Fig. 10. Parameters of the hyperfine interactions in all three alloys are presented in Table 6. For the first two sextets, the hyperfine parameters are similar to those for $(\text{Fe}_{0.7}\text{Co}_{0.3})_2\text{B}$. The appearance of a third sextet with a significantly reduced hyperfine field (20–21 T) appears to be the result of substitution of Re or W elements that form an additional defect position. The Mössbauer spectra obtained after annealing at 750°C, see Fig. 11, were fitted in the same way as the spectra for 600°C. The hyperfine parameters of all three sextets are generally similar to those determined after annealing at 600°C, see Table 6. However, the width of the sextet lines became narrower, indicating a well-crystallized structure after annealing at 750°C. The hyperfine parameters of $(\text{Fe}_{0.675}\text{Co}_{0.275}\text{W}_{0.05})_2\text{B}$ alloy annealed at 600°C are comparable to those determined for the sample annealed at 750°C. It is worth noting that such consistency was also observed for lattice parameter, see Table 2. This is the effect of the lowest crystallization temperature ($T_{p1} = 510^\circ\text{C}$) among all studied systems (Fig. 7). This indicates that the $(\text{Fe}_{0.675}\text{Co}_{0.275}\text{W}_{0.05})_2\text{B}$ alloy is in fully crystallized and ordered form at the lowest annealing temperature already. For the other two alloys, changes in the relative fractions of the sub-spectra are related to atomic ordering as the annealing temperature increases up to 750°C, see Table 6. Based on the analysis of the Mössbauer spectra of all samples annealed at 750°C, it appears that the additional substitution-related sextet (A_3) partially replaces both main spectral components (A_1 and A_2). A substantial difference is observed in the relative spectral contribution of this additional component, which is significantly larger for the Re-substituted alloy than for the W-substituted one.

3.5.2. rf-Mössbauer spectroscopy

The influence of chemical composition in the amorphous alloys was studied by the unconventional rf-Mössbauer technique

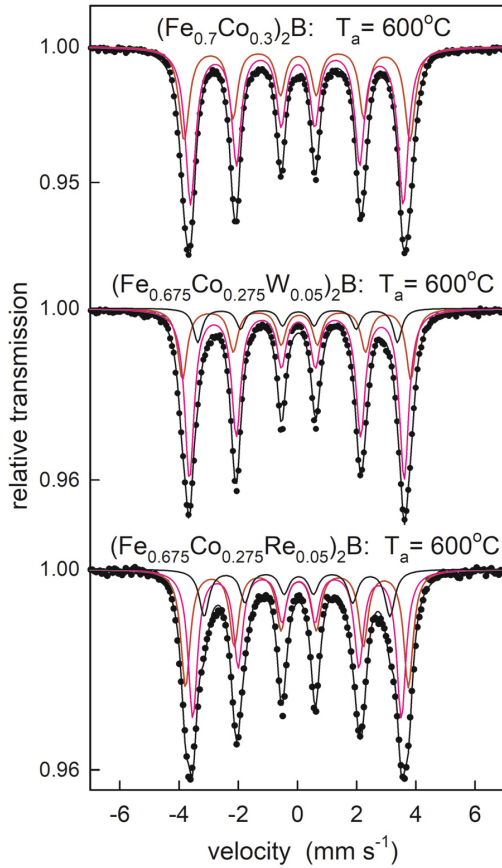


Fig. 10. Mössbauer spectra of $(\text{Fe}_{0.7}\text{Co}_{0.3})_2\text{B}$, $(\text{Fe}_{0.675}\text{Co}_{0.275}\text{W}_{0.05})_2\text{B}$, and $(\text{Fe}_{0.675}\text{Co}_{0.275}\text{Re}_{0.05})_2\text{B}$ alloys after annealing at $T_a = 600^\circ\text{C}$ for 60 min.

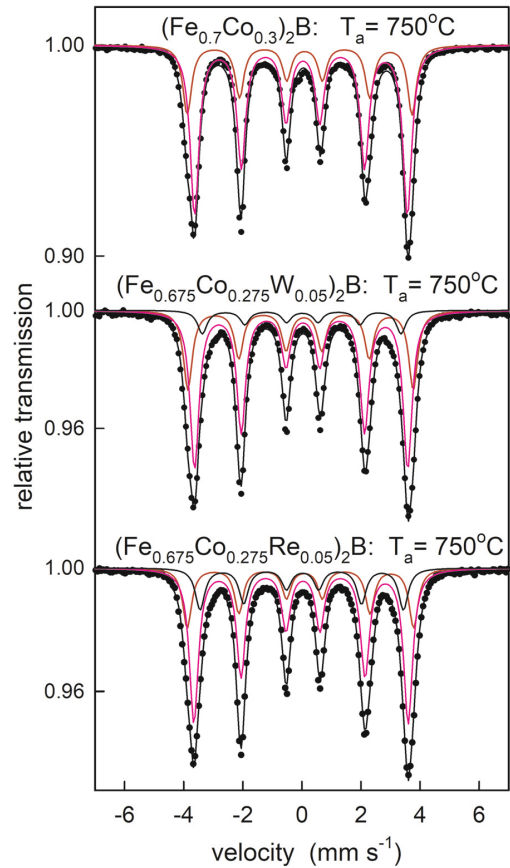


Fig. 11. Mössbauer spectra of $(\text{Fe}_{0.7}\text{Co}_{0.3})_2\text{B}$, $(\text{Fe}_{0.675}\text{Co}_{0.275}\text{W}_{0.05})_2\text{B}$, and $(\text{Fe}_{0.675}\text{Co}_{0.275}\text{Re}_{0.05})_2\text{B}$ alloys after annealing at $T_a = 750^\circ\text{C}$ for 60 min.

described in detail elsewhere [50]. As the most representative example, the Mössbauer spectra obtained for the $(\text{Fe}_{0.675}\text{Co}_{0.275}\text{Re}_{0.05})_2\text{B}$ alloy are shown in Fig. 12. The rf-Mössbauer spectra reveal that the amorphous alloy is magnetically soft with a low coercive field in the range of a few Oe as evidenced by significant narrowing of the magnetically split sextet, which is clearly seen

already at about 8 Oe, see Fig. 12(b). As the radio-frequency field intensity increases, a complete collapse of the magnetic hyperfine structure into a non-magnetic quadrupole doublet is observed, see Fig. 12(c)–12(e). The rf-collapse effect is due to the fast magnetization reversal, induced by the rf field, which leads to averaging of the hyperfine field to zero [50]. This means that the intensity of the

Table 6

The values of hyperfine field (H_{hf}), isomer shift (IS), quadrupole shift (QS), and relative spectral area of each sextet (A) for $(\text{Fe}_{0.7}\text{Co}_{0.3})_2\text{B}$, $(\text{Fe}_{0.675}\text{Co}_{0.275}\text{W}_{0.05})_2\text{B}$, and $(\text{Fe}_{0.675}\text{Co}_{0.275}\text{Re}_{0.05})_2\text{B}$ alloys after annealing at 600 and 750°C for 60 min.

	$(\text{Fe}_{0.7}\text{Co}_{0.3})_2\text{B}$		$(\text{Fe}_{0.675}\text{Co}_{0.275}\text{Re}_{0.05})_2\text{B}$		$(\text{Fe}_{0.675}\text{Co}_{0.275}\text{W}_{0.05})_2\text{B}$	
T_a [$^\circ\text{C}$]	600	750	600	750	600	750
H_{hf1} [T]	23.7	23.7	23.4	23.8	24.0	23.8
H_{hf2} [T]	22.3	22.4	21.9	22.5	22.6	22.5
H_{hf3} [T]	–	–	19.5	21.4	21.2	21.1
IS_1 [mm s^{-1}]	0.12	0.12	0.12	0.13	0.12	0.12
IS_2 [mm s^{-1}]	0.11	0.11	0.12	0.12	0.11	0.11
IS_3 [mm s^{-1}]	–	–	0.12	0.12	0.11	0.11
QS_1 [mm s^{-1}]	–0.04	–0.16	–0.06	–0.13	–0.10	–0.12
QS_2 [mm s^{-1}]	–0.04	–0.06	–0.05	–0.06	–0.05	–0.06
QS_3 [mm s^{-1}]	–	–	–0.06	–0.03	–0.03	–0.03
A_1 [%]	38	29	38	24	25	25
A_2 [%]	62	71	45	58	62	64
A_3 [%]	–	–	17	18	13	11

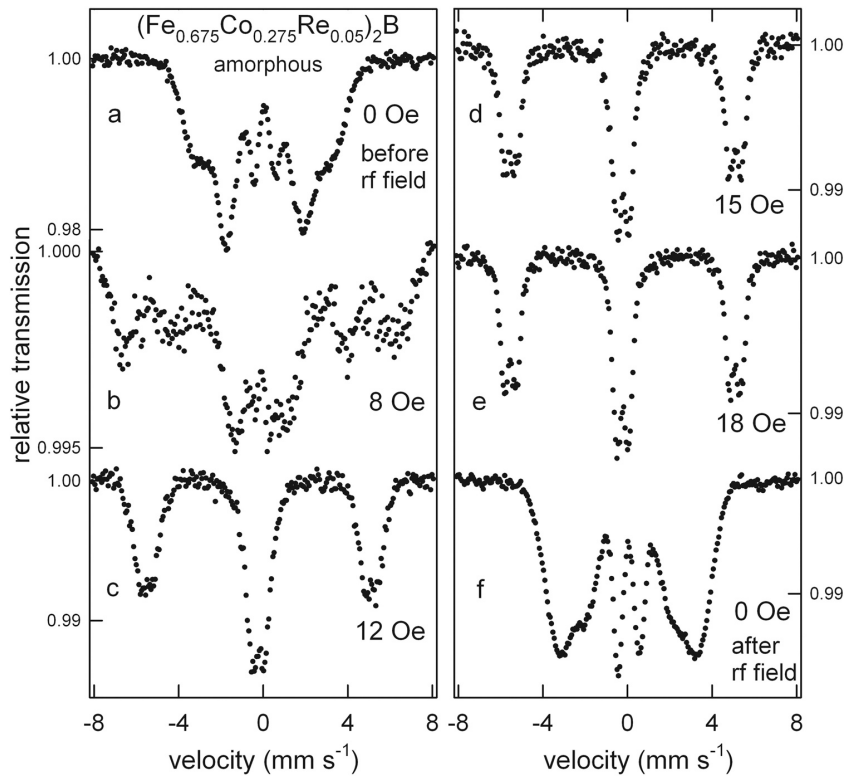


Fig. 12. rf-Mössbauer spectra of the amorphous $(\text{Fe}_{0.675}\text{Co}_{0.275}\text{Re}_{0.05})_2\text{B}$ alloy in various rf-fields.

applied rf-field is large enough to overcome the local magnetic anisotropy field. The rf field also has another effect whereby sidebands appear in the spectrum [50]. The rf sidebands visible at about $\pm 5 \text{ mm s}^{-1}$ reflect the shape of the collapsed spectrum, i.e. quadrupole doublets, see Fig. 12(c)-12(e). Their high intensity indicates that the alloy has large magnetostriction. The spectrum recorded after exposure to the rf field shows that the sample has retained an amorphous structure, see Fig. 12(a), 12(f). The average hyperfine field is 18.9 T, which is actually identical to that of the as-quenched alloy. The slightly different shape of the spectrum obtained after rf field exposure in comparison with the spectrum of the as-quenched sample is related to a significant reduction in the intensity of the second and fifth lines. This indicates a change from a preferential in-plane spin alignment for the as-quenched alloy to a more out-of-

plane arrangement after rf field exposure. The most probable reason for this feature is related to surface stresses induced by the formation of some crystallites on the surface of the ribbon (surface crystallization), while the bulk of the ribbon remains amorphous.

A similar dependence of the rf-Mössbauer spectra was recorded for the $(\text{Fe}_{0.7}\text{Co}_{0.3})_2\text{B}$ amorphous alloy, see Fig. 13. A narrowing of the magnetic hyperfine structure is observed at 10 Oe, while the complete rf-collapse effect occurs at the rf field intensity of 12 Oe, see Fig. 13(b)-13(d). The rf sidebands are significantly less intense than those observed for Re substitution, strongly suggesting smaller magnetostriction of the non-substituted alloy. In contrast to the $(\text{Fe}_{0.675}\text{Co}_{0.275}\text{Re}_{0.05})_2\text{B}$ ribbon, which remained fully amorphous after exposure to the rf field, the $(\text{Fe}_{0.7}\text{Co}_{0.3})_2\text{B}$ alloy starts to crystallize at the intensity of about 12 Oe. The Mössbauer spectrum

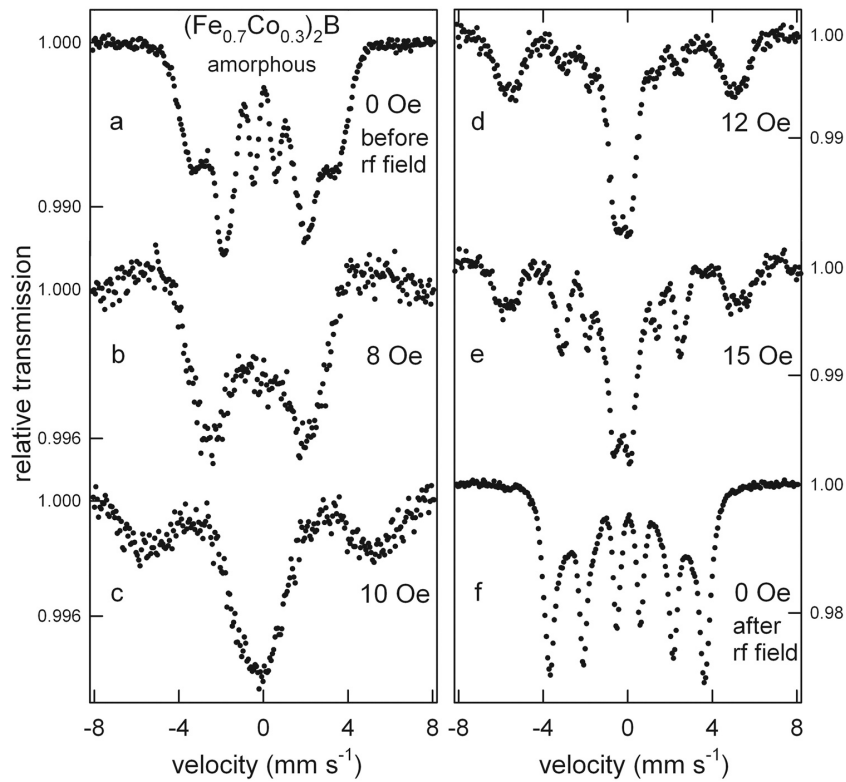


Fig. 13. rf-Mössbauer spectra of the amorphous $(\text{Fe}_{0.7}\text{Co}_{0.3})_2\text{B}$ alloy in various rf-fields.

recorded after exposure to the rf field is completely different from the spectrum of the as-quenched alloy, see Fig. 13(a) and 13(f), but similar to that of the annealed sample (Fig. 10). This indicates that the amorphous phase present in the as-quenched alloy was almost completely crystallized when the sample was exposed to the rf field of 15 Oe. For the $(\text{Fe}_{0.675}\text{Co}_{0.275}\text{W}_{0.05})_2\text{B}$ alloy, the narrowing of the magnetically split sextet is barely visible at 10 Oe and higher rf fields (Fig. 14). The small rf sidebands observed for this sample are evidence of non-zero magnetostriction. Furthermore, similarly to the case of the non-substituted alloy, the crystallization process starts at the rf field intensity of about 12 Oe, see Fig. 14(d), 14(e). The

spectrum obtained after rf field exposure, see Fig. 14(f), resembles the corresponding spectrum of the undoped alloy shown in Fig. 13(f). Such rf field-induced crystallization, which was observed in the case of $(\text{Fe}_{0.7}\text{Co}_{0.3})_2\text{B}$ and $(\text{Fe}_{0.675}\text{Co}_{0.275}\text{W}_{0.05})_2\text{B}$ amorphous alloys, has been previously reported for Co-containing amorphous alloys such as FeCoZrSi [51]. The origin of rf-crystallization is most probably related to mechanical deformations forced in the samples by the rf field via magnetoacoustic vibrations [51]. It seems that among the FeCoB alloys studied, the addition of Re plays a crucial role in the stabilization of the amorphous phase.

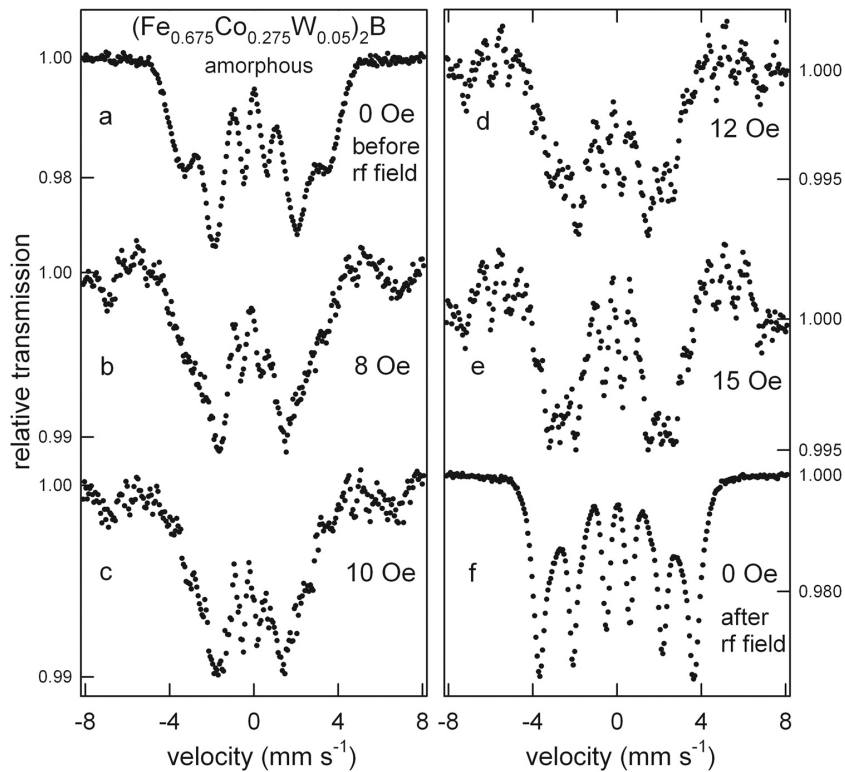


Fig. 14. rf-Mössbauer spectra of the amorphous $(\text{Fe}_{0.675}\text{Co}_{0.275}\text{W}_{0.05})_2\text{B}$ alloy in various rf-fields.

4. Conclusions

Density functional theory calculations and complementary experimental methods, as for example X-ray diffraction, magnetometry, and Mössbauer spectroscopy techniques were utilized to determine physical properties of $(\text{Fe,Co})_2\text{B}$ alloys with specific $5d$ substitutions. The main objective of the undertaken research was to evaluate their suitability as hard magnetic materials.

The first-principles calculation were applied to the systematic study of $(\text{Fe,Co})_2\text{B}$ alloys with $3d$, $4d$, and $5d$ substitutions. Their results show a twofold increase in magnetocrystalline anisotropy for $(\text{Fe}_{0.66}\text{Co}_{0.28}\text{Re}_{0.06})_2$, from 1.17 to 2.34 MJ m^{-3} . However, the determined values are significantly overestimated due to the use of the virtual crystal approximation. Calculations also show that no other dopants from the d -block introduce a significant improvement in magnetocrystalline anisotropy. In contrast to previous results, this means that no noticeable increase in magnetocrystalline anisotropy is predicted for the W-doped system. Calculations also indicate relatively good temperature stability of the magnetocrystalline anisotropy of Re-doped alloy in the relevant temperature range up to 700 K . When $(\text{Fe}_{0.7}\text{Co}_{0.3})_2\text{B}$ is doped with both Re or W, the total magnetization decreases by 12 – 14% .

$(\text{Fe}_{0.7}\text{Co}_{0.3})_2\text{B}$, $(\text{Fe}_{0.675}\text{Co}_{0.275}\text{Re}_{0.05})_2\text{B}$, and $(\text{Fe}_{0.675}\text{Co}_{0.275}\text{W}_{0.05})_2\text{B}$ precursors were synthesized by melt-spinning method. After annealing, all of the mentioned samples crystallized in a desired tetragonal $(\text{Fe,Co})_2\text{B}$ structure (CuAl_2 -type with space group $I4/mcm$). With increasing annealing temperature, we observed a decrease in a and an increase in c lattice parameter. Calorimetric measurements exhibit the presence of significant exothermic reaction in the range of 500 – 600°C for all the alloys considered. In addition, small

exothermic effects were also detected at around 800°C for $(\text{Fe}_{0.7}\text{Co}_{0.3})_2\text{B}$ and $(\text{Fe}_{0.675}\text{Co}_{0.275}\text{Re}_{0.05})_2\text{B}$. Changes in the onset temperature are correlated with atomic packing and the shortest interatomic distances. The more densely packed structure (with shorter interatomic distances), the higher the value of the onset temperature and the higher is the thermal stability of amorphous phase. Due to this fact, the onset temperature for the alloy $(\text{Fe}_{0.675}\text{Co}_{0.275}\text{W}_{0.05})_2\text{B}$ is the lowest and coincides with the lowest estimated value of the shortest interatomic distance. Thermomagnetic measurements confirmed the crystallization of the $(\text{Fe,Co})_2\text{B}$ phase as evidenced by a decrease in magnetization at about 600°C (T_c of the $(\text{Fe,Co})_2\text{B}$ alloy). The value of magnetic moment is higher for the substituted samples than for the parent $(\text{Fe}_{0.7}\text{Co}_{0.3})_2\text{B}$ alloy, see Table IV, which contradicts our calculations in which we observed the inverse relation. At first, calculations do not take into account any extrinsic parameters, as for example those connected with samples microstructure. Secondly, even though all the alloys were isothermally annealed at the same temperatures, such treatment leads to crystallization products which differ by a quality of the crystalline structure for each composition due to variations in crystallization temperatures. So one has to bear in mind that the influence of these factors on the value of magnetic moment/magnetization for particular alloy, can have a bigger impact than simply the intrinsic effect of the W or Re substitution. Moreover, coercivity increased to above 300 Oe in all of the considered samples after crystallization of $(\text{Fe,Co})_2\text{B}$ phase, which T_c is just slightly dependent on $5d$ substitution. More importantly, both Re and W improve saturation magnetization of heat treated samples in comparison to parent $(\text{Fe}_{0.7}\text{Co}_{0.3})_2\text{B}$ alloy.

Mössbauer spectroscopy measurements showed that the crystallization process of the amorphous alloys was completed after annealing at 750°C. In addition to the two non-equivalent iron sites in the tetragonal structure, an additional magnetic spectral component with a reduced hyperfine field was detected for both substituted alloys, indicating the presence of Re or W defect positions. The relative fraction of this substitution-related sextet was shown to be significantly higher for the $(\text{Fe}_{0.675}\text{Co}_{0.275}\text{Re}_{0.05})_2\text{B}$ alloy than for the $(\text{Fe}_{0.675}\text{Co}_{0.275}\text{W}_{0.05})_2\text{B}$ one. Radio frequency Mössbauer studies showed that Re atoms stabilized the amorphous phase, while the alloys $(\text{Fe}_{0.7}\text{Co}_{0.3})_2\text{B}$ and $(\text{Fe}_{0.675}\text{Co}_{0.275}\text{W}_{0.05})_2\text{B}$ began to crystallize when exposed to an rf field of about 12 Oe. The higher stability of the Re-substituted amorphous alloy observed in rf-Mössbauer studies is consistent with the results of our thermomagnetic and differential scanning calorimetry measurements. As a result of undertaken research novel compositions with high potential due to the high values of magnetization saturation and Curie temperature were characterized. In spite of high values of the magnetic anisotropy energy predicted theoretically, the coercivity is limited to about 300 Oe, being still the weakest characteristic of considered materials. Nevertheless, coercivity as an extrinsic parameter, still can be improved by e.g. microstructural optimization.

CRediT authorship contribution statement

Andrzej Musiał: Writing – original draft, Formal analysis, Investigation. **Wojciech Marciniak:** Formal analysis. **Zbigniew Śniadecki:** Conceptualization, Writing – review & editing, Supervision. **Mirosław Werwiński:** Formal analysis, Investigation, Writing – review & editing. **Piotr Kuświk:** Investigation. **Bogdan Idzikowski:** Writing – review & editing, Supervision. **Mieszko Kołodziej:** Formal analysis, Writing – review. **Agnieszka Grabias:** Investigation, Writing – review & editing. **Michał Kopcewicz:** Supervision. **Jozef Marcin:** Investigation. **Jozef Kováč:** Investigation.

Declaration of Competing Interest

The authors declare that they have no known competing financial interests or personal relationships that could have appeared to influence the work reported in this paper.

Acknowledgments

AM work was supported by the National Science Centre, Poland, within the project No. 2016/23/N/ST3/03820. MW and WM acknowledge the financial support of the National Science Centre Poland under the decision DEC-2018/30/E/ST3/00267. M. Kołodziej was financially supported by the project “Środowiskowe interdyscyplinarne studia doktoranckie w zakresie nanotechnologii” (“Environmental interdisciplinary doctoral studies in nanotechnology”) No. POWR.03.02.00–00–I032/16 under the European Social Fund - Operational Programme Knowledge Education Development, Axis III Higher Education for Economy and Development, Action 3.2 PhD Programme. Part of the computations was performed on the resources provided by the Poznań Supercomputing and Networking Center (PSNC). We thank Justyna Rychły and Justyn Snarski-Adamski for help with language editing and discussion.

Appendix A. Supporting information

Supplementary data associated with this article can be found in the online version at doi:10.1016/j.jallcom.2022.166047.

References

- [1] B. Das, R. Choudhary, R. Skomski, B. Balasubramanian, A.K. Pathak, D. Paudyal, D.J. Sellmyer, Anisotropy and orbital moment in Sm-Co permanent magnets, *Phys. Rev. B* 100 (2019) 024419.
- [2] Y. Toga, M. Nishino, S. Miyashita, T. Miyake, A. Sakuma, Anisotropy of exchange stiffness based on atomic-scale magnetic properties in the rare-earth permanent magnet $\text{Nd}_2\text{Fe}_{14}\text{B}$, *Phys. Rev. B* 98 (2018) 054418.
- [3] J. Cui, M. Kramer, L. Zhou, F. Liu, A. Gabay, G. Hadjipanayis, B. Balasubramanian, D. Sellmyer, Current progress and future challenges in rare-earth-free permanent magnets, *Acta Mater.* 158 (2018) 118.
- [4] K. Skokov, O. Gutflisch, Heavy rare earth free, free rare earth and rare earth free magnets - vision and reality, *Scr. Mater.* 154 (2018) 289.
- [5] J. Mohapatra, J.P. Liu, Chapter 1 - Rare-Earth-Free Permanent Magnets: The Past and Future, in: E. Brück (Ed.), *Handbook of Magnetic Materials*, 27 Elsevier, 2018, pp. 1–57.
- [6] M. Sakurai, J.R. Chelikowsky, Metastable B-doped FeNi compounds for permanent magnets without rare earths, *Phys. Rev. Mater.* 4 (2020) 084402.
- [7] X. Zhao, C.-Z. Wang, Y. Yao, K.-M. Ho, Large magnetic anisotropy predicted for rare-earth-free $\text{Fe}_{16-x}\text{Co}_x\text{N}_2$ alloys, *Phys. Rev. B* 94 (2016) 224424.
- [8] K. Patel, J. Zhang, S. Ren, Rare-earth-free high energy product manganese-based magnetic materials, *Nanoscale* 10 (2018) 11701.
- [9] Y. Jia, Y. Wu, S. Zhao, S. Zuo, K.P. Skokov, O. Gutflisch, C. Jiang, H. Xu, Li_0 rare-earth-free permanent magnets: the effects of twinning versus dislocations in mn -alloys, *Phys. Rev. Mater.* 4 (2020) 094402.
- [10] A. Vishina, O.Y. Vekilova, T. Björkman, A. Bergman, H.C. Herper, O. Eriksson, High-throughput and data-mining approach to predict new rare-earth free permanent magnets, *Phys. Rev. B* 101 (2020) 094407.
- [11] A. Edström, M. Werwiński, D. Iuşan, J. Ruz, O. Eriksson, K.P. Skokov, I.A. Radulov, S. Ener, M.D. Kuz'min, J. Hong, M. Fries, D.Y. Karpenkov, O. Gutflisch, P. Toson, J. Fidler, Magnetic properties of $(\text{Fe}_{1-x}\text{Co}_x)_2\text{B}$ alloys and the effect of doping by 5d elements, *Phys. Rev. B* 92 (2015) 174413.
- [12] K.D. Belashchenko, L. Ke, M. Däne, L.X. Benedict, T.N. Lamichhane, V. Taupour, A. Jesche, S.L. Bud'ko, P.C. Canfield, V.P. Antropov, Origin of the spin reorientation transitions in $(\text{Fe}_{1-x}\text{Co}_x)_2\text{B}$ alloys, *Appl. Phys. Lett.* 106 (2015) 062408.
- [13] W. Wallisch, J. Fidler, P. Toson, H. Sassik, R. Svagera, J. Bernardi, Synthesis and characterisation of $(\text{Fe,Co})_{2-x}\text{B}$ microcrystalline alloys, *J. Alloy. Compd.* 644 (2015) 199.
- [14] T.N. Lamichhane, O. Palasyuk, V.P. Antropov, I.A. Zhuravlev, K.D. Belashchenko, I.C. Nlebedim, K.W. Dennis, A. Jesche, M.J. Kramer, S.L. Bud'ko, R.W. McCallum, P.C. Canfield, V. Taupour, Reinvestigation of the intrinsic magnetic properties of $(\text{Fe}_{1-x}\text{Co}_x)_2\text{B}$ alloys and crystallization behavior of ribbons, *J. Magn. Magn. Mater.* 513 (2020) 167214.
- [15] M.D. Kuz'min, K.P. Skokov, H. Jian, I. Radulov, O. Gutflisch, Towards high-performance permanent magnets without rare earths, *J. Phys.:Condens. Matter* 26 (2014) 064205.
- [16] K.M. Kim, H.W. Kwon, J.G. Lee, J.H. Yu, Coercivity and phase evolution in mechanically milled $(\text{FeCo})_2\text{B}$ -type hard magnetic alloy, *IEEE Trans. Magn.* 54 (2018) 1.
- [17] I.A. Zhuravlev, V.P. Antropov, K.D. Belashchenko, Spin-fluctuation mechanism of anomalous temperature dependence of magnetocrystalline anisotropy in itinerant magnets, *Phys. Rev. Lett.* 115 (2015) 217201.
- [18] A. Gueddouh, Magnetic moment collapse induced by high-pressure in semiborides TM_2B (TM = Fe, Co). A first-principles study, *Chin. J. Phys.* 56 (2018) 944.
- [19] X. Wei, Z. Chen, J. Zhong, L. Wang, W. Yang, Y. Wang, Effect of alloying elements on mechanical, electronic and magnetic properties of Fe_2B by first-principles investigations, *Comput. Mater. Sci.* 147 (2018) 322.
- [20] M. Däne, S.K. Kim, M.P. Surh, D. Åberg, L.X. Benedict, Density functional theory calculations of magnetocrystalline anisotropy energies for $(\text{Fe}_{1-x}\text{Co}_x)_2\text{B}$, *J. Phys.:Condens. Matter* 27 (2015) 266002.
- [21] S. Pal, K. Skokov, T. Groeb, S. Ener, O. Gutflisch, Properties of magnetically semihard $(\text{Fe,Co}_{1-x})_2\text{B}$ compounds, *J. Alloy. Compd.* 696 (2017) 543.
- [22] S. Ener, M. Fries, F. Hammerath, I. Opahle, E. Simon, P. Fritsch, S. Wurmehl, H. Zhang, O. Gutflisch, Magnetic and magnetocaloric properties of the $\text{Co}_{2-x}\text{Mn}_x\text{B}$ system by experiment and density functional theory, *Acta Mater.* 165 (2019) 270.
- [23] M. Abramchuk, T. Mier, F. Tafti, Tuning the magnetic and structural properties of a three-metal boride alloy: $\text{Mn}_{0.95-x}\text{Fe}_{1.05-x}\text{Co}_x\text{B}$, *J. Alloy. Compd.* 805 (2019) 909.
- [24] A. Iga, Magnetocrystalline anisotropy in $(\text{Fe}_{1-x}\text{Co}_x)_2\text{B}$ system, *Jpn. J. Appl. Phys.* 9 (1970) 415.
- [25] M.C. Cadaville, I. Vincze, Nuclear magnetic resonance of ^{59}Co in $(\text{Fe}_{1-x}\text{Co}_x)_2\text{B}$ ferromagnetic borides, *J. Phys. F: Met. Phys.* 5 (1975) 790.
- [26] K. Koepf, H. Eschrig, Full-potential nonorthogonal local-orbital minimum-basis band-structure scheme, *Phys. Rev. B* 59 (1999) 1799.
- [27] J.P. Perdew, K. Burke, M. Ernzerhof, Generalized gradient approximation made simple, *Phys. Rev. Lett.* 77 (1996) 3865.
- [28] K. Schwarz, P. Mohn, Itinerant metamagnetism in YCo_2 , *J. Phys. F: Met. Phys.* 14 (1984) L129.
- [29] M. Werwiński, S. Kontos, K. Gunnarsson, P. Svedlindh, J. Cedervall, V. Höglin, M. Sahlberg, A. Edström, O. Eriksson, J. Ruz, Magnetic properties of Fe_2SiB_2 and its alloys with P, S, and Co, *Phys. Rev. B* 93 (2016) 174412.
- [30] K. Momma, F. Izumi, VESTA: A three-dimensional visualization system for electronic and structural analysis, *J. Appl. Crystallogr.* 41 (2008) 653.

- [31] R. Hasegawa, R. Ray, Magnetization of glassy Co-B alloys, *J. Appl. Phys.* 50 (1979) 1586.
- [32] R.A. Brand, J. Lauer, D.M. Herlach, The evaluation of hyperfine field distributions in overlapping and asymmetric Mossbauer spectra: A study of the amorphous alloy $\text{Pd}_{77.5-x}\text{Cu}_6\text{Si}_{16.5}\text{Fe}_x$, *J. Phys. F. Met. Phys.* 13 (1983) 675.
- [33] M. Werwiński, A. Edström, J. Ruzs, D. Hedlund, K. Gunnarsson, P. Svedlindh, J. Cedervall, M. Sahlberg, Magnetocrystalline anisotropy of Fe_3PB_2 and its alloys with Co and 5d elements: a combined first-principles and experimental study, *Phys. Rev. B* 98 (2018) 214431.
- [34] R. Wienke, G. Schütz, H. Ebert, Determination of local magnetic moments of 5d impurities in Fe detected via spin-dependent absorption, *J. Appl. Phys.* 69 (1991) 6147.
- [35] H. Akai, Nuclear spin-lattice relaxation of impurities in ferromagnetic iron, *Hyperfine Inter.* 43 (1988) 253.
- [36] P.H. Dederichs, R. Zeller, H. Akai, H. Ebert, Ab-initio calculations of the electronic structure of impurities and alloys of ferromagnetic transition metals, *J. Magn. Mater.* 100 (1991) 241.
- [37] V.A. Barinov, V.A. Tsurin, S.I. Novikov, I.R. Shein, V.T. Surikov, Short-range atomic order in Fe_2B powders, *Phys. Met. Met.* 103 (2007) 470.
- [38] I. Khan, J. Hong, Potential rare earth free permanent magnet: interstitial boron doped FeCo, *J. Phys. D. Appl. Phys.* 47 (2014) 415002.
- [39] M.E. Mcherry, M.A. Willard, D.E. Laughlin, Amorphous and nanocrystalline materials for applications as soft magnets, *Prog. Mater. Sci.* 44 (1999) 291.
- [40] P. Rogl, J. Schuster, H. Nowotny, Phase equilibrium and compound formation in Fe-M(metal)-B-X(nonmetal) systems, "Boron in Steel, Proc. Intern. Symp on Boron Steels TMS-AIME, The Metall. Soc. of AIME, Milwaukee, WI, USA, 1979, pp. 33-43.
- [41] H. Jian, K.P. Skokov, M.D. Kuz'min, I. Radulov, O. Gutfleisch, Magnetic properties of $(\text{Fe,Co})_2\text{B}$ alloys with easy-axis anisotropy, *IEEE Trans. Magn.* 50 (2014) 1.
- [42] T. Spassov, V. Diakovich, A modified Johnson-Mehl-Avrami kinetic model of overall crystallization of Fe-Co-B metallic glasses, *J. Alloy. Compd.* 198 (1993) 187.
- [43] K. Fukamichi, M. Kikuchi, S. Arakawa, T. Masumoto, Invar-type new ferromagnetic amorphous Fe-B alloys, *Solid State Commun.* 23 (1977) 955.
- [44] R.S. Sundar, S.C. Deevi, Soft magnetic FeCo alloys: alloy development, processing, and properties, *Int. Mater. Rev.* 50 (2005) 157.
- [45] A. Musiał, Z. Śniadecki, N. Pierunek, Y. Ivanisenko, D. Wang, M.H. Fawey, B. Idzikowski, Tuning of the magnetic properties of $\text{Hf}_2\text{Co}_{11}\text{B}$ alloys through a combined high pressure torsion and annealing treatment, *J. Alloy. Compd.* 787 (2019) 794.
- [46] G. Williamson, W. Hall, X-ray line broadening from filed aluminium and wolfram, *Acta Metall.* 1 (1953) 22.
- [47] K.A. Murphy, N. Hershkowitz, Temperature-dependent hyperfine interactions in Fe_2B , *Phys. Rev. B* 7 (1973) 23.
- [48] I.D. Weisman, L.J. Swartzendruber, L.H. Bennet, Resonance studies in ferromagnetic Fe_2B and Fe_2Zr , *Phys. Rev.* 177 (1969) 465.
- [49] A. Grabias, M. Kopcewicz, J. Latuch, D. Oleszak, M. Płkaka, M. Kowalczyk, Influence of cobalt content on the structure and hard magnetic properties of nanocomposite (Fe,Co)-Pt-B alloys, *J. Magn. Mater.* 434 (2017) 126.
- [50] M. Kopcewicz, Mössbauer effect studies of amorphous metals in magnetic radiofrequency fields, *Struct. Chem.* 2 (1991) 313.
- [51] M. Kopcewicz, A. Grabias, J. Latuch, Magnetic properties of $\text{Fe}_{80-x}\text{Co}_x\text{Zr}_7\text{Si}_{13}$ ($x=0-30$) amorphous alloys, *J. Appl. Phys.* 110 (2011) 103907.



Contents lists available at ScienceDirect

Journal of Magnetism and Magnetic Materials

journal homepage: www.elsevier.com/locate/jmmm

Research articles

DFT calculation of intrinsic properties of magnetically hard phase L1₀ FePtJoanna Marciniak^{a,b,*}, Wojciech Marciniak^{a,c}, Mirosław Werwiński^a^a Institute of Molecular Physics, Polish Academy of Sciences, M. Smoluchowskiego 17, 60-179 Poznań, Poland^b Institute of Materials Engineering, Poznan University of Technology, Piotrowo 3, 60-965 Poznań, Poland^c Institute of Physics, Poznan University of Technology, Piotrowo 3, 60-965 Poznań, Poland

ARTICLE INFO

Keywords:

Magnetostriction
Magnetic moments
Magnetocrystalline anisotropy
Density functional theory
L1₀ FePt
Fully relativistic methods

ABSTRACT

Due to its strong magnetocrystalline anisotropy, FePt L1₀ phase is considered as a promising magnetic recording media material. Although the magnetic properties of this phase have already been analyzed many times using density functional theory (DFT), we decided to study it again, emphasizing on full potential methods, including spin-polarized relativistic Korringa–Kohn–Rostoker (SPR-KKR) and full-potential local-orbital (FPLO) scheme. In addition to the determination of exact values of the magnetocrystalline anisotropy constants K_1 and K_2 , the magnetic moments, the Curie temperature, and the magnetostriction coefficient, we focused on the investigation of the magnetocrystalline anisotropy energy (MAE) dependence on the magnetic moment values using the fully relativistic fixed spin moment (FSM) method with various exchange–correlation potentials. We present nearly identical MAE(m) curves near the equilibrium point, along with different equilibrium values of MAE and magnetic moments. For a magnetic moment reduced by about 10%, we determined a theoretical MAE maximum in the ground state (0 K) equal to about 20.3 MJm⁻³ and independent of the choice of the exchange–correlation potential form. These calculations allow us to understand the discrepancies between the previous MAE results for different exchange–correlation potentials.

1. Introduction

In 2011, the interest in rare-earth-free hard magnetic materials increased significantly due to the dramatic rise in prices of rare earth elements known as the rare earth crisis [1]. Several articles summarize results of research on magnetic materials free of rare earths, among others, see Refs. [2,3]. One of the promising materials is the ordered L1₀ FePt alloy, for which measurements at 4.2 K revealed an unusually high value of magnetocrystalline anisotropy constant K_1 of 1.92 meV f.u.⁻¹ (11.0 MJ m⁻³) [4]. Another interesting property of the FePt L1₀ phase, concerning permanent-magnet applications, is the relatively high Curie temperature (T_C) of about 775 K estimated for the bulk material from experiments on nanoparticles [5]. In the literature, the crystallographic parameters of the tetragonal FePt L1₀ structure vary: $a = 3.85$ – 3.88 Å, $c = 3.74$ – 3.79 Å, and the ratio $c/a = 0.966$ – 0.981 [6–10]. Values of the total spin magnetic moments in the range 3.06– $3.24\mu_B$ per formula unit were obtained to date [9,11–13]. The magnetostriction coefficient λ_{001} varies between approximately 3.4×10^{-5} [14] and 6.4×10^{-5} [15] for disordered films of FePt alloys. For comparison, the highest value of magnetostriction coefficient, equal to 1.1 – 1.4×10^{-3} , was recorded for the Terfenol-D alloy [16].

Our aim in the following work is twofold. Firstly, we want to present a thorough benchmark study regarding the basic magnetic properties – magnetocrystalline anisotropy energy (MAE), magnetocrystalline

anisotropy constants K_1 and K_2 , magnetic moments [11,12], and Curie temperature [18] – of this interesting, already well studied phase. To obtain these parameters, we utilize two density functional theory (DFT) codes and a possibly broad spectrum of exchange–correlation functionals (described in Section 2). Secondly and more importantly, we try to broaden the understanding of the magnetic properties of the presented alloy by fixed spin moment analysis and magnetostriction coefficient calculations, though the comparative experimental results of the latter present in literature are sparse [14], especially for the bulk alloy [15].

2. Calculations' details

In this work, *ab initio* calculations were performed using FPLO18, FPLO5 (full-potential local-orbital) [19,20], and SPR-KKR 7.7.1 (spin-polarized relativistic Korringa–Kohn–Rostoker) codes [21,22].

The FPLO18 code was used for calculations necessary to determine spin and orbital magnetic moments, MAE, magnetocrystalline anisotropy constants K_1 and K_2 , and the magnetostriction coefficient. Dependence of MAE on the spin magnetic moment was performed using the fixed spin moment (FSM) method.

* Corresponding author at: Institute of Molecular Physics, Polish Academy of Sciences, M. Smoluchowskiego 17, 60-179 Poznań, Poland.
E-mail address: joanna.marciniak@ifmpan.poznan.pl (J. Marciniak).

<https://doi.org/10.1016/j.jmmm.2022.169347>

Received 11 July 2021; Received in revised form 10 March 2022; Accepted 28 March 2022

Available online 22 April 2022

0304-8853/© 2022 Elsevier B.V. All rights reserved.

J. Marciniak et al.

Journal of Magnetism and Magnetic Materials 556 (2022) 169347

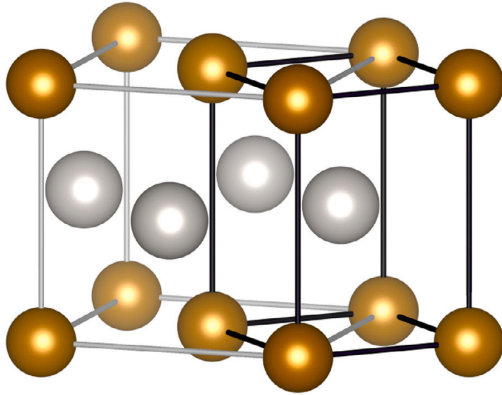


Fig. 1. Crystal structure of FePt L1₀ phase, in face-centered tetragonal (gray lines) and body-centered tetragonal (black lines) representations. The latter was used for calculations in this work. VESTA code was used for visualization [17].

The FPLO5 code was used as a base for the material's Curie temperature calculations, and the SPR-KKR code was used to obtain T_C , MAE and magnetocrystalline anisotropy constants for cross-reference. The main reason for the use of FPLO5 and SPR-KKR, compared to FPLO18, is that both codes have the chemical disorder implemented by means of the coherent potential approximation (CPA) [23], which allows utilizing the approach described further to obtain Curie temperature with relatively low computational effort.

The high precision of FPLO is due, among other factors, to the implementation of a full-potential approach that does not incorporate shape approximation into the crystalline potential and to the expansion of extended states in terms of localized atomic-like basis orbitals [20,24]. The use of full potential is particularly essential for the accurate determination of such a subtle quantity as MAE, and the MAE results obtained for FePt using this method are considered among the most accurate [12]. SPR-KKR 7.7.1 also has the ability for full potential calculation, which, oppositely to FPLO, does not lie in the basic principles of the code.

All calculations were performed after a proper optimization of the system geometry utilizing Perdew–Burke–Ernzerhof (PBE) exchange–correlation functional [25] in corresponding codes. The calculations were made for the body-centered representation of the FePt L1₀ structure, see Fig. 1, belonging to the $P4/mmm$ space group, with Fe atoms occupying the (0, 0, 0) position and Pt atoms occupying the (0.5, 0.5, 0.5) site. Lattice parameters of $a = 3.88/\sqrt{2}$ Å and $c = 3.73$ Å, derived from face-centered tetragonal (fct) structure of Alsaad et al. [9], were used as initial values for geometry optimization. Final lattice parameters used in further calculations are: $a = 2.74 \approx 3.87/\sqrt{2}$ Å, $c = 3.76$ Å and $a = 2.74 \approx 3.87/\sqrt{2}$ Å, $c = 3.74$ Å, optimized with FPLO and SPR-KKR codes, respectively, see Fig. 2.

Main calculations were performed using the Perdew–Burke–Ernzerhof (PBE) (FPLO18 and SPR-KKR), Vosko–Wilk–Nusair (VWN) (SPR-KKR) [26] and Perdew–Wang 92 (PW92) (FPLO18 and FPLO5) [27] exchange–correlation potentials. Additional results of Curie temperature and MAE dependence on the magnetic moment were obtained in FPLO5 and FPLO18, respectively. In both codes, we used additionally von Barth–Hedin (vBH) [28] and Perdew–Zunger (PZ) [29] potentials together with the exchange only approximation.

All calculations in FPLO18 were performed in the fully relativistic approach for a $56 \times 56 \times 42$ k-point mesh with energy convergence criterion at the level of 10^{-8} Ha and electron density convergence criterion of 10^{-6} , which yields an accurate value of the system's MAE within a reasonable computation time. Curie temperature calculations were

performed in the scalar-relativistic approach in CPA for a $12 \times 12 \times 12$ k-point mesh and the same energy and density convergence criteria.

The convergence criterion at the level of 10^{-6} and 5 000 k-points per reduced Brillouin zone, around 75 000 k-points in a full Brillouin zone, were used to perform fully relativistic calculations in SPR-KKR. All calculations were carried out in the full-potential (FP) approach with the angular momentum cutoff criterion set at the level of $l_{max} = 5$ (parameter NL = 6 in the SPR-KKR configuration file) unless otherwise stated. The atomic sphere approximation (ASA) calculations in SPR-KKR were performed for comparison, and all computational parameters were consistent between both approaches.

The Curie temperature of the system was determined based on the disordered local moment (DLM) theory [30] and assuming that the energy difference between the ferromagnetic state (ordered spin magnetic moments) and the paramagnetic state (disordered spin magnetic moments — modeled based on two types of CPA atomic sites with antiparallel magnetic moments) is proportional to the thermal energy needed for the ferromagnetic–paramagnetic transition. In order to determine the Curie temperature, we use the formula [31,32]:

$$k_B T_C = \frac{2}{3} \frac{E_{DLM} - E_{FM}}{n}, \quad (1)$$

where E_{DLM} is the total energy of the DLM configuration, E_{FM} is the total energy of the ferromagnetic configuration, n is the total number of magnetic atoms, and k_B is the Boltzmann constant.

MAE was determined by the formula:

$$MAE = E(\theta = 90^\circ) - E(\theta = 0^\circ), \quad (2)$$

where θ is the angle between the magnetization direction and the c axis. We determined the hard magnetic axis in the computational cell to be [1 1 0] ([1 0 0] in the standard face-centered representation). However, difference between energy values in the x - y plane is insignificant in our case and omitted in further study. In order to determine the magnetocrystalline anisotropy constants K_1 and K_2 , the dependence $MAE(\theta)$ was used, which for a tetragonal cell takes the approximated form:

$$MAE = K_1 \sin^2 \theta + K_2 \sin^4 \theta. \quad (3)$$

In order to calculate the magnetostriction coefficient λ_{001} , MAE and energy dependence on the lattice parameter c were fit with linear and quadratic functions, respectively [33,34], as presented in Fig. 5. The relation between energy and MAE versus magnetization angle θ can be presented as follows:

$$\begin{aligned} E(\theta = 0^\circ) &= ac^2 + \beta c + \gamma; \\ E(\theta = 90^\circ) &= ac^2 + \beta c + \gamma + MAE(c). \end{aligned} \quad (4)$$

Considering the lattice parameter elongation derivative of the MAE for the optimized lattice parameter ($c = 3.76$ Å), the magnetostriction coefficient λ_{001} takes the form:

$$\lambda_{001} = -\frac{2}{3} \frac{\frac{d(MAE)}{dc}}{\beta}. \quad (5)$$

3. Results and discussion

Before the actual calculations, the geometry of the crystal structure was optimized. The procedure consisted of a simple least-squares third-order function fit to the $E(V)$ dependency under a constant c/a ratio and then the same kind of fit to the energy dependence $E(c/a)$ at a constant volume corresponding to the minimum energy devised before. For the FPLO18 with PBE, the equilibrium volume of the fct cell V_{eq} is equal to 56.42 \AA^3 and the equilibrium c/a ratio is equal to 0.972, see Fig. 2. For the SPR-KKR code and PBE exchange–correlation functional, a value is lower by 0.5%, whereas c is smaller by 7.2% than that resultant from FPLO calculations. All results provide very good agreement with previous experimental and calculations data [6–10].

Table 1

Spin magnetic moments m_s , orbital magnetic moments m_l , and total magnetic moments m (in μ_B), as well as magnetocrystalline anisotropy energy MAE (in MJ m^{-3} , and meV f.u.^{-1}) and magnetocrystalline anisotropy constants K_1 and K_2 (in MJ m^{-3}) of the L1₀ FePt. The values of MAE, K_1 and K_2 in MJ m^{-3} from [11] were recalculated by authors. SPR-KKR angular momentum cutoff l_{max} was set to 5, unless otherwise stated.

	$m_{s,Fe}$	$m_{l,Fe}$	$m_{s,Pt}$	$m_{l,Pt}$	m	K_1	K_2	MAE (MJ m^{-3})	MAE (meV f.u.^{-1})
FPLO PBE	2.95	0.065	0.22	0.057	3.28	15.3	0.39	15.66	2.76
FPLO PW 92	2.85	0.067	0.24	0.057	3.21	–	–	17.01	2.99
FPLO PZ	2.81	0.067	0.24	0.057	3.17	–	–	17.71	3.12
FPLO vBH	2.81	0.067	0.24	0.057	3.17	–	–	17.69	3.12
FPLO Exchange only	3.07	0.066	0.22	0.056	3.41	–	–	13.03	2.29
SPR-KKR PBE ASA	3.07	0.072	0.33	0.046	3.51	16.4	0.77	17.14	2.99
SPR-KKR PBE FP	2.98	0.064	0.33	0.047	3.42	16.7	0.47	17.17	3.00
SPR-KKR VWN ASA	2.95	0.071	0.33	0.041	3.39	21.4	−0.13	21.29	3.72
SPR-KKR VWN FP	2.89	0.066	0.34	0.046	3.33	17.9	0.76	18.63	3.25
SPR-KKR VWN	2.91	0.073	0.32	0.043	3.35	17.6	0.29	17.98	3.14
ASA $l_{\text{max}} = 3$									
SPR-KKR VWN	2.83	0.065	0.34	0.044	3.28	17.5	0.54	17.96	3.01
ASA $l_{\text{max}} = 3$ [11]									
VASP PBE [12]	2.83	0.056	0.39	0.044	3.32	15.3	0.74	15.7	2.74

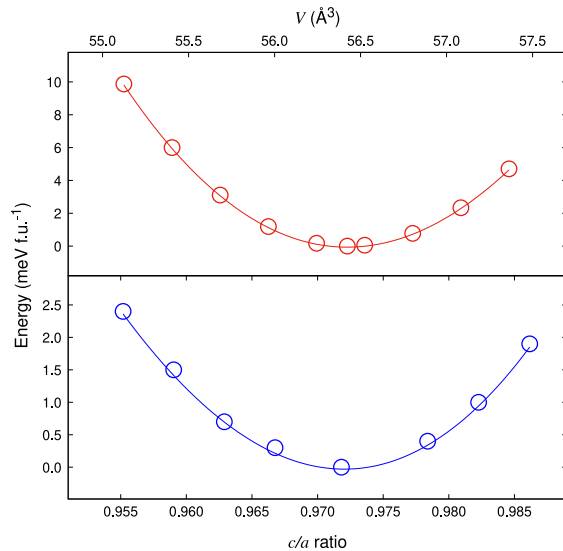


Fig. 2. Optimization of the FePt L1₀ phase geometry in FPLO18 code using the PBE potential. Energy minimum shifted to the lowest obtained energy. The top figure (red line) depicts the energy versus volume dependence for fixed c/a ratio equal to 0.972, and the bottom figure (blue line) presents the energy versus c/a ratio for constant volume equal to 56.42 \AA^3 (for fct cell). Obtained lattice parameters are $a = 3.87 \text{ \AA}$ and $c = 3.76 \text{ \AA}$, see the fct structure presented in Fig. 1.

For FPLO18-PBE, the spin magnetic moment $m_s = 2.95\mu_B$ and the orbital magnetic moment $m_l = 0.065\mu_B$ were observed on Fe atoms. On Pt atoms, these moments were $m_s = 0.22\mu_B$ and $m_l = 0.057\mu_B$. For values obtained using methods other than the FPLO18 code with PBE, see Table 1. The sum of magnetic moments in the cell varies between 3.17 and $3.512\mu_B$, a discrepancy of about 10% relative to either of the values. The calculated magnetic moments, presented also in the Table 1, are consistent with the values published previously [9,11–13].

As mentioned in Section 2, Curie temperatures were calculated with the DLM method using Eq. (1) for all exchange–correlation potentials implemented in FPLO5 and for VWN and PBE exchange–correlation potentials in SPR-KKR. Two approaches were used to simulate the paramagnetic phase. In the first one, we assume no Pt contribution to the total magnetic moment and introduce coexisting antiparallel

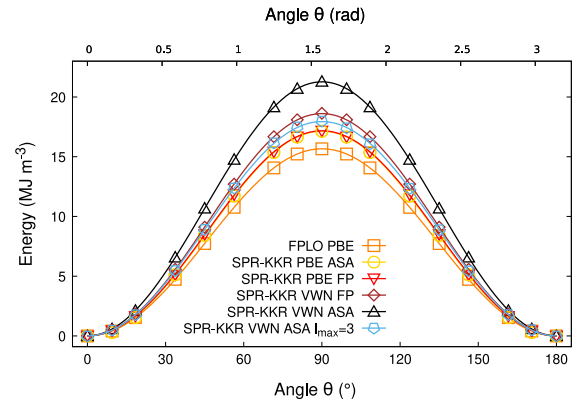


Fig. 3. Energy of the L1₀ FePt phase, as a function of the angle between magnetization direction and the c axis, calculated with various exchange–correlation potentials in FPLO18 and SPR-KKR 7.7.1. Exact values of magnetocrystalline anisotropy constants K_1 and K_2 are presented in Table 1. SPR-KKR angular momentum cutoff l_{max} was set to 5, unless stated otherwise.

spin orientations on the Fe atom only, i.e. $\text{Fe}_{0.51}\text{Fe}_{0.51}\text{Pt}$. In the second approach, we introduce coexisting antiparallel spin orientations on both Fe and Pt atoms, i.e. $\text{Fe}_{0.51}\text{Fe}_{0.51}\text{Pt}_{0.51}\text{Pt}_{0.51}$. T_C values obtained using both approaches are mostly identical, as in both cases, the Pt atoms are going to be in a non-magnetic state (magnetic moments equal to or near $0\mu_B$), as expected. All Pt moments are presented in Table 2.

Results of calculated Curie temperatures vary considerably for different exchange–correlation potentials, from about 430 K to 900 K. All of them are also presented in Table 2. Overall, the magnetic moments on Pt in the DLM stable states are minor, if any, and has a negligible physical impact on the T_C value. As shown in Table 2, in all considered cases the magnetic moment on Pt atom is below numerical accuracy. T_C 's obtained with the VWN potential are low, suggesting that this form of exchange–correlation potential in the local density approximation is not adequate to properly capture interatomic exchange interactions and thus T_C values. On the other hand, FPLO exchange only approach seems to be sufficient. We were unable to obtain a stable DLM state using SPR-KKR with PBE exchange–correlation potential, so T_C for this case was not included in Table 2. The results, except for the one obtained in SPR-KKR VWN, agree well with the estimation from experiment by Rong et al. (775 K) [18]. However, the DLM approach is known

J. Marciniak et al.

Journal of Magnetism and Magnetic Materials 556 (2022) 169347

Table 2
Curie temperatures and total magnetic moments on Pt atoms in L1₀ Fe_{0.51}Fe_{0.51}Pt_{0.51}Pt_{0.51} obtained using SPR-KKR and FPLO5 codes.

	T_C (K)	m_{Pt} (μ_B)
SPR-KKR VWN ASA	426	0
SPR-KKR VWN	595	0
FPLO5 Exchange only	878	$<10^{-6}$
FPLO5 PW92	796	$<10^{-6}$
FPLO5 PZ	754	$<10^{-6}$
FPLO5 vBH	756	0
experiment [18]	775	–

to overestimate values of T_C considerably [22,31], so slightly higher values could be expected.

The magnetocrystalline anisotropy constants K_1 and K_2 are summarized in Table 1, and the results obtained are also shown graphically in Fig. 3, along the fits of Eq. (3) for each data series. These data series were performed for the angle between the easy magnetization axis and defined magnetization direction in the $(0; \pi)$ range. Dependencies are symmetrical in relation to $\theta = \frac{\pi}{2}$, as expected. Eq. (3) was fitted to the whole angular range to improve the accuracy of the fit. Presented values do not differ significantly, except for the calculations with the SPR-KKR code using the VWN potential in ASA. This difference means that the calculations using this potential depend relatively strong on the applied approach — ASA or FP, as mentioned earlier. Out of other results, these from FPLO18 and FP PBE SPR-KKR are the lowest, indicating better agreement to experiment. The difference between FPLO and SPR-KKR can be ascribed to the implemented basis. Moreover, our convergence tests suggested that the minimal usable angular momentum expansion in the system is $l_{max} = 4$ (parameter NL = 5 in the SPR-KKR configuration file), and $l_{max} = 5$, used in our work, gave yet further noticeable improvement. Taking into account the above, we are convinced that LDA-ASA approach may be insufficient to capture the magnetism of L1₀ FePt properly, which is exemplified by our result for SPR-KKR VWN approach in a higher basis of $l_{max} = 5$.

All obtained magnetocrystalline anisotropy constants agree with earlier results of Khan et al. [$K_1 = 17.2 \text{ MJ m}^{-3}$ (3.01 meV f.u.⁻¹), $K_2 = 0.53 \text{ MJ m}^{-3}$ (0.09 meV f.u.⁻¹)] and Wolloch et al. [$K_1 = 15.3 \text{ MJ m}^{-3}$ (2.67 meV f.u.⁻¹), $K_2 = 0.74 \text{ MJ m}^{-3}$ (0.13 meV f.u.⁻¹)] [11,12]. However, the obtained magnetocrystalline anisotropy constants with K_1 values in range 15.3–21.4 MJ m⁻³ differ significantly from the values obtained experimentally ($K_1 = 11 \text{ MJ m}^{-3}$) [4]. Origin of the difference can be connected with imperfections of both, calculations and experiments. Weaknesses of calculations are the impossibility of accurately determination of the exchange–correlation potential and difficulty in the exact evaluation of spin–orbit interactions [35]. On the other hand, experiments were performed on nanoparticles or bulk samples with inhomogeneous microstructures that impact obtained properties [36]. Thin films are deposited on substrates, which can induce strain in the examined structure and introduce some differences in properties [35]. The most important fact is that the ground state is not measured in experiments [37], so these values cannot be directly compared. It was checked by Daalderop et al. [35] and Strange et al. [37] that all the approximations in the intrinsic properties calculations cannot account for the discrepancy.

The combination of the FSM method with fully relativistic calculations further allows testing the dependence of the MAE on the total magnetic moment, which allows for determining a hypothetical maximum MAE depending on the magnetic moment for a given material. The MAE values obtained with various exchange–correlation potentials

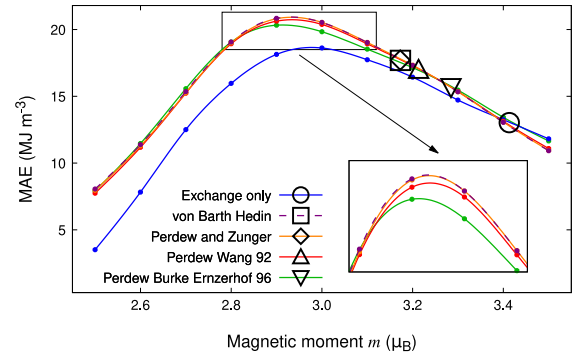


Fig. 4. Dependencies of the magnetocrystalline anisotropy energy on the fixed spin moment (lines) resultant from the calculations with different exchange–correlation potentials performed in FPLO18. Equilibrium magnetocrystalline anisotropy values versus equilibrium total magnetic moments are marked with empty symbols.

in FPLO18 code are 13.03–17.71 MJ m⁻³ and correlate with the total magnetic moment in the range 3.17–3.41 μ_B f.u.⁻¹.

Treating L1₀ FePt as a weak ferromagnet, MAE versus FSM dependency could be mapped to the MAE versus temperature dependency [4, 38], employing the Callen and Callen model [39]. Our analysis of the total Fe 3d and Pt 5d density of states at the majority spin channel pointed us towards a conclusion that treating L1₀ FePt as a weak ferromagnet can be, at least, ambiguous — and with the artificially decreased total moment situation gets even more complex. Mryasov et al. have earlier shown that a precise classification of FePt could be not so simple [40]. Moreover, standard DFT as a zero kelvin model, omits a range of other temperature-dependent phenomena. Concluding, the mentioned procedure applied to other magnetic materials [38] and experimental data regarding FePt [4] could not be reliably reproduced by the DFT method.

Fig. 4 presents nearly identical MAE(m) dependencies obtained near the equilibrium value with various exchange–correlation potentials, except for the exchange only approach. However, exact values of the equilibrium total magnetic moment differ between the employed potentials. This fact leads us to the conclusion, that observed wide distribution of the calculated MAE values for L1₀ FePt in [12] can be explained by the fact that different exchange–correlation potentials lead to different values of magnetic moment. On the other hand, there is a system property independent of the choice of exchange–correlation potential, indicated by all considered exchange–correlation potential (except exchange only approach), which is an MAE maximum of about 20.3 MJ m⁻³ observed for magnetic moment of about 2.9 μ_B . In all cases, the equilibrium MAE results obtained for the optimized structure lie to the right of the MAE maximum. Hence, the modifications leading to the reduction of the L1₀ FePt magnetization should increase the MAE to the hypothetical maximum value of 20.3 MJ m⁻³ at 0 K. A reduction in magnetization on the order of a few percent can be achieved, for example, by replacing a few percent of Fe with related elements exhibiting lower magnetic moment or completely non-magnetic, such as, for example, the 3d elements Ni, Ti or V. Alternatively, one can try to slightly increase the Pt content at the expense of Fe or doping FePt with elements such as C, B and N, which should locate in the interstitial gaps. It is worth noting that one would expect a monotonic increase in magnetic moments with decreasing temperature, leading to an MAE maximum at a few kelvins [4]. Taking this fact into account, for room temperature applications, the goal should be to increase the magnetic moment of L1₀ FePt, which should correspond to an increase of MAE.

The magnetostriction coefficient λ_{001} , determined from the Eq. (5), is 4.3×10^{-4} . Magnetostriction coefficient λ_S equals $3.4 \times 10^{-5} - 6.4 \times 10^{-5}$ for disordered FePt thin films [14,15]. Hence, the calculated value is an

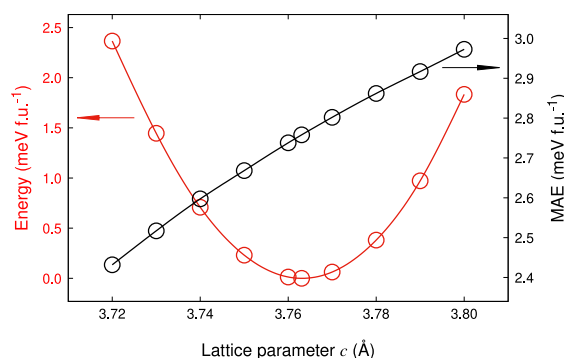


Fig. 5. Dependence of the calculated total energy and magnetocrystalline anisotropy energy on the lattice parameter of L1₀ FePt calculated with FPLO18 code.

order of magnitude greater than that determined from the experiments, which is an expected behavior, as the calculations conducted by us relate to a perfect infinite single crystal. Compared to Terfenol-D ($1.1\text{--}1.4 \times 10^{-3}$ [16]), the calculated magnetostriction coefficient of the FePt L1₀ structure is an order of magnitude lower.

4. Summary and conclusions

The magnetocrystalline anisotropy constants K_1 and K_2 , magnetic moments, and Curie temperatures were calculated for L1₀ FePt using full-potential methods and, where possible, compared with equivalent ASA calculations. The results are in good agreement with the literature values of other calculations, though reproduce well-known discrepancy between DFT calculations and experiments. We have shown that the MAE results calculated with different exchange–correlation potentials correlate with the magnetic moment values, which explains the observed dispersion of the values determined so far. The correlation of MAE(m) FSM results near the equilibrium state is exceptional. For the magnetic moment reduced by about 10%, we determined a theoretical maximum in MAE of 20.3 MJ m^{-3} , which is about 30% higher than the theoretical equilibrium ground state value. We also derived the Curie temperature of L1₀ FePt using multiple exchange–correlation functionals in the DLM approach and found it to be in decent agreement with the experimental value. The evaluated magnetostriction coefficient λ_{001} is in reasonable agreement with the measured values of disordered thin films of FePt alloy.

CRedit authorship contribution statement

Joanna Marciniak: Conceptualization, Formal analysis, Investigation, Writing – original draft, Visualization, Data curation. **Wojciech Marciniak:** Conceptualization, Validation, Investigation, Writing – review & editing, Software. **Mirosław Werwiński:** Conceptualization, Validation, Resources, Writing – review & editing, Supervision, Project administration, Funding acquisition.

Declaration of competing interest

The authors declare that they have no known competing financial interests or personal relationships that could have appeared to influence the work reported in this paper.

Acknowledgments

We acknowledge the financial support of the National Science Centre Poland under the decision DEC-2018/30/E/ST3/00267. The computations were in the main part performed on resources provided by the Poznan Supercomputing and Networking Center (PSNC). We thank Paweł Leśniak and Daniel Depcik for compiling the scientific software and administration of the computing cluster at the Institute of Molecular Physics, Polish Academy of Sciences. We thank Ján Rusz for valuable discussion and suggestions.

References

- [1] K. Bourzac, The rare-earth crisis, *Technol. Rev.* (114) (2011) 58–63.
- [2] M.D. Kuz'min, K.P. Skokov, H. Jian, I. Radulov, O. Gutfleisch, Towards high-performance permanent magnets without rare earths, *J. Phys. Condens. Matter* 26 (6) (2014) 064205, <http://dx.doi.org/10.1088/0953-8984/26/6/064205>.
- [3] R. Skomski, J.M.D. Coey, Magnetic anisotropy — How much is enough for a permanent magnet? *Scr. Mater.* 112 (2016) 3–8, <http://dx.doi.org/10.1016/j.scriptamat.2015.09.021>.
- [4] N. Hai, N. Dempsey, D. Givord, Magnetic properties of hard magnetic FePt prepared by cold deformation, *IEEE Trans. Magn.* 39 (5) (2003) 2914–2916, <http://dx.doi.org/10.1109/TMAG.2003.815762>.
- [5] C.-b. Rong, D. Li, V. Nandwana, N. Poudyal, Y. Ding, Z.L. Wang, H. Zeng, J.P. Liu, Size-dependent chemical and magnetic ordering in L1₀-FePt nanoparticles, *Adv. Mater.* 18 (22) (2006) 2984–2988, <http://dx.doi.org/10.1002/adma.200601904>.
- [6] P. Ravindran, A. Kjekshus, H. Fjellvåg, P. James, L. Nordström, B. Johansson, O. Eriksson, Large magnetocrystalline anisotropy in bilayer transition metal phases from first-principles full-potential calculations, *Phys. Rev. B* 63 (14) (2001) 144409, <http://dx.doi.org/10.1103/PhysRevB.63.144409>.
- [7] Z. Lu, R.V. Chepulskii, W.H. Butler, First-principles study of magnetic properties of L1₀-ordered MnPt and FePt alloys, *Phys. Rev. B* 81 (9) (2010) 094437, <http://dx.doi.org/10.1103/PhysRevB.81.094437>.
- [8] T.J. Klemmer, N. Shukla, C. Liu, X.W. Wu, E.B. Svedberg, O. Mryasov, R.W. Chantrell, D. Weller, M. Tanase, D.E. Laughlin, Structural studies of L1₀ FePt nanoparticles, *Appl. Phys. Lett.* 81 (12) (2002) 2220–2222, <http://dx.doi.org/10.1063/1.1507837>.
- [9] A. Alsaad, A.A. Ahmad, T.S. Obeidat, Structural, electronic and magnetic properties of the ordered binary FePt, MnPt, and CrPt₃ alloys, *Heliyon* 6 (3) (2020) e03545, <http://dx.doi.org/10.1016/j.heliyon.2020.e03545>.
- [10] H.B. Luo, W.X. Xia, A.V. Ruban, J. Du, J. Zhang, J.P. Liu, A. Yan, Effect of stoichiometry on the magnetocrystalline anisotropy of Fe–Pt and Co–Pt from first-principles calculation, *J. Phys. Condens. Matter* 26 (38) (2014) 386002, <http://dx.doi.org/10.1088/0953-8984/26/38/386002>.
- [11] S. Ayaz Khan, P. Blaha, H. Ebert, J. Minář, O. Šíp, Magnetocrystalline anisotropy of FePt: A detailed view, *Phys. Rev. B* 94 (14) (2016) 144436, <http://dx.doi.org/10.1103/PhysRevB.94.144436>.
- [12] M. Wolloch, D. Suess, P. Mohn, Influence of antisite defects and stacking faults on the magnetocrystalline anisotropy of FePt, *Phys. Rev. B* 96 (10) (2017) 104408, <http://dx.doi.org/10.1103/PhysRevB.96.104408>.
- [13] T. Burkert, O. Eriksson, S.I. Simak, A.V. Ruban, B. Sanyal, L. Nordström, J.M. Wills, Magnetic anisotropy of L1₀ FePt and Fe_{1-x}Mn_xPt, *Phys. Rev. B* 71 (13) (2005) 134411, <http://dx.doi.org/10.1103/PhysRevB.71.134411>.
- [14] F.E. Spada, F.T. Parker, C.L. Platt, J.K. Howard, X-Ray diffraction and Mössbauer studies of structural changes and L1₀ ordering kinetics during annealing of polycrystalline Fe₅₁Pt₄₉ thin films, *J. Appl. Phys.* 94 (8) (2003) 5123–5134, <http://dx.doi.org/10.1063/1.1606522>.
- [15] J. Aboaf, T. McGuire, S. Herd, E. Klokholm, Magnetic, transport, and structural properties of iron-platinum thin films, *IEEE Trans. Magn.* 20 (5) (1984) 1642–1644, <http://dx.doi.org/10.1109/TMAG.1984.1063266>.
- [16] L. Sandlund, M. Fahlander, T. Cedell, A.E. Clark, J.B. Restorff, M. Wun-Fogle, Magnetostriction, elastic moduli, and coupling factors of composite Terfenol-D, *J. Appl. Phys.* 75 (10) (1994) 5656–5658, <http://dx.doi.org/10.1063/1.355627>.
- [17] K. Momma, F. Izumi, VESTA : A three-dimensional visualization system for electronic and structural analysis, *J. Appl. Crystallogr.* 41 (3) (2008) 653–658, <http://dx.doi.org/10.1107/S0021889808012016>.
- [18] C.-B. Rong, Y. Li, J.P. Liu, Curie temperatures of annealed FePt nanoparticle systems, *J. Appl. Phys.* 101 (9) (2007) 09K505, <http://dx.doi.org/10.1063/1.2709739>.
- [19] H. Eschrig, M. Richter, I. Opahle, Chapter 12 - relativistic solid state calculations, in: P. Schwerdtfeger (Ed.), *Theoretical and Computational Chemistry, in: Relativistic Electronic Structure Theory*, vol. 14, Elsevier, 2004, pp. 723–776, [http://dx.doi.org/10.1016/S1380-7323\(04\)80039-6](http://dx.doi.org/10.1016/S1380-7323(04)80039-6).
- [20] K. Koepnik, H. Eschrig, Full-potential nonorthogonal local-orbital minimum-basis band-structure scheme, *Phys. Rev. B* 59 (3) (1999) 1743–1757, <http://dx.doi.org/10.1103/PhysRevB.59.1743>.

- [21] H. Ebert, B.L. Gyorffy, M. Bottoni, D. Banea, M. Kosuth, J. Minar, A. Perlov, V. Popescu, The Munich SPR-KKR Package, Version 7.7, 2017.
- [22] H. Ebert, D. Ködderitzsch, J. Minár, Calculating condensed matter properties using the KKR-Green singles function method—recent developments and applications, Rep. Progr. Phys. 74 (9) (2011) 096501, <http://dx.doi.org/10.1088/0034-4885/74/9/096501>.
- [23] P. Soven, Coherent-potential model of substitutional disordered alloys, Phys. Rev. 156 (3) (1967) 809–813, <http://dx.doi.org/10.1103/PhysRev.156.809>.
- [24] H. Eschrig, 2. The essentials of density functional theory and the full-potential local-orbital approach, in: W. Hergert, M. Däne, A. Ernst (Eds.), Computational Materials Science: from Basic Principles To Material Properties, in: Lecture Notes in Physics, Springer, Berlin, Heidelberg, 2004, pp. 7–21, http://dx.doi.org/10.1007/978-3-540-39915-5_2.
- [25] J.P. Perdew, K. Burke, M. Ernzerhof, Generalized gradient approximation made simple, Phys. Rev. Lett. 77 (18) (1996) 3865–3868, <http://dx.doi.org/10.1103/PhysRevLett.77.3865>.
- [26] S.H. Vosko, L. Wilk, M. Nusair, Accurate spin-dependent electron liquid correlation energies for local spin density calculations: A critical analysis, Can. J. Phys. 58 (8) (1980) 1200–1211, <http://dx.doi.org/10.1139/p80-159>.
- [27] J.P. Perdew, Y. Wang, Accurate and simple analytic representation of the electron-gas correlation energy, Phys. Rev. B 45 (23) (1992) 13244–13249, <http://dx.doi.org/10.1103/PhysRevB.45.13244>.
- [28] U. von Barth, L. Hedin, A local exchange-correlation potential for the spin polarized case. I, J. Phys. C Solid State Phys. 5 (13) (1972) 1629–1642, <http://dx.doi.org/10.1088/0022-3719/5/13/012>.
- [29] J.P. Perdew, A. Zunger, Self-interaction correction to density-functional approximations for many-electron systems, Phys. Rev. B 23 (10) (1981) 5048–5079, <http://dx.doi.org/10.1103/PhysRevB.23.5048>.
- [30] J. Staunton, B.L. Gyorffy, A.J. Pindor, G.M. Stocks, H. Winter, The “disordered local moment” picture of itinerant magnetism at finite temperatures, J. Magn. Mater. 45 (1) (1984) 15–22, [http://dx.doi.org/10.1016/0304-8853\(84\)90367-6](http://dx.doi.org/10.1016/0304-8853(84)90367-6).
- [31] B.L. Gyorffy, A.J. Pindor, J. Staunton, G.M. Stocks, H. Winter, A first-principles theory of ferromagnetic phase transitions in metals, J. Phys. F Met. Phys. 15 (6) (1985) 1337–1386, <http://dx.doi.org/10.1088/0305-4608/15/6/018>.
- [32] L. Bergqvist, P.H. Dederichs, A theoretical study of half-metallic antiferromagnetic diluted magnetic semiconductors, J. Phys. Condens. Matter 19 (21) (2007) 216220, <http://dx.doi.org/10.1088/0953-8984/19/21/216220>.
- [33] R. Wu, A.J. Freeman, Spin-orbit induced magnetic phenomena in bulk metals and their surfaces and interfaces, J. Magn. Mater. 200 (1) (1999) 498–514, [http://dx.doi.org/10.1016/S0304-8853\(99\)00351-0](http://dx.doi.org/10.1016/S0304-8853(99)00351-0).
- [34] M. Werwiński, W. Marciniak, Ab initio study of magnetocrystalline anisotropy, magnetostriction, and Fermi surface of $L1_0$ FeNi (tetraenaite), J. Phys. Appl. Phys. 50 (49) (2017) 495008, <http://dx.doi.org/10.1088/1361-6463/aa958a>.
- [35] G.H.O. Daalderop, P.J. Kelly, M.F.H. Schuurmans, First-principles calculation of the magnetocrystalline anisotropy energy of iron, cobalt, and nickel, Phys. Rev. B 41 (17) (1990) 11919–11937, <http://dx.doi.org/10.1103/PhysRevB.41.11919>.
- [36] L.-W. Liu, C.-C. Hu, Y.-C. Xu, H.-B. Huang, J.-W. Cao, L. Liang, W.-F. Rao, Magnetic properties of $L1_0$ FePt thin film influenced by recoverable strains stemmed from the polarization of $Pb(Mg_{1/3}Nb_{2/3})O_3$ - $PbTiO_3$ substrate, Chin. Phys. B 27 (7) (2018) 077503, <http://dx.doi.org/10.1088/1674-1056/27/7/077503>.
- [37] P. Strange, J.B. Staunton, B.L. Gyorffy, H. Ebert, First principles theory of magnetocrystalline anisotropy, Phys. B Condens. Matter 172 (1) (1991) 51–59, [http://dx.doi.org/10.1016/0921-4526\(91\)90416-C](http://dx.doi.org/10.1016/0921-4526(91)90416-C).
- [38] A. Edström, M. Werwiński, D. Iuşan, J. Ruzs, O. Eriksson, K.P. Skokov, I.A. Radulov, S. Ener, M.D. Kuz'min, J. Hong, M. Fries, D.Y. Karpinkov, O. Gutfließ, P. Toson, J. Fidler, Magnetic properties of $(Fe_{1-x}Co_x)_2B$ alloys and the effect of doping by 5d elements, Phys. Rev. B 92 (17) (2015) 174413, <http://dx.doi.org/10.1103/PhysRevB.92.174413>.
- [39] H.B. Callen, E. Callen, The present status of the temperature dependence of magnetocrystalline anisotropy, and the $(L+1)^2$ power law, J. Phys. Chem. Solids 27 (8) (1966) 1271–1285, [http://dx.doi.org/10.1016/0022-3697\(66\)90012-6](http://dx.doi.org/10.1016/0022-3697(66)90012-6).
- [40] O.N. Mryasov, U. Nowak, K.Y. Guslienko, R.W. Chantrell, Temperature-dependent magnetic properties of FePt: Effective spin Hamiltonian model, Europhys. Lett. 69 (5) (2005) 805, <http://dx.doi.org/10.1209/epl/i2004-10404-2>.

3 Summary and Conclusions

The work presents the influence of the chemical neighborhood of iron on the magnetic properties of iron-based alloys and compounds. Quantum mechanical calculations — mainly density functional theory — in various implementations are used to study spin and orbital magnetic moments, magnetocrystalline anisotropy energy, and magnetic phase transition temperatures for some of the investigated systems. Electronic structure analysis, based on the electronic density of states, is performed for selected materials. For some of the systems, total energy considerations are presented.

YbFe_4Al_8 is investigated as a system with an antiferromagnetic ordering of the iron magnetic moments. It is shown that only iron sublattices carry significant magnetic moments, and the most stable magnetic configuration is AFM-C with antiparallel chains of magnetic moments. Mulliken electronic population analysis shows that in this compound, ytterbium and iron atoms are donors, and aluminum atoms accept electrons. A more accurate description of the valence band and resolution of the magnetism of ytterbium ions requires approaches beyond the GGA used in the work. When using GGA, however, it is shown that the most accurate representation of ytterbium valence is achieved without the intra-atomic repulsion term U .

Reverting to simpler compounds and adding cobalt into the equation, a comprehensive study of MAE, magnetic moments, and T_C of Fe–Co alloys across a wide range of tetragonal deformations is presented. The research completes the understanding of the stability of the alloy by bridging the Bain and Burgers transformation pathways. Analysis reveals a previously uncharted high-MAE region, distinct from known structures and accessible through uniaxial compression. The new structure is located at a saddle point of the energy surface. Hence, it could be stabilized – e.g., by epitaxial growth on suitable square-lattice substrates combined with interstitial doping.

The previously known maximum in Fe–Co MAE is also studied — in particular, for the system doped interstitially with carbon. Full configuration space analysis of the interstitially doped $2 \times 2 \times 2$ (Fe/Co)₁₆ supercells of the 2-atom body-centered tetragonal representation was performed. Lattice parameters and equilibrium lattice parameters c/a ratio are derived, allowing for subsequent MAE, magnetic moments, and mixing enthalpies estimation. A comprehensive qualitative analysis of these properties' dependence on short- and long-range ordering parameters is delivered. The structural phase transition from the body-centered-tetragonal structure above 70% cobalt content is reproduced and the structural stability of Fe–Co–C alloys in the tetragonal range is confirmed. A broad MAE maximum at about 50% cobalt content is presented. Notably, several high-MAE and energetically preferable structures are found for as high iron content as 75% in Fe–Co–C alloy. In addition, there is a positive correlation between mixing enthalpy and MAE.

Fe–Co–B-based alloys with $3d$, $4d$, and $5d$ substitutions were also considered. Rhenium and tungsten dopants have previously been shown to substantially increase the alloy's MAE. In the calculations presented in this work, only rhenium dopant was shown to increase MAE by about a factor of two. The accompanying experiment, on the other hand, does not reach the predicted magnetic hardness. The VCA treatment of the chemical disorder of iron and cobalt may have overestimated the calculated MAE.

In the end, the cobalt addition is taken from the equation again, and the highly or-

dered L1₀ FePt is presented. The work revisits the computational consideration of this material. It emphasizes full-potential methods. The exact values of MAE, magnetocrystalline anisotropy constants K_1 and K_2 , magnetic moments, T_C , and the magnetostriction coefficient are presented. In addition, MAE dependence on the magnetic moment values is investigated using the fully relativistic fixed spin moment method with different exchange-correlation potentials. Nearly identical MAE(m) curves near the equilibrium point are obtained, showing that the discrepancies in MAE values found in the literature may stem primarily from the exact exchange-correlation potential formulation. Nevertheless, the curves exhibit a maximum for magnetic moment reduced by about 10%. This theoretical MAE maximum slightly exceeds 20 MJ m⁻³ and does not depend on the exchange-correlation potential form chosen. The calculated magnetostriction coefficient stays in reasonable agreement with the measurements of the property in disordered thin FePt films.

In summary, several iron-containing magnetic materials were studied. Most of them are ferromagnetic, though one system is antiferromagnetic, for which the exact magnetic structure was resolved. The work focuses on understanding the chemical neighborhood effect on the magnetism of iron with the far-reaching aim of developing new permanent magnets. Based on the acquired knowledge, several new structures, such as uniaxially compressed Fe–Co alloy or highly ordered Fe₁₂Co₄C, are proposed as candidates for rare-earth free hard magnetic materials. The effects of the addition of high-SOC atoms to both pure iron and Fe–Co-based alloys are also assessed. Hence, this study considers iron-based alloys comprehensively.

Popular science summary

This dissertation presents the results of research on the key magnetic properties of various iron-based materials. The aim was to analyze the influence of the crystal structure and composition of these materials on the change of magnetic moments, Curie temperature, and magnetocrystalline anisotropy energy (MAE). The research used computer simulations based on the principles of quantum mechanics.

A magnetic moment is a property resulting from the internal structure of the atom and is a fundamental microscopic property that affects the macroscopic maximum magnetization, i.e. the ability of a material to generate a constant magnetic field. Magnetic moments can be arranged in different ways, which affects the macroscopic behavior of a magnet. Materials in which magnetic moments are oriented parallel and in the same direction (ferromagnetic structure) generate an external magnetic field. Materials in which magnetic moments are oriented parallel and alternately in opposite directions (antiferromagnetic structure) do not generate an external magnetic field but have other interesting properties. This ordering is maintained only below a certain critical temperature — for a ferromagnet, it is the Curie temperature; for an antiferromagnet, the Néel temperature. MAE describes how difficult (or easy) it is to change the orientation of magnetic moments in space, i.e., to change the direction of the generated magnetic field.

Materials with both high (magnetically hard) and low (magnetically soft) MAE are useful from a technological point of view. They are the basis for sound processing technology (loudspeakers and microphones), information recording and processing (e.g., hard drives), or renewable energy (generators in wind turbines and hydroelectric power plants). Their presence is not always visible at first glance. For example, an average non-electric passenger car contains dozens of electric motors based on magnetic materials — in anti-lock braking systems (ABS), windscreen wipers, injection pumps, fans, and many other — both key mechanisms and amenities.

In this thesis, ferro- and antiferromagnetic materials were investigated. An example of the latter group is YbFe_4Al_8 . This system contains a rare-earth element — ytterbium (Yb). Heavy elements of this kind, with a complicated electronic structure, pose a problem in their correct representation in computer simulations. The article regarding this compound presents the influence of calculation parameters and the used approximations on the representation accuracy of electrons participating in the formation of chemical bonds (valence electrons). The most probable antiferromagnetic structure for this system was also resolved — antiparallel columns of magnetic moments, the projection of which from above looks like a chessboard.

Moving on to ferromagnetic materials, the first to be considered was a disordered alloy of iron and cobalt (Fe–Co). It is important as a potential permanent magnet that does not contain rare earth elements — in contrast to, e.g., popular neodymium magnets ($\text{Nd}_2\text{Fe}_{14}\text{B}$). The rare earth market, due to geopolitical events, is considered unstable after the *rare earth crisis* of 2011. A new high-MAE structure is presented for the Fe–Co alloy. It can be obtained by compressing in one direction (uniaxially) the body-centered cubic structure (the smallest crystal cell resembles a cube with atoms in each corner and one centrally located). Analysis of the energy during further deformations of the discovered structure showed that, although it is not stable, it may be easier to stabilize than the previously known uniaxially stretched structure.

The uniaxially stretched structure, in its carbon-stabilized form, was also investigated. The study involved a system of $2 \times 2 \times 2$ body-centered cubic cells repeating infinitely in every direction (periodic boundary conditions). For all 65 536 possible site occupancies in this system, the energy of a given configuration, MAE, and the values of magnetic moments on each atom were determined. The energy analysis revealed highly ordered structures with high MAE for cobalt contents as low as 25%, which is a significant improvement over currently known materials. The price of such a material largely depends on the price of cobalt. A positive correlation between high MAE and favorable configuration energy was also shown. The results are also consistent with a transition to a different crystal structure for cobalt contents above 70%.

Based on Fe–Co alloys doped with lighter atoms, using $(\text{Fe–Co})_2\text{B}$ (containing boron) as an example, the influence of heavier elements from groups $3d$, $4d$ and $5d$ of the periodic table on magnetic properties was investigated. In contrast to the previous results in the literature, suggesting a magnetic properties improvement for doping with rhenium (Re) and tungsten (W), an increase in MAE (nearly twofold) was demonstrated only for doping with rhenium. However, the experiment accompanying the calculations did not show a significant increase in MAE for either tungsten or rhenium.

The last material studied in the dissertation was the L1_0 FePt system, which consists of alternating one-atom-thick layers of pure iron and pure platinum. This material is interesting due to its very high MAE value, which makes it particularly suitable for use in high-density magnetic memories. It has been studied before, and the article included in this dissertation is another approach to this topic, focusing on using more accurate methods and examining the influence of calculation parameters on the values of magnetic properties obtained so far. The work shows that the differences in the previously obtained MAEs may result from the differences in the determined magnetic moments, resulting from the description of intraatomic interactions used. The analysis of the dependence of MAE on the value of the magnetic moment indicates a theoretical maximum of an extremely high value of 20 MJ m^{-3} for a magnetic moment lower than the equilibrium one. This result is important because such lower values of the magnetic moment occur at room temperature.

In summary, various magnetic materials, whose common component is iron, have been studied using computer simulations. The work focuses on analyzing the influence of the chemical neighborhood of iron atoms on the magnetic properties of materials. The long-term motivation is the search for better permanent magnets that do not contain rare earth elements or have the lowest possible content of them. Based on the knowledge gained during the work, new potential permanent magnets were proposed — such as compressed Fe–Co and highly ordered $\text{Fe}_{12}\text{Co}_4\text{C}$. The influence of doping iron-based magnetic materials with other, heavier elements from the $3d$, $4d$, and $5d$ groups was also investigated. This work presents iron-based magnetic materials in a way that is, although certainly not complete, exhaustive in the face of current computer simulation capabilities.

Streszczenie popularnonaukowe

W niniejszej rozprawie przedstawione zostały wyniki badań nad kluczowymi właściwościami magnetycznymi różnych materiałów na bazie żelaza. Celem była analiza wpływu struktury krystalicznej i składu tych materiałów na zmianę momentów magnetycznych, temperatury Curie i energii anizotropii magnetokrystalicznej (MAE). W badaniach wykorzystano symulacje komputerowe oparte o zasady mechaniki kwantowej.

Moment magnetyczny jest właściwością wynikającą z wewnętrznej struktury atomu i jest podstawową wielkością mikroskopową wpływającą na makroskopową maksymalną magnetyzację, czyli zdolność materiału do wytwarzania stałego pola magnetycznego. Momenty magnetyczne mogą być uporządkowane w różny sposób, co wpływa na makroskopowe zachowanie magnesu. Materiały, w których momenty magnetyczne są zorientowane równoległe i w tym samym kierunku (struktura ferromagnetyczna) wytwarzają zewnętrzne pole magnetyczne. Materiały, w których momenty magnetyczne są zorientowane równoległe i naprzemiennie w przeciwnych kierunkach (struktura antyferromagnetyczna) nie wytwarzają zewnętrznego pola magnetycznego, ale mają inne ciekawe właściwości. Uporządkowanie utrzymuje się jedynie poniżej pewnej krytycznej temperatury — dla ferromagnetyku jest to temperatura Curie, dla antyferromagnetyku — temperatura Néela. MAE opisuje, na ile trudno (lub łatwo) jest zmienić orientację momentów magnetycznych w przestrzeni, czyli zmienić kierunek wytwarzanego pola magnetycznego.

Zarówno materiały o wysokiej (magnetycznie twarde) jak i niskiej (magnetycznie miękkie) MAE są użyteczne z technologicznego punktu widzenia. Są one podstawą technologii przetwarzania dźwięku (głośniki i mikrofony), zapisu i przetwarzania informacji (np. dyski twarde), czy energii odnawialnej (prądnice w turbinach wiatrowych i elektrowniach wodnych). Ich obecność nie zawsze jest widoczna na pierwszy rzut oka. Dla przykładu przeciętny, spalinowy samochód osobowy zawiera w sobie dziesiątki silników elektrycznych opartych o materiały magnetyczne — obsługujących przeciwblokujące systemy hamulcowe (ABS), wycieraczki szyb, pompy wtryskowe, wentylatory i wiele innych — zarówno kluczowych mechanizmów, jak i udogodnień.

W pracy zostały zbadane materiały ferro- i antyferromagnetyczne. Przykładem tej drugiej grupy jest YbFe_4Al_8 . W tym układzie znajduje się atom z grupy pierwiastków ziem rzadkich — iterb (Yb). Ciężkie pierwiastki tego typu, o skomplikowanej strukturze elektronowej, stanowią problem w prawidłowym ich odwzorowaniu w symulacjach komputerowych. W artykule o tym związku przedstawiony został wpływ parametrów obliczeń i stosowanych przybliżeń na odwzorowanie elektronów biorących udział w tworzeniu wiązań chemicznych (elektronów walencyjnych). Pokazana została też najbardziej prawdopodobna struktura antyferromagnetyczna dla tego układu — antyrównoległe kolumny momentów magnetycznych, których rzut od góry wygląda jak szachownica.

Przechodząc do materiałów ferromagnetycznych, jako pierwszy rozważony został nieuporządkowany stop żelaza i kobaltu (Fe-Co). Jest on istotny jako potencjalny magnes trwały, który nie zawiera pierwiastków ziem rzadkich — w przeciwieństwie np. do popularnych magnesów neodymowych ($\text{Nd}_2\text{Fe}_{14}\text{B}$). Rynek pierwiastków ziem rzadkich, ze względu na wydarzenia geopolityczne, uznawany jest za niestabilny po tzw. kryzysie ziem rzadkich z 2011 roku. Dla stopu Fe-Co znaleziona została nowa struktura o wysokiej MAE, możliwa do uzyskania poprzez ściśnięcie w jednym kierunku (jednoosiowe) struktury kubicznej przestrzennie centrowanej (najmniejsza komórka kryształu przypomina sześcienną

kostkę z atomami w każdym z rogów oraz jednym umieszczonym centralnie). Analiza energii przy dalszych odkształceniach odkrytej struktury pokazała, że, o ile nie jest ona stabilna, to z dużym prawdopodobieństwem może być prostsza do ustabilizowania niż dotychczas znana, rozciągnięta w jednym kierunku, struktura o wysokiej MAE.

Jednoosiowo rozciągnięta struktura również została zbadana, w jej odmianie stabilizowanej domieszką węgla. Badaniom poddano układ $2 \times 2 \times 2$ przestrzennie centrowanych komórek kubicznych powtarzających się w nieskończoność w każdym kierunku (periodyczne warunki brzegowe). Dla wszystkich 65 536 możliwych obsadzeń miejsc w tym układzie wyznaczona została energia danej konfiguracji, MAE i wartości momentów magnetycznych na każdym z atomów. Analiza energii pozwoliła na wskazanie wysoko uporządkowanych struktur o wysokiej MAE dla zawartości kobaltu tak niskiej jak 25%, co jest znaczącą poprawą względem obecnie znanych materiałów. Cena takiego materiału w znacznej większości zależy od ceny kobaltu. Pokazana została również pozytywna korelacja pomiędzy wysoką MAE, a korzystną energią konfiguracji. Wyniki są ponadto zgodne z przejściem do innej struktury krystalicznej dla zawartości kobaltu powyżej 70%.

Bazując na stopach Fe–Co z domieszkami lżejszych atomów, na przykładzie $(\text{Fe–Co})_2\text{B}$ (zawierającego bor), zbadany został wpływ zawartości cięższych pierwiastków z grup 3d, 4d i 5d układu okresowego na właściwości magnetyczne. W przeciwieństwie do dotychczasowych wyników obecnych w literaturze, sugerujących poprawę właściwości magnetycznych dla domieszkowania renem (Re) i wolframem (W), wykazano wzrost MAE (blisko dwukrotny) jedynie dla domieszkowania renem. Towarzyszący obliczeniom eksperyment nie wykazał jednak znaczącego wzrostu MAE ani dla wolframu, ani dla renu.

Ostatnim materiałem zbadanym w ramach rozprawy był układ $L1_0$ FePt, który składa się z ułożonych naprzemiennie warstw czystego żelaza i czystej platyny. Materiał ten jest interesujący ze względu na bardzo wysoką wartość MAE, doskonałą do zastosowania w pamięciach magnetycznych o dużej gęstości danych. Był on już wcześniej badany, a artykuł wchodzący w skład tej rozprawy stanowi kolejne podejście do tego tematu, skupiające się na wykorzystaniu dokładniejszych metod i zbadaniu wpływu parametrów obliczeniowych na uzyskane dotychczas wartości właściwości magnetycznych. Praca pokazuje, że różnice uzyskiwanych wcześniej MAE mogą wynikać z różnic wyznaczonych momentów magnetycznych, które to z kolei wynikały z zastosowanego opisu oddziaływań wewnątrzatomowych. Analiza zależności MAE od wartości momentu magnetycznego wskazuje teoretyczne maksimum o ekstremalnie wysokiej wartości 20 MJ m^{-3} dla momentu magnetycznego mniejszego niż równowagowy. Wynik ten jest o tyle istotny, że właśnie takie, niższe wartości momentu magnetycznego występują w temperaturze pokojowej.

Podsumowując, z pomocą symulacji komputerowych zbadane zostały różne materiały magnetyczne, których wspólnym składnikiem jest żelazo. Praca skupia się na analizie wpływu chemicznego sąsiedztwa atomów żelaza na właściwości magnetyczne materiałów. Długoterminową motywacją jest poszukiwanie lepszych magnesów trwałych niezawierających pierwiastków ziem rzadkich lub o jak najmniejszej ich zawartości. Bazując na wiedzy zdobytej w trakcie realizacji pracy zaproponowane zostały nowe potencjalne magnesy trwałe — takie jak ściśnięte Fe–Co oraz silnie uporządkowany stop $\text{Fe}_{12}\text{Co}_4\text{C}$. Zbadany został również wpływ na domieszkowanie materiałów magnetycznych na bazie żelaza innymi, cięższymi pierwiastkami z grup 3d, 4d i 5d. Niniejsza praca przedstawia więc materiały magnetyczne na bazie żelaza w sposób, chociaż z pewnością nie kompletny, to wyczerpujący w obliczu obecnych możliwości symulacji komputerowych.

Other articles by the Author are listed separately. Those are referred to throughout this Guide by the respective capital Latin letters [A–D]:

Other works of the Author

- ^AM. Werwiński and W. Marciniak, “Ab initio study of magnetocrystalline anisotropy, magnetostriction, and Fermi surface of $L1_0$ FeNi (tetrataenite)”, [Journal of Physics D: Applied Physics](#) **50**, 495008 (2017).
- ^BJ. Rychły-Gruszecka, J. Marciniak, J. Snarski-Adamski, J. Meixner, W. Marciniak, J. Ruzs, and M. Werwiński, “Structural and Magnetic Properties of Ultrathin Films Calculated from First-Principles”, in [2024 IEEE International Magnetic Conference - Short papers \(INTERMAG Short papers\)](#) (May 2024), pp. 1–2.
- ^CB. Wasilewski, W. Marciniak, and M. Werwiński, “Curie temperature study of $Y(Fe_{1-x}Co_x)_2$ and $Zr(Fe_{1-x}Co_x)_2$ systems using mean field theory and Monte Carlo method”, [Journal of Physics D: Applied Physics](#) **51**, 175001 (2018).
- ^DW. Marciniak, J. Marciniak, J. Á. Castellanos-Reyes, and J. Ruzs, “Mode-Dependent Phonon Relaxation in fcc Ni: Insights from Molecular Dynamics Simulations with Frozen-Trajectory Excitations”, [arXiv preprint, 10.48550/arXiv:2409.20334](#) (2024).

Bibliography

- ¹R. Skomski, “Permanent Magnets: History, Current Research, and Outlook”, in *Novel Functional Magnetic Materials: Fundamentals and Applications*, edited by A. Zhukov (Springer International Publishing, Cham, 2016), pp. 359–395.
- ²J. M. D. Coey, “Permanent magnet applications”, *J. Magn. Magn. Mater.* **248**, 441–456 (2002).
- ³J. M. D. Coey, “Perspective and Prospects for Rare Earth Permanent Magnets”, *Engineering* **6**, 119–131 (2020).
- ⁴K. Barmak, J. Kim, L. H. Lewis, K. R. Coffey, M. F. Toney, A. J. Kellock, and J.-U. Thiele, “On the relationship of magnetocrystalline anisotropy and stoichiometry in epitaxial L₁₀ CoPt (001) and FePt (001) thin films”, *J. Appl. Phys.* **98**, 033904 (2005).
- ⁵M. Tang, K. Shen, S. Xu, H. Yang, S. Hu, W. Lü, C. Li, M. Li, Z. Yuan, S. J. Pennycook, K. Xia, A. Manchon, S. Zhou, and X. Qiu, “Bulk Spin Torque-Driven Perpendicular Magnetization Switching in L₁₀ FePt Single Layer”, *Adv. Mater.* **32**, 2002607 (2020).
- ⁶J. M. D. Coey, “New permanent magnets; manganese compounds”, *J. Phys.: Condens. Matter* **26**, 064211 (2014).
- ⁷R. Skomski and J. M. D. Coey, “Magnetic anisotropy — How much is enough for a permanent magnet?”, *Scr. Mater.* **112**, 3–8 (2016).
- ⁸K. J. Gschneidner, *Rare Earth Crisis—Supply/Demand Situation 2010–2015*.
- ⁹X. Yang, J. Dong, Q. Zheng, B. Bian, and J. Du, “Crystallographic disorder-order transition of self-assembly FeCo mesocrystals independent of ligand”, *J. Alloys Compd.* **976**, 173155 (2024).
- ¹⁰D. R. Hartree, “The Wave Mechanics of an Atom with a Non-Coulomb Central Field. Part II. Some Results and Discussion”, *Math. Proc. Camb. Philos. Soc.* **24**, 111–132 (1928).
- ¹¹V. Fock, “Näherungsmethode zur Lösung des quantenmechanischen Mehrkörperproblems”, *Z. Physik* **61**, 126–148 (1930).
- ¹²J. C. Slater, “The Self Consistent Field and the Structure of Atoms”, *Phys. Rev.* **32**, 339–348 (1928).
- ¹³P.-O. Löwdin, “Quantum Theory of Many-Particle Systems. III. Extension of the Hartree-Fock Scheme to Include Degenerate Systems and Correlation Effects”, *Phys. Rev.* **97**, 1509–1520 (1955).
- ¹⁴P. Hohenberg and W. Kohn, “Inhomogeneous Electron Gas”, *Phys. Rev.* **136**, B864–B871 (1964).
- ¹⁵W. Kohn and L. J. Sham, “Self-Consistent Equations Including Exchange and Correlation Effects”, *Phys. Rev.* **140**, A1133–A1138 (1965).
- ¹⁶J. P. Perdew, K. Burke, and M. Ernzerhof, “Generalized Gradient Approximation Made Simple”, *Phys. Rev. Lett.* **77**, 3865–3868 (1996).
- ¹⁷C. Adamo and V. Barone, “Toward reliable density functional methods without adjustable parameters: The PBE0 model”, *J. Chem. Phys.* **110**, 6158–6170 (1999).

- ¹⁸J. P. Perdew, A. Ruzsinszky, G. I. Csonka, O. A. Vydrov, G. E. Scuseria, L. A. Constantin, X. Zhou, and K. Burke, “Restoring the Density-Gradient Expansion for Exchange in Solids and Surfaces”, *Phys. Rev. Lett.* **100**, 136406 (2008).
- ¹⁹K. H. J. Buschow and F. R. De Boer, *Physics of Magnetism and Magnetic Materials* (Springer US, Boston, MA, 2003).
- ²⁰A. I. Liechtenstein, M. I. Katsnelson, V. P. Antropov, and V. A. Gubanov, “Local spin density functional approach to the theory of exchange interactions in ferromagnetic metals and alloys”, *J. Magn. Magn. Mat.* **67**, 65–74 (1987).
- ²¹G. H. O. Daalderop, P. J. Kelly, and M. F. H. Schuurmans, “First-principles calculation of the magnetic anisotropy energy of $(\text{Co})_n/(\text{X})_m$ ”, *Phys. Rev. B* **42**, 7270–7273 (1990).
- ²²O. Eriksson, A. Bergman, L. Bergqvist, and J. Hellsvik, *Atomistic Spin Dynamics: Foundations and Applications* (Oxford University Press, Feb. 2017).
- ²³D. P. Landau and K. Binder, *A Guide to Monte Carlo Simulations in Statistical Physics*, 3rd ed. (Cambridge University Press, Cambridge, 2009).
- ²⁴*Tutorial — UppASD Manual documentation.*
- ²⁵B. L. Gyorffy, A. J. Pindor, J. Staunton, G. M. Stocks, and H. Winter, “A first-principles theory of ferromagnetic phase transitions in metals”, *J. Phys. F: Met. Phys.* **15**, 1337 (1985).
- ²⁶L. Bergqvist and P. H. Dederichs, “A theoretical study of half-metallic antiferromagnetic diluted magnetic semiconductors”, *J. Phys.: Condens. Matter* **19**, 216220 (2007).
- ²⁷V. L. Moruzzi, P. M. Marcus, K. Schwarz, and P. Mohn, “Ferromagnetic phases of bcc and fcc Fe, Co, and Ni”, *Phys. Rev. B* **34**, 1784–1791 (1986).
- ²⁸O. Gunnarsson and B. I. Lundqvist, “Exchange and correlation in atoms, molecules, and solids by the spin-density-functional formalism”, *Phys. Rev. B* **13**, 4274–4298 (1976).
- ²⁹D. C. Langreth and M. J. Mehl, “Beyond the local-density approximation in calculations of ground-state electronic properties”, *Phys. Rev. B* **28**, 1809–1834 (1983).
- ³⁰W. Pauli, “Zur Quantenmechanik des magnetischen Elektrons”, *Z. Physik* **43**, 601–623 (1927).
- ³¹P. A. M. Dirac, “The quantum theory of the electron”, *Proc. R. Soc. (London) A.* **117**, 610–624 (1928).
- ³²H. Ebert, D. Ködderitzsch, and J. Minár, “Calculating condensed matter properties using the KKR-Green’s function method—recent developments and applications”, *Rep. Prog. Phys.* **74**, 096501 (2011).
- ³³J. Koringa, “On the calculation of the energy of a Bloch wave in a metal”, *Physica* **13**, 392–400 (1947).
- ³⁴W. Kohn and N. Rostoker, “Solution of the Schrödinger Equation in Periodic Lattices with an Application to Metallic Lithium”, *Phys. Rev.* **94**, 1111–1120 (1954).
- ³⁵O. K. Andersen, “Linear methods in band theory”, *Phys. Rev. B* **12**, 3060–3083 (1975).
- ³⁶H. L. Skriver, *The LMTO Method: Muffin-Tin Orbitals and Electronic Structure* (Springer Science & Business Media, Dec. 2012).

- ³⁷P. Schwerdtfeger, “The Pseudopotential Approximation in Electronic Structure Theory”, *ChemPhysChem* **12**, 3143–3155 (2011).
- ³⁸J. M. Soler, E. Artacho, J. D. Gale, A. García, J. Junquera, P. Ordejón, and D. Sánchez-Portal, “The SIESTA method for ab initio order-N materials simulation”, *J. Phys.: Condens. Matter* **14**, 2745 (2002).
- ³⁹C.-K. Skylaris, P. D. Haynes, A. A. Mostofi, and M. C. Payne, “Introducing ONETEP: Linear-scaling density functional simulations on parallel computers”, *J. Chem. Phys.* **122**, 084119 (2005).
- ⁴⁰O. K. Andersen and O. Jepsen, “Explicit, First-Principles Tight-Binding Theory”, *Phys. Rev. Lett.* **53**, 2571–2574 (1984).
- ⁴¹O. K. Andersen, Z. Pawłowska, and O. Jepsen, “Illustration of the linear-muffin-tin-orbital tight-binding representation: Compact orbitals and charge density in Si”, *Phys. Rev. B* **34**, 5253–5269 (1986).
- ⁴²O. Gunnarsson, O. Jepsen, and O. K. Andersen, “Self-consistent impurity calculations in the atomic-spheres approximation”, *Phys. Rev. B* **27**, 7144–7168 (1983).
- ⁴³H. L. Skriver, “Crystal structure from one-electron theory”, *Phys. Rev. B* **31**, 1909–1923 (1985).
- ⁴⁴L. Vitos, J. Kollár, and H. L. Skriver, “Full charge-density calculation of the surface energy of metals”, *Phys. Rev. B* **49**, 16694–16701 (1994).
- ⁴⁵L. Nordheim, “Zur Elektronentheorie der Metalle. I”, *Ann. Phys. (Berlin)* **401**, 607–640 (1931).
- ⁴⁶B. L. Gyorffy, “Coherent-Potential Approximation for a Nonoverlapping-Muffin-Tin-Potential Model of Random Substitutional Alloys”, *Phys. Rev. B* **5**, 2382–2384 (1972).
- ⁴⁷P. Soven, “Coherent-Potential Model of Substitutional Disordered Alloys”, *Phys. Rev.* **156**, 809–813 (1967).
- ⁴⁸A. Zunger, S.-H. Wei, L. G. Ferreira, and J. E. Bernard, “Special quasirandom structures”, *Phys. Rev. Lett.* **65**, 353–356 (1990).
- ⁴⁹K. Koepnik and H. Eschrig, “Full-potential nonorthogonal local-orbital minimum-basis band-structure scheme”, *Phys. Rev. B* **59**, 1743–1757 (1999).
- ⁵⁰H. Eschrig, M. Richter, and I. Opahle, “Chapter 12 - Relativistic Solid State Calculations”, in *Theoretical and Computational Chemistry*, Vol. 14, edited by P. Schwerdtfeger, Relativistic Electronic Structure Theory (Elsevier, Jan. 2004), pp. 723–776.
- ⁵¹M. H. Kryder, E. C. Gage, T. W. McDaniel, W. A. Challener, R. E. Rottmayer, G. Ju, Y.-T. Hsia, and M. F. Erden, “Heat Assisted Magnetic Recording”, *Proc. IEEE* **96**, 1810–1835 (2008).
- ⁵²P. Alippi, P. M. Marcus, and M. Scheffler, “Strained Tetragonal States and Bain Paths in Metals”, *Phys. Rev. Lett.* **78**, 3892–3895 (1997).
- ⁵³T. Burkert, L. Nordström, O. Eriksson, and O. Heinonen, “Giant Magnetic Anisotropy in Tetragonal FeCo Alloys”, *Phys. Rev. Lett.* **93**, 027203 (2004).

- ⁵⁴A. Winkelmann, M. Przybylski, F. Luo, Y. Shi, and J. Barthel, “Perpendicular Magnetic Anisotropy Induced by Tetragonal Distortion of FeCo Alloy Films Grown on Pd(001)”, *Phys. Rev. Lett.* **96**, 257205 (2006).
- ⁵⁵F. Yildiz, M. Przybylski, and J. Kirschner, “Volume contribution to perpendicular anisotropy in Fe_{0.5}Co_{0.5} alloy films on Pd(001), Ir(001), and Rh(001)”, *J. Appl. Phys.* **105**, 07E129 (2009).
- ⁵⁶F. Yildiz, M. Przybylski, X.-D. Ma, and J. Kirschner, “Strong perpendicular anisotropy in Fe_{1-x}Co_x alloy films epitaxially grown on mismatching Pd(001), Ir(001), and Rh(001) substrates”, *Phys. Rev. B* **80**, 064415 (2009).
- ⁵⁷F. Luo, X. L. Fu, A. Winkelmann, and M. Przybylski, “Tuning the perpendicular magnetic anisotropy in tetragonally distorted Fe_xCo_{1-x} alloy films on Rh (001) by varying the alloy composition”, *Appl. Phys. Lett.* **91**, 262512 (2007).
- ⁵⁸G. Andersson, T. Burkert, P. Warnicke, M. Björck, B. Sanyal, C. Chacon, C. Zlotea, L. Nordström, P. Nordblad, and O. Eriksson, “Perpendicular Magnetocrystalline Anisotropy in Tetragonally Distorted Fe-Co Alloys”, *Phys. Rev. Lett.* **96**, 037205 (2006).
- ⁵⁹P. Warnicke, G. Andersson, M. Björck, J. Ferré, and P. Nordblad, “Magnetic anisotropy of tetragonal FeCo/Pt(001) superlattices”, *J. Phys.: Condens. Matter* **19**, 226218 (2007).
- ⁶⁰G. Andersson, M. Björck, H. Lidbaum, B. Sanyal, C. Chacon, C. Zlotea, and S. Valizadeh, “Structure of Fe–Co/Pt(001) superlattices: a realization of tetragonal Fe–Co alloys”, *J. Phys.: Condens. Matter* **19**, 016008 (2006).
- ⁶¹C. Neise, S. Schönecker, M. Richter, K. Koepernik, and H. Eschrig, “The effect of chemical disorder on the magnetic anisotropy of strained Fe–Co films”, *Phys. Status Solidi B* **248**, 2398–2403 (2011).
- ⁶²I. Turek, J. Kudrnovský, and K. Carva, “Magnetic anisotropy energy of disordered tetragonal Fe-Co systems from ab initio alloy theory”, *Phys. Rev. B* **86**, 174430 (2012).
- ⁶³S. Steiner, S. Khmelevskiy, M. Marsmann, and G. Kresse, “Calculation of the magnetic anisotropy with projected-augmented-wave methodology and the case study of disordered Fe_{1-x}Co_x alloys”, *Phys. Rev. B* **93**, 224425 (2016).
- ⁶⁴L. Reichel, G. Giannopoulos, S. Kauffmann-Weiss, M. Hoffmann, D. Pohl, A. Edström, S. Oswald, D. Niarchos, J. Ruzs, L. Schultz, and S. Fähler, “Increased magnetocrystalline anisotropy in epitaxial Fe-Co-C thin films with spontaneous strain”, *J. Appl. Phys.* **116**, 213901 (2014).
- ⁶⁵E. K. Delczeg-Czirjak, A. Edström, M. Werwiński, J. Ruzs, N. V. Skorodumova, L. Vitos, and O. Eriksson, “Stabilization of the tetragonal distortion of Fe_xCo_{1-x} alloys by C impurities: A potential new permanent magnet”, *Phys. Rev. B* **89**, 144403 (2014).
- ⁶⁶M. H. Han, W. J. Kim, E. K. Lee, H. Kim, S. Lebègue, and J. J. Kozak, “Theoretical study of the microscopic origin of magnetocrystalline anisotropy in Fe₁₆N₂ and its alloys: comparison with the other L1₀ alloys”, *J. Phys.: Condens. Matter* **32**, 035801 (2019).
- ⁶⁷S. Uchida, T. Kawakatsu, A. Sekine, and T. Ukai, “Magnetocrystalline anisotropy energies of Fe₁₆N₂ and Fe₁₆C₂”, *J. Magn. Magn. Mater.* **310**, 1796–1798 (2007).

- ⁶⁸L. Reichel, L. Schultz, D. Pohl, S. Oswald, S. Fähler, M. Werwiński, A. Edström, E. K. Delczeg-Czirjak, and J. Ruzs, “From soft to hard magnetic Fe–Co–B by spontaneous strain: a combined first principles and thin film study”, *J. Phys.: Condens. Matter* **27**, 476002 (2015).
- ⁶⁹G. Giannopoulos, R. Salikhov, G. Varvaro, V. Psycharis, A. M. Testa, M. Farle, and D. Niarchos, “Coherently strained [Fe–Co(C)/Au–Cu]_n multilayers: a path to induce magnetic anisotropy in Fe–Co films over large thicknesses”, *J. Phys. D: Appl. Phys.* **51**, 055009 (2018).
- ⁷⁰G. Giannopoulos, R. Salikhov, B. Zingsem, A. Markou, I. Panagiotopoulos, V. Psycharis, M. Farle, and D. Niarchos, “Large magnetic anisotropy in strained Fe/Co multilayers on AuCu and the effect of carbon doping”, *APL Mater.* **3**, 041103 (2015).
- ⁷¹L. Reichel, L. Schultz, and S. Fähler, “Lattice relaxation studies in strained epitaxial Fe–Co–C films”, *J. Appl. Phys.* **117**, 17C712 (2015).
- ⁷²D. Odkhuu and S. C. Hong, “First-Principles Prediction of Possible Rare-Earth Free Permanent Magnet of Tetragonal FeCo with Enhanced Magnetic Anisotropy and Energy Product through Interstitial Nitrogen”, *Phys. Rev. Appl.* **11**, 054085 (2019).
- ⁷³N. J. Szymanski, V. Adhikari, M. A. Willard, P. Sarin, D. Gall, and S. V. Khare, “Prediction of improved magnetization and stability in Fe₁₆N₂ through alloying”, *J. Appl. Phys.* **126**, 093903 (2019).
- ⁷⁴S. Kikkawa and Y. Masubuchi, “Magnetic iron nitrides inspired by historic research on α''-Fe₁₆N₂”, *J. Solid State Chem.* **51**, 19–26 (2018).
- ⁷⁵M. Kim, “Periodicity Dependence of Magnetic Anisotropy and Magnetization of FeCo Heterostructure”, *J. Magn.* **21**, 6–11 (2016).
- ⁷⁶A. Sakuma, “First-principles study on the effects of atomic configuration on the magnetic anisotropy energy of (Fe,Co)₁₆(N,C)₂ alloys”, *J. Appl. Phys.* **133**, 205102 (2023).
- ⁷⁷I. Galanakis, P. M. Oppeneer, P. Ravindran, L. Nordström, P. James, M. Alouani, H. Dreyse, and O. Eriksson, “Sign reversal of the orbital moment via ligand states”, *Phys. Rev. B* **63**, 172405 (2001).
- ⁷⁸J. Snarski-Adamski, J. Rychły, and M. Werwiński, “Magnetic properties of 3d, 4d, and 5d transition-metal atomic monolayers in Fe/TM/Fe sandwiches: Systematic first-principles study”, *J. Magn. Magn. Mater.* **546**, 168828 (2022).
- ⁷⁹M. Werwiński, A. Edström, J. Ruzs, D. Hedlund, K. Gunnarsson, P. Svedlindh, J. Cedervall, and M. Sahlberg, “Magnetocrystalline anisotropy of Fe₅PB₂ and its alloys with Co and 5d elements: A combined first-principles and experimental study”, *Phys. Rev. B* **98**, 214431 (2018).
- ⁸⁰A. Edström, M. Werwiński, D. Iuşan, J. Ruzs, O. Eriksson, K. P. Skokov, I. A. Radulov, S. Ener, M. D. Kuz'min, J. Hong, M. Fries, D. Y. Karpenkov, O. Gutfleisch, P. Toson, and J. Fidler, “Magnetic properties of (Fe_{1-x}Co_x)₂B alloys and the effect of doping by 5d elements”, *Phys. Rev. B* **92**, 174413 (2015).
- ⁸¹M. Zakotnik, I. R. Harris, and A. J. Williams, “Multiple recycling of NdFeB-type sintered magnets”, *J. Alloys Compd.* **469**, 314–321 (2009).

- ⁸²B. Sprecher, Y. Xiao, A. Walton, J. Speight, R. Harris, R. Kleijn, G. Visser, and G. J. Kramer, “Life Cycle Inventory of the Production of Rare Earths and the Subsequent Production of NdFeB Rare Earth Permanent Magnets”, *Environ. Sci. Technol.* **48**, 3951–3958 (2014).
- ⁸³Y. Yang, A. Walton, R. Sheridan, K. Güth, R. Gauß, O. Gutfleisch, M. Buchert, B.-M. Steenari, T. Van Gerven, P. T. Jones, and K. Binnemans, “REE Recovery from End-of-Life NdFeB Permanent Magnet Scrap: A Critical Review”, *J. Sustain. Metall.* **3**, 122–149 (2017).
- ⁸⁴N. Hai, N. Dempsey, and D. Givord, “Magnetic properties of hard magnetic FePt prepared by cold deformation”, *IEEE Trans. Magn.* **39**, 2914–2916 (2003).
- ⁸⁵C.-b. Rong, D. Li, V. Nandwana, N. Poudyal, Y. Ding, Z. L. Wang, H. Zeng, and J. P. Liu, “Size-Dependent Chemical and Magnetic Ordering in L1₀-FePt Nanoparticles”, *Adv. Mater.* **18**, 2984–2988 (2006).
- ⁸⁶S. Mandal, M. Debata, P. Sengupta, and S. Basu, “L1₀ FeNi: a promising material for next generation permanent magnets”, *Crit. Rev. Solid State* **48**, 703–725 (2023).
- ⁸⁷K. Takanashi, M. Mizuguchi, T. Kojima, and T. Tashiro, “Fabrication and characterization of L1₀-ordered FeNi thin films”, *J. Phys. D: Appl. Phys.* **50**, 483002 (2017).
- ⁸⁸H. An, K. Ando, Y. Nakamura, and J. Shi, “Formation and Perpendicular Magnetic Coupling of A1 and L1₀ CoPt in CoPt/TiN Films on Glass Substrate”, *IEEE Trans. Magn.* **55**, 1–4 (2019).
- ⁸⁹*HAMR / Seagate US*, <https://www.seagate.com/innovation/hamr/>.
- ⁹⁰J. Marciniak, M. Werwiński, and J. Rychły-Gruszecka, “First-principles study of the magnetic anisotropy of ultrathin B-, C-, and N-doped FeCo films”, *J. Magn. Magn. Mater.* **589**, 171563 (2024).
- ⁹¹J. Marciniak and M. Werwiński, “L1₀ FePt thin films with tilted and in-plane magnetic anisotropy: A first-principles study”, *Phys. Rev. B* **108**, 214406 (2023).

Appendices

A Co-authors contribution statements

This appendix contains contribution statements of the co-authors, according to the Contributor Roles Taxonomy (CRrediT). Part of the files are signed with electronic signature and, as such, were not modified in any way, e.g., to include the external page numbering. Hence, for consistency, all pages are not externally numbered.

dr hab. inż. Agnieszka Grabias
Łukasiewicz – Institute of Microelectronics and Photonics
Al. Lotników 32/46
02-668 Warszawa

Warszawa, 20.09.2024

Research article co-author contribution statement

I declare that in the following publication:

A. Musiał, W. Marciniak, Z. Śniadecki, M. Werwiński, P. Kuświk, B. Idzikowski, M. Kołodziej, A. Grabias, M. Kopcewicz, J. Marcin, J. Kováč, *Structural transformation and magnetic properties of $(Fe_{0.7}Co_{0.3})_2B$ alloys doped with 5d elements: A combined first-principles and experimental study*, Journal of Alloys and Compounds 921 (2022) 166047

according to the Contributor Roles Taxonomy (CRediT) author statement, my contributions were: investigation (spectral measurements) and writing – review and editing.

I agree to include the aforementioned work as a part of the PhD thesis of Wojciech M. Marciniak, which consists of a series of scientific articles.

AGrabias

.....
dr hab. inż. Agnieszka Grabias

prof. dr hab. Bogdan Idzikowski
Institute of Molecular Physics
Polish Academy of Sciences
ul. Smoluchowskiego 17
60-179 Poznań

Poznań, September 20, 2024

Research article co-author contribution statement

I declare that in the following publication:

A. Musiał, W. Marciniak, Z. Śniadecki, M. Werwiński, P. Kuświk, B. Idzikowski, M. Kołodziej, A. Grabias, M. Kopcewicz, J. Marcin, J. Kováč, *Structural transformation and magnetic properties of $(Fe_{0.7}Co_{0.3})_2B$ alloys doped with 5d elements: A combined first-principles and experimental study*, Journal of Alloys and Compounds 921 (2022) 166047

according to the Contributor Roles Taxonomy (CRediT) author statement, my contributions were: supervision and writing – review and editing.

I agree to include the aforementioned work as a part of the PhD thesis of Wojciech M. Marciniak, which consists of a series of scientific articles.



prof. dr hab. Bogdan Idzikowski

dr Mieszko Kołodziej
Institute of Molecular Physics
Polish Academy of Sciences
ul. Smoluchowskiego 17
60-179 Poznań

Poznań, 24.09.2024
Place and date

Research article co-author contribution statement

I declare that in the following publication:

A. Musiał, W. Marciniak, Z. Śniadecki, M. Werwiński, P. Kuświk, B. Idzikowski, M. Kołodziej, A. Grabias, M. Kopcewicz, J. Marcin, J. Kováč, *Structural transformation and magnetic properties of $(Fe_{0.7}Co_{0.3})_2B$ alloys doped with 5d elements: A combined first-principles and experimental study*, Journal of Alloys and Compounds 921 (2022) 166047

according to the Contributor Roles Taxonomy (CRediT) author statement, my contributions were: formal analysis and writing - review.

I agree to include the aforementioned work as a part of the PhD thesis of Wojciech M. Marciniak, which consists of a series of scientific articles.

Mieszko Kołodziej
dr Mieszko Kołodziej

Dr. Jozef Kováč
Institute of Experimental Physics
Slovak Academy of Sciences
Watsonova 47
040 01 Kosice, Slovakia

30.9.2024

.....
Place and date

Research article co-author contribution statement

I declare that in the following publication:

A. Musiał, W. Marciniak, Z. Śniadecki, M. Werwiński, P. Kuświk, B. Idzikowski, M. Kołodziej, A. Grabias, M. Kopcewicz, J. Marcin, J. Kováč, *Structural transformation and magnetic properties of $(Fe_{0.7}Co_{0.3})_2B$ alloys doped with 5d elements: A combined first-principles and experimental study*, Journal of Alloys and Compounds 921 (2022) 166047

according to the Contributor Roles Taxonomy (CRediT) author statement, my contribution was investigation (magnetic and thermomagnetic measurements).

I agree to include the aforementioned work as a part of the PhD thesis of Wojciech M. Marciniak, which consists of a series of scientific articles.



.....
Dr. Jozef Kováč

dr hab. Piotr Kuświk, prof. IFM PAN
Institute of Molecular Physics
Polish Academy of Sciences
ul. Smoluchowskiego 17
60-179 Poznań

Poznań, September 20, 2024

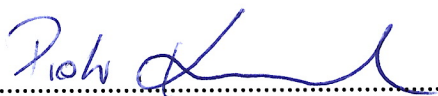
Research article co-author contribution statement

I declare that in the following publication:

A. Musiał, W. Marciniak, Z. Śniadecki, M. Werwiński, P. Kuświk, B. Idzikowski, M. Kołodziej, A. Grabias, M. Kopcewicz, J. Marcin, J. Kováč, *Structural transformation and magnetic properties of $(Fe_{0.7}Co_{0.3})_2B$ alloys doped with 5d elements: A combined first-principles and experimental study*, Journal of Alloys and Compounds 921 (2022) 166047

according to the Contributor Roles Taxonomy (CRediT) author statement, my contribution was: investigation (Scanning electron microscope measurements).

I agree to include the aforementioned work as a part of the PhD thesis of Wojciech M. Marciniak, which consists of a series of scientific articles.



dr hab. Piotr Kuświk, prof. IFM PAN

Dr. Jozef Marcin
Institute of Experimental Physics
Slovak Academy of Sciences
Watsonova 47
040 01 Kosice, Slovakia

KOSICE 30/9/2024
.....
Place and date

Research article co-author contribution statement

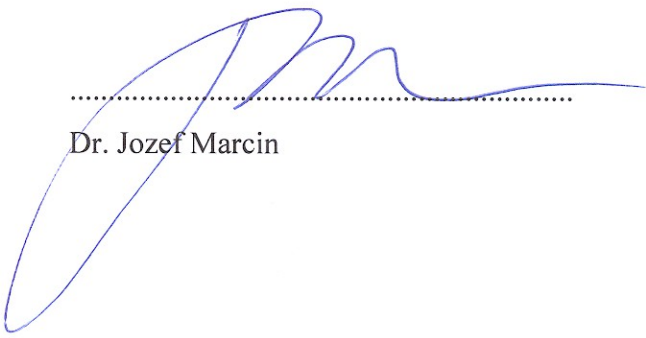
I declare that in the following publication:

A. Musiał, W. Marciniak, Z. Śniadecki, M. Werwiński, P. Kuświk, B. Idzikowski, M. Kołodziej, A. Grabias, M. Kopcewicz, J. Marcin, J. Kováč, *Structural transformation and magnetic properties of $(\text{Fe}_{0.7}\text{Co}_{0.3})_2\text{B}$ alloys doped with 5d elements: A combined first-principles and experimental study*, Journal of Alloys and Compounds 921 (2022) 166047

according to the Contributor Roles Taxonomy (CRediT) author statement, my contribution was investigation (magnetic and thermomagnetic measurements).

I agree to include the aforementioned work as a part of the PhD thesis of Wojciech M. Marciniak, which consists of a series of scientific articles.

.....
Dr. Jozef Marcin



dr Andrzej Musiał
Institute of Molecular Physics
Polish Academy of Sciences
ul. Smoluchowskiego 17
60-179 Poznań

Poznań, September 20, 2024
Place and date

Research article co-author contribution statement

I declare that in the following publication:

A. Musiał, W. Marciniak, Z. Śniadecki, M. Werwiński, P. Kuświk, B. Idzikowski, M. Kołodziej, A. Grabias, M. Kopcewicz, J. Marcin, J. Kováč, *Structural transformation and magnetic properties of $(Fe_{0.7}Co_{0.3})_2B$ alloys doped with 5d elements: A combined first-principles and experimental study*, Journal of Alloys and Compounds 921 (2022) 166047

according to the Contributor Roles Taxonomy (CRediT) author statement, my contributions were: writing – original draft, formal analysis, and investigation.

I agree to include the aforementioned work as a part of the PhD thesis of Wojciech M. Marciniak, which consists of a series of scientific articles.

Andrzej Musiał.....
dr Andrzej Musiał

dr hab. Zbigniew Śniadecki, prof. IFM PAN

Poznań, September 20, 2024

Institute of Molecular Physics

Polish Academy of Sciences

ul. Smoluchowskiego 17

60-179 Poznań

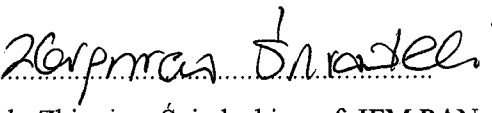
Research article co-author contribution statement

I declare that in the following publication:

A. Musiał, W. Marciniak, Z. Śniadecki, M. Werwiński, P. Kuświk, B. Idzikowski, M. Kołodziej, A. Grabias, M. Kopcewicz, J. Marcin, J. Kováč, *Structural transformation and magnetic properties of $(Fe_{0.7}Co_{0.3})_2B$ alloys doped with 5d elements: A combined first-principles and experimental study*, Journal of Alloys and Compounds 921 (2022) 166047

according to the Contributor Roles Taxonomy (CRediT) author statement, my contributions were: conceptualization, writing – review and editing, and supervision.

I agree to include the aforementioned work as a part of the PhD thesis of Wojciech M. Marciniak, which consists of a series of scientific articles.


.....
dr hab. Zbigniew Śniadecki, prof. IFM PAN

dr hab. Mirosław Werwiński, prof. IFM PAN

Poznań; September 20, 2024

Institute of Molecular Physics

Polish Academy of Sciences

ul. Smoluchowskiego 17

60-179 Poznań

Research article co-author contribution statement

I declare that in the following publication:

A. Musiał, W. Marciniak, Z. Śniadecki, M. Werwiński, P. Kuświk, B. Idzikowski, M. Kołodziej, A. Grabias, M. Kopcewicz, J. Marcin, J. Kováč, *Structural transformation and magnetic properties of $(Fe_{0.7}Co_{0.3})_2B$ alloys doped with 5d elements: A combined first-principles and experimental study*, Journal of Alloys and Compounds 921 (2022) 166047

according to the Contributor Roles Taxonomy (CRediT) author statement, my contributions were: writing – review and editing, formal analysis, and investigation (DFT calculations).

I agree to include the aforementioned work as a part of the PhD thesis of Wojciech M. Marciniak, which consists of a series of scientific articles.

Mirosław Werwiński

.....
dr. hab. Mirosław Werwiński, prof. IFM PAN

dr hab. Mirosław Werwiński, prof. IFM PAM
Institute of Molecular Physics
Polish Academy of Sciences
ul. Smoluchowskiego 17
60-179 Poznań, Poland

Poznań, September 25, 2024

Research article co-author contribution statement

I hereby declare that in the work:

W. Marciniak and M. Werwiński, *Structural and magnetic properties of Fe-Co-C alloys with tetragonal deformation: A first-principles study*, Phys. Rev. B 108, 214433 (2023),

I contributed in the following ways, according to the Contributor Roles Taxonomy (**CRedit**) guidelines: **Conceptualization**, **Resources** (Access to the Poznań Supercomputing and Networking Centre and scientific software licenses), **Writing – review & editing**, **Supervision**, **Project administration**, and **Funding acquisition**.

I also confirm that I am aware of, and I agree to include the aforementioned work as a part of the PhD thesis of Wojciech M. Marciniak, which consists of a series of research articles.

.....
dr hab. Mirosław Werwiński, prof. IFM PAN

Joanna Marciniak
Institute of Molecular Physics
Polish Academy of Sciences
ul. Smoluchowskiego 17
60-179 Poznań, Poland

Poznań, October 14, 2024

Research article co-author contribution statement

I hereby declare that in the work:

W. Marciniak, J. Marciniak, J. Á. Castellanos-Reyes, and M. Werwiński, *Giant magnetocrystalline anisotropy energy in Fe-Co alloy under uniaxial compression: first-principles prediction*, *arXiv preprint*, 10.48550/arXiv.2409.11388 (2024),

I contributed in the following ways, according to the Contributor Roles Taxonomy (**CRedit**) guidelines: **Investigation** (optimizing structures in FPLO5 and MAE calculation on these structures in SPR-KKR), **Formal Analysis** (of the mentioned data), **Validation**, and **Writing – review & editing**.

I also confirm that I am aware of, and I agree to include the aforementioned work as a part of the PhD thesis of Wojciech M. Marciniak, which consists of a series of research articles.

.....
Joanna Marciniak

dr hab. Mirosław Werwiński, prof. IFM PAM
Institute of Molecular Physics
Polish Academy of Sciences
ul. Smoluchowskiego 17
60-179 Poznań, Poland

Poznań, September 25, 2024

Research article co-author contribution statement

I hereby declare that in the work:

W. Marciniak, J. Marciniak, J. Á. Castellanos-Reyes, and M. Werwiński, *Giant magnetocrystalline anisotropy energy in Fe–Co alloy under uniaxial compression: first-principles prediction, arXiv preprint*, 10.48550/arXiv.2409.11388 (2024),

I contributed in the following ways, according to the Contributor Roles Taxonomy (**CRedit**) guidelines: **Conceptualization**, **Resources** (Access to the Poznań Supercomputing and Networking Centre and scientific software licenses), **Writing – review & editing**, **Supervision**, **Project administration**, and **Funding acquisition**.

I also confirm that I am aware of, and I agree to include the aforementioned work as a part of the PhD thesis of Wojciech M. Marciniak, which consists of a series of research articles.

.....
dr hab. Mirosław Werwiński, prof. IFM PAN



UPPSALA
UNIVERSITET

Dr. José Ángel CASTELLANOS-REYES
Postdoctoral Researcher
Department of Physics and Astronomy
Uppsala University
Box 516, 75120 Uppsala, Sweden
✉ angel.castellanos.research@gmail.com
☎ +46 733676648

To

dr hab. Mirosław SZYBOWICZ, prof. PUT

Head of the Materials Engineering and Technical Physics Discipline Council
Poznań University of Technology
5 M. Skłodowska-Curie Square
60-965 Poznan, Poland

Research article co-author contribution statement

September 18, 2024

Dear Professor Szybowicz,

I hereby declare that I contributed to the work W. Marciniak, J. Marciniak, J. Á. Castellanos-Reyes, M. Werwiński, *Giant magnetocrystalline anisotropy energy in Fe-Co alloy under uniaxial compression: first-principles prediction*, arXiv preprint, 10.48550/arXiv.2409.11388 (2024) in the following ways, according to the Contributor Roles Taxonomy (**CRedit**) guidelines:

Investigation/Validation and **Analysis** regarding UppASD calculations of the critical temperature, **Writing - Original Draft** in parts related to the aforementioned calculations, and **Writing - Review & Editing** of the whole manuscript.

I also confirm that I am aware of and agree to include the aforementioned work as a part of the PhD thesis of Wojciech M. Marciniak, which consists of a series of scientific articles.

A handwritten signature in blue ink, appearing to read 'José Ángel Castellanos-Reyes'.

Sincerely,
Dr. José Ángel Castellanos-Reyes

Joanna Marciniak
Institute of Molecular Physics
Polish Academy of Sciences
ul. Smoluchowskiego 17
60-179 Poznań, Poland

Poznań, October 14, 2024

Research article co-author contribution statement

I hereby declare that in the work:

J. Marciniak, W. Marciniak, and M. Werwiński, *DFT calculation of intrinsic properties of magnetically hard phase $L1_0$ FePt*, Journal of Magnetism and Magnetic Materials 556, 169347 (2022),

I contributed in the following ways, according to the Contributor Roles Taxonomy (**CRedit**) guidelines: **Conceptualization**, **Investigation**, **Formal analysis** (FPLO calculations), **Data curation** (FPLO calculations), **Visualization**, and **Writing - original draft**.

I also confirm that I am aware of, and I agree to include the aforementioned work as a part of the PhD thesis of Wojciech M. Marciniak, which consists of a series of research articles.

.....
Joanna Marciniak

dr hab. Mirosław Werwiński, prof. IFM PAM
Institute of Molecular Physics
Polish Academy of Sciences
ul. Smoluchowskiego 17
60-179 Poznań, Poland

Poznań, September 25, 2024

Research article co-author contribution statement

I hereby declare that in the work:

J. Marciniak, W. Marciniak, and M. Werwiński, *DFT calculation of intrinsic properties of magnetically hard phase $L1_0$ FePt*, Journal of Magnetism and Magnetic Materials 556, 169347 (2022),

I contributed in the following ways, according to the Contributor Roles Taxonomy (**CRedit**) guidelines: **Conceptualization**, **Validation** (Both FPLO and SPR-KKR calculations), **Resources** (Access to the Poznań Supercomputing and Networking Centre and scientific software licenses), **Writing – review & editing**, **Supervision**, **Project administration**, and **Funding acquisition**.

I also confirm that I am aware of, and I agree to include the aforementioned work as a part of the PhD thesis of Wojciech M. Marciniak, which consists of a series of research articles.

.....
dr hab. Mirosław Werwiński, prof. IFM PAN

dr hab. Anna Bajorek, prof. UŚ
Institute of Physics
University of Silesia in Katowice
75 Pułku Piechoty 1A
41-500 Chorzów

Katowice, 22/09/2024

.....
Place and date

Research article co-author contribution statement

I declare that in the following publication:

W. Marciniak, G. Chełkowska, A. Bajorek, A. Kowalczyk, A. Szajek, M. Werwiński, *Electronic structure of YbFe₄Al₈ antiferromagnet: A combined X-ray photoelectron spectroscopy and first-principles study*, Journal of Alloys and Compounds 910 (2022) 164478.

my contributions were: conceptualization, experimental investigation, verification of the results, formal analysis, writing and editing of the manuscript.

I agree to include the aforementioned work as a part of the PhD thesis of Wojciech M. Marciniak, which consists of a series of scientific articles.


.....
dr hab. Anna Bajorek, prof. UŚ

prof. dr hab. Grażyna Chełkowska
Institute of Physics
University of Silesia in Katowice
75 Pułku Piechoty 1A
41-500 Chorzów

Research article co-author contribution statement

I declare that in the following publication:

W. Marciniak, G. Chełkowska, A. Bajorek, A. Kowalczyk, A. Szajek, M. Werwiński, *Electronic structure of YbFe₄Al₈ antiferromagnet: A combined X-ray photoelectron spectroscopy and first-principles study*, Journal of Alloys and Compounds 910 (2022) 164478.

my contributions were: conceptualization, experimental investigation, verification of the results, formal analysis, writing and editing of the manuscript.

I agree to include the aforementioned work as a part of the PhD thesis of Wojciech M. Marciniak, which consists of a series of scientific articles.

.....

prof. dr hab. Grażyna Chełkowska

Dr. hab. Andrzej Kowalczyk, prof. IFM PAN

Poznań, September 30, 2024

Institute of Molecular Physics

Polish Academy of Sciences

ul. Smoluchowskiego 17

60-179 Poznań

Research article co-author contribution statement

I declare that in the following publication:

W. Marciniak, G. Chelkowska, A. Bajorek, A. Kowalczyk, A. Szajek, M. Werwiński, *Electronic structure of YbFe₄Al₈ antiferromagnet: A combined X-ray photoelectron spectroscopy and first-principles study*, Journal of Alloys and Compounds 910 (2022) 164478.

my contributions were: conceptualization, experimental investigation, verification of the results, formal analysis, writing and editing of the manuscript.

I agree to include the aforementioned work as a part of the PhD thesis of Wojciech M. Marciniak, which consists of a series of scientific articles.



.....
Dr. hab. Andrzej Kowalczyk, prof. IFM PAN

dr hab. Andrzej Szajek, prof. IFM PAN
Instytut Fizyki Molekularnej
Polskiej Akademii Nauk
ul. Smoluchowskiego 17
60-179 Poznań

Poznań, September 20, 2024

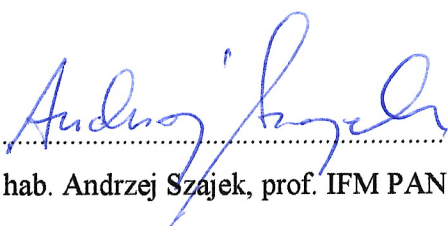
Research article co-author contribution statement

I declare that in the following publication:

W. Marciniak, G. Chełkowska, A. Bajorek, A. Kowalczyk, A. Szajek, M. Werwiński, *Electronic structure of YbFe₄Al₈ antiferromagnet: A combined X-ray photoelectron spectroscopy and first-principles study*, Journal of Alloys and Compounds 910 (2022) 164478.

my contributions were: conceptualization, initial set of DFT calculations, verification of the computational results, formal analysis, writing and editing of the related parts of the manuscript.

I agree to include the aforementioned work as a part of the PhD thesis of Wojciech M. Marciniak, which consists of a series of scientific articles.



.....
Dr. hab. Andrzej Szajek, prof. IFM PAN

dr hab. Mirosław Werwiński, prof. IFM PAN
Institute of Molecular Physics
Polish Academy of Sciences
ul. Smoluchowskiego 17
60-179 Poznań

Poznań; October 21, 2024

Research article co-author contribution statement

I declare that in the following publication:

W. Marciniak, G. Chełkowska, A. Bajorek, A. Kowalczyk, A. Szajek, M. Werwiński, *Electronic structure of YbFe₄Al₈ antiferromagnet: A combined X-ray photoelectron spectroscopy and first-principles study*, Journal of Alloys and Compounds 910 (2022) 164478

I contributed in the following ways, according to the Contributor Roles Taxonomy (CRediT) guidelines: Conceptualization, Validation, Investigation (part of FPLO calculations), Formal analysis (part), Resources (Access to the Poznań Supercomputing and Networking Centre and scientific software licenses), Writing – review & editing, Supervision, Project administration, and Funding acquisition.

I agree to include the aforementioned work as a part of the PhD thesis of Wojciech M. Marciniak, which consists of a series of scientific articles.

.....

dr hab. Mirosław Werwiński, prof. IFM PAN